Exploiting Nonlinearity in Optical Fibres and Nanomaterials for Short-Pulse Laser Technology

Robert I. Woodward

Femtosecond Optics Group
Department of Physics
Imperial College London
United Kingdom

Thesis submitted for the degree of Doctor of Philosophy
and for the Diploma of Imperial College

November 2015

For my family

The copyright of this thesis rests with the author and is made available under a Creative Commons Attribution-Non Commercial-No Derivatives licence. Researchers are free to copy, distribute or transmit the thesis on the condition that they attribute it, that they do not use it for commercial purposes and that they do not alter, transform or build upon it. For any reuse or distribution, researchers must make clear to others the license terms of this work.

The work presented in this thesis was conducted from October 2012 to October 2015, submitted in November 2015 and revised in March 2016. All work is original, except where the contributions of others are explicitly referenced and acknowledged in the text.

Robert Woodward
London, UK

ABSTRACT

The importance of short-pulse laser technology in all branches of science and engineering continues to grow, increasing demands on their performance. In this thesis, we explore approaches for advancing such technologies using optical nonlinearity in emerging nanomaterials and fibres to manipulate the spectral and temporal properties of light.

Firstly, we introduce a long-cavity mode-locked fibre laser architecture for generating high-energy pulses with a giant chirp at low repetition rates. Chirped fibre Bragg gratings are developed for pulse compression (and peak-power enhancement) by a factor of a hundred and the system is shown to be an ideal pump source for low-threshold supercontinuum generation in photonic crystal fibre (PCF). Experimental work is supported by numerical simulations to reveal insight into the pulse dynamics.

Two-dimensional nanomaterials, specifically few-layer transition metal dichalcogenides such as MoS_2 are then considered. We report a harmonic generation microscopy technique for rapidly characterising the structure and optical properties of nanomaterial samples. These materials are then integrated into fibre lasers to act as saturable absorbers for pulse generation by Q-switching and mode-locking. We present a range of sources with pulse durations from femtoseconds to microseconds and kilohertz to megahertz repetition rates, operating throughout the near-infrared, highlighting the wide parameter space that can be accessed. We also propose a theory based on edge states to explain the wideband saturable absorption.

Finally, we study stimulated Brillouin scattering in PCF with a focus on the role of acoustic dynamics. With careful choice of wavelength relative to the microstructured fibre length scales, PCFs are shown to exhibit a stronger Brillouin response than conventional fibre, which we use to develop a compact self-mode-locked Brillouin laser.

We conclude that emerging nanomaterials and optical fibre designs could be leveraged to yield tangible benefits for short-pulse laser technology and we place our results in context of ongoing research.

ACKNOWLEDGEMENTS

First and foremost, I thank Prof. Roy Taylor for his excellent guidance, supervision and support, which have made my time in the Femtosecond Optics Group both highly interesting and enjoyable. His wisdom, generosity and vast knowledge, coupled with a sharp sense of humour, have been much appreciated. I also thank Dr Sergei Popov for sharing his extensive expertise and experience in industrial photonics.

The PhD process has been made all the more enjoyable with the support and friendship of many good colleagues. Since my first days in the lab, Dr Edmund Kelleher has provided great support and tuition as the resident postdoc, also offering much-appreciated advice on starting a research career. I must thank him particularly for introducing me to Python and the world of numerical modelling. It is in collaboration with Ed that much of the code in this thesis has been developed, which has always been fun and occasionally even useful! Dr Robbie Murray and Tim Runcorn have also been valued team members: Robbie's flair for fashioning complex optomechanical setups from scraps of old kit and Tim's perfectionist's vision for developing practical systems have been invaluable, as has been their company over numerous 'lab beers'. Thanks must also go to group alumni Dr Ben Chapman, Dr Carlos Schmitt Castellani and Dr Meng Zhang, for their encouragement and support in the early days.

A great number of other people at Imperial have also contributed to this work. I thank Martin Kehoe and Simon Johnson in the Optics Workshop for their ability to craft precision components from the roughest of sketches. Thanks also to Paul Brown and Linda Jones, whose company has been regularly enjoyed, with all of the above people, over a wide array of coffees and teas, cakes and biscuits, and glasses of wine and beers.

I have also been fortunate to collaborate with many groups and to travel during my PhD. I am thankful to Prof. Perry Shum for hosting my placement at Nanyang Technological University, Singapore and to Profs Thoroh de Souza and Christiano de Matos for supporting my three-week stay with Mackgraphe, Brazil; both experiences proved academically enriching and highly rewarding. I must also thank Roy for permitting, and even actively supporting, these sustained periods of absence from the lab. Closer to home, I thank Prof. Andrea Ferrari and Dr Tawfique Hasan for their collaboration in fabricating the nanomaterials used in this work and Prof. Raman Kashyap for fibre grating fabrication.

Of course, I am very grateful to my family for their support and encouragement in all that I do, without which none of this would have been possible. Finally, I thank Arisa; her love and companionship are a continual source of inspiration and happiness.

CONTENTS

1 Introduction **1**

1.1 Thesis Overview . . . 2
1.2 Historical Perspective . . . 3
1.3 Light Guidance in Fibre . . . 7
1.3.1 Step-Index Fibre . . . 7
1.3.2 Introduction to Electromagnetism . . . 8
1.3.3 Linear Propagation Effects . . . 9
1.3.4 Nonlinear Propagation Effects . . . 16
1.4 Photonic Crystal Fibre . . . 25
1.5 Short-Pulse Fibre Laser Technology . . . 26
1.5.1 Rare-Earth-Doped Fibre Lasers . . . 27
1.5.2 Short-Pulse Generation . . . 28
1.6 Nanomaterials . . . 32
1.7 Summary . . . 33

2 Simulation of Short-Pulse Fibre Lasers **35**

2.1 Mathematical Description of Optical Pulses . . . 36
2.1.1 Numerical Representation . . . 37
2.1.2 Pulse Visualisation . . . 37
2.2 Propagation Modes of Optical Fibres . . . 39
2.2.1 Step-Index Fibre . . . 39
2.2.2 Photonic Crystal Fibre . . . 42
2.3 Pulse Propagation using a Generalised Nonlinear Schrödinger Equation . 45
2.3.1 Linear Effects . . . 47
2.3.2 Nonlinear Effects . . . 48
2.3.3 Numerical Solution . . . 49
2.3.4 Modelling Noise . . . 51
2.4 Rare-Earth Doped Fibre Amplifiers . . . 51
2.4.1 Spectroscopy of Ytterbium . . . 52
2.4.2 Modelling Pulse Amplification . . . 53
2.5 Complete Model of a Mode-Locked Soliton Laser . . . 55
2.5.1 Laser Design . . . 55
2.5.2 Simulation Results . . . 56
2.5.3 Experimental Comparisons . . . 58

2.6 Summary . . . 58

3 Long-Cavity Mode-Locked Lasers 61

3.1 Introduction: Pulse Shaping in Mode-Locked Lasers . . . 62
3.1.1 Historical Perspective . . . 62
3.1.2 State of the Art . . . 64
3.2 Long-Cavity Chirped-Pulse Generation . . . 66
3.2.1 Results and Discussion . . . 66
3.2.2 Numerical Simulations . . . 70
3.2.3 Scalar Nanosecond Chirped-Pulse Generation . . . 73
3.3 Pulse Compression by Chirp Compensation . . . 77
3.3.1 CFBG Design and Fabrication . . . 83
3.3.2 Modelling of CFBG Properties . . . 87
3.3.3 Improved Experimental Compression . . . 92
3.4 Supercontinuum Generation with Long-Cavity Lasers . . . 94
3.4.1 Introduction to Supercontinuum Generation . . . 94
3.4.2 Experimental Setup and Results . . . 96
3.4.3 Simulation and Discussion . . . 97
3.5 Radiation Build-Up Dynamics . . . 103
3.5.1 Introduction to Dark Solitons . . . 103
3.5.2 Dark Soliton Creation and Decay . . . 105
3.5.3 Interactions and Collisions . . . 109
3.5.4 Discussion . . . 112
3.6 Summary . . . 113

4 Few-Layer Transition Metal Dichalcogenides 115

4.1 Introduction: Optical Properties of Nanomaterials . . . 116
4.1.1 Carbon Nanotubes . . . 116
4.1.2 Graphene . . . 117
4.1.3 Few-Layer Transition Metal Dichalcogenides . . . 118
4.2 Nonlinear Microscopy for Material Characterisation . . . 122
4.2.1 Introduction to Harmonic Generation . . . 123
4.2.2 Harmonic Generation from Surfaces . . . 124
4.2.3 Monolayer and Few-Layer MoS_2 Fabrication . . . 124
4.2.4 Experimental Microscope Setup . . . 126
4.2.5 Polarisation-Resolved Microscopy . . . 130
4.2.6 Determination of Nonlinear Susceptibility . . . 132
4.2.7 Imaging Few-Layer Flakes . . . 138
4.2.8 Discussion and Potential Applications of Nanomaterial-Based Harmonic Generation . . . 141

4.3 Few-Layer MoS_2 as a Wideband Saturable Absorber 142
4.3.1 Brief History of Saturable Absorbers 142
4.3.2 Few-Layer MoS_2-PVA Saturable Absorber Fabrication 148
4.3.3 Q-switched Yb-doped Fibre Laser 153
4.3.4 Mode-locked Er-doped Fibre Laser 155
4.3.5 Edge-State Saturable Absorption 156
4.4 Opportunities for Other Transition Metal Dichalcogenides 159
4.4.1 Q-switched Yb-, Er-, and Tm-doped Fibre Lasers with $MoSe_2$ . . . 160
4.4.2 Visible Short-Pulse Fibre Lasers 163
4.5 Summary 164

5 Stimulated Brillouin Scattering in Photonic Crystal Fibre 167
5.1 Introduction: Brillouin Scattering in Fibre 168
5.1.1 Fundamental Principles 168
5.1.2 Peculiar Observations in Small-Core PCF 170
5.2 Experimental Characterisation of Stimulated Brillouin Scattering 171
5.2.1 Experimental Setup 171
5.2.2 Initial Characterisation 172
5.2.3 Comparison between 532 and 1550 nm Pump Light 175
5.2.4 Modelling Mode Shapes 178
5.2.5 Optoacoustic Interactions 178
5.2.6 Is PCF Advantageous for Stimulated Brillouin Scattering? 180
5.3 Brillouin PCF Laser 181
5.3.1 Laser Design 181
5.3.2 Temporal Dyamics 181
5.4 Summary 184

6 Conclusion and Outlook 185

List of Publications 191

References 195

Acronyms 229

1

INTRODUCTION

"Physics would be dull and life most unfulfilling if all physical phenomena around us were linear. Fortunately, we are living in a nonlinear world. While linearisation beautifies physics, nonlinearity provides excitement in physics."
— Yuen-Ron Shen, *The Principles of Nonlinear Optics*, 1984

The dependence of a material's optical properties upon the intensity of light has given rise to a vast and vibrant field of science – nonlinear optics – where a myriad of fascinating nonlinear phenomena have enabled countless technologies. Progress in nonlinear optics is directly coupled to laser physics: sources of intense coherent light are required to investigate fundamental light-matter interactions, which in turn can be exploited to improve the performance and versatility of such laser systems. Short-pulse lasers are an exemplary case.[1] By utilising nonlinearity, the output of a laser can be transformed from a continuous wave to periodic bursts of light, significantly raising the peak power and creating optical sources that expand the parameter space over which light-matter interactions can be explored.

Short-pulse lasers have been a revolutionary technology, which are now integral tools in science, industry and medicine. While such devices can be developed with a variety of materials and geometries, the fibre laser is one of the most promising: enabling flexible, compact and reliable pulse sources for turn-key operation by the end user.

Optical fibre also presents an ideal platform for nonlinear optics, where the confinement of light over long distances permits the accumulation of significant nonlinear effects. Such phenomena were initially considered detrimental (e.g. in the context of optical fibre communications), although many years of research have transformed the view of nonlinearity from a challenging obstacle to an opportunity for spectral and temporal control of light.

Over the last decade, *photonic crystal fibres* (PCFs) – microstructured fibres enabling precise control of the guidance properties – have evolved from a research topic into

[1] There is no standard definition for the duration of a *short* pulse, but this is generally accepted to describe pulse widths on microsecond timescales or shorter. Pulses shorter than a few picosecond are typically called *ultrashort* and the devices which produce them are known as *ultrafast* lasers.

successful commercial products. The ability to precisely define characteristics such as dispersion enables us to control the magnitude and effect of nonlinearity, presenting substantial opportunities for enhancing short-pulse lasers systems.

More recently, nanomaterials have emerged as a promising platform for nonlinear optics. Quantum confinement in such low-dimensional systems gives rise to completely new physical phenomena and remarkable material properties. In addition to considerable fundamental interest in nanomaterials, they could yield tangible benefits and new photonic devices if their novel properties can be practically harnessed.

Laser technology has advanced at a staggering pace over the last 55 years. However, ever-growing end-user demands for more powerful and versatile devices continue to drive research in this diverse and exciting field. This thesis explores nonlinear optical effects manifesting in fibres and nanomaterials and considers if the opportunities they present could be practically exploited to improve short-pulse fibre laser systems.

1.1 Thesis Overview

This thesis is organised as follows. In this chapter, we introduce the linear and nonlinear optical phenomena governing light propagation in fibre and techniques to generate short pulses. The basic properties of photonic crystal fibres and nanomaterials are also discussed.

Chapter 2 presents the development of numerical models for simulating short-pulse fibre lasers, which have guided much of the experimental work in this thesis. We begin by considering how to treat electromagnetic propagation mathematically then show how to compute the properties of common fibre geometries, how to model amplification in a ytterbium-doped fibre amplifier and how to simulate pulse propagation along lengths of fibre.

In Chapter 3 we introduce a long-cavity laser architecture for the production of highly chirped pulses at a low repetition rate. Techniques to compress these pulses are considered and we demonstrate the system to be an ideal pump source for low-threshold supercontinuum generation in PCF. The nonlinear wave dynamics during radiation build-up in long-cavity lasers are also discussed.

Chapter 4 reports experimental progress in quantifying and exploiting the nonlinear optical properties of few-layer forms of transition metal dichalcogenides, specifically molybdenum disulfide (MoS_2). We develop a nonlinear microscopy technique for in-situ characterisation, then consider the application of the nanomaterial as a saturable absorber for passive pulse generation.

Stimulated Brillouin scattering in PCF is the focus of Chapter 5. Small-core PCFs are considered as a medium to enhance the effect and we discuss the impact of the PCF structure upon acousto-optic interactions. The temporal dynamics of the process are also explored as a means of generating pulses.

Finally, Chapter 6 concludes the thesis with a critical assessment of the opportunities offered by new fibres and nanomaterials for short-pulse laser technology. We also consider

the broader implications of the work and propose possible routes forward.

1.2 Historical Perspective

The 20th century saw rapid progress in optical science and the birth of many new research fields including fibre optics, laser physics and nonlinear optics. Here, we present a brief history of fibre laser technology but note that the full story, including contributions from thousands of scientists and engineers, is unfortunately beyond the scope of this section. For a more detailed account, Refs. [Tow99, Hec04, Tay07, Hec10] are recommended to the interested reader.

Laser Development

In May 1960, Ted Maiman demonstrated the first laser – *light amplification by stimulated emission of radiation* – producing a coherent beam of light from a flashlamp-pumped ruby crystal [Mai60]. This was made possible by many earlier pioneering contributions including Albert Einstein's theory of stimulated emission [Ein17], the development of the maser [Gor55] and Charles Townes and Arthur Schawlow's theory of optical masers [Sch58], not to mention the efforts of independent inventor Gordon Gould who coined the term 'laser' [Tay07].

After the first demonstration of coherent light from Maiman's laser, the field advanced rapidly and ruby lasers were available commercially within a year, quickly finding medical applications [Hec10]. Many other types of laser soon emerged, including gas lasers (the Helium-Neon laser was also the first laser to operate continuously rather than with pulsed excitation [Jav61]), glass lasers [Sni61b], semiconductor lasers [Hal62] and dye lasers [Sor66], and our understanding of these devices and their performance quickly advanced.

Nonlinear Optics

The invention of the laser enabled new experiments to study the interaction of intense coherent light with matter. The start of this field of nonlinear optics is often taken as Peter Franken's seminal observation of second-harmonic generation in quartz [Fra61]. However, it should be noted that nonlinear optical effects had been observed before this, notably John Kerr's report in 1875 and Friedrich Pockel's work in 1894 which confirmed that the application of a strong field could change a material's refractive index [Ker75, Poc94]. Self-induced nonlinearity (without requiring a strong external field) was also observed as early as 1941 when Gilbert Lewis[2] reported nonlinear fluorescence in an organic dye [Lew41], although the laser undoubtedly catalysed further progress.

[2]Gilbert Lewis's contribution to photonics is particularly notable as he also introduced the word *photon* in a 1926 letter to Nature: "I therefore take the liberty of proposing for this hypothetical new atom, which is not light but plays an essential part in every process of radiation, the name photon" [Lew26].

Many other nonlinear effects were observed and explained such as third-harmonic generation [Ter62], stimulated Raman scattering [Woo62] and stimulated Brillouin scattering [Chi64], leading to the development of new technologies and applications; not least, laser wavelength conversion. Further applications and an entirely new field of *ultrafast science* were enabled by exploiting nonlinear optical effects to develop short-pulse lasers, periodically producing bursts of light through mechanisms which later came to be known as Q-switching [McC62] and mode-locking [Lam64, Har64].

Nonlinear effects are limited by the length of light-matter interaction, which can be small for light passing through bulk materials. Therefore, one technology which opened new opportunities in nonlinear optics with the possibility of propagating light through kilometres of material was the optical fibre.

Optical Fibre

The principle of guiding light by *total internal reflection*, which underpins the operation of optical fibres, was initially demonstrated in a water fountain by Daniel Colladon in 1842 [Col42]. However, it wasn't until the early 20th century that glass fibres were considered as waveguides. Initially, bundles of multimode fibres were proposed [Han27] and demonstrated [Lam30] for transmitting images, targeting medical applications.

However, early fibres suffered from light leakage when in contact with other materials or contaminants. The introduction of a lower-refractive-index cladding layer around the fibre solved this problem [vH54], and the reduced index difference between core and cladding (compared to the difference between a glass core and air cladding) enabled the fabrication of single-mode fibres [Sni59, Ost59]. Meanwhile, growing demands for bandwidth in the telecommunications sector encouraged engineers to consider higher frequencies than radio and microwaves. Optical frequencies and laser sources, combined with the possibility of waveguide transmission, made optical fibres an attractive platform for communications, although the high loss remained a barrier to practical long distance transmission. Charles Kao considered this problem theoretically, concluding in 1966 that the losses were due to impurities and not intrinsic to silica glass; specifically, he proposed that fibre attenuation could be reduced to below 20 dB km $^{-1}$ [Kao66]. This claim stoked great interest around the world and the Corning Glass Works were later able to produce a fibre that met this specification [Kap70]. For his contribution, Kao was awarded the 2009 Nobel Prize in Physics. Another key development for optical fibre communications was the erbium-doped fibre amplifier [Mea87], building upon earlier work by Elias Snitzer on rare-earth-doped fibres [Koe64], which enabled the development of all-fibre lasers without any bulk elements.

Low-loss fibres and increasing output powers from laser sources permitted the propagation of high-power light, confined to a small area, over long distances. Nonlinearity, therefore, was able to play a significant role in the propagation. The field of nonlinear fibre optics was born.

Nonlinear Fibre Optics

The first nonlinear effect to be observed in optical fibres was stimulated Raman scattering [Sto72], shortly followed by stimulated Brillouin scattering [Ipp72b], parametric four-wave mixing [Sto75a] and self-phase modulation [Sto78]. In a seminal contribution from Hasegawa and Tappert, it was realised that optical fibres, through a balance between self-phase modulation and anomalous dispersion [Has73a], could support *soliton* pulses, which are stationary (or periodic) pulse solutions of the nonlinear Schrödinger equation [Zak72]. Experimental verification followed by the end of the decade [Mol80] and soliton pulse shaping effects quickly became commonplace for the control and generation of ultrashort pulses. Compression and optical-switching techniques were also developed using nonlinear fibre-optic effects. Additionally, completely new amplifier and laser designs were developed by exploiting stimulated Raman scattering and four-wave mixing to demonstrate Raman fibre lasers and parametric oscillators, which could access spectral regions that were not covered by common rare-earth dopants [Sto75b, Hil76b, Sto82a].

As it became clear that exploitation of nonlinearity, dispersion and their interplay in fibre could improve the performance of laser systems, researchers began to develop new designs of optical fibre to enhance their nonlinearity or alter the dispersion map. Small, highly germanium-doped cores were employed to enhance the fibre nonlinearity (since germanium has a higher nonlinear coefficient than silica), forming *highly-nonlinear fibre* (HNLF) [Sud86] and the geometry of step-index fibres was tailored to yield particular waveguide dispersion, creating *dispersion-shifted fibre* (DSF) [Coh79]. However, fundamental limitations restricted the parameter space of dispersion, nonlinearity, birefringence etc. that could be accessed by engineering conventional fibre designs.

A breakthrough idea came in 1996, proposing a completely new design of optical fibre: the photonic crystal fibre (PCF) [Kni96]. Inspired by periodic structures suggested by Eli Yablonovitch to create a photonic bandgap crystal [Yab87], Philip Russell realised that low-loss light guidance in a hollow-core fibre could be possible by using a photonic bandgap from a crystal cladding structure. Due to challenges in fabricating such a complex structure, the first PCF with a microstructured cladding was produced with a solid-core, formed by stacking 217 silica capillaries [Kni96]. While the guidance mechanism was still total internal reflection and there was no transmission bandgap, these fibres enabled unprecedented control of their properties: the dispersion, nonlinearity, birefringence and modal content could all be varied over much greater ranges than previously possible, simply by changing the geometry of the cladding microstructure. The original photonic bandgap design was also realised in practice two years later [Cre99].

These new fibres heralded new opportunities in the field of nonlinear fibre optics, helping to push the performance of fibre lasers and systems, enabling completely new devices and applications. Of particular note is *supercontinuum generation*: the extreme spectral broadening of light. Supercontinuum generation depends on a cascade of nonlinear processes which can be controlled by dispersive effects, suggesting PCFs to be an

ideal platform for this purpose, in addition to a testbed for fundamental studies of the underlying nonlinear wave dynamics [Ran00].

Fibre Laser Technology

The benefits of the optical fibre format extend beyond their use as a passive waveguide and platform for nonlinear optics. During the early days of laser research, Elias Snitzer demonstrated neodymium-doped glass rod lasers and proposed fibre cavity designs, which paved the way to fibre lasers [Sni61b, Sni61a]. However, the potential benefits of fibre lasers compared to bulk lasers were not practically realised in this period and industrial application was limited by their low output power and a lack of suitable and compact pump sources.

Fibre laser development accelerated quickly, however, after techniques for adding dopants during the vapour-deposition fabrication process were reported to produce low-loss active silica fibres [Poo85] and semiconductor laser diodes were introduced as pump sources [Mea85]. Notably, this work led to the development of *erbium-doped fibre amplifiers* [Mea87] with an emission window coinciding with the lowest loss region for optical fibre – such devices are still the backbone of long distance optical communication today.

Another important development in doped fibres was the *double-clad* design, including both inner and outer cladding layers [Sni88]. The multimode nature of the inner cladding makes it possible to pump fibre lasers with high-power multimode diodes (offering significantly higher power than single-mode diodes). The pump light then interacts with ions in the smaller doped core to achieve a high-brightness single-mode output. The benefits of the fibre gain medium were also enhanced by the development of fibre-integrated component such as *fused fibre couplers* and *fibre Bragg gratings*, enabling all-fibre alignment-free laser systems [Kaw81, Kas90]. Additionally, many of the aforementioned nonlinear effects have been exploited in fibre to extend the performance and versatility of fibre systems.

Over many years, fibre laser technology has evolved into a mature and commercially successful industry. Recent progress is considered in detail within the chapters of this thesis which address various aspects of the field. Therefore, we conclude this section by noting that the global laser market is now valued at more than $9 billion and short-pulse fibre lasers represent one of the fastest growing sectors, stemming from great success in industrial manufacturing and emerging biomedical opportunities [Ove14]. This has only been possible thanks to the pursuits of generations of scientists and engineers over the last century.

1.3 Light Guidance in Fibre

1.3.1 Step-Index Fibre

Conventional optical fibres consist of a dielectric *core* with refractive index n_{core} enclosed within a dielectric *cladding* layer, which has a slightly lower index n_{clad} (Fig. 1.1). This refractive index profile led to the name *step-index fibres*. Light is guided by total internal reflection at the core-cladding interface, enabling energy to be transferred along the fibre. Typically, the cladding layer material is pure silica and the core is doped silica, including dopants such as germanium, aluminium or phosphorous to increase the refractive index [Agr13].

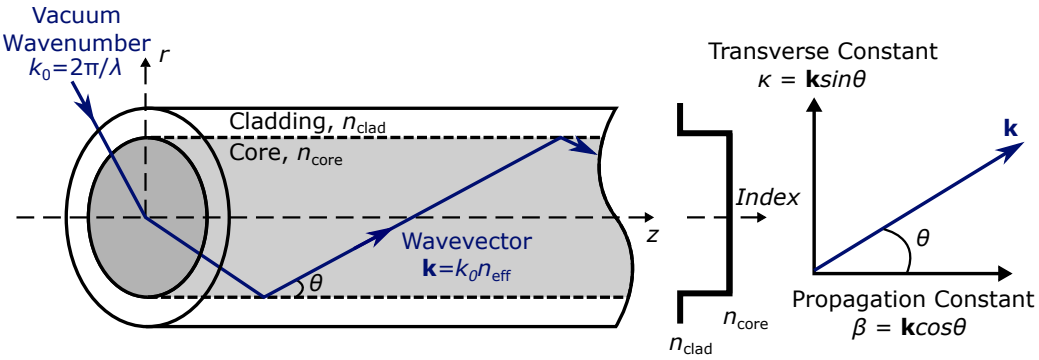


Fig. 1.1: Schematic of a step-index fibre showing the refractive index profile and a propagating ray with the definition of the wavevector and propagation constant. The significance of the effective refractive index n_{eff} is introduced in Section 1.3.3. A fibre can support many rays with different angles θ (dependent on fibre geometry), known as modes, each with a different wavevector.

A simple ray optics picture can be used to describe the propagation of light along the core of a fibre, governed by the geometry of the structure and Snell's law. However, for a more complete description of the optical field, an electromagnetic approach is required to find wave configurations in the fibre which are solutions to Maxwell's equations and satisfy the boundary conditions set by the waveguide structure.

The set of fields meeting this criteria are known as *modes*.[3] The core diameter d_{c} and refractive index step size ($\Delta n = n_{\text{core}} - n_{\text{clad}}$) of a fibre determine the number of supported modes at a given wavelength, which is an important parameter that sets the bandwidth for data transmission and the brightness of a fibre laser source. Single-mode fibres are generally preferred for fibre lasers due to the high brightness and high beam quality of light at the output, which can be focussed to a small diffraction-limited spot. A more detailed discussion of fibre modes and computation of their propagation characteristics is presented in Section 2.2.

[3] Technically, these are *guided modes* with the energy largely confined to the core as light propagates. Fibres also support a continuum of unguided *radiation modes*, where the energy is unconfined and quickly dissipates. Such radiation modes do not contribute to nonlinear effects and are neglected herein.

1.3.2 Introduction to Electromagnetism

James Clerk Maxwell famously identified the connection between electromagnetism and optics in the 1860s, leading to a set of four equations which can be used to describe all electromagnetic phenomena [Max65]:

$$\nabla \cdot \mathbf{D} = \rho \tag{1.3.1a}$$

$$\nabla \cdot \mathbf{B} = 0 \tag{1.3.1b}$$

$$\nabla \times \mathbf{E} = -\frac{\partial \mathbf{B}}{\partial t} \tag{1.3.1c}$$

$$\nabla \times \mathbf{H} = \mathbf{J} + \frac{\partial \mathbf{D}}{\partial t} \tag{1.3.1d}$$

where **D** and **B** are electric and magnetic flux densities, **E** and **H** are the electric and magnetic field vectors, ρ is the charge density, **J** is the current density and t is the time coordinate. The flux densities for an applied field can also be related to induced electric and magnetic polarisations, **P** and **M**, respectively: $\mathbf{D} = \varepsilon_0\mathbf{E} + \mathbf{P}$ and $\mathbf{B} = \mu_0\mathbf{H} + \mathbf{M}$, where ε_0 and μ_0 are the permittivity and permeability of free-space, which are linked to the speed of light in a vacuum by $c = 1/\sqrt{\mu_0\varepsilon_0}$.

For propagation in a non-magnetic (**M**=0) optical waveguide, without charges ($\rho = 0$) or currents (**J**$= 0$), these equations can be simplified to a single *wave equation* [Sny83]:

$$\nabla^2\mathbf{E} - \mu_0\varepsilon_0\frac{\partial^2\mathbf{E}}{\partial t^2} = \mu_0\frac{\partial^2\mathbf{P}}{\partial t^2} \tag{1.3.2}$$

The *electric polarisation* **P** is the dipole moment per unit volume of the medium, resulting from electrons oscillating about their equilibrium positions in response to an oscillating electric field. The strength of the electric field and induced polarisation are related by the *electric susceptibility function* $\boldsymbol{\chi}$ of the material, which can be Taylor expanded into $\boldsymbol{\chi}^{(n)}$ terms, describing the n^{th} order susceptibility [Boy07]:

$$\mathbf{P} = \varepsilon_0\boldsymbol{\chi}\mathbf{E} = \varepsilon_0(\boldsymbol{\chi}^{(1)} \cdot \mathbf{E} + \boldsymbol{\chi}^{(2)} : \mathbf{EE} + \boldsymbol{\chi}^{(3)} \vdots \mathbf{EEE} + ...) \tag{1.3.3}$$

When a material polarisation is induced by a field, the oscillating dipoles can radiate new fields with a phase delay. Since the electric field and induced polarisation are vector quantities, the susceptibilities are tensors. Consequently, Eqn. 1.3.3 can be used to relate the direction of the induced material polarisation (and new radiated fields) to the direction of the incident electric field (i.e. the polarisation of light, where the term polarisation here is, confusingly, a distinct term to the material polarisation). This enables much information about the nonlinear response of materials to be determined by comparing the polarisation of incident light and light generated through nonlinearity, as we demonstrate in Section 4.2.5.

Finally, it should be noted that this mathematical treatment of nonlinearity embeds all the atomic and molecular physics describing the origin of the nonlinear response in the

coefficients $\boldsymbol{\chi}^{(n)}$. For a complete analysis, nonlinearity should be considered quantum mechanically, including the numerous origins (broadly separated into bound-electron and nuclei mechanisms), each on their own timescales. However, in this thesis the use of nonlinear susceptibility coefficients $\boldsymbol{\chi}^{(n)}$ is sufficient to quantitatively describe observed phenomena and provide insight into the underlying physics.

1.3.3 Linear Propagation Effects

Solutions to Maxwell's Wave Equation

A material's response to low-intensity fields can be considered harmonic, resulting in linear polarisation of the material. Eqn. 1.3.3 therefore reduces to $\mathbf{P} = \varepsilon_0 \boldsymbol{\chi}^{(1)} \mathbf{E}$. In this case, the general solution to the wave equation (Eqn. 1.3.2) is a monochromatic plane wave [Agr13]:

$$\mathbf{E}(\mathbf{r}, t) = \mathbf{A} \exp(i[\omega t - \mathbf{k} \cdot \mathbf{r}]) \tag{1.3.4}$$

where $\mathbf{A}$ represents the field amplitude, ω is the angular frequency of light and $\mathbf{k}$ is the wavelength-dependent complex *wavevector*; $\mathbf{r}$ is the spatial position vector and t is the time coordinate.

To simplify the mathematics, we reduce this to a scalar problem by considering the electric field of a wave propagating along the axis (z direction) of a lossless fibre and assume a linear optical polarisation:

$$E(z, t) = A \exp(i[\omega t - \beta z]) \tag{1.3.5}$$

where β is the axial component of the wavevector (as illustrated in Fig. 1.1). This quantity is also known as the *propagation constant*, which describes the wavelength-dependent phase shift per unit propagation distance: $\beta(\omega) = n\omega/c$ where n is the refractive index of the material and c is the speed of light in a vacuum.

By substituting Eqn. 1.3.5 back into the wave equation, the *dispersion relation* is found:

$$\omega^2 = \frac{1}{\varepsilon_0 \mu_0} \frac{\beta^2}{1 + \chi^{(1)}} \tag{1.3.6}$$

which enables the refractive index to be related to the linear susceptibility $\chi^{(1)}$:

$$n(\omega) = \sqrt{1 + \chi^{(1)}(\omega)} \tag{1.3.7}$$

The refractive index is a complex frequency-dependent quantity, which can be expressed in terms of a real and imaginary component, $n(\omega) = n_{\mathrm{re}}(\omega) + i n_{\mathrm{im}}(\omega)$. It follows that the solution to the wave equation can be rewritten to include loss by representing the field as

a travelling wave with an exponentially decaying amplitude:

$$E(z,t) = A \exp\left[\frac{-\alpha z}{2}\right] \exp\left[i(\omega t - \beta z)\right] \tag{1.3.8}$$

where α is the *attenuation coefficient*, as determined by the imaginary part of the refractive index:

$$\alpha = 2\,\frac{\omega}{c}\,n_{\mathrm{im}}(\omega) \tag{1.3.9}$$

and the real part of the refractive index determines the *phase velocity*:

$$v_p = \frac{c}{n_{\mathrm{re}}(\omega)} = \frac{\omega}{\beta(\omega)} \tag{1.3.10}$$

The discussion so far has centred on light propagating in a homogeneous material with refractive index n. In a fibre, however, the field solution can overlap both core and cladding materials and is influenced by the waveguide geometry. Therefore, an *effective* refractive index $n_{\mathrm{eff}}(\omega)$ is used to describe the propagation, and each supported fibre mode will have a different effective index and propagation constant. Additionally, fields consisting of a finite-width spectrum (such as a pulse) can be described by summation of the many monochromatic plane wave solutions to the wave equation within this spectrum.

Chromatic Dispersion

The frequency dependence of the effective refractive index dictates that the phase velocity in a medium depends on the optical wavelength. This effect is known as *chromatic dispersion*, consisting of two contributing effects: *material dispersion* and *waveguide dispersion* [Agr13].

Material dispersion arises from the difference between oscillation amplitudes of the bound electrons in a medium for different incident frequencies, which are related to absorption resonances. For wavelengths far from a resonance, the material refractive index is well approximated by the *Sellmeier equation* [Sel71, Mal65]:

$$n^2(\lambda) = 1 + \sum_j \frac{A_j \lambda^2}{\lambda^2 - B_j^2} \tag{1.3.11}$$

where the coefficients A_j and B_j relate to the strength and wavelength of the j^{th} resonance.

Waveguide dispersion arises because the field of a guided mode is spatially confined and overlaps both core and cladding materials (specifically, this changes the tilt of the wavevector with respect to the fibre axis). The spatial extent of the field is strongly frequency-dependent, thus the effect of the waveguide structure on the phase delay during propagation depends on the wavelength of guided light.

To consider the effect of chromatic dispersion mathematically, the propagation constant,

β, is Taylor expanded about the centre frequency of the propagating light, ω_0 [Agr13]:

$$\beta(\omega) = \beta_0 + \beta_1(\omega - \omega_0) + \frac{1}{2!}\beta_2(\omega - \omega_0)^2 + \frac{1}{3!}\beta_3(\omega - \omega_0)^3 + ... \tag{1.3.12}$$

where

$$\beta_n = \left(\frac{\mathrm{d}^n\beta}{\mathrm{d}\omega^n}\right)_{\omega=\omega_0} \tag{1.3.13}$$

Dispersion has a particularly important effect on *pulsed* light, since narrow pulses possess a broad spectrum. The envelope of the pulse propagates at the group velocity v_g, which is related to the first-order propagation constant term by:

$$v_g = \frac{1}{\beta_1} \tag{1.3.14}$$

The group velocity of different spectral components within the envelope can vary, which is known as *group velocity dispersion* (GVD). This is described by β_2 (ps^2 km^{-1}), which is the derivative of the inverse group velocity with respect to frequency. The GVD of a waveguide is more commonly represented by the*dispersion parameter*, D (ps nm^{-1} km^{-1}) [Agr13]:

$$D = \frac{d\beta_1}{d\lambda} = -\frac{2\pi c}{\lambda^2}\beta_2 \tag{1.3.15}$$

Higher order terms such as third-order dispersion should also be included in a thorough treatment of dispersion, especially in cases where the GVD is almost zero.

A key parameter for fibres is the *zero-dispersion wavelength* (ZDW), as the sign of dispersion D determines the nonlinear phenomena that can be observed. When $D > 0$, low-frequency (long wavelength) waves propagate with greater group velocity than high-frequency light, termed *normal dispersion*. The reverse occurs for $D < 0$, referred to as *anomalous dispersion*.[4]

The impact of these effects is considered for the fundamental mode in a standard step-index telecommunications fibre, such as Corning SMF-28e, with a core diameter $d_c = 8.2$ µm and a refractive index step of $\Delta n = 0.005$ (the numerical modelling procedures to obtain this data and to perform subsequent simulations are presented in Chapter 2). Fig. 1.2 shows the contributions of the silica material and the waveguide geometry to the total effective refractive index and the fibre dispersion. To first-order accuracy, the net dispersion can be found by summing the separate material and waveguide effects [Mar79]. It can be seen that the dominant contribution is from the material, especially at shorter wavelengths, due to strong confinement of light to the core (at wavelengths below 1200 nm, more than 85% of the optical power is in the core).

To elucidate the role of dispersion, we consider its effect on a *transform-limited* pulse. The

[4] 'Normal' and 'anomalous' can also be used to refer to the phase velocity dispersion, rather than the group velocity dispersion. In this case, $\frac{\mathrm{d}n}{\mathrm{d}\lambda} < 0$ indicates normal dispersion (which is exhibited by silica throughout the transparency window). However, as is typical in the fibre-optic community, we use these terms in the context of GVD.

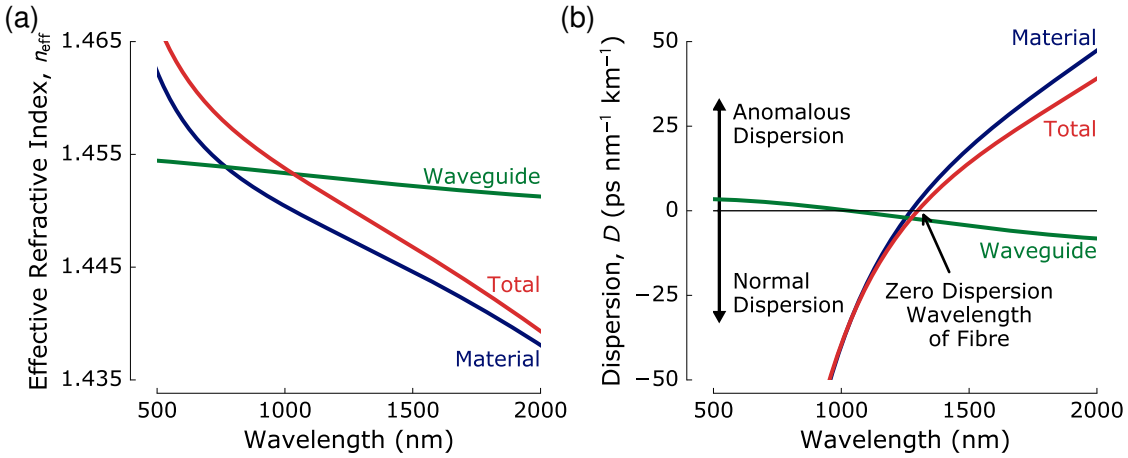


Fig. 1.2: Properties of standard telecommunications fibre showing the contributions of material and waveguide effects (numerically computed): (a) effective refractive index; (b) dispersion.

term transform-limited defines the width of the pulse spectrum as the minimum possible value for the given pulse duration, as mathematically determined by the Fourier transform. Therefore, there is no change in instantaneous frequency across the pulse and if one was to probe the spectral content of a small time-slice of the pulse, the full bandwidth would be observed. However, various optical phenomena can impart a time dependence on the instantaneous frequency, which is known as a *chirp*. Different mathematical definitions of chirp exist in the literature but here, we define the term to be the change in instantaneous frequency (differentiated phase delay with respect to time) about the centre frequency ω_0. This is illustrated in Fig. 1.3: a linearly up-chirped pulse is shown with a gradual change in the instantaneous frequency across its duration, compared to a transform-limited pulse with a constant frequency at all times. It should be noted that both pulses have the same envelope amplitude and thus, the same intensity / power profile (related to the amplitude squared) that could be measured by recording the time-dependent optical power experimentally. This highlights that to fully describe an optical pulse, both the intensity and phase must be known. Another important metric for quantifying pulses is the *time-bandwidth product* (TBP): the product of the pulse duration and spectral width. A minimum value exists for transform-limited pulses, which is 0.315 for sech-shaped envelopes. Chirped pulses will yield higher TBPs [Agr13].

We demonstrate the effect of dispersion by simulating the propagation of a transform-limited sech-shaped pulse, which is described by a time-dependent power profile:

$$P(t) = P_0 \operatorname{sech}^2\left(\frac{t}{t_0}\right) \tag{1.3.16}$$

where P_0 is the peak power, t_0 is the $1/e$ duration, which is related to the *full width at half maximum* (FWHM) pulse duration by $t_{\text{fwhm}} = 1.76\, t_0$. The pulse profile and spectrum for the input pulse with $P_0 = 30$ W and $t_{\text{fwhm}} = 1$ ps, centred at a wavelength of 1550 nm are

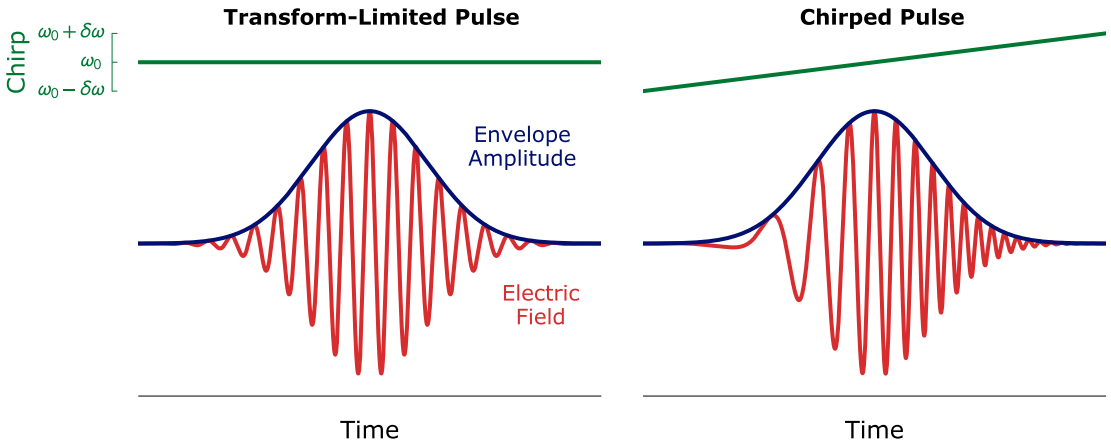


Fig. 1.3: Electric field and envelope amplitudes for a transform-limited and up-chirped pulse. The instantaneous frequency of the field increases with time in the chirped pulse, but is constant in the transform-limited case.

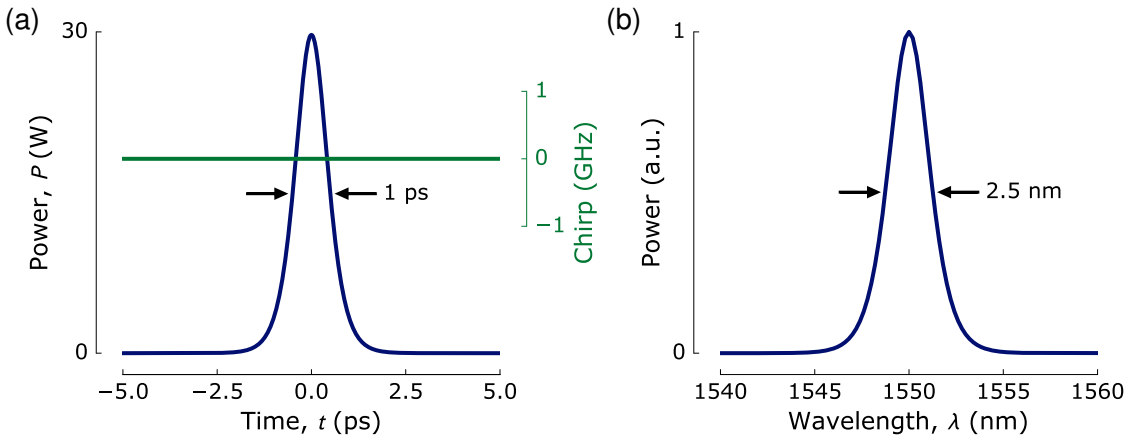


Fig. 1.4: Simulated transform-limited sech-shaped pulse: (a) pulse shape; (b) optical spectrum.

shown in Fig. 1.4.

As this pulse propagates along a fibre with normal dispersion, $D = -15$ ps nm^{-1} km^{-1} (loss and nonlinearity are neglected), the temporal envelope broadens and reduces in amplitude (Fig 1.5a) since different spectral components within the pulse spectrum travel at different group velocities. The total pulse spectrum is unchanged, although dispersion spreads the spectral content linearly throughout the pulse duration. Therefore, the output pulse is up-chirped: the leading part of the pulse contains the longer wavelengths (lower frequencies) and the trailing edge consists of the shorter wavelengths (higher frequencies). If the dispersion is anomalous, $D = +15$ ps nm^{-1} km^{-1}, the output pulse and spectral intensity are identical, although the sign of the frequency sweep is reversed, causing a down-chirp (Fig 1.5b).

Finally, it should be noted that this discussion of dispersion can apply for each guided mode in a fibre. While material dispersion is unchanged, each mode has a different spatial shape and hence, experiences different waveguide dispersion. If an incident pulse excites multiple modes in a fibre, each with different group velocities, this can be a further source of temporal broadening during propagation, known as *intermodal dispersion*.

Attenuation

The intensity of light in a fibre will decrease as it propagates due to various loss mechanisms, which are spectrally dependent (Fig. 1.6). Silica has a transmission window extending from ∼300 to 2400 nm, limited by absorption from electronic resonances at *ultraviolet* (UV) wavelengths and vibrational resonances of the glass network in the *infrared* (IR) region [Wal86]. In addition to increasing absorption near a resonance, the refractive index is increased due to a larger phase delay from the oscillating dipoles. The relationship between absorption and dispersion is expressed by the Kramers-Kronig relations [Kra27, Kro25], and explains the sharp increase in the material refractive index as the wavelength approaches the UV electronic resonance (Fig. 1.2).

Within the transmission window, Rayleigh scattering represents the dominant loss, arising due to random density fluctuations in the amorphous glass structure on sub-wavelength length scales. Additionally, impurities in the fibre can introduce loss peaks: the presence of moisture during fibre manufacture leads to hydrogen bonding to the silica network, producing SiOH groups [Sto82b]. OH has a strong absorption band at ∼2700 nm, and additional absorption peaks arise at harmonic frequencies (known as *overtones*) and from mixing between silica and OH vibration frequencies. These are often called water absorption peaks, of which the strongest contribution is at ∼1384 nm [Sto82b, Wal86]. It should also be noted that light can be attenuated by confinement loss, where energy from the mode leaks out, although this is generally negligible for conventional step-index fibre and is only considered for PCFs. Modern step-index fibres are capable of exhibiting a loss below 0.5 dB km^{-1} from 1200-1700 nm, reducing to ∼0.2 dB km^{-1} in the telecommunications band around 1550 nm [Agr13].

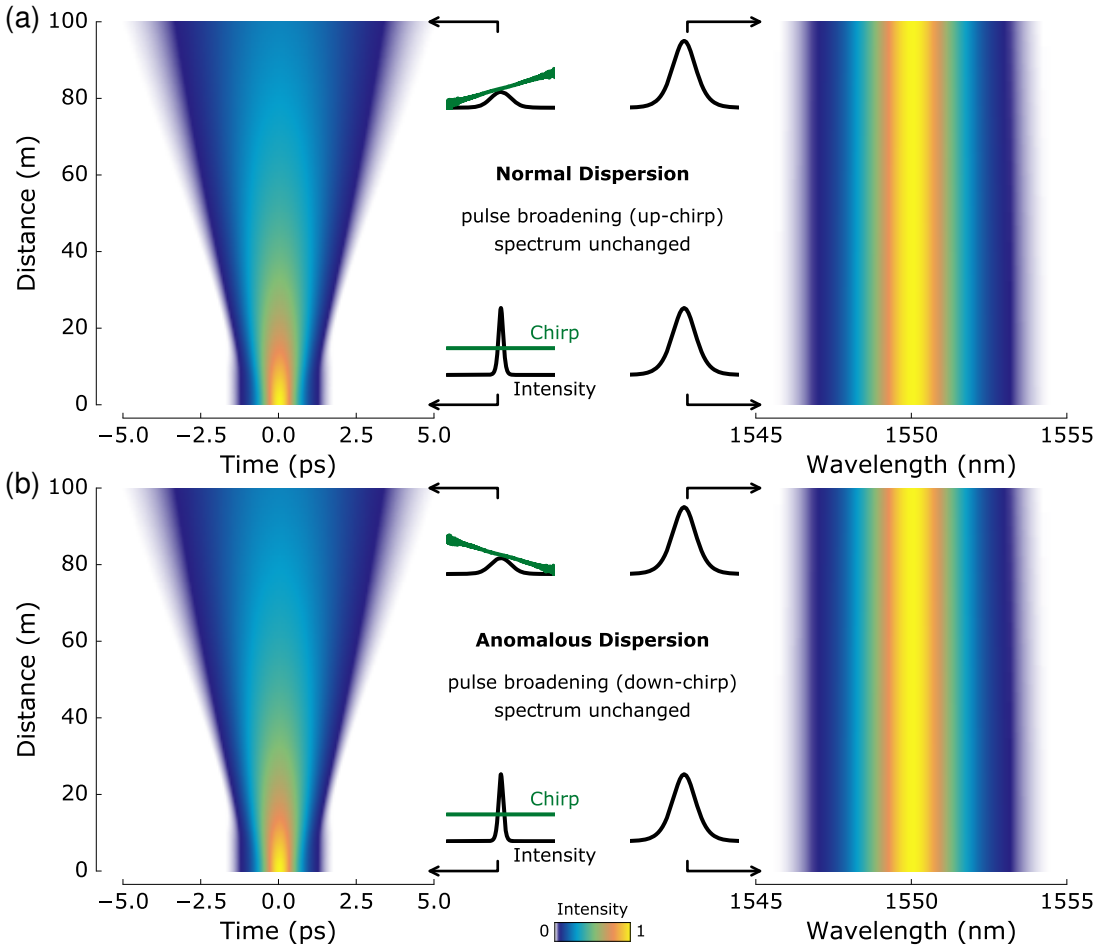


Fig. 1.5: Simulated propagation of a 1 ps transform-limited pulse along a linear dispersive fibre (neglecting nonlinearity) with (a) normal and (b) anomalous dispersion. The outer plots show the evolution of the pulse (left) and spectral (right) intensities with distance; the inner plots show the pulse shape, chirp and spectral shape at the input and output.

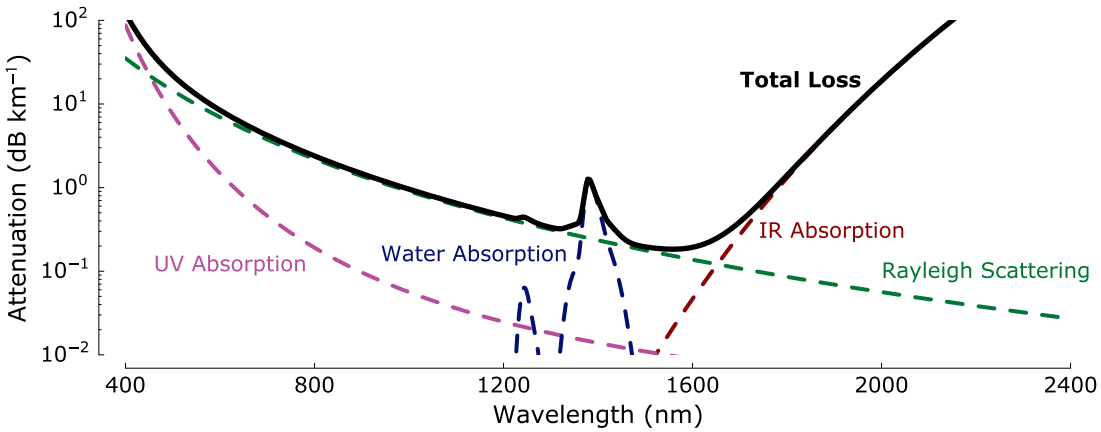


Fig. 1.6: Typical attenuation spectrum for a step-index fibre, showing contributions from UV, IR and water absorption and Rayleigh scattering (computed using the loss model from Section 2.3.1).

Birefringence

Ideal single-mode optical fibres are isotropic structures which can support two identical propagation modes polarised in orthogonal directions. In practice, however, random variations in core shape from manufacturing imperfections and mechanical/thermal stresses break the circular symmetry. Therefore, optical fibres exhibit *birefringence* as the two polarisation axis modes have different propagation constants [Pas08].

For pulse propagation, this can lead to temporal broadening if the input excites modes in both polarisation axes since the two modes can have different group velocities. This is known as *polarisation-mode dispersion*.

Additionally, the state of polarisation of light in the fibre can change during propagation due to coupling and energy transfer between these two modes. External disturbances can also change the fibre birefringence, making it difficult to predict the output pulse properties since the change in polarisation inside the fibre is effectively random.

Polarisation-maintaining (PM) fibres solve this problem by possessing a strong built-in birefringence. This can be achieved by the making the core shape elliptical or by including stress rods in one axis (either in cylindrical or bow-tie shaped designs), which becomes known as the *slow axis* and possesses a larger index than the orthogonal*fast axis* (Fig. 1.7). It follows that random perturbations of each axis index will be small compared to the intrinsic birefringence, negating their effect. For a more complete understanding based on mode-coupling, it should be noted that the very different propagation constants along the two axes due to high birefringence causes the relative phase between them to be short-lived so mode-coupling is very inefficient [Pas08]. Therefore, if light is launched along one axis, the state of polarisation can be maintained along the fibre even in the presence of external disturbances.

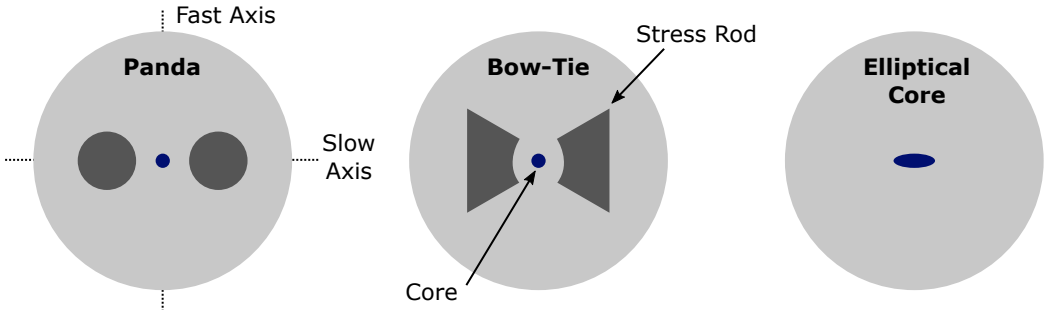


Fig. 1.7: Cross-sections of different designs of polarisation-maintaining high-birefringence fibre.

1.3.4 Nonlinear Propagation Effects

A material's response to an electric field will become nonlinear for high-intensity fields. In this case, the higher-order susceptibility terms in Eqn. 1.3.3 cannot be neglected. However, all even-order terms ($\chi^{(2)}$, $\chi^{(4)}$, etc.) are zero in fibre since the glass material possesses

inversion symmetry (specifically, this is due to the amorphous nature of the glass structure as silica molecules are actually non-centrosymmetric and thus lack inversion symmetry). The strength of the nonlinear terms reduce with increasing order, meaning that the only significant nonlinearity in silica fibres is third-order ($\chi^{(3)}$). A variety of different nonlinear phenomena can occur, manifesting from two fundamental mechanisms: the *Kerr effect* and *stimulated inelastic scattering* [Boy07, Agr13].

The Kerr effect is an instantaneous[5] nonlinear response which originates from optical interaction with electrons of the medium, leading to an intensity-dependent refractive index. This depends on the real part of $\chi^{(3)}$ and leads to effects such as *self-phase modulation*, *cross-phase modulation* and *four-wave mixing*.

Two inelastic scattering mechanisms are considered in fibre: *Raman* and *Brillouin* scattering, both of which are non-instantaneous. Raman scattering arises from interaction between light and *optical phonons* (i.e. quanta of lattice vibrations), whereas Brillouin scattering is due to *acoustic phonon* interaction. The acoustic phonons are essentially sound waves, with adjacent atoms being displaced in the same direction; optical phonons result in displacement of adjacent atoms in opposite directions. At low optical intensities, these inelastic scattering processes are *spontaneous* and driven by thermal fluctuations; they can be described by linear optics since the scattered intensity is proportional to the incident power. At high intensities, however, interaction between incident and scattered light can nonlinearly enhance the process (effectively providing positive feedback). This can result in strong *stimulated* nonlinear scattering effects, which are related to the imaginary part of $\chi^{(3)}$.

Each of these effects can be usefully exploited to achieve a particular optical function, or can manifest as an unwanted source of loss or distortion depending on the application. We now briefly summarise these nonlinear phenomena, providing the toolkit of nonlinearity from which to develop enhanced photonic devices.

Self-Phase Modulation

Self-phase modulation (SPM) is a self-induced phase delay arising as the phase velocity is determined by the medium's refractive index, which varies with the light intensity due to the Kerr effect [Sto78]. To consider this quantitatively, the real part of the refractive index can be expressed as:

$$n(\omega, I) = n_0(\omega) + n_2 I \tag{1.3.17}$$

where $I = |E|^2$ is the optical intensity, n_0 is the linear index and n_2 is introduced as the nonlinear index, which for silica is accepted as $n_2 = 2.74 \times 10^{-20}$ m^2 W^{-1} and is almost wavelength-independent [Mil98].

For pulsed excitation, the nonlinear refractive index results in a phase delay with the same shape as the pulse envelope. Differentiating this time-dependent phase with respect

[5] Strictly, a response is never instantaneous, but this assumption holds in silica for pulses longer than ~10 fs, as considered in this thesis.

to time yields the instantaneous frequency, which is also time-dependent. Therefore, SPM adds a nonlinear chirp to the pulse.

To illustrate this effect, we simulate a 1 ps duration, 30 W peak-power, transform-limited sech-shaped pulse (introduced in Eqn. 1.3.16) propagating along a dispersionless ($D = 0$) nonlinear fibre. The nonlinearity of fibre is commonly described by the nonlinear coefficient:

$$\gamma = \frac{2\,\pi\,n_2}{\lambda\,A_{\text{eff}}} \tag{1.3.18}$$

where A_{eff} is the effective area of the mode shape in the fibre, defined as:

$$A_{\text{eff}} = \frac{\left(\int I\,\mathrm{d}A\right)^2}{\int I^2\,\mathrm{d}A} \tag{1.3.19}$$

Here, we set $\gamma = 2$ W km^{-1}, which is typical for telecommunications fibre. As the pulse propagates, the spectrum broadens as new frequencies are created by the time-varying phase delay and the output pulse is nonlinearly chirped (Fig. 1.8). The pulse duration and intensity, however, are unchanged.

While this simulation is instructive, it is unphysical to model a fibre without dispersion. Consequently, we now consider more realistic situations with both dispersion and nonlinearity, to explore the interplay between these two effects.

First, we study propagation with normal dispersion and nonlinearity, using $D = -15$ ps nm^{-1} km^{-1} and $\gamma = 2$ W km^{-1} (Fig. 1.9a). The pulse broadens in both time and wavelength space: temporal spreading is greater than with dispersion alone due to the SPM-widened spectrum, although the spectral broadening is reduced as the pulse peak power falls as it disperses. Dispersion also acts to linearise the SPM-induced chirp, resulting in a relatively linear up-chirp. This pulse shaping mechanism and the nature of the chirp is exploited in Chapter 3 to develop a low repetition rate, high-energy pulse source.

Next, we consider the interaction between anomalous dispersion and nonlinearity, with $D = +15$ ps nm^{-1} km^{-1} and $\gamma = 2$ W km^{-1}(Fig. 1.9b). Remarkably, neither the spectrum nor pulse change during the propagation. Such pulses are known as *fundamental solitons*.

Solitons

Fundamental solitons are solitary pulses which propagate at a constant speed without temporal or spectral evolution, maintained by a balance between anomalous dispersion and SPM [Zak72, Has73a]. Specifically, anomalous dispersion and SPM generate opposite chirps, which under certain conditions can perfectly cancel out. For a given fibre group velocity dispersion β_2 and nonlinear coefficient γ, a sech-shaped pulse with a $1/e$ duration t_0 will propagate as a soliton if the peak power is:

$$P_0 = \frac{|\beta_2|^2\,N^2}{\gamma\,t_0^2} \tag{1.3.20}$$

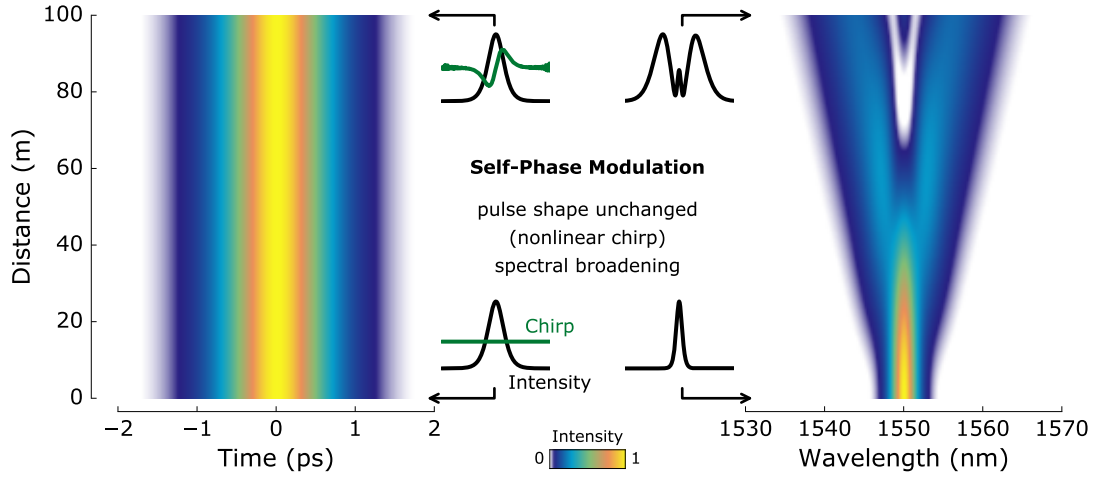


Fig. 1.8: Simulated propagation of a 1 ps transform-limited pulse along a dispersionless nonlinear fibre experiencing self-phase modulation. The outer plots show the evolution of the pulse (left) and spectral (right) intensities with distance; the inner plots show the pulse shape, chirp and spectral shape at the input and output.

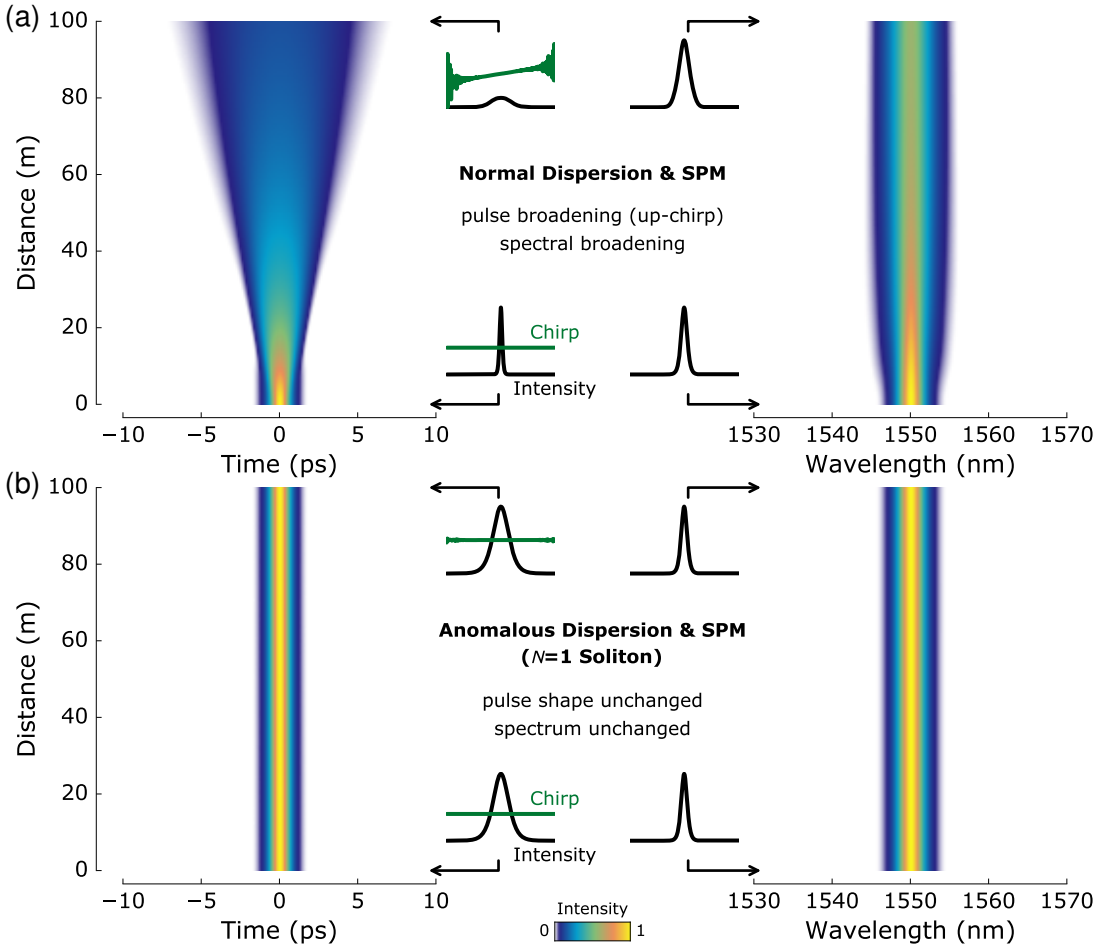


Fig. 1.9: Simulated propagation of a 1 ps transform-limited pulse along a nonlinear fibre with (a) normal and (b) anomalous dispersion. The outer plots show the evolution of the pulse (left) and spectral (right) intensities with distance; the inner plots show the pulse shape, chirp and spectral shape at the input and output.

where N is the soliton order, which is one for a fundamental soliton. For the simulated fibre in Fig. 1.9, the fundamental soliton power for a 1 ps FWHM pulse is 30 W, which explains our choice of pulse peak power to illustrate this effect.

Higher-order solitons ($N > 1$) can also exist in fibres, with a peak power N^2 times greater than the $N = 1$ soliton. These pulses are effectively a co-propagating group of N fundamental solitons and mutual interference between these components leads to a periodic evolution (in the absence of perturbations and higher order effects such as Raman scattering), as shown for an $N = 2$ and $N = 3$ soliton in Fig. 1.10. The period is equal to a characteristic length scale known as the *soliton period*:

$$z_0 = \frac{\pi}{2}\frac{t_0^2}{\beta_2} \tag{1.3.21}$$

which is 26.4 m for the simulations shown in Fig. 1.10. It should also be noted that pulses propagating in anomalously dispersive fibre at arbitrary powers with non-sech-shaped envelopes can evolve into solitons. Soliton dynamics underpin many nonlinear fibre-optic devices, such as supercontinuum light sources, which we demonstrate and discuss further in Section 3.4.

From a more general perspective, solitons are a complete field of mathematical physics, which manifest as a balance between spreading and focussing effects in many physical systems beyond fibre-optics (e.g. hydrodynamics [Rus44] and Bose-Einstein condensates [Rup95]). Mathematically, solitons are analytical solutions of the nonlinear partial differential equations which describe these systems. Analytical solutions also exist in the case of normal dispersion and nonlinearity, known as *dark* solitons, in contrast to the *bright* solitons described above. We have observed these dark structures within simulations of the bright pulse formation dynamics in mode-locked fibre lasers, as discussed in Section 3.5.

Cross-Phase Modulation

Cross-phase modulation (XPM) is the phase delay of an optical signal produced by a different wave, which is co-propagating with the signal [Isl87]. The mechanism is similar to SPM, but the change in refractive index experienced by the signal beam is determined by the intensity of the other wave, which can be expressed as [Agr13]:

$$\Delta n_{\mathrm{XPM}}(\omega_1) = 2n_2 I(\omega_2) \tag{1.3.22}$$

where n_2 is the same nonlinear index introduced to describe SPM and $I(\omega_2)$ is the intensity of the second wave. XPM can be practically utilised to synchronise two mode-locked fibre lasers or for pulse diagnostics, but can also cause problems in optical systems such as channel cross-talk in optical fibre communications.

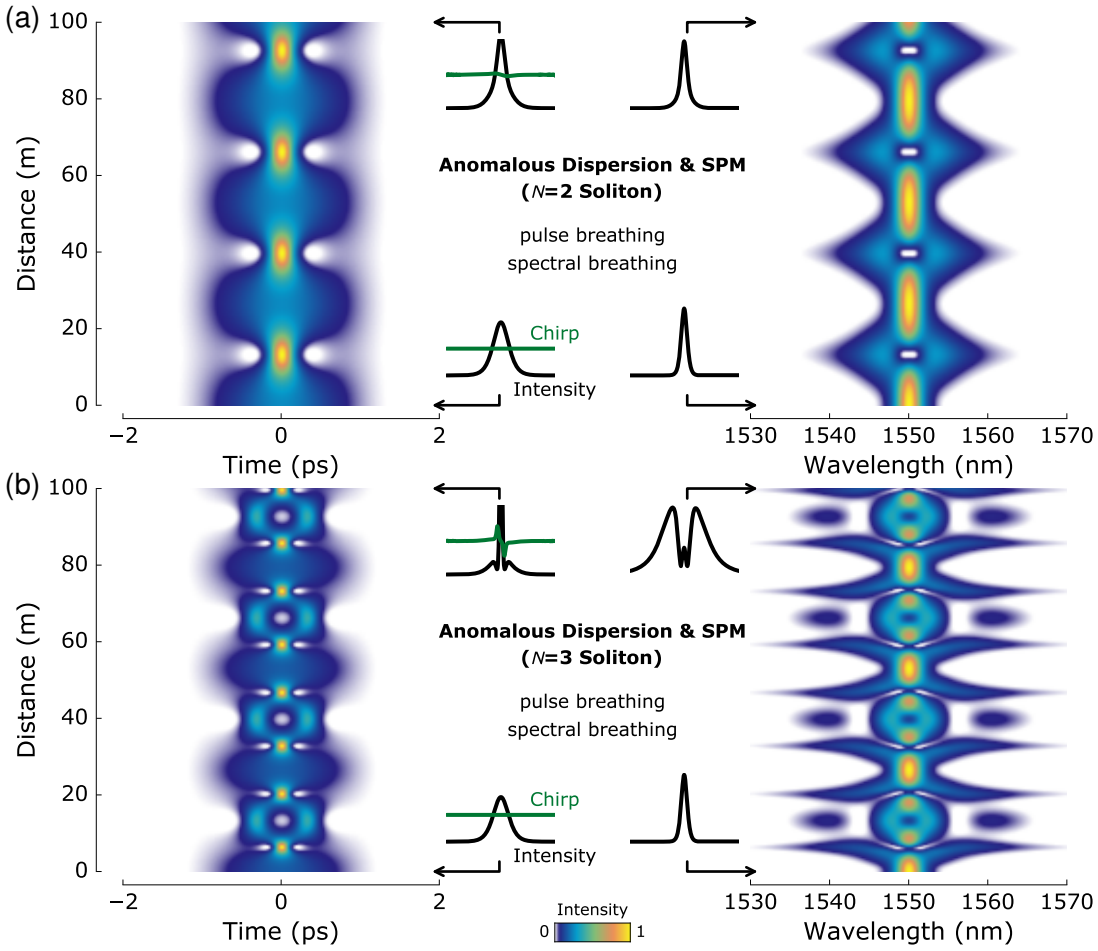


Fig. 1.10: Simulated propagation of a 1 ps transform-limited pulse along an anomalously dispersive nonlinear fibre with peak power corresponding to an (a) N=2 soliton and (b) N=3 soliton. The outer plots show the evolution of the pulse (left) and spectral (right) intensities with distance; the inner plots show the pulse shape, chirp and spectral shape at the input and output.

Four-Wave Mixing

Four-wave mixing (FWM) is the general term for coupling between four waves through the real part of $\chi^{(3)}$, which can be used to generate light at different wavelengths from the pump light [Sto75a].[6] Energy conservation dictates that:

$$\omega_1 + \omega_2 = \omega_3 + \omega_4 \tag{1.3.23}$$

where ω_i is the angular frequency of the i^{th} wave.

Numerous different mechanisms exist to achieve wavelength conversion, either seeding the FWM process from noise or with pump and signal inputs to amplify the signal. All four waves can be at different frequencies (non-degenerate / two-pump FWM), two-waves can be at the same (pump) frequency (semi-degenerate FWM), three-waves can be at the same frequency (third-harmonic generation) or all four waves can be at the same frequency (degenerate FWM).

In fibre systems, semi-degenerate FWM is often exploited, with energy transfer from the two degenerate pump waves ($\omega_1 = \omega_2$) to a lower frequency (ω_3) known as the *Stokes* signal and a higher frequency (ω_4) known as the *anti-Stokes* signal. Efficient FWM can only occur in fibres if the process is *phase-matched* – i.e. a fixed phase relationship between the waves must be maintained during propagation. This condition corresponds to minimising the phase mismatch, given by [Agr13]:

$$\Delta k = \beta(\omega_1) + \beta(\omega_2) - \beta(\omega_3) - \beta(\omega_4) + 2\gamma P_0 \tag{1.3.24}$$

where the fibre propagation constants determine the linear phase mismatch and $2\gamma P_0$ accounts for a nonlinear phase shift. By solving this equation for a range of pump wavelengths, the intensity-dependent phase-matched Stokes and anti-Stokes wavelengths can be found, which are plotted for a standard telecommunications fibre in Fig. 1.11a. We illustrate the effect of four-wave mixing for wavelength conversion by simulating a 250 W peak power 50 ps pulse at 1290 nm input into this fibre. As the pulse propagates, sidebands emerge at ∼1115 nm and ∼1529 nm (the phase matched wavelengths for a 1290 nm pump) and grow in intensity, also experiencing spectral broadening from SPM (Fig. 1.11b). This technique can enable the generation of light at difficult-to-access spectral regions (e.g. where a suitable laser gain medium is not available).

Stimulated Raman Scattering

Raman scattering is the inelastic scattering of photons from molecular vibrations and rotations, which downshift the light frequency by the energy of the vibrational/rotational

[6] In a rigorous mathematical treatment, most $\chi^{(3)}$ processes are actually treated as four-wave interactions, although many of these waves are often the same frequency, zero or negatives of each other – e.g. the intensity-dependent index can be described energetically by $\omega = \omega - \omega + \omega$ [New11]. Practically, however, the term FWM is commonly used to describe $\chi^{(3)}$ processes for wavelength conversion.

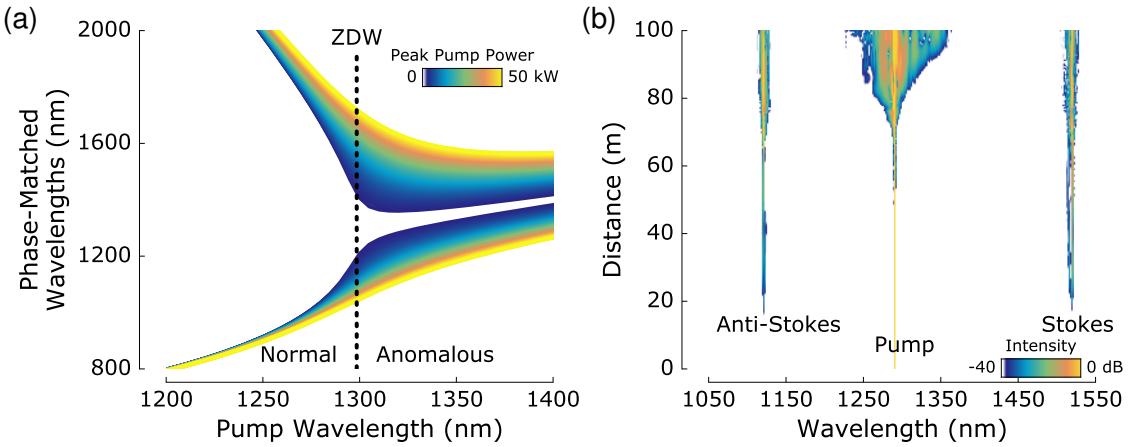


Fig. 1.11: Four-wave mixing in fibre: (a) power-dependent phase-matching curves for standard telecommunications fibre; (b) simulation showing growth of sidebands about the pump, seeded by noise.

mode [Ram28, Sto72]. This can be described quantum mechanically as the annihilation of a pump photon to generate an optical phonon and a lower-frequency Stokes photon. Raman scattering occurs spontaneously at low pump intensities but becomes stimulated as the pump intensity increases due to feedback, where the presence of both pump and Stokes fields drives further vibrations and results in strong scattering.

The amorphous nature of silica means the molecular vibration frequencies of the material spread out and form a continuum, giving a broad gain bandwidth of ∼40 THz, peaked at a shift of 13.2 THz from the pump (Fig. 1.12a). Since Raman scattering is related to molecular vibrations and the motion of nuclei, which are much heavier (and slower) than electrons, the process cannot be considered to be instantaneous. Instead, the Raman response can be described by oscillations with a period less than 100 fs, which corresponds to the THz frequency shift (greater physical insight into this process is offered in a discussion of how Raman gain can be numerically modelled in Section 2.3.2).

At very high pump intensities, the Stokes light can become sufficiently intense to act as a pump for a higher Stokes order, cascading the process to greater frequency shifts from the original pump wavelength. The Raman scattering process can be seeded by either an input signal (to provide distributed amplification) or by noise.

A simulation demonstrating the effect of stimulated Raman scattering is shown in Fig. 1.12b: as a 10 ps pulse at 1550 nm propagates, the spectrum is initially broadened by SPM, before becoming depleted as light is converted to the Stokes line at ∼1660 nm (13.2 THz from the pump wavelength). The gain shape is wavelength independent and the process is automatically phase-matched, making Raman scattering a useful process for wavelength conversion and for distributed amplifiers (particularly useful for long-distance telecommunications).

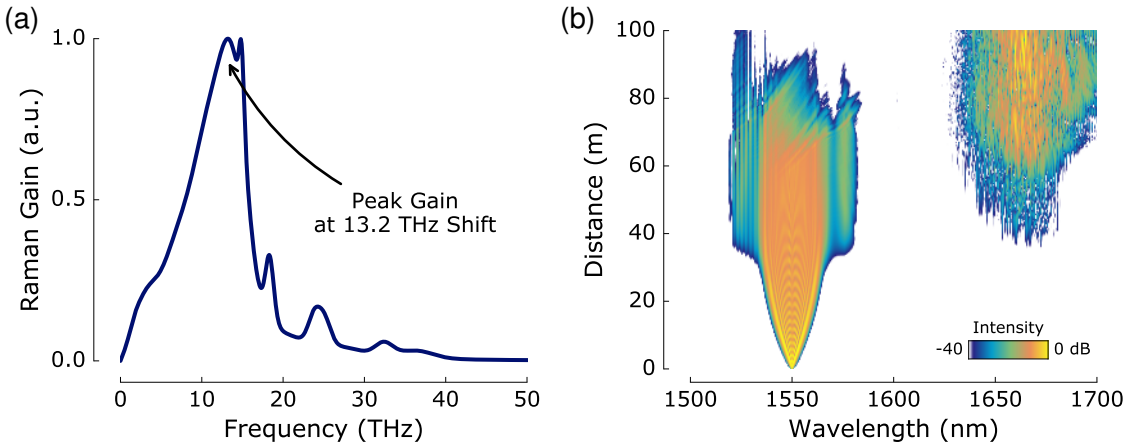


Fig. 1.12: Stimulated Raman scattering in silica fibre: (a) Raman gain spectrum (modelled as discussed in Section 2.3.2); (b) simulation showing pump depletion and transfer of energy to the Stokes line.

Stimulated Brillouin Scattering

Brillouin scattering is the inelastic scattering of light from acoustic waves propagating in the fibre core [Bri22, Ipp72b]. The acoustic waves modulate the material density, causing a periodic refractive index modulation that effectively creates a Bragg grating structure. Therefore, a fraction of the pump light is reflected (backscattered) and downshifted in frequency by the Doppler shift of the difference in propagation velocities of the optical and acoustic waves. This backscattered light is referred to as the Stokes signal (Fig. 1.13).

At low pump intensities, spontaneous Brillouin scattering occurs, with acoustic waves arising from thermally-induced periodic density variations, creating a very weak Bragg grating effect. However, significant backscattering can be achieved under intense pump illumination as the beating between pump and backscattered light reinforces the acoustic wave through electrostriction. This regime, in which strong scattering results from pump-induced acoustic waves, is known as stimulated Brillouin scattering (SBS).

The frequency shift and width of the Brillouin gain spectrum are wavelength dependent, but are typically $\sim$11 GHz and $\sim$20 MHz (at 1550 nm), respectively. The shift is clearly much smaller, and the gain much narrower than for Raman scattering, which can be understood by the different nature of acoustic and optical phonons. While molecular vibrations are highly oscillatory and decay rapidly, acoustic waves travel at a slower velocity of $\sim$6000 m s^{-1} in silica and have a longer lifetime of $\sim$10 ns. Additionally, the acoustic waveguiding properties of optical fibres can have a great effect on the Brillouin scattering process, which we explore in Chapter 5. Stimulated Brillouin scattering is usefully used in many sensing applications, although it can also be a major limitation by restricting the transmission of high optical intensities.

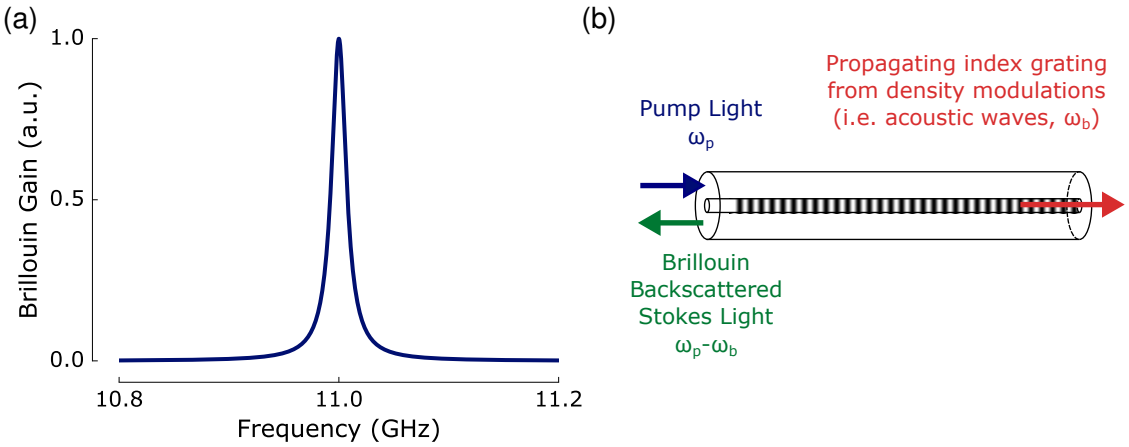


Fig. 1.13: Stimulated Brillouin scattering in silica fibre: (a) Brillouin gain spectrum at 1550 nm (modelled by a Lorentzian spectrum [Boy07]); (b) illustration of forwards-travelling pump and acoustic waves, causing energy transfer to the backscattered Stokes wave.

1.4 Photonic Crystal Fibre

While conventional optical fibres have enabled many nonlinear fibre-optic-based devices, there are fundamental limitations to the fibre properties that can be achieved. Due to core-confinement of the fundamental mode, material dispersion is the dominant contributing factor to the net dispersion profile, giving a ZDW at ∼1270 nm [Mal65]. It is possible to shift this through waveguide dispersion to longer wavelengths, although not significantly towards shorter wavelengths, restricting applications such as pulse compression and controlling supercontinuum generation, where anomalous dispersion at visible wavelengths is desirable [Dud10]. The nonlinearity of conventional fibres can be enhanced by core-size reduction and doping with materials that have a higher nonlinear coefficient, although there are also limits here on the required core-cladding index contrast for guidance in small-core fibres and highly-doped cores can present problems when splicing to normal fibres. This inflexibility led to a search for new designs of optical fibre waveguides. One proposed solution was photonic crystal fibre (PCF).

PCFs, which are also known as holey fibres (HFs) and microstructured optical fibres (MOFs), consist of a microstructured cladding with periodically arranged air holes [Kni96]. The fibre material is typically silica and the air holes are arranged in a hexagonal shape (Fig. 1.14a). The structure is described by two key parameters – the air hole size d and the pitch (i.e. hole-to-hole spacing) Λ – and the waveguiding properties of the fibre can be significantly varied by adjusting the air-fill fraction (d/Λ). *Scanning electron microscope* (SEM) images of low ($d/\Lambda \sim 0.4$) and high ($d/\Lambda \sim 0.9$) air-fill fraction PCFs are shown in Figs. 1.14b & c respectively.

The core of a PCF can be solid (formed by removing an air hole from the centre of the microstructure) or hollow (by making a large central air hole). Light in hollow-core PCFs is guided in the core by a photonic bandgap effect [Cre99]. Since the nonlinearity of air is

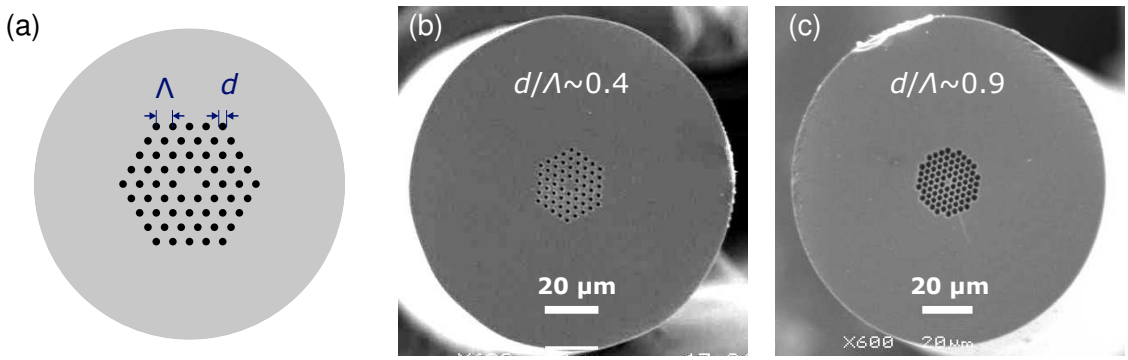


Fig. 1.14: Solid-core PCF structures: (a) schematic illustration; SEM image of (b) low air-fill fraction ($d/\Lambda \sim 0.4$) PCF and (c) high air-fill fraction ($d/\Lambda \sim 0.9$) PCF.

low, these fibres exhibit greatly reduced nonlinear coefficients, which can be useful for high-power short-pulse delivery applications, but they are not considered further in this thesis. While the photonic bandgap of the cladding can influence light in solid-core PCFs, the guidance is best described by analogy with a step-index fibre: the cladding region of silica and air holes has a lower index than the solid silica core, so light is guided by total internal reflection [Kni98] (the guidance properties are discussed in more detail in Section 2.2.2 on PCF modelling).

Compared to the small permissible core-cladding index contrast of a few percent for conventional fibre, PCFs can support differences exceeding 25% [Rus06]. This enables much stronger waveguide dispersion (which can even become the dominant effect over material dispersion). Therefore, PCFs offer great flexibility for engineering the net fibre dispersion and it has been possible to fabricate fibres with ZDWs in the visible spectral region and even with double and triple ZDWs [Kni00]. Very small fibre cores can also be realised, with properties approaching those of a glass strand in air where the strong confinement yields a large nonlinear coefficient. Additionally, PCF structures have enabled stronger birefringence than standard fibres [OB00] and novel properties such as endlessly-single-mode operation [Bir97] and tailorable acoustic interactions [Dai06]. While the ease of handling and attenuation values of PCF are worse than standard fibre at present, as the technology advances the loss continues to be reduced and compatibility is emerging with existing fibre systems (for example, relatively low-loss fusion splicing between standard fibre and PCF is now commonplace).

1.5 Short-Pulse Fibre Laser Technology

Fibre lasers are broadly categorised as any laser where the active gain medium is an optical fibre. These devices offer numerous advantages over bulk crystal, dye and gas alternatives, including excellent diffraction-limited beam quality (M^2 values close to the optimum value of 1), high efficiency and rapid heat dissipation through the large surface area of the medium (air cooling is therefore sufficient, which consequently enables

high power handling) [Pas08]. Additionally, all-fibre laser systems can be constructed without any bulk elements in the cavity, offering turn-key alignment-free operation with a small-device footprint since fibres can be coiled and packed into compact devices.

The vast majority of fibre lasers are based on energy transitions from rare-earth ion dopants embedded in the silica fibre core. However, it is also possible for lasing to be achieved using nonlinear gain from the processes we outlined in Section 1.3.4, such as in a Raman laser, Brillouin laser or a fibre optical parametric oscillator.

For any given application, in addition to choosing the active medium to provide gain at the required wavelength, the time-domain properties of the laser output are an important consideration. In many cases, a series of short optical pulses are preferred to a continuous wave of light (for instance, in laser machining, sub-picosecond pulses are often used to minimise heating of the workpiece, resulting in higher quality manufacturing with better precision [Ste10]). The pulse duration, repetition frequency and energy are all key parameters which may be specified by end users.

In this section, we briefly review common rare-earth ions for fibre lasers and techniques for generating short pulses.

1.5.1 Rare-Earth-Doped Fibre Lasers

Rare-earth ions from the lanthanide series of the periodic table are widely used active dopants, each with a unique absorption and emission spectrum [Dig01]. Optical pumping within an absorption band excites electrons from the ground state of the material to a higher-energy metastable level, which can create a population inversion. This enables stimulated emission and a signal to experience gain if its wavelength lies within an emission band (i.e. at a resonant frequency).

Early fibre lasers were predominantly based on neodymium Nd^{3+}-doped[7] glass, with emission bands at $\sim$1060 nm and $\sim$1320 nm, following the pioneering work of Elias Snitzer [Sni61b]. Since then, silica fibres have been doped with many different rare-earth materials and shown to enable laser action. Today, the most important elements are [Dig01]:

- Ytterbium (Yb^{3+}), which has a similar emission window at $\sim$1060 nm to Nd^{3+}, but the absorption band at $\sim$980 nm is closer in wavelength (compared to $\sim$808 nm for Nd^{3+}), reducing the *quantum defect* and improving the high-power handling.

- Erbium (Er^{3+}), which can provide gain at $\sim$1550 nm, overlapping with the loss minimum of silica fibres and consequently becoming the dominant dopant for telecommunications applications.

- Thulium (Tm^{3+}), which has a broad emission window around 1900 nm where demands for laser sources are currently increasing, fuelled by applications in military

[7] For optical applications, the trivalent (3+) form of rare-earth ions is predominantly used since it is the most stable.

countermeasures and molecular spectroscopy.

Fig. 1.15 shows the emission cross sections (a quantity that describes the likelihood of stimulated emission) for these three main dopants. The high-intensity feature at 975 nm for ytterbium (with a peak at $\sim 25 \times 10^{-25}$ m^2) is not shown in full here since the detailed spectroscopy of ytterbium and further discussion regarding the modelling of ytterbium-doped fibre amplifiers is presented in Section 2.4.

It is apparent that wide gaps exist in the near-infrared region which are not covered by these three rare-earth ions, driving research to consider other dopants to operate here, in addition to operating at visible and mid-infrared wavelengths. For instance, bismuth is emerging as a suitable dopant with emission in the 1150 to 1550 nm region [Dia12]. Additionally, many opportunities are offered by moving away from silica glass as the host material, since silica has a limited transmission window and relatively high phonon energy that reduces the upper-state lifetime of closely-space energy levels, inhibiting lasing from certain transitions. Fluoride fibres are suitable candidates and have been shown to lase at visible wavelengths when doped with praseodymium (Pr^{3+}) or dysprosium (Dy^{3+}) [All91, Lim00]. Additionally, erbium and thulium also have other emission bands (not shown in Fig. 1.15), which are inhibited from lasing in silica but can operate with fluoride hosts. Er^{3+}-fluoride fibre lasers have been demonstrated at 2900 nm [Pol01] and at 500 nm (by upconversion) [Whi91], and Tm-fluoride fibres have been used to produce blue upconversion lasers [Gru92a]. However, the lower loss, greater environmental stability and ease of handling of silica fibres has enabled silica to remain as the dominant glass host for fibre lasers to date.

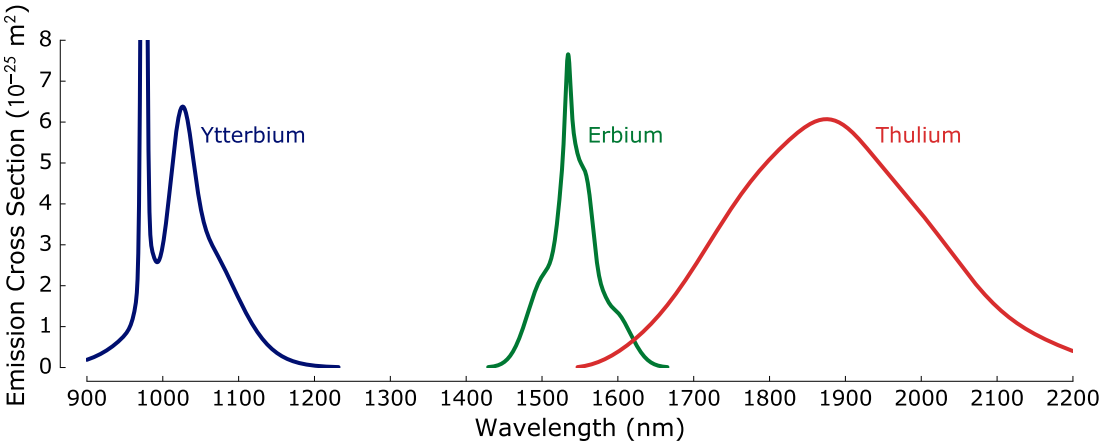


Fig. 1.15: Emission cross-sections of common rare-earth-dopants in silica fibres. Data sources: Ytterbium [Pas97], Erbium [Bar91] and Thulium [Jac99].

1.5.2 Short-Pulse Generation

Pulse generation, in the simplest implementation, could be achieved by a continuous wave (cw) laser source propagating through a fast on-off modulator. While this is adequate for

some applications, the efficiency can be poor (as directly related to the modulator duty cycle) and the pulse duration and light extinction are limited to the modulator switching speed and modulation depth. Therefore, more sophisticated techniques are often required, typically by modulating the field inside a laser cavity, either by Q-switching, mode-locking or gain-switching [Sve10].

Q-Switching

Q-switching generates optical pulses by modulating the laser cavity quality factor, or *Q factor*, which is the ratio of energy stored in the cavity to energy lost in each oscillation cycle. Q factor modulation is achieved by inserting an optical loss modulator into the cavity. The modulator is initially set to yield high losses (low Q factor), which prevents lasing. Energy accumulates in the gain medium as the laser is pumped, increasing the population inversion. When the cavity loss is switched low (high Q factor), the optical power in the cavity increases sharply. This saturates the gain medium, causing the power to decay and resulting in the formation of a burst of light, i.e. a pulse. By cycling the loss modulation, a train of short pulses is produced, as illustrated in Fig. 1.16.

The loss modulator can be an actively controlled device such as an electronic shutter or a passive element exhibiting intensity-dependent absorption, known as a *saturable absorber* (SA). Passive Q-switching eliminates the need for complicated electronic systems to drive the modulator, but the repetition rate and pulse duration of the laser are then power-dependent. Q-switched fibre lasers can typically produce ns-µs pulses at kHz repetition rates.

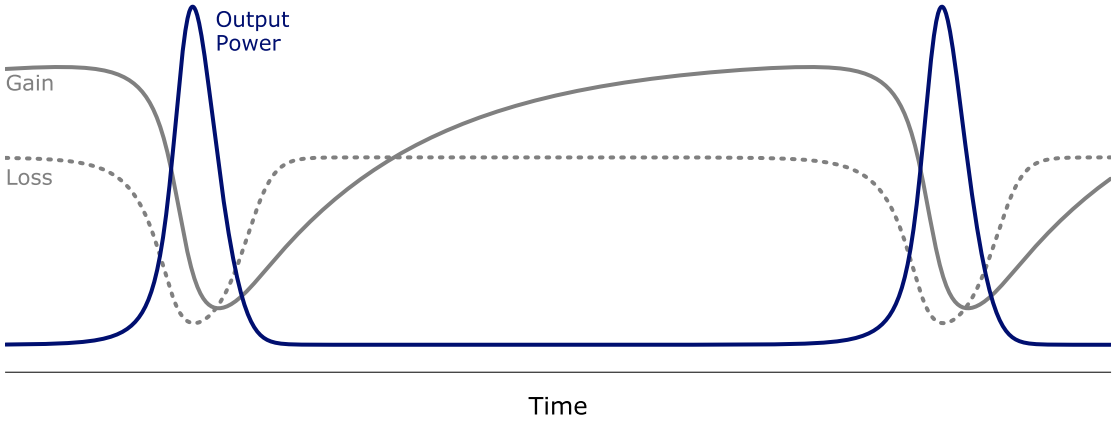


Fig. 1.16: Illustration of passive Q-switching dynamics, showing the formation of pulses by modulation of the cavity gain and loss.

Mode-Locking

Mode-locking establishes a fixed phase difference between longitudinal modes of the laser cavity, creating periodic interference that produces a train of pulses. Numerous longi-

tudinal modes exist within the gain bandwidth of a laser cavity and during continuous wave operation, the modes oscillate independently so the beam intensity has a random time dependence. By establishing a fixed phase relationship between adjacent cavity modes, the electric field becomes a temporally periodic function, with a repetition period corresponding to the cavity round trip time. If a large number of modes are locked with a broad gain bandwidth, ultrashort sub-picosecond pulses can be generated.

Similar to Q-switching, mode-locking is achieved by inserting an optical loss modulator into the cavity, which can be actively driven or a passive saturable absorber. Amplitude modulation adds sidebands to each mode in the frequency domain, spaced apart by the modulation frequency. If this modulation frequency is equal to the cavity-mode spacing, coupling between the in-phase driven sidebands and the cavity modes will phase-lock adjacent modes together.

Passive mode-locking with a saturable absorber can also be explained in the time domain. As the pump power increases and light starts to resonate in the cavity, noise fluctuations will result in intensity variations on the absorber. The nonlinear absorption of the device results in preferential transmission of greater intensities, which therefore experience greater gain and continue to grow. Over many cycles of the cavity, noise fluctuations can build up into a pulse. The peak of the pulse saturates the absorber more strongly than the pulse wings, resulting in temporal narrowing until an equilibrium is established where the minimum pulse duration is set by the cavity gain bandwidth (typically, this is less than the gain bandwidth of the active material alone due to spectrally-dependent loss in other cavity components). Compared to Q-switched lasers, mode-locked fibre lasers can produce ultrashort pulses (fs-ps durations) at repetition rates corresponding to the cavity length (typically MHz). Further discussion of saturable absorbers is presented in Chapter 4, where we study the nonlinear optical properties of emerging few-layer transition metal dichalcogenides.

While mode-locking and Q-switching both depend on an intracavity modulator, the tendency for a laser to operate in either regime depends on the cavity design and modulator properties. Additionally, the two mechanisms can occur simultaneously, known as *Q-switched mode-locking*. This regime can be advantageous for delivering bursts of high-energy ultrashort pulses, or considered an instability if a continuous train of mode locked pulses (known as *cw mode locking*) is desired.

Gain Switching

Gain-switching produces short pulses by modulating the pump power to the active fibre, which switches the gain on and off rapidly. There is a delay between the gain medium being pumped and the onset of lasing while the spontaneously emitted light is amplified by many round-trips of the cavity. This has the effect of storing gain in the gain medium. If the pump power is switched off as lasing starts, then the stored energy can be extracted in the form of a pulse shorter than the pump pulse, as shown in Fig. 1.18. The build-up time

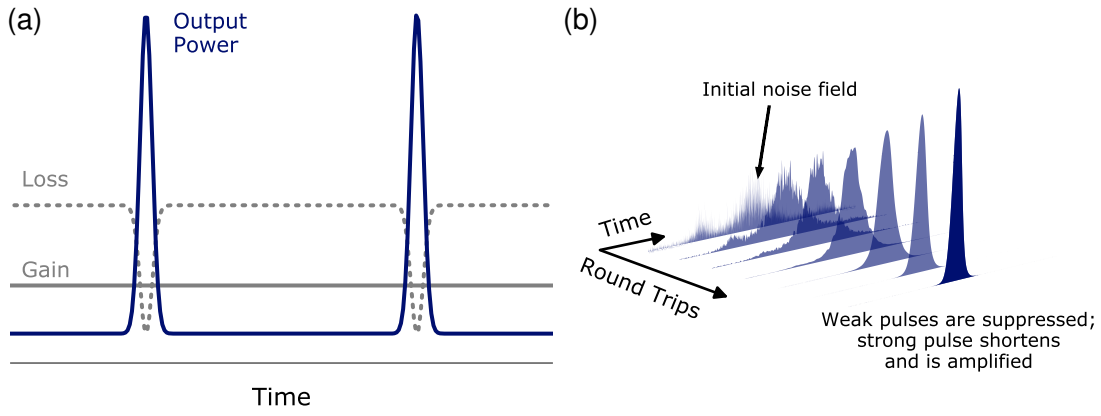


Fig. 1.17: Illustration of mode-locking dynamics: (a) steady-state evolution of power, loss and gain; (b) initial growth of a pulse from noise.

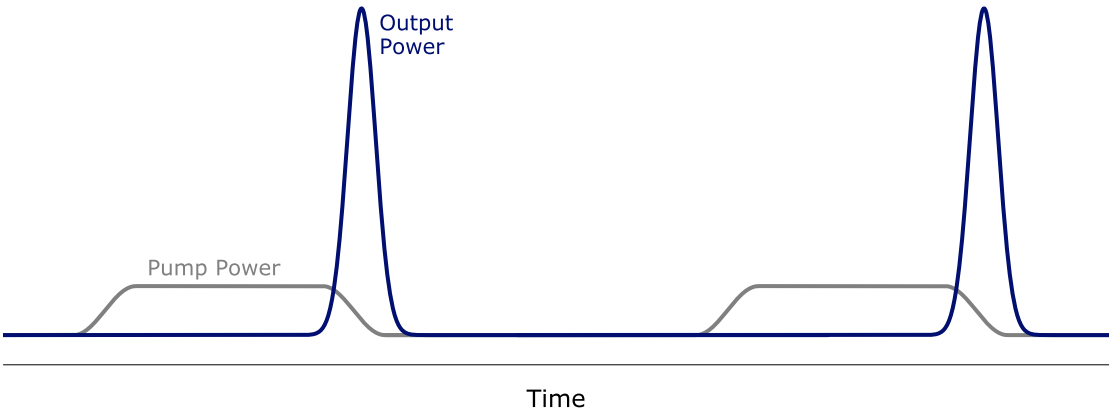


Fig. 1.18: Illustration of gain switching dynamics, showing the formation of pulses by modulation of the pump power.

and hence the required pump pulse duration can be reduced by using more intense pump pulses. Therefore, providing the pump source can produce pulses with sufficient power, the gain-switched laser can emit significantly shorter pulses. However, this setup requires a separate technique for pulsing the pump light and the generated pulse durations are typically > 100 ps.

1.6 Nanomaterials

Materials science is critically important to the development of optical technologies. Indeed, advancements in understanding and fabrication of materials have underpinned many of the major optical discoveries over the last century. Materials are typically used on macroscopic length scales with millions of constituent atoms in their chemical structure. In this case, the material properties are independent of size.

However, for the continued development of new and improved devices, there is great interest in exploring new materials with novel and tunable properties. The development of quantum mechanics over the the last century has provided theoretical tools to analyse size-dependent behaviour on the nanoscale and researchers have considered how material characteristics change towards quantum length scales. Many chemical structures with well-known unit cells (for crystals, the unit cell describes the periodic atomic arrangement) have been studied and new physical phenomena have emerged when moving from the bulk to the nanoscale (where the atomic structure is unchanged but there are significantly fewer unit cells making up the material).

The term *nanomaterial* was introduced in the 1970s to describe these low-dimensional material structures with size-dependent properties. However, the optical applications of nanoscale materials date back over a millennium. Most famously, the 'Lycurgus Cup' from 4th-century Rome exhibits direction-dependent colour due to a dichroic glass containing gold and silver nanoparticles of only $\sim$70 nm diameter, and Medieval stain glass windows routinely contained metal oxide nanoparticles to provide their rich vibrant colours [Col09]. While the science behind these phenomena was not likely understood at the time, one of the first academic studies on nanomaterials was still published over 150 years ago when Michael Faraday synthesised colloidal 'ruby' gold nanoparticles in 1857 [Far57].

More recently, the explosion of interest and rapid progress in nanoscience can be attributed to the invention of high-resolution microscopy techniques to characterise and advance our understanding of these structures. Reports of remarkable properties and the potential for new photonic devices have also fuelled research in this field.

Briefly, nanomaterials can be categorised into zero-dimensional (0D), one-dimensional (1D) and two-dimensional (2D) structures, where the number of dimensions refers to macroscopic dimensions. Zero-dimensional nanomaterials include clusters of isolated particles, such as buckminsterfullerene [Kro85] – for which the 1996 Nobel Prize in Physics was awarded for its discovery. One-dimensional materials include tubes and fibres with nanoscale ($<$100 nm) diameters, such as carbon nanotubes [Iij91]. Two-dimensional materi-

als are flat sheets made up of a small number of layers of atoms, such as graphene [Nov04]; the experimental fabrication of this resulted in a second Nobel Prize in Physics (2010) related to the field of nanomaterials.

To this day, 'new' nanomaterials are emerging by exfoliating few-layer forms of existing materials and nanomaterial-enabled optical systems are beginning to transition from laboratories to commercial products. In this thesis, we investigate the nonlinear optical properties of few-layer transition metal dichalcogenides and exploit them as saturable absorbers for short pulse generation in Chapter 4.

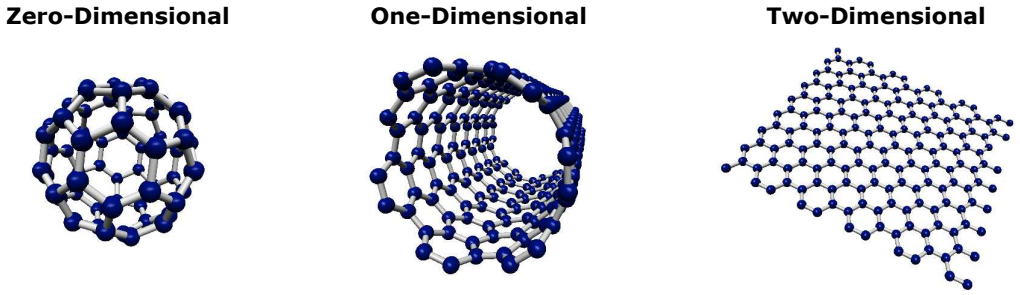


Fig. 1.19: Illustration of atomic arrangements in 0D, 1D and 2D nanomaterials. All atoms in these representations are identical, which is the case for carbon-based materials: buckminsterfullerene, carbon nanotubes and graphene.

1.7 Summary

This chapter has outlined the major historical developments leading to the success of fibre lasers today and introduced the main fundamental and technological concepts that we use in this thesis. We discussed light guidance in optical fibres and reviewed the linear and nonlinear phenomena which can be used to control the temporal and spectral optical properties. Photonic crystal fibres and nanomaterials were introduced as versatile platforms for exploiting nonlinear effects. We also briefly considered the underlying technology of rare-earth-doped fibres and pulse generation techniques. As the following chapters intend to demonstrate, nonlinearity can be a powerful tool in the development of short-pulse fibre lasers.

2

SIMULATION OF SHORT-PULSE FIBRE LASERS

Fibre lasers offer vast design freedom. It is therefore desirable to develop models for simulating laser behaviour to elucidate the influence of cavity design on the spectral and temporal output properties. This can enable quicker experimentation than constructing a system physically and can provide additional insight into intracavity pulse dynamics.

Models for light-matter interaction in optical components are typically derived from Maxwell's equations and fundamental quantum mechanics, and a trade-off exists between model accuracy and the computational cost of finding solutions. Therefore, various approaches for fibre laser simulations have been proposed in the literature, using different assumptions to simplify the problem while retaining the core physics.

In this chapter, we adopt an *experimentalist's approach* to short-pulse fibre laser simulations, with an emphasis on numerically efficient algorithms that can be quickly and conveniently solved on non-specialist hardware.[1] In Section 2.1 we establish a mathematical representation for electromagnetic pulses and discuss how to interpret and visualise their properties. The computation of propagation modes and the properties of step-index fibres and *photonic crystal fibres* (PCFs) are examined in Section 2.2. Section 2.3 introduces the Generalised Nonlinear Schrödinger Equation that can describe pulse propagation in waveguides, including numerical treatment of the nonlinear fibre optics effects we introduced in Chapter 1. Finally, models for rare-earth doped fibre amplifiers are considered in Section 2.4, before all of these approaches are combined to present a complete simulation of a mode-locked fibre soliton laser in Section 2.5.

[1] All numerical work in this thesis was implemented in Python (using the scientific computing library, SciPy) and executed on an average-specification personal computer.

2.1 Mathematical Description of Optical Pulses

An optical pulse can be fully described by its electric field, which is a real-valued function of space and time: $\mathcal{E}(x,y,z,t)$. To simplify the mathematics, we introduce a complex-valued '*analytic signal*'[2] for the electric field $E(x,y,z,t)$ which satisfies: $\mathcal{E}(x,y,z,t) = \frac{1}{2}[E(x,y,z,t) + c.c.]$ where $c.c.$ denotes the complex conjugate. Further simplifications can be made by treating the spatial (transverse mode) profile in the $x-y$ plane separately from temporal and spectral evolution in the direction of propagation z, assuming a fixed linear polarisation state, and separating the field into a rapidly varying carrier wave that is modulated by a pulse envelope. The electric field is thus defined as [Agr13, Tre00]:

$$E(x,y,z,t) = F(x,y)\, A(z,t) \exp(-i\omega_0 t) \tag{2.1.1}$$

where $F(x,y)$ is the spatial light profile, $A(z,t)$ is the envelope and ω_0 is the reference carrier angular frequency (often chosen to correspond to the central wavelength of the pulse spectrum).

All spectral and temporal information about the pulse is contained in the envelope function:

$$A(z,t) = |A(z,t)| \exp[i\phi(z,t)] \tag{2.1.2}$$

where $|A(z,t)|$ and $\phi(z,t)$ are the temporal amplitude and phase, respectively. The envelope is normalised such that $|A(z,t)|^2$ corresponds to the instantaneous optical power in watts.

The pulse envelope in the frequency domain is related to the time-domain representation, $A(z,t)$ by the Fourier transform $\mathcal{F}$:

$$\begin{aligned} \tilde{A}(z,\omega-\omega_0) &= \mathcal{F}[A(z,t)] && (2.1.3)\\ &= \int_{-\infty}^{+\infty} A(z,t) \exp[i(\omega-\omega_0)t]\, \mathrm{d}t && (2.1.4)\\ &= |\tilde{A}(z,\omega-\omega_0)| \exp[i\varphi(z,\omega-\omega_0)] && (2.1.5) \end{aligned}$$

where $|\tilde{A}(\omega-\omega_0)|$ and $\varphi(z,\omega-\omega_0)$ are the spectral amplitude and phase of the pulse.[3] These spectral quantities are shifted to a centre frequency of zero, since the carrier was decoupled from the envelope. While it is preferable to visualise pulses in the time-domain without a rapidly oscillating carrier components, we often choose to plot the spectrum centred at the real wavelength for clarity. Mathematically, this corresponds to the Fourier transform of the real electric field $\tilde{\mathcal{E}}(z,\omega)$ rather than the complex field envelope $\tilde{A}(z,\omega-\omega_0)$. This convention is widely adopted however and henceforth, we

[2] The analytic signal technique, first introduced by Gabor in 1946, is commonly used in oscillation theory to define the amplitude, phase and frequency of a real-valued time function by using complex exponential notation [Gab46].

[3] The tilde above a function indicates that it is the Fourier transform. Strictly, since the electric field is a real-valued function, its Fourier transform contains both positive and negative frequencies, but we often ignore the negative frequencies.

use $\tilde{A}(z,\omega)$, $|\tilde{A}(\omega)|$ and $\varphi(\omega)$ to represent the spectral quantities of the pulse envelope, shifted to the true frequency.

2.1.1 Numerical Representation

At any given position in z, the field envelope functions $A(t)$ and $\tilde{A}(\omega)$ can be represented digitally as one-dimensional arrays by approximating them onto a discrete grid of points. The temporal grid is created with a sufficient time span T to contain the whole pulse envelope (including any phase delays during propagation), and consisting of $N = 2^n$ evenly spaced points (where n is an integer[4]), which correspond to samples taken at intervals of $\Delta t = T/N$. The spectral grid contains the same number of points, corresponding to regular sampling at N frequency intervals Δf centred about zero, such that $\Delta f = 1/T$ and the maximum frequency is related to half the temporal point spacing according to the Nyquist sampling theorem.

A continuous field is therefore represented on the numerical grid by sampling, storing the amplitude and phase at every grid point as a complex value. The *Fast Fourier Transform* (FFT) algorithm is used to switch between time and frequency domains. Careful selection of the numerical grid is the first step in any simulation, since a trade-off exists between computational cost and the accuracy of numerical representation of the field.

When considering propagation of a field envelope, we sample the evolution of the field along z to build two-dimensional arrays in time $A(z,t)$ and frequency $\tilde{A}(z,\omega)$. For convenience and efficiency, we often let the numerical grid (which represents the simulation window) travel at a velocity $v_{g,\text{window}}$ equal to the group velocity of the input pulse (illustrated in Fig. 2.1).[5] This corresponds to a coordinate transform from a laboratory time frame t to the simulation window time frame t'.

$$t' = t - \frac{z}{v_{g,\text{window}}} \tag{2.1.6}$$

and is discussed further in the context of pulse propagation equations in Section 2.3.

2.1.2 Pulse Visualisation

A major benefit of numerical modelling is that the pulse $A(z,t)$ can be fully known at every position in the laser or along a length of fibre, offering not just the output properties of a system, but a complete insight into the dynamic evolution of the pulse. Such understanding of the dynamics may not even be possible from experimental studies, since intracavity measurements would perturb the field.

[4] The number of grid points is chosen as a power of two since this is a condition under which the FFT is particularly efficient and fast.

[5] However, for greater flexibility, it is possible to define a simulation grid which is not centred at the frequency of the pulse and which travels at a group velocity corresponding to any carrier arbitrary frequency ω_{ref}. This corresponds to replacing ω_0 with the reference frequency ω_{ref}.

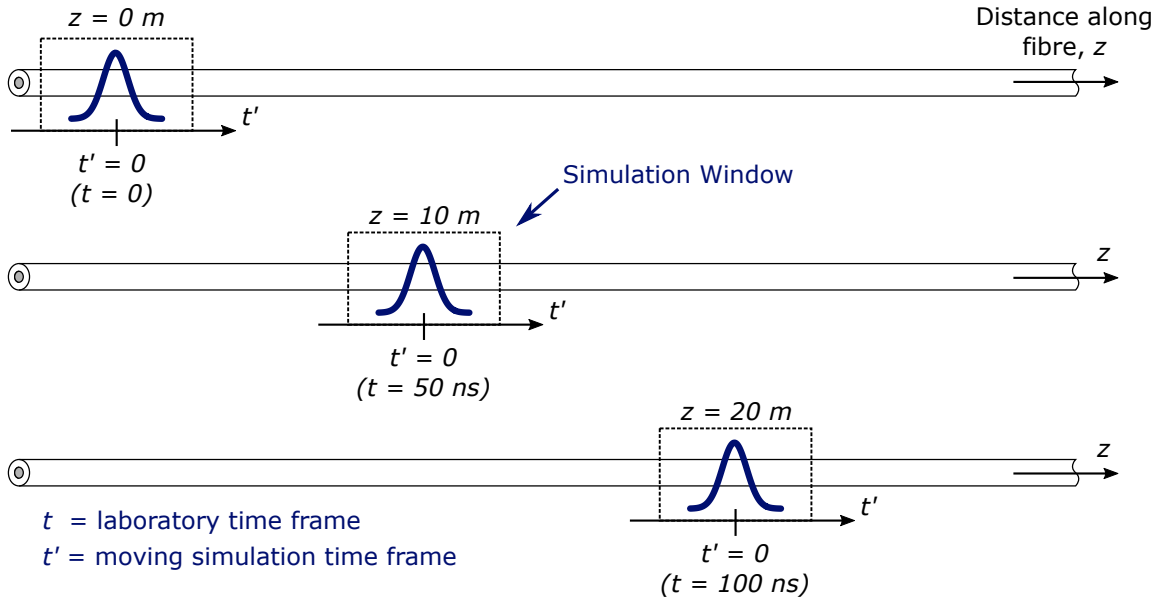


Fig. 2.1: Illustration of simulation time grid in a travelling reference frame t' along a fibre, relative to the laboratory time frame t. Here, the simulation window propagates at the group velocity of the pulse, fixing the pulse centre at $t' = 0$ for all positions in the fibre.

The pulse shape is given by the intensity $I(z,t) = |A(z,t)|^2$ [with units of watts, where the power is distributed over the transverse mode profile described by $F(x,y)$] and the spectral intensity is $S_\omega(z,\omega) = |\tilde{A}(z,\omega)|^2$. To visualise the spectrum on a wavelength axis, rather than a frequency axis, a scaling factor must be introduced such that the integrated area under the spectrum remains constant: $S_\lambda(z,\lambda) = S_\omega(z, 2\pi c/\lambda)\frac{2\pi c}{\lambda^2}$ [Tre00]. The temporal phase can be extracted from the field by $\phi(z,t) = \arctan\left\{\frac{\mathrm{Im}[A(z,t)]}{\mathrm{Re}[A(z,t)]}\right\}$ and similarly for the spectral phase, $\varphi(z,\omega) = \arctan\left\{\frac{\mathrm{Im}[\tilde{A}(z,\omega)]}{\mathrm{Re}[\tilde{A}(z,\omega)]}\right\}$.

Additionally, it can be useful to compute the instantaneous angular frequency, given by: $\omega_{\mathrm{inst}}(z,t) = \omega_0 + \frac{\mathrm{d}\phi(z,t)}{\mathrm{d}t}$, to observe the distribution of frequency components within the pulse shape. We refer to a change in instantaneous frequency with time as *chirp*, as introduced in Section 1.3.3.

The spectral and temporal content of a pulse is perhaps visualised in a most complete format by the *spectrogram*, computed by Fourier transforming small temporal sections of the signal [section size defined by a Gaussian gate function $g(t)$] in turn to build up a picture of the time-dependent spectrum.[6] Mathematically, this corresponds to:

$$\mathrm{SGM}(z,\omega,t) = \left|\int_{-\infty}^{\infty} A(z,t)g(t-\tau)\exp(i\omega\tau)\mathrm{d}\tau\right|^2 \tag{2.1.7}$$

These concepts are illustrated graphically in Fig. 2.2 for a linearly up-chirped pulse. The spectrogram can be seen to clearly and compactly illustrate the distribution of spectral content within the pulse envelope.

[6] This measurement can also be made experimentally using a cross-correlation frequency-resolved optical gating (XFROG) technique [Tre00].

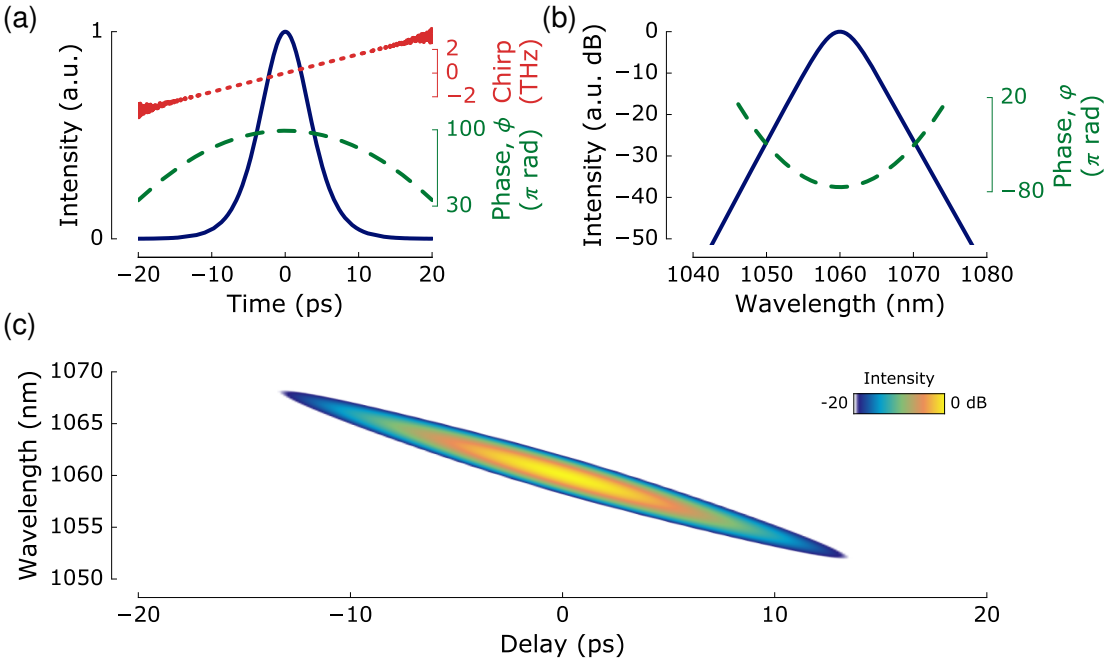


Fig. 2.2: Visualisation of a linearly up-chirped sech pulse: (a) pulse profile, temporal phase and chirp (instantaneous frequency); (b) optical spectrum and spectral phase; (c) spectrogram, measured with a 2 ps width gate window.

2.2 Propagation Modes of Optical Fibres

Fibres can support a number of guided propagation modes (as introduced in Section 1.3), which depend on the waveguide structure and optical frequency, with each propagation mode possessing distinct properties. Therefore, to determine fibre behaviour at a given wavelength, it is necessary to compute the supported modes and their respective characteristics, which we now summarise for both conventional step-index fibre and PCF.

2.2.1 Step-Index Fibre

Electric and magnetic fields are vector quantities, resulting in 6 separate field components (E_x, E_y, E_z, H_x, H_y, H_z) which must each satisfy the Helmholtz wave equation (derived from Maxwell's equations) in homogeneous regions of constant refractive index (i.e. in both the core and cladding) [Sny83]. Solutions of interest are restricted to those travelling along the fibre axis z. Depending on the combination of field components, different types of supported modes can be determined including transverse electric (TE), transverse magnetic (TM) and hybrid (HE and EH) modes.[7]

For each type of mode, it is possible to form a characteristic eigenvalue equation by enforcing continuity of the mode and its derivative across the core-cladding boundary. The eigenvalue solutions are the propagation constants β for supported modes, and the

[7] TM and TE modes correspond to *meridional* rays travelling along the fibre axis while hybrid modes relate to *skew* rays which follow a helical path along z without passing through the z axis. They are defined as TE ($E_z = 0$, $H_z \neq 0$), TM ($E_z \neq 0$, $H_z = 0$), HE ($E_z \neq 0$, $H_z \neq 0$, $H_z > E_z$) and EH ($E_z \neq 0$, $H_z \neq 0$, $E_z > H_z$).

eigenfunctions are the transverse mode profiles. To determine the optical properties of a given mode, the eigenvalue β is computed across a range of wavelengths, describing the frequency-dependent phase delay.

Fortunately, for most step-index fibres, the problem can be simplified using a *weakly-guiding approximation* ($n_{\text{core}} \approx n_{\text{clad}}$) since the index difference Δn between the core and cladding is typically small [Glo71]. This assumes guided rays are approximately paraxial with weak longitudinal field components, leading to identical continuity conditions for electric and magnetic fields. Consequently, this becomes a scalar problem and the types of fields can be neglected, yielding the following eigenvalue equation [Glo71]:

$$\frac{J_{l-1}(U)}{J_l(U)} = -\frac{W}{U}\frac{K_{l-1}(W)}{K_l(W)} \tag{2.2.1}$$

where U and W are dimensionless parameters, J_l is an ordinary Bessel function of the first kind and K is a modified Bessel function of the second kind (the Bessel function order is indicated by the subscript l). The dimensionless parameters are defined as the normalised core parameter $U = a\sqrt{k_0^2 n_{\text{core}}^2 - \beta^2}$ and the normalised cladding parameter $W = a\sqrt{\beta^2 - k_0^2 n_{\text{clad}}^2}$, in addition to the normalised waveguide parameter $V = a\sqrt{k_0^2 n_{\text{core}}^2 - k_0^2 n_{\text{clad}}^2}$ such that $V^2 = U^2 + W^2$, where $k_0 = 2\pi/\lambda$ is the free-space wavenumber, a is the core radius and β is the propagation constant to be found.

Many solutions can exist to the eigenvalue equation (Eqn. 2.2.1): for a given l index there will be m solutions, where each solution derived from this weakly guiding analysis is known as a linearly polarised LP_{lm} mode.[8] [9] Since the equation is transcendental, it can be solved numerically by root-finding, using the known boundaries of the problem based on Bessel function zeros to define a parameter range in which to search for a solution [Kaw01]:

$$\text{LP}_{01} \text{ mode}: \quad 0 \leq U \leq j_{0,1} \tag{2.2.2a}$$

$$\text{LP}_{0m} \text{ mode}: \quad j_{1,m-1} \leq U \leq j_{0,m} \quad \text{for } m \geq 2 \tag{2.2.2b}$$

$$\text{LP}_{lm} \text{ mode}: \quad j_{l-1,m} \leq U \leq j_{l,m} \quad \text{for } l \geq 1, m \geq 1 \tag{2.2.2c}$$

where $j_{l,m}$ is the mth zero of the lth-order Bessel function of the first kind. When a mode is unsupported by the fibre at a particular wavelength, no solution can be found in the corresponding range. Practically, we implemented this procedure using a bounded root-finding algorithm (using Brent's method).

Once a solution U is found for a given mode, the propagation constant β is extracted. Since this can be Taylor expanded (Eqn. 1.3.12) and written in terms of group velocity

[8] l and m are often denoted as the azimuthal and radial mode indices, respectively. Specifically, l is the number of intensity maxima/minima within a full rotation in the plane of the mode and m is the number of maxima/minima that occur when moving from the fibre centre outwards to infinity.

[9] It is also possible to identify the degenerate vector modes which comprise each LP mode. For instance, LP_{01} is equivalent to HE_{11} and LP_{11} is a set of vector modes including TE_{01}, TM_{01} and HE_{21}.

dispersion β_2, third order dispersion β_3 etc., values for β_n at a given wavelength can be obtained by differentiation:

$$\beta_n(\lambda) = \left(\frac{\mathrm{d}^n\beta}{\mathrm{d}\omega^n}\right)_{\omega=2\pi c/\lambda} \tag{2.2.3}$$

This is achieved numerically by fitting the computed array of β values across the transparency window of silica with a polynomial, permitting facile differentiation.[10]

Modal intensity profiles are most conveniently defined in terms of radial r and azimuthal ϕ cylindrical coordinates [Buc95]:

$$I_{lm} = I_0 J_l^2\left(\frac{Ur}{a}\right)\cos^2(l\phi) \qquad r \leq a \text{ (core)} \tag{2.2.4a}$$

$$I_{lm} = I_0\left(\frac{J_l(U)}{K_l(W)}\right)^2 K_l^2\left(\frac{Wr}{a}\right)\cos^2(l\phi) \qquad r \geq a \text{ (cladding)} \tag{2.2.4b}$$

where I_0 is the peak intensity. The effective area A_{eff} and nonlinear parameter γ can then be computed using Eqns. 1.3.18 and 1.3.19.

Finally, we note that fibres have two orthogonal polarisation axes, meaning that a single LP mode includes a set of nondegenerate submodes (known as polarisation modes), distinguished by the orientation of the electric field. Even slight birefringence in the fibre from bends or manufacturing imperfections can yield small changes in the index of each polarisation axis, giving different modal properties (this is the origin of polarisation mode dispersion). However, we neglect this effect henceforth and consider only a single polarisation mode propagating in fibre, as is the case for light launched along a principal axes of polarisation-maintaining fibre.

Single-Mode Fibre for Yb-Doped Fibre Lasers

In this thesis, we regularly work at wavelengths within the ytterbium gain band and IPG Flexcore is used as passive single-mode fibre (with step index profile $\Delta n \sim 0.006$ and core diameter $d_c \sim 5.3$ μm, equivalent to the commercially available Corning Hi1060 fibre). While Flexcore is single-moded at ∼1060 nm, multiple modes are supported at shorter wavelengths. Our model calculates that LP_{01}, LP_{11}, LP_{21} and LP_{02} modes exist for light at 520 nm, with spatial distributions and dispersion curves as shown in Fig. 2.3.

The wavelength at which a mode ceases to be supported is known as the *cut-off wavelength* and as the wavelength approaches this value, the dispersion curve varies substantially and the effective area sharply increases, reducing the mode power within the core (this is seen in Fig. 2.3 for LP_{21} and LP_{02}, which both cut off at ∼580 nm.). Since single-mode operation is desired for high beam quality in fibre lasers, the cut-off wavelength for the LP_{11} mode is a particularly important parameter. At this cut-off, n_{eff} approaches

[10] The order of the polynomial n is determined by an optimised fitting, but limited to $n < 8$ since interpolation with high-order polynomials can yield unphysical numerical artefacts [Run01].

n_{clad} ($W \to 0$) and from Eqn. 2.2.2, it can be seen that this value corresponds to $U = j_{0,1}$, and thus the waveguide parameter $V = j_{0,1} = 2.405$. Finally, it should be noted that the properties of manufactured fibres may vary slightly, thus the numerical models here are intended for guidance purposes and the computed values will not be exact.

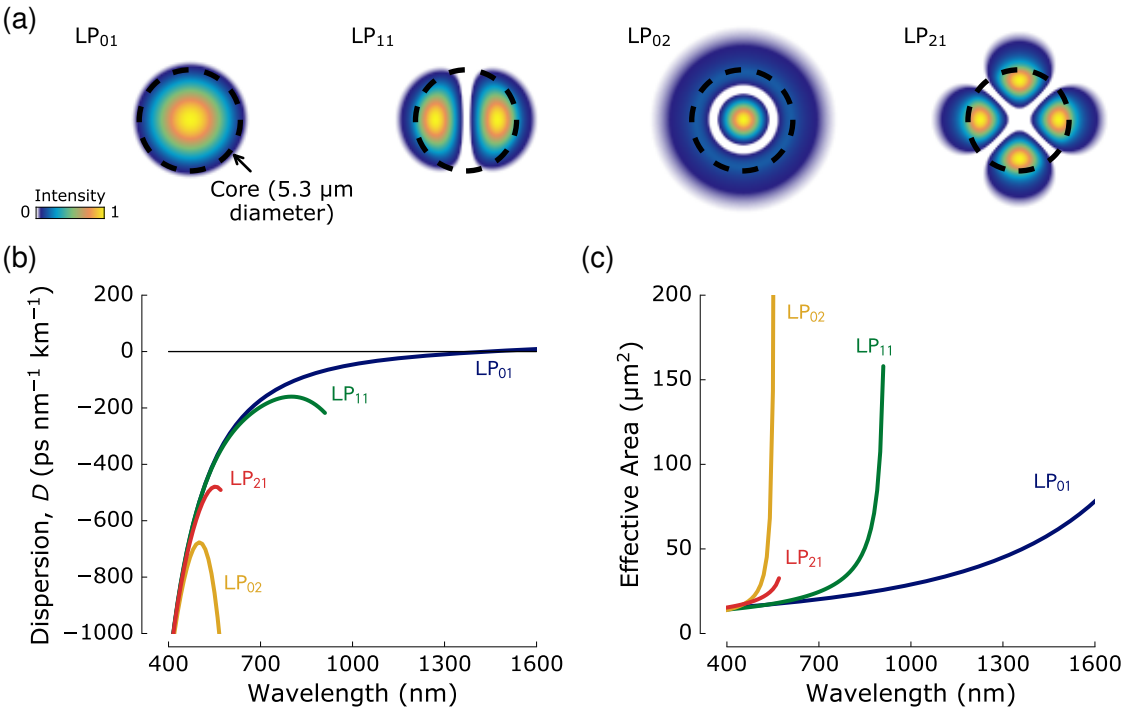


Fig. 2.3: Modal properties for Flexcore fibre (step-index fibre with 5.3 μm core diameter and Δn=0.006): (a) spatial intensity profiles for guided modes at 520 nm; (b) dispersion and (c) effective area within the guidance range of each mode. LP_{lm} refers to a linearly polarised mode with azimuthal mode index l and radial mode index m.

2.2.2 Photonic Crystal Fibre

One of the greatest strengths of PCF is the ability to possess a high index contrast between the core and cladding region, to achieve strong waveguide effects. Unfortunately, this limits the validity of a weakly guiding approximation, complicating the modal analysis. While numerical methods such as finite element analysis have been demonstrated to accurately determine PCF properties, these are typically slow and computationally demanding [Zol05]. However, a good approximate model for PCFs can be obtained using an *effective index method*, which generalises the analysis of step-index fibres to account for the microstructured cladding [Bir97, Kni98].

The effective index model reduces a PCF structure to a step-index fibre with a solid silica core where $n_{\text{core}} = n_{\text{silica}}$ and a cladding where n_{clad} is computed as the effective index of the fundamental mode that could exist in an infinite periodic lattice with the same microstructure as the PCF cladding (known as the *fundamental space filling mode*,

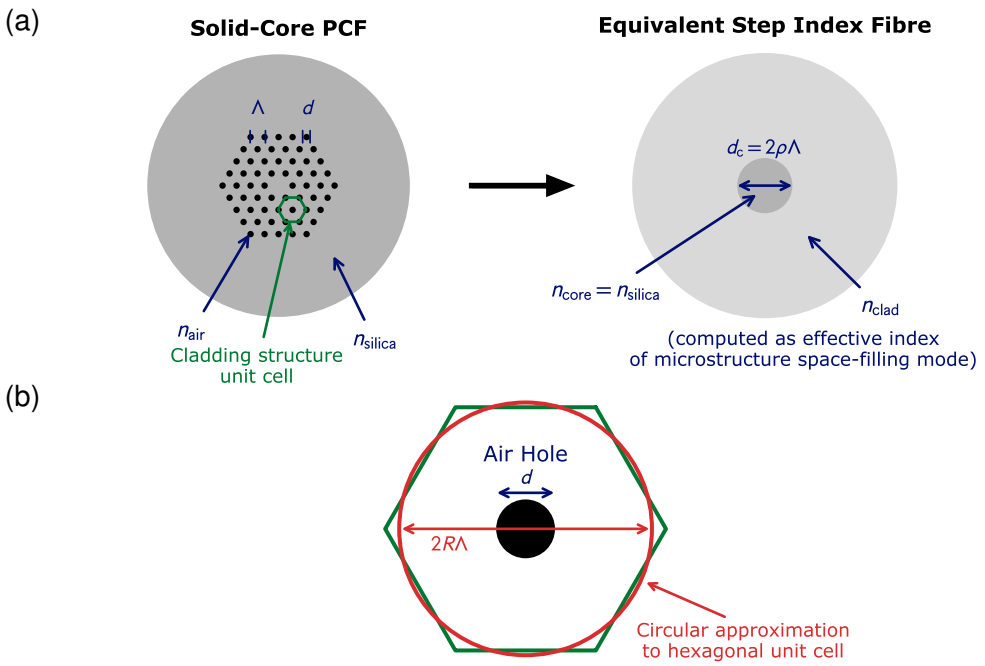


Fig. 2.4: Illustration of PCF modelling method: (a) the structure is treated as a step-index fibre with core diameter related to the air hole pitch, core index equal to the index of silica and cladding index computed as the effective index of the space-filling mode for the microstructure; (b) circular unit cell approximation for calculating the space-filling mode of the microstructure. R and ρ are scaling factors, described in the main text.

FSM). This is illustrated in Fig. 2.4a. Computation of PCF properties is therefore a two-step problem: first, the fundamental space filling mode for the microstructured cladding is found to determine n_{clad}; second, the mode propagation constant is found for the equivalent step-index fibre [Kni96].

As the weakly guiding assumption cannot be used here, a vector analysis is required, distinguishing between different types of modes as discussed earlier. The fundamental mode of the microstructured cladding will have the same symmetry as the photonic crystal and is thus computed within a unit cell of the structure centred on an air hole [Bir97, Li04, Mid00]. This is simplified by approximating the hexagonal cell as a circle with diameter $2R\Lambda$ where Λ is the hole pitch and R is a scaling factor (Fig. 2.4b). R is commonly accepted as $R = 0.5$ [Mid00] or $R = \sqrt{(\sqrt{3})/(2\pi)}$ [Li06] in the literature; we find better agreement with experiments using the latter. A full derivation of the eigenvalue equation for the microstructured cladding's space filling mode (i.e. the fundamental HE_{11} mode) is presented in Refs. [Mid00, Li06]; here, we quote the result which we then solve (to find n_{FSM}) by numerical root finding:

$$\left(\frac{P_1'(ga_h)}{ga_hP_1(ga_h)} + \frac{I_1'(fa_h)}{fa_hI_1(fa_h)}\right)\left(\frac{n_{\text{silica}}^2 P_1'(ga_h)}{ga_hP_1(ga_h)} + \frac{n_{\text{air}}^2 I_1'(fa_h)}{fa_hI_1(fa_h)}\right) = \left(\frac{1}{(ga_h)^2} + \frac{1}{(fa_h)^2}\right)^2 n_{\text{FSM}}^2 \tag{2.2.5}$$

where $g = \sqrt{k_0^2 n_{\text{silica}}^2 - k_0^2 n_{\text{FSM}}^2}$, $f = \sqrt{k_0^2 n_{\text{FSM}}^2 - k_0^2 n_{\text{air}}^2}$, a_h is half the air hole diameter, I_1 is a modified Bessel function of the first kind and order 1, primes denote differentiation with respect to the argument and:

$$P_1(ga_h) = J_1(ga_h)Y_1(gR) - Y_1(ga_h)J_1(gR) \tag{2.2.6}$$

where Y_1 is a Bessel function of the second kind and order 1.

Finally, we find the fundamental mode for the PCF as the HE_{11} mode of the equivalent step-index fibre with core diameter $d_c = 2\rho\Lambda$, where ρ is a scaling factor. Values of $\rho = 0.625$ [Bir99] and $\rho = 1/\sqrt{3}$ [Kos04] have been proposed; we observe the former to yield better accuracy. The HE_{11} eigenvalue equation, to be solved (for β) by root-finding, is [Li04, Sny83]:

$$\left(\frac{J_1'(U)}{UJ_1(U)} + \frac{K_1'(W)}{WK_1(W)}\right)\left(\frac{n_{\text{core}}^2 J_1'(U)}{UJ_1(U)} + \frac{n_{\text{clad}}^2 K_1'(W)}{WK_1(W)}\right) = \left(\frac{1}{U^2} + \frac{1}{W^2}\right)^2 \left(\frac{\beta}{k}\right)^2 \tag{2.2.7}$$

where U and W are defined as in Section 2.2.1, but with $n_{\text{core}} = n_{\text{silica}}$, $n_{\text{clad}} = n_{\text{FSM}}$ and effective core radius $a = 0.5d_c = \rho\Lambda$.[11]

The computed mode profile for a PCF with $\Lambda = 3.2$ μm and $d = 1.6$ μm is shown in Fig. 2.5a, in addition to an indication of the core size for the equivalent step index fibre (black dashed line). A limitation of this method is that the mode profile is uniform in the cladding, when in reality the field will be more concentrated in the silica bridges and not in the air holes. Therefore, to gain insight into the exact mode shape, more complicated modelling techniques are required, as we discuss in Section 5.2.4 in the context of acousto-optic interactions in PCF. However, this vector analytical effective index method can accurately predict the dispersion of PCF structures [Li08] and is used in Section 3.4.3 for modelling supercontinuum generation in PCF. As an example, we compute the dispersion for a 3.2 μm pitch PCF while considering the impact of varying the air hole size (Fig. 2.5b). With increasing air hole size, the effective index contrast becomes greater, providing stronger anomalous waveguide dispersion. This shifts the *zero-dispersion wavelength* (ZDW) towards shorter wavelengths. From the large coloured region in Fig. 2.5b, it can be seen that PCFs offer great flexibility, allowing dispersion to be controlled over a wide parameter range by changing the microstructure geometry.

[11] During the writing of this thesis, we became aware of empirically-derived expressions proposed by Saitoh and Koshiba [Sai05] as an alternative method for determining the propagation constant of PCF modes. These expressions give excellent accuracy over a wide parameter range (failing, however, for very small pitch values and large d/Λ ratios). While these empirical equations were not employed in this thesis, our preliminary investigations found that they could be evaluated more quickly and conveniently than the root finding approach we have just outlined, while returning similar results. Therefore, since the aim of this chapter is to introduce accurate and efficient modelling techniques, we feel that this work deserves mention and will be considered further for future simulations.

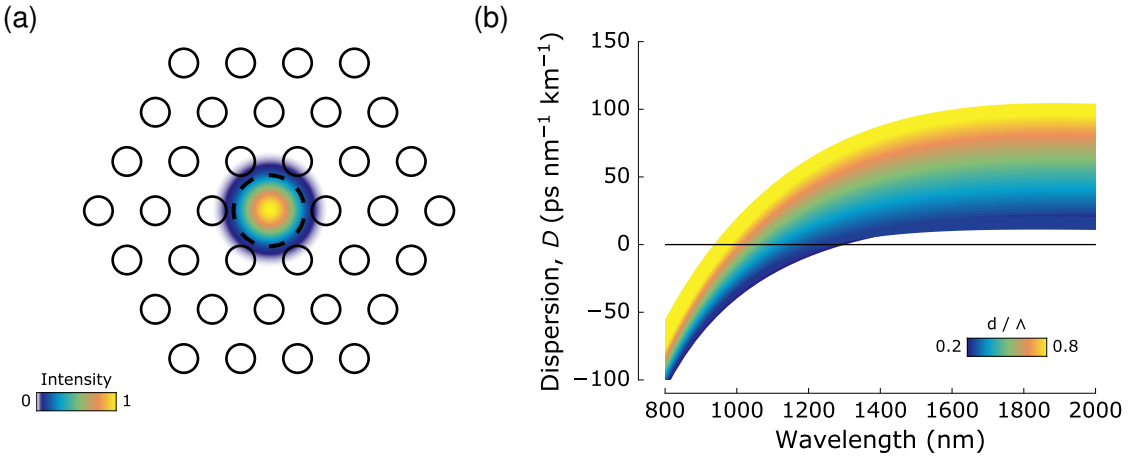


Fig. 2.5: Simulated properties of PCFs with $\Lambda = 3.2$ µm : (a) mode intensity profile when $d = 1.6$ µm where the dotted line is the effective core diameter for the equivalent step-index fibre; (b) dispersion curves as d/Λ varies from 0.2 to 0.8.

2.3 Pulse Propagation using a Generalised Nonlinear Schrödinger Equation

The *nonlinear Schrödinger equation* (NLSE) is a nonlinear partial differential equation for describing wave propagation in nonlinear medium.[12] Different variations of the equation have been applied in numerous distinct fields, including fluids [Zak68], Bose-Einstein condensates [Rup95] and notably for this work, to accurately predict the propagation of light in optical fibre [Has73a]. The celebrated formulation of the NLSE to describe the evolution of a time-domain pulse envelope $A(z,t)$ in fibre (in one time dimension t and one spatial dimension along the fibre axis z) including only the effects of group velocity dispersion β_2 and Kerr nonlinearity is:

$$\frac{\partial A}{\partial z} = -i\frac{\beta_2}{2}\frac{\partial^2 A}{\partial t^2} + i\gamma|A(z,t)|^2 A(z,t) \tag{2.3.1}$$

This form of the equation is integrable, and its solutions (obtained via an inverse scattering transform [Zak72]) are solitons (discussed in Section 1.3.4).

For a more complete description of nonlinear fibre optics, however, higher-order effects must be considered. Notable contributions from Kodama and Hasegawa [Kod87], Blow and Wood [Blo89] and Mamyshev and Chernikov [Mam90] derived an extended or *generalised NLSE* (GNLSE) by including a nonlinear polarisation term in Maxwell's equations. The GNLSE can be formulated in either the time domain or frequency domain, although the frequency-domain equation more naturally allows for the inclusion of wavelength-

[12] Its name derives from the similarity in appearance to the well-known Schrödinger equation in quantum mechanics.

dependent loss, nonlinearity and effective area [Fra91].[13] It is this formulation that we have adopted in this thesis to describe the pulse envelope:

$$\begin{aligned}\frac{\partial \tilde{A}(z,\omega)}{\partial z} = &\underbrace{\frac{g(\omega)-\alpha(\omega)}{2}}_{\text{Gain/Loss}}\tilde{A}(z,\omega) + \underbrace{i[\beta(\omega)-\beta(\omega_0)-\beta_1(\omega_0)(\omega-\omega_0)]}_{\text{Dispersion (in co-moving frame)}}\tilde{A}(z,\omega) \\ &+ \left(i\gamma(\omega)\underbrace{\left[1+\frac{\omega-\omega_0}{\omega_0}\right]}_{\text{Self-Steepening}} \right. \\ &\left. \times \mathcal{F}\left\{ A(z,t')\left[\underbrace{(1-f_r)|A(z,t')|^2}_{\text{Kerr}} + \underbrace{f_r\int_{-\infty}^{+\infty} h_R(T')|A(z,t'-T')|^2 \mathrm{d}T'}_{\text{Raman}} \right] \right\} \right)\end{aligned} \tag{2.3.2}$$

where $g(\omega)$ and $\alpha(\omega)$ are the gain and attenuation coefficients respectively, f_r is the fractional Raman contribution and $h_R(t)$ is the Raman impulse response.

The validity of Eqn. 2.3.2 is based on the following assumptions:[14]

- All electric fields are linearly polarised in the same direction.
- Only one transverse mode exists in the fibre.
- Unidirectional propagation; any backwards propagating waves (e.g. from Brillouin scattering) are neglected.
- Weak nonlinearity, such that the nonlinear change in refractive index is much less than the linear index.
- Negligible third-harmonic generation.

Many of these assumptions can be relaxed by adopting more complex variations of the GNLSE and including correction terms, although these cases are beyond the scope of the experiments in this thesis. Additionally, theoretical work continues to this day to expand the validity of such numerical modelling techniques, providing insight into new parameter ranges and 'extreme' nonlinear optical phenomena [Con13, Tan14, Kol14].

The significance of each term in Eqn. 2.3.2 is discussed in the following subsections, complementing the more verbose discussion of the physical implications of these effects on the pulse shape and spectrum in Section 1.3.

[13] In addition to the original references we have mentioned, many excellent monographs exist on this topic, summarising derivations and verifying the accuracy of simplified equations under various assumptions, such as Refs. [Gen07, Dud10, Cou11, Agr13, Lav15].

[14] A common misconception is assuming that a *slowly varying* envelope is required for the GNLSE. Numerous studies have shown, however, that this equation (which is also often referred to as a *generic nonlinear envelope equation*) remains valid down to few-cycle pulses [Bra97, Gen07].

2.3.1 Linear Effects

Gain and Loss

Light propagating along a fibre may experience gain, in the case of an active fibre (described in Section 2.4), or loss due to absorption and scattering. In simulations, $g(\omega)$ and $\alpha(\omega)$ are arrays of values based on the same numerical grid as the field, thus including the spectral dependence.

There are numerous sources of loss in a fibre, as introduced and shown visually in Fig. 1.6 in Section 1.3.3. The total attenuation is found by summing the independent contributions including Rayleigh scattering, UV absorption, IR absorption and impurity absorption [Wal86]:

$$\alpha(\lambda) = \frac{A_{\text{rayleigh}}}{\lambda^4} + A_{\text{uv}}\ \exp\left(\frac{B_{\text{uv}}}{\lambda}\right) + A_{\text{ir}}\ \exp\left(\frac{-B_{\text{ir}}}{\lambda}\right) + \alpha_{\text{imp}} \tag{2.3.3}$$

where A_{rayleigh}, A_{uv}, B_{uv}, A_{ir} and B_{ir} are magnitude and shape coefficients for each term and α_{imp} is the combined loss from impurities. The dominant impurity losses are from OH absorption at 1240 nm and 1384 nm, which can be modelled by a superposition of i Gaussian profiles:

$$\alpha_{\text{imp}} = \sum_i A_i \exp\left[\frac{-(\lambda - \lambda_i)^2}{2\sigma_i^2}\right] \tag{2.3.4}$$

where each Gaussian term has peak amplitude A_i, centre wavelength λ_i and width σ_i. Different coefficients for the above expressions have been presented in literature, depending on the structure and material of the fibre; here, we follow the single-mode fibre model of Ref. [Wal86] and adjust the amplitude of the water peak to match datasheet values. Finally, we note that fibre loss is commonly specified in units of dB km^{-1}, requiring a conversion to units of m^{-1}: $\alpha\ [\text{m}^{-1}] = \alpha\ [\text{dB km}^{-1}] \times 10^{-4} / \log_{10} e$.

Dispersion

Dispersion is included through the propagation constant β, which is computed for the fibre at every frequency in the numerical grid (as in Section 2.2).

We keep the pulse centred in our simulation window using a coordinate transform (Eqn. 2.1.6) where $v_{g,\text{window}} = 1/\beta_1(\omega_0)$. In the frequency domain, this is equivalent to subtracting $\beta_1(\omega_0)(\omega - \omega_0)$ from β, including a frequency shift by the reference frequency. We also subtract off $\beta(\omega_0)$ to measure the propagation constant relative to the value at the reference frequency.

As an aside, we note that if only the group velocity dispersion β_2 (and possibly higher order dispersion coefficients) is known at a particular reference frequency ω_{ref} (e.g. from a datasheet, when there is insufficient information to compute the full propagation constant at every wavelength), this can be included instead by replacing the $\beta(\omega) - \beta(\omega_0) -$

$\beta_1(\omega_0)(\omega - \omega_0)$ term in Eqn. 2.3.2 with:

$$\beta_{\text{window}} = \sum_{m \geq 2} \frac{\beta_m}{m!} \frac{1}{(\omega - \omega_{\text{ref}})^m} \tag{2.3.5}$$

which follows from the Taylor expansion of the propagation constant (Eqn. 1.3.12) without including the phase offset (β_0) or group velocity term (β_1).

2.3.2 Nonlinear Effects

While Eqn. 2.3.2 is formulated in the frequency domain, computation of nonlinear effects requires the time-domain envelope to be used to determine intensities. Nonlinear polarisation is divided into an instantaneous Kerr term (electronic) and a delayed Raman response (vibrational), which are treated separately and weighted by the fractional Raman contribution factor f_r. For silica fibres, a value of $f_r = 0.18$ is typically used [Sto89].

Kerr Nonlinearity

The Kerr effect is assumed to be instantaneous and is included in the GNLSE in the same manner as in the basic NLSE: related to $\gamma(\omega)|A(z,t)|^2 A(z,t)$. The frequency-dependence of the nonlinearity, due to the increased effective area at longer wavelengths, is intrinsically included by computing the array of $\gamma(\omega)$ values from the effective areas $A_{\text{eff}}(\omega)$ that are obtained by integrating over the modal profiles (as discussed in Section 2.2) at every wavelength in the grid.

Self-Steepening

A consequence of the instantaneous Kerr effect (causing a change in the refractive index) is that the group velocity also becomes intensity dependent. The effect can be important for ultrashort pulses where the pulse peak experiences a higher refractive index than the wings and thus a greater delay, pushing the peak towards the trailing edge. This causes a self-induced steepening of the trailing edge [Agr13].

Self-steepening can lead to an *optical shock* (similar to acoustic shocks observed on the leading edge of sound waves) and interplay with group velocity dispersion can result in *optical wave breaking*, distorting the pulse shape and spectrum [Tom85]. To include self-steepening in the GNLSE, a correction factor $\frac{\omega - \omega_0}{\omega_0}$ is included in the nonlinear term [Lav15].

Stimulated Raman Scattering

The Raman term in Eqn. 2.3.2 is a time-domain convolution integral between the pulse envelope intensity and the Raman impulse response function h_R, which accounts for the delayed (non-instantaneous) nature of the effect. This can be efficiently evaluated in the

frequency domain, where convolution operations become products:

$$\int_{-\infty}^{+\infty} h_R(T')|A(z,t'-T')|^2 \mathrm{d}T' = \mathcal{F}^{-1}[\mathcal{F}(|A(z,t')|^2) \times h_R(\omega)] \tag{2.3.6}$$

The delayed Raman response $h_R(t)$, from which $h_R(\omega)$ is found via the FFT, can be described simply by a single damped harmonic oscillation with a Lorentzian lineshape [Blo89]. However, for a negligibly increased computational cost, a more accurate *intermediate-broadening model* can be used based on multiple vibrational modes with lineshapes given by the convolution of a Gaussian and Lorentzian [Hol02]:

$$h_R(t) = \sum_i \frac{M_i}{\omega_i} \exp(-\gamma_i t) \exp\left(-\frac{\Gamma_i^2 t^2}{4}\right) \sin(\omega_i t) H(t) \tag{2.3.7}$$

where for the i^{th} vibrational mode, M_i is the amplitude, ω_i is the central frequency, γ_i is the Lorentzian linewidth, Γ_i is the Gaussian linewidth and $H(t)$ is a unit step function. Coefficients for the silica vibrational modes are given in Ref. [Hol02], resulting in the time and frequency responses shown in Fig. 2.6, where the imaginary part of the spectrum corresponds to the well-known Raman gain curve.

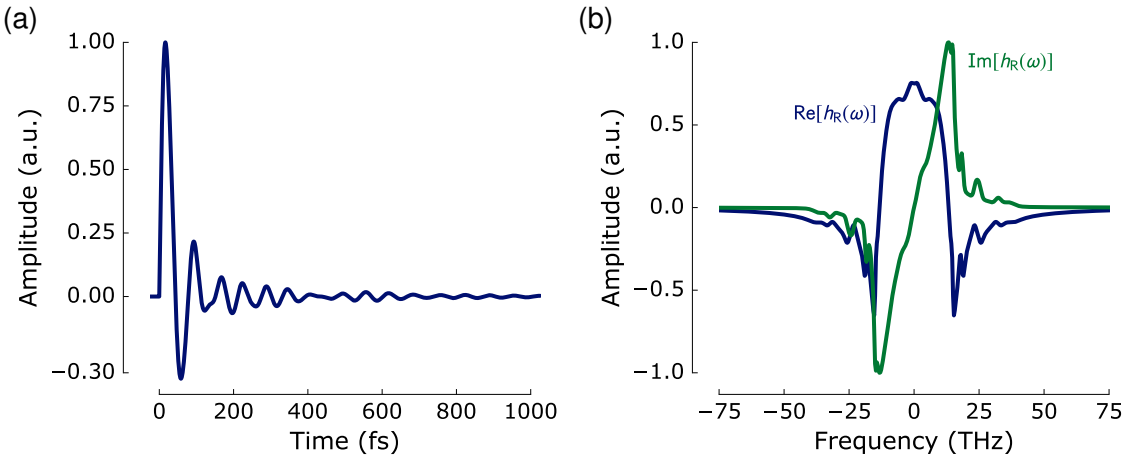


Fig. 2.6: Delayed Raman response in silica, computed using an intermediate-broadening model [Hol02]: (a) impulse response $h_R(t)$; (b) spectral profile $h_R(\omega)$.

2.3.3 Numerical Solution

Numerical Integration

Traditionally, the GNLSE is solved using a pseudospectral *split-step method* where the nonlinear and dispersive terms are integrated separately, one after the other, within a single Δz interval [Har73]. For our work, we adopted a similar, but augmented approach by transforming the problem into an *interaction picture*[15], which decouples the linear and nonlinear

[15]The name and concept of this method derive from quantum mechanics, where different representations or 'pictures' of problems are often chosen to provide physical insight and to simplify calculations.

terms by a change of unknown variable and removes the stiff dispersive part [Hul07]. This technique, initially pioneered for the study of Bose-Einstein condensates [CD00], has recently been applied to pulse propagation in fibre, enabling greater accuracy and efficiency than conventional split-step methods [Hul07].

Briefly, the GNLSE (Eqn. 2.3.2) can be expressed in terms of a linear operator $\hat{L}$ and a nonlinear operator $\hat{N}$:[16]

$$\frac{\partial \tilde{A}}{\partial z} = \hat{L}\tilde{A} + \hat{N}(\tilde{A}) \tag{2.3.8}$$

where:

$$\hat{L} = \frac{g(\omega) - \alpha(\omega)}{2} + i[\beta(\omega) - \beta(\omega_0) - \beta_1(\omega_0)(\omega - \omega_0)] \tag{2.3.9}$$

and

$$\begin{aligned}\hat{N}(\tilde{A}) = \hat{N}[\mathcal{F}(A)] =& i\gamma(\omega)\left(1 + \frac{\omega - \omega_0}{\omega_0}\right) \times \mathcal{F}(A(z,t') \times \\ & \{(1 - f_r)|A(z,t')|^2 + f_r \mathcal{F}^{-1}[\mathcal{F}(|A(z,t')|^2) \times h_R(\omega)]\})\end{aligned} \tag{2.3.10}$$

To move into the interaction picture, we use the transformation:

$$\tilde{A}_{\mathrm{IP}} = \tilde{A}\exp(-z\hat{L}) \tag{2.3.11}$$

which is inserted into Eqn. 2.3.8 to yield:

$$\frac{\partial \tilde{A}_{\mathrm{IP}}}{\partial z} = \exp(-z\hat{L})\hat{N}[\exp(z\hat{L})(\tilde{A}_{\mathrm{IP}})] = \exp(-z\hat{L})\hat{N}(\tilde{A}) \tag{2.3.12}$$

Eqn. 2.3.12 can now be efficiently solved using conventional numerical integration routines, such as Runge-Kutta schemes which are included with most popular programming languages. Mathematically, numerical integration is achieved by splitting the interval (i.e. from $z = 0$ to $z =$ fibre length) into many steps over which to propagate, starting from an initial condition $\tilde{A}(z = 0, \omega)$. Simulation accuracy is determined by the step size Δz, and while smaller steps reduce the error, they increase the computation time. Additionally, the required step size to achieve a particular error tolerance depends on the simulation: generally, the more complex the pulse evolution dynamics, the smaller the required step size. Therefore, an adaptive algorithm is required to efficiently control the step size.

Adaptive Step Size Control

While generic integrators may offer built-in adaptive stepping to achieve a particular local error, it is more flexible to manually implement this with knowledge of the particular problem (the fourth-order Runge-Kutta in the interaction picture method (RK4-IP), proposed by Johan Hult, is particularly popular here [Hul07]).

[16] Our definitions of operators apply for the frequency-domain GNLSE formulation and thus differ from those originally presented in Ref. [Hul07] for use with the time-domain GNLSE.

A *step-doubling* algorithm is often used for this purpose: two small steps and an equivalent large step are taken from each point, with the difference in outcome indicating the local error [Sin03]. If the error is above a given tolerance, the last step is discarded, the step size is halved and the simulation continues from the last acceptable step (if, however, the error is much smaller than permitted, the step size is increased to speed-up the computation).

However, this approach requires that multiple steps are computed for each integration step to achieve error control, which amounts to additional computational cost. It would therefore be advantageous to obtain an estimate of the local error directly within each integration step, such as using an *embedded* Runge-Kutta integration algorithm. Fortunately, Balac and Mahé have recently applied this technique to the GNLSE [Bal13]. Their embedded Runge-Kutta scheme with orders 3 and 4, applied in the interaction picture (ERK4(3)-IP) provides a local error estimation for each step with no significant additional processing, enabling efficient step size control. This adaptive integration technique was used for all GNLSE simulations in this thesis. For brevity, we omit here the full details of this algorithm and refer the numerically-minded reader to Ref. [Bal13] (particularly Eqns. 23 & 27).

2.3.4 Modelling Noise

Many processes in nonlinear optics are seeded by noise, necessitating the inclusion of shot noise (i.e. quantum noise related to the discrete nature of photons) to build a reliable numerical model. We implement this with a semiclassical *one photon per mode* model: prior to running a simulation, at every point in the numerically gridded spectral representation of the input electric field, a photon is added with a random phase [Pas04, Dru01].

In the time domain, this corresponds to a noise field modelled as random samples from a complex Gaussian distribution with zero mean and a variance given by [Pas04]:

$$\sigma^2 = \frac{\hbar\omega}{2\Delta t} \tag{2.3.13}$$

where $\hbar$ is the reduced Planck constant and Δt is the temporal resolution of the numerical grid.

2.4 Rare-Earth Doped Fibre Amplifiers

To model optical propagation along active fibres (i.e. amplification), it is necessary to compute the gain coefficients $g(\omega)$ along z from consideration of stimulated emission and energy transitions within the rare-earth atomic system. In the simplest implementation, the gain of a doped fibre amplifier can be modelled using a parabolic gain profile in the spectral domain (with central wavelength and bandwidth determined by the active ion)

with instantaneous gain saturation included through a two-level model:

$$g = \frac{g_0}{1 + E/E_{\text{sat}}} \tag{2.4.1}$$

where g_0 is the small signal gain, E is the input pulse energy and E_{sat} is the amplifier saturation energy [Die06].

However, this approach is difficult to relate to experimental parameters and neglects the detailed spectral profile of the active ion, which can be important for shaping ultrashort pulses. Therefore, in this section we describe an improved model for rare-earth doped fibre amplifiers. We focus specifically on ytterbium-doped fibre, since this is the main laser ion employed in this thesis, but the approach could be applied generally to other dopants. We begin with a brief review of the spectroscopy of ytterbium, followed by discussion of Yb:fibre modelling.

2.4.1 Spectroscopy of Ytterbium

Trivalent ytterbium Yb^{3+} has a relatively simple energy structure consisting of only two manifolds: ground $^2F_{7/2}$ and excited $^2F_{5/2}$, split into 4 and 3 Stark levels, respectively (Fig. 2.7a). As with all trivalent rare-earth ions, the electronic transitions are shielded from the host material, resulting in only a weak influence of the host lattice on the emission and absorption cross sections [Dig01]. Therefore, the following discussion will be generally applicable to various host materials, although where spectroscopic data is required, we use measurements from Yb^{3+} in germanosilicate glass, obtained from Ref. [Pas95].

Effective absorption and emission cross sections are shown in Fig. 2.7b, where the characteristic features can be related to the energy level structure.[17] In terms of absorption, the dominant peak at ∼975 nm corresponds to excitation between the lowest Stark levels in each manifold and the second peak at ∼910 nm is related to transitions from the lowest ground level to higher Stark levels in the excited manifold. A small absorption plateau beyond 975 nm exists from transitions starting in the second-to-bottom Stark level in the ground manifold (notably, this can cause reabsorption of light emitted here and a shift to longer laser wavelengths with long lengths of doped fibre). The cross section of this transition is low since the occupation of Stark levels follows a Boltzmann distribution: the population of second Stark level in the $^2F_{7/2}$ manifold is only 6% of the lowest Stark level [Pas95].

Considering the emission cross section, the dominant laser transition is at ∼975 nm (this is only accessible when pumped with light shorter than this wavelength) between the lowest $^2F_{5/2}$ manifold level and the ground level. This corresponds to three-level laser behaviour. Laser action is also possible from the lowest $^2F_{5/2}$ manifold level to

[17] Every Yb^{3+} ion within the amorphous glass host has a distinct absorption and emission cross section, which will differ slightly due to the weak influence of the local environment. The presented measurements are therefore an average over a large ion population, also taking into account level occupation probabilities, giving broad features and preventing the individual Stark-split levels from being resolved. Hence, they are described as *effective* cross sections [Pas08].

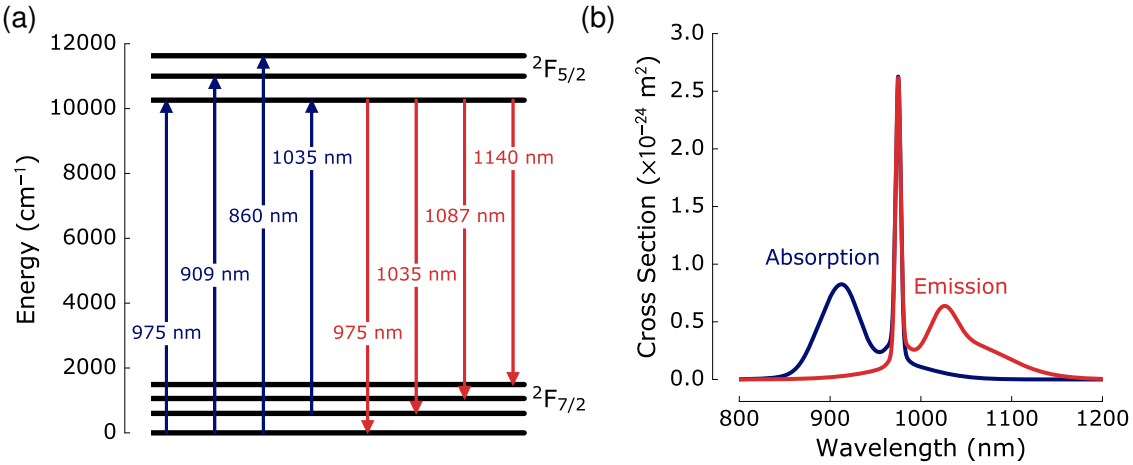


Fig. 2.7: Spectroscopy of Yb^{3+}: (a) energy level structure showing two manifolds, each with numerous Stark levels, highlighting salient transitions; (b) effective absorption and emission cross sections of Yb^{3+} in a germanosilicate host. Adapted from Ref. [Pas95].

the upper Stark levels in the ground manifold, corresponding to the emission cross-section peak at ∼1035 nm and at longer wavelengths ∼1087 nm and ∼1140 nm. Due to the energy separation between the transition-terminating level in the $^2F_{7/2}$ manifold and the lowest Stark level, four-level laser behaviour is observed by moving to longer wavelengths [Pas97].

In this thesis, double-clad Yb-doped fibre amplifiers were used extensively, which were often commercial units from IPG Photonics. We used multimode InGaAs laser diodes to pump at the strongest absorption transition and typically achieved lasing at ∼1030-1070 nm.

2.4.2 Modelling Pulse Amplification

Analysis of amplification in active media usually begins with *rate equations*: differential equations expressing the temporal evolution of the electronic level populations, dependent on the local field intensity, and coupled by spectrally-dependent effective absorption and emission cross sections. Due to near-instantaneous non-radiative (phonon-mediated) transitions between Stark levels within each manifold, we can consider the population of whole manifolds (neglecting relative occupancy of sub-levels), leaving just two coupled ordinary differential rate equations for Yb^{3+}. Steady-state populations are determined at a given distance along the fibre z by equating time derivatives to zero. The use of a steady-state analysis could be questioned for modelling *pulse* amplification where the intensity varies over the duration of the pulses. However, such time scales are negligible compared to the ∼1 ms upper state lifetime, enabling gain $g(\omega)$ to be calculated by treating the signal as *continuous wave* (CW) light with an equivalent average power P_{av}. Differential gain equations can be derived and then included as $g(\omega)$ in Eqn. 2.3.2 for solution using numerical integration methods [Pas97, Bai14].

However, this additional term adds significant complexity and computational cost to

the required numerical integration. Fortunately, a simplification was proposed by Barnard et al. by ignoring the effect of *amplified spontaneous emission* (ASE) (this is valid providing the peak gain is not extremely high) to find analytical solutions for the gain [Bar94].

In this method, the evolution of co-propagating pump power P_p and signal power P_s are described by coupled transcendental equations [Bar94]:

$$P_p(z) = P_{p,in} \exp\left(-\alpha_p z + \frac{P_{p,in} - P_p(z)}{P_p^{IS}} + \frac{P_{s,in} - P_s(z)}{P_p^{CS}}\right) \tag{2.4.2a}$$

$$P_s(z) = P_{s,in} \exp\left(-\alpha_s z + \frac{P_{s,in} - P_s(z)}{P_s^{IS}} + \frac{P_{p,in} - P_p(z)}{P_s^{CS}}\right) \tag{2.4.2b}$$

where subscripts p and s denote quantities at pump and signal wavelengths, P_{in} is the input ($z = 0$) power, α is the absorption per unit length, P^{IS} is the intrinsic saturation power coefficient characterising how the pump/signal saturates its own absorption and P^{CS} is the cross saturation coefficient describing the saturation of pump (signal) absorption by signal (pump) light. The intrinsic saturation and cross saturation parameters can be measured in transmission experiments, or computed using standard spectroscopic data and measured / manufacturer-provided active fibre absorption, core size and length values (we often chose the latter for simplicity), as described in full in Ref. [Bar94].

Monochromatic signal and pump waves are assumed and the spectral profile of the gain $g_p(\omega)$ is applied separately to the calculation of its value $g_m(z, P_{av})$: net gain coefficient $g(z, \omega, P_{av}) = g_m(z, P_{av}) g_p(\omega)$ [Run14]. The gain magnitude is [Bar94]:

$$g_m(z, P_{av}) = \frac{1}{P_s(z)} \frac{\mathrm{d}P_s(z)}{\mathrm{d}z} = \frac{P_p(z) \alpha_p P_p^{IS}}{P_s^{CS}[P_p^{IS} + P_p(z)]} - \alpha_s \tag{2.4.3}$$

and the spectral profile $g_p(\omega)$ is computed as the effective emission cross section minus the absorption cross section, normalised to one at the signal wavelength used for gain magnitude calculations [Run14].

This method was implemented in our model as follows. We assumed that any changes in pulse shape along the active fibre did not affect the gain (i.e. neglecting spectral changes). This enabled the smoothly varying gain coefficients along the entire active fibre to be precomputed using only $\sim$100 samples and the known input field, which greatly reduced the required computation compared to solving Eqns 2.4.2 and 2.4.3 for every step in the GNLSE propagator.

To compute the gain coefficient at one of the sampled z positions: $P_{p,in}$ was the user-chosen amplifier pump power and $P_{s,in}$ was calculated as the average pulse input power in a laboratory reference frame (not average power in the simulation window), obtained as the energy in the simulation frame ($\int_{\text{time window}} |A(z,t)|^2 \mathrm{d}t$) multiplied by the repetition rate of the laser pulses being amplified. Eqns. 2.4.2 were then solved for $P_p(z)$ and $P_s(z)$ at a given z position by two-dimensional root finding (we used the Levenberg-Marquardt method), followed by insertion of these values into Eqn. 2.4.3 to find the

gain magnitude. Finally, the net gain coefficient was obtained by including the spectral response (implemented using a sum of Gaussians fitting to the transition cross section data in Fig. 2.7b), forming an array of gain values at each wavelength within the numerical grid.

Once the gain arrays had been computed at ∼100 positions from $z = 0$ to the end of the active fibre, they were fitted with a spline, enabling interpolation within the GNLSE propagator (Eqn. 2.3.2) at any position z. Thus, $g(\omega)$ was able to be included in Eqn. 2.3.2 at any z position as a one-dimensional array and the efficient interaction-picture numerical integration technique could still be used, yielding quick and accurate solutions.

2.5 Complete Model of a Mode-Locked Soliton Laser

To conclude our chapter on modelling methods, we combine the aforementioned approaches into a complete model for simulating a mode-locked fibre laser, which is compared to an experimental realisation of the system.

2.5.1 Laser Design

A Yb:fibre ring cavity design with net anomalous dispersion (Fig. 2.8) was chosen since this type of cavity is well understood and widely reported experimentally in the literature (e.g. Ref. [Agr01] and references therein). The ytterbium-doped fibre amplifier included a 0.8 m length of active fibre, pumped by a 962 nm laser diode and all passive cavity fibre was IPG Flexcore, as described in earlier sections of this chapter. The total cavity length was ∼20 m. Within the ytterbium gain band, silica fibre is normally dispersive; therefore, we included a *chirped fibre Bragg grating* (CFBG) in the laser (with a three-port circulator) to shift the net cavity dispersion into the anomalous regime. We present a thorough discussion of CFBGs and their impact on pulse shaping in Chapter 3. Here, however, we approximated the CFBG and circulator arrangement as a short length of fibre to introduce the equivalent dispersion into the cavity and a Gaussian filter with the equivalent bandwidth. To initiate mode-locking, intensity discrimination was provided by a fast saturable absorber (experimentally, this was a carbon nanotube saturable absorber, as discussed in Chapter 3), modelled phenomenologically as an instantaneous two-level intensity-dependent absorption [Gar00]:

$$\alpha(I,t) = \frac{\alpha_s}{1 + I(t)/I_{sat}} + \alpha_{ns} \tag{2.5.1}$$

where α_s is the saturable loss, α_{ns} is the non-saturable loss, $I(t)$ is the simulation field intensity and I_{sat} is the saturation intensity.

A shot noise field was created to seed the simulation, which was propagated through each cavity element in turn. The final output coupler component stored 30% of the field as the cavity output and fed back 70% of the light. The simulation continued over many

cavity round trips until a convergence criteria ($< 1\%$ change in pulse duration and spectral width over continuous iterations) was met.

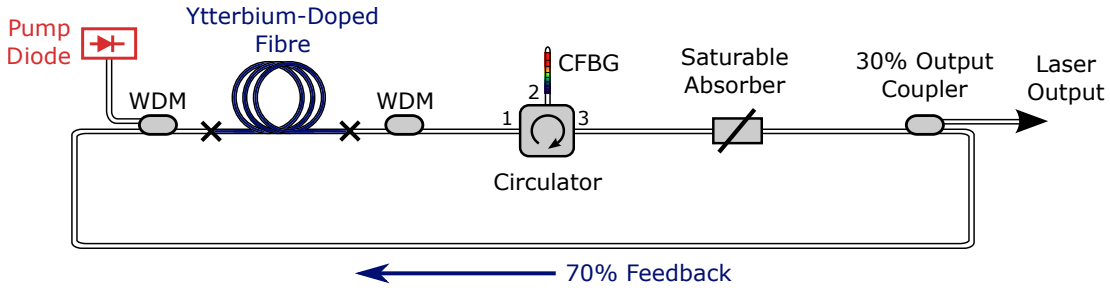


Fig. 2.8: Schematic of soliton mode-locked Yb:fibre laser. For the simulation, all fibre was assumed to be polarisation maintaining. Experimentally, non-polarisation-maintaining fibre was used, with the addition of a polarisation controller in the feedback loop to enable manual optimisation of mode-locking.

2.5.2 Simulation Results

The simulation was run numerous times with different random shot noise seed fields, always converging to the same steady-state solution[18] – this confirmed that the state was an attractor and represented the expected output characteristics for each pulse in the pulse train from a physical mode-locked system.

The temporal evolution of the field (measured at the output port each round trip) is shown in Fig. 2.9, growing from shot noise into a stable pulse. We note that while the pulse forms at a random temporal position within the simulation grid due to noise, for clarity we have presented all temporal representations of the field shifted such that the steady-state pulse is centred on zero. The simulated laser spectrum had a central wavelength of 1068 nm, with 0.56 nm FWHM (Fig. 2.10a). Experimentally, we measured ultrashort pulses with an autocorrelator; therefore, the autocorrelation of the simulated pulse field is shown in Fig. 2.10b, in addition to the original pulse envelope in Fig. 2.10c. The modelled pulse duration was 3.4 ps, and a small down-chirp was observed across the pulse (shown more clearly in the spectrogram in Fig. 2.10d), suggesting that the pulse duration could be reduced with dispersion management.

Spectral sidebands were also observed, related to solitonic pulse shaping effects (introduced in Section 1.3.4). While 'true' solitons (in the mathematical sense) can only propagate in lossless (i.e. conservative) media, soliton shaping can still be present in a laser cavity (a dissipative system) with net anomalous dispersion to compensate the nonlinear phase accumulation on each round-trip.

Amplification, loss and changes in fibre dispersion/nonlinearity act as periodic perturbations every round-trip, suggesting a continuous variation in the required pulse properties to maintain a fundamental soliton, according to the relationship between fibre

[18]Simulation time was typically less than one minute (executed on an average-specification personal computer).

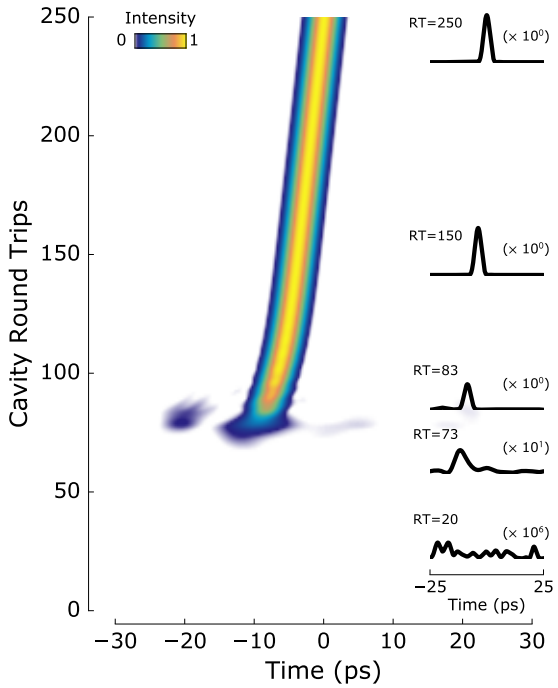


Fig. 2.9: Simulated temporal evolution of pulse envelope in mode-locked Yb:fibre laser as radiation builds up. Insets show the field at particular round trips: the intensity is normalised to the height of the final pulse and the magnification of the plot is shown beneath the round trip (RT) index. Below ∼70 round trips, the field is too weak to appear on the colour scale, but is shown in the annotated insets.

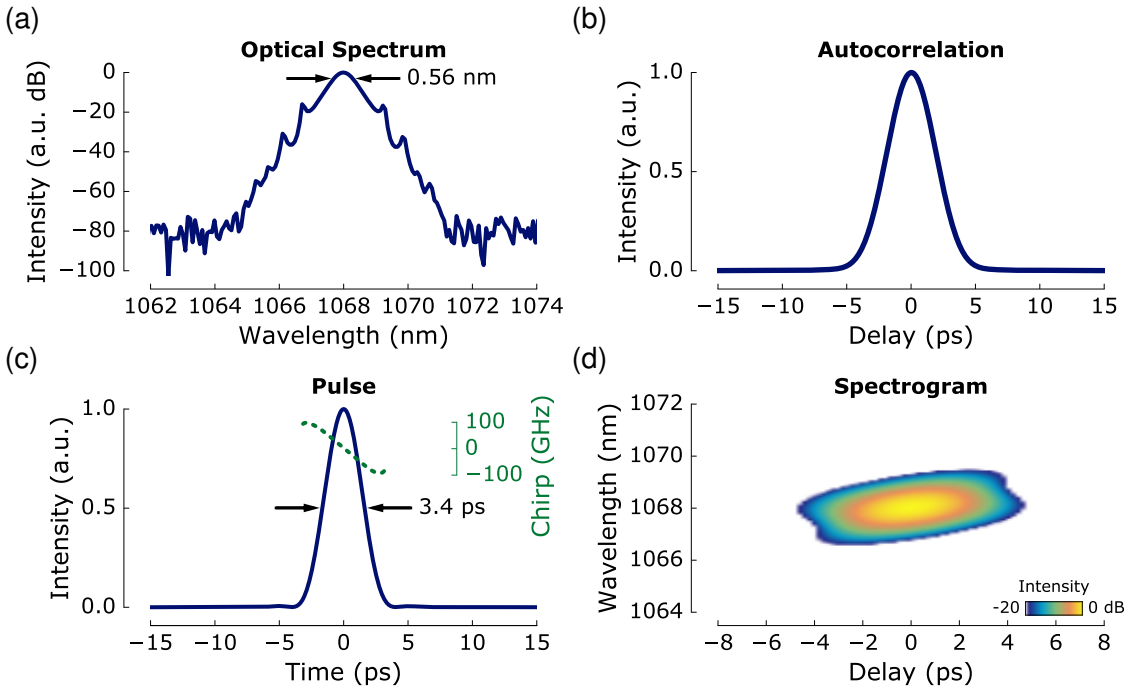


Fig. 2.10: Simulation of mode-locked Yb:fibre laser: (a) optical spectrum; (b) autocorrelation trace; (c) pulse envelope and chirp; (d) spectrogram.

properties and the soliton power and duration (Eqn. 1.3.20). If the length scale of disturbances (in this case, the cavity length) is significantly shorter than the characteristic soliton length (Eqn. 1.3.21), stable soliton propagation is possible with equivalent peak power to the averaged pulse peak power over the cavity, known as *guiding-centre solitons* [Has90] or *average solitons* [Kel91]. When the cavity length exceeds the soliton period, disturbances are no longer averaged out and the pulse adjusts itself during propagation to remain as a fundamental soliton by shedding radiation into a *dispersive wave*. At certain wavelengths the soliton and dispersive wave are phase matched, allowing energy coupling between them and giving rise to resonant sidebands in the optical spectrum [Mol86, Kel92b, Den94].

In our laser, the soliton period z_0 was $\sim$5 m, which is shorter than the 20 m cavity length, explaining the observation of spectral sidebands. The presence of strong sidebands was actually undesirable as they indicate a non-negligible loss of energy from the pulse to maintain a soliton, highlighting that the cavity design could be altered for improved efficiency.

2.5.3 Experimental Comparisons

The proposed system was constructed experimentally and exhibited self-started mode-locking above the lasing threshold. While the simulation assumed *polarisation-maintaining* (PM) fibre, in the experiment we used non-PM fibre and included a polarisation controller in the feedback loop to manually optimise the mode-locking condition. A stable 10 MHz pulse train was generated, with an optical spectrum at $\sim$1068 nm (Fig. 2.11) and 0.44 nm spectral bandwidth. Temporally, autocorrelation measurements of the pulses were well-fitted with a sech^2 shape of 5.1 ps FWHM, corresponding to a pulse duration of 3.3 ps after deconvolution.

We concluded that the experimental results and simulation were in reasonably good agreement: the model was able to accurately predict the output pulse properties. Even though minor differences were observed (e.g. the spectral width), these could be attributed to uncertainties in the component parameters and possible polarisation effects in the non-PM cavity compared to the PM model. The simulation correctly captured the expected dynamics, however, including spectral sidebands from soliton-dispersive wave interaction, suggesting that the model was suitable for extension to investigate new parameter regimes.

2.6 Summary

In this chapter we have presented a number of computationally efficient techniques for modelling pulse propagation in optical fibres and simulating short-pulse fibre lasers. After introducing a formal mathematical description for the electric fields of optical pulses on numerical grids, we detailed the computation of propagation modes and their properties in step-index and photonic crystal fibres and discussed the numerical propagation of a field in fibre, governed by a generalised nonlinear Schrödinger equation. Gain calculations

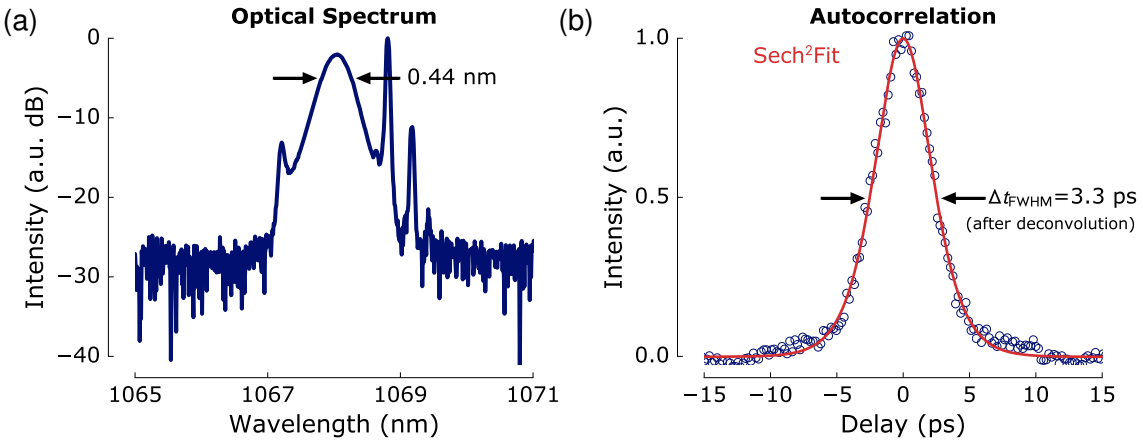


Fig. 2.11: Experimental characterisation of mode-locked Yb:fibre laser: (a) optical spectrum; (b) autocorrelation trace.

in a ytterbium-doped fibre amplifier were also presented and all of these concepts were combined to simulate a complete mode-locked fibre laser operating in the net-anomalous dispersion regime. Good agreement was found between simulations and experimental measurements, validating the model.

The numerical methods outlined in this chapter enabled accurate, yet quick, modelling of nonlinear fibre optic effects and short-pulse fibre laser systems, and were used extensively in this thesis to guide experimental designs and provide insight beyond experimental observations.

3

Long-Cavity Mode-Locked Lasers

Passively mode-locked fibre lasers have become established tools for generating picosecond and femtosecond pulses at megahertz repetition rates. Ever-growing demands from laser end-users for higher energy and more versatile pulse sources, however, are driving research to consider new laser designs to broaden the achievable parameter space that such devices can achieve.

In this chapter we report the development of a long-cavity mode-locked laser architecture, which can produce highly-chirped, compressible nanosecond pulses at sub-megahertz repetition rates. We begin by presenting a brief history of pulse shaping in fibre lasers and the limitations of various possible operating regimes in Section 3.1. Our long-cavity design is introduced and demonstrated experimentally in Section 3.2, supported by numerical modelling and with consideration of design improvements to enhance operating stability. In Section 3.3 we consider techniques to significantly enhance the pulse peak power by compression, followed by application of these pulses for low-threshold supercontinuum generation in Section 3.4. Finally, we note that long-cavity lasers can exhibit rich nonlinear wave dynamics that are of fundamental interest to nonlinear science, which we discuss in Section 3.5 in the context of our observation of dark soliton structures during radiation build-up. The chapter is concluded in Section 3.6 with an outlook of the opportunities for the long-cavity laser design.

The results presented herein have been published in the following journal articles and conference proceedings: [Woo14b, Woo14e, Woo15e, Woo15f, Woo15g, Woo16].

3.1 Introduction: Pulse Shaping in Mode-Locked Lasers

It has long been understood that cavity dispersion and nonlinearity strongly influence the formation and steady-state characteristics of pulses generated in a mode-locked laser, in addition to contributions from the spectral filtering effect of a finite gain bandwidth, gain saturation and loss. Interplay between these effects has led to the categorisation of laser operation into several distinct regimes (summarised in Fig. 3.1), each with different intracavity dynamics and output properties.

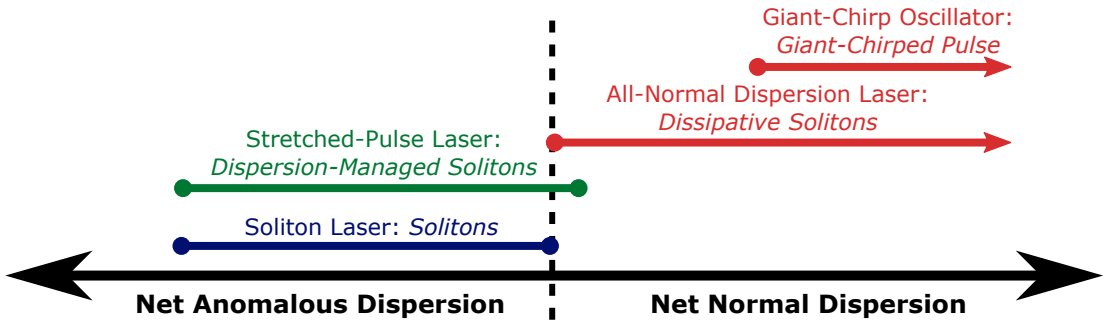


Fig. 3.1: Illustration comparing different operating regimes of mode-locked fibre lasers with different dispersion maps, including the laser names and terms for describing the pulses they generate.

3.1.1 Historical Perspective

Mode-locking was proposed theoretically in 1964 [Lam64], shortly followed by the first demonstration of active mode-locking [Har64].[1] Passively mode-locked lasers [Moc65, DeM66] were also reported soon after, but plagued by instabilities; it was not until 1972 that a continuously passively mode-locked pulse train was stably demonstrated, using a dye saturable absorber in a dye laser cavity [Ipp72b].

In this same year, Zakharov and Shabat solved the *nonlinear Schrödinger equation* (NLSE) using an inverse scattering transform to reveal the existence of *soliton* solutions [Zak72] (introduced in Section 1.3.4). Remarkably, soliton waves had been observed in nature as far back as 1844 by John Scott Russell [Rus44], although it was only realised that the NLSE was an appropriate equation to describe light propagation in fibres in 1973, leading to the prediction of fibre-optic soliton propagation due to a balance between self-phase modulation and anomalous dispersion [Has73a].[2] Experimental demonstration of optical solitons in fibre followed seven years later [Mol80].

[1] Prior to this work, however, a report had been published in German showing pulse generation through the inclusion of an active modulator in a ruby laser [Gue63]. This was perhaps the real first report of active mode-locking, although it was not identified at the time.

[2] Research into the theoretical existence of solitary waves greatly pre-dated this study, following attempts to explain Russell's observations by Joseph Boussinesq [Bou71] and Lord Rayleigh [Ray76], and the proposal of the Kortewerg and de Vries (KdV) equation to describe water waves [Kor95]. The term soliton was coined by Kruskal and Zabusky in 1965 after further study of the KdV equation to describe the particle-like behaviour of such solitary waves [Zab65].

Soliton Lasers

The concepts of mode-locking and soliton propagation were finally united in 1984 with the report of soliton generation in a mode-locked laser: the *soliton laser* [Mol84]. The prospect of a pulse which could propagate over long distances while maintaining both its temporal and spectral shape was a major incentive to further research, largely motivated by the growing telecommunications industry at the time. However, one of the conditions for fundamental soliton propagation is also a major limitation: the *soliton area theorem*. This condition expresses the energy of a soliton pulse E_p as a function of the $1/e$ pulse duration t_0 and fibre dispersion β_2 and nonlinearity γ [Zak72, Has73a]:

$$E_p = \frac{2|\beta_2|}{|\gamma|T} \tag{3.1.1}$$

This limits the maximum practical pulse energy of a soliton laser to $\sim$0.1 nJ since the fundamental soliton condition is only satisfied for a specific energy with given fibre properties and pulse duration. If higher energy pulses form in a net-anomalous dispersion cavity, disturbances cause them to split, leading to unstable multiple pulsing operation or multiple fundamental solitons stably and equally spaced in the cavity during one round-trip. This latter situation is known as *harmonic mode-locking*, which can be a useful regime for increasing the laser repetition rate, although is often undesirable if the target is high-energy single-pulse generation [Gru92b].

Stretched-Pulse Lasers

To circumvent this trade-off between pulse energy and duration due to soliton quantisation, Tamura et al. proposed a new laser cavity design: the *stretched-pulse laser* [Tam93]. By including segments of normally and anomalously dispersive fibre, the pulse in the cavity broadens and recompresses during each round trip, so the cavity-averaged peak power is reduced. Therefore, the accumulated nonlinear phase shift is reduced and the pulse energy can be increased before the onset of multiple pulsing operation. This regime exists for net anomalous or small normal GVD and can generate pulses with energies up to a few nanojoules [Ren12]. Such pulses are known as *dispersion-managed solitons* and by the nature of temporal, periodic 'pulse breathing' in the cavity, the choice of output position from the cavity determines whether the pulses are chirped or transform-limited.

All-Normal Dispersion Lasers

More recently, work has considered the merits of strong normal dispersion fibre cavities. Here, solitonic shaping is absent and the interaction of linear and nonlinear effects leads to a positive monotonic frequency sweep (*up-chirp*) across the pulse, such that the pulse width is many times larger than its transform-limited duration and is compressible [Tre68]. It is therefore possible to exploit the properties of linearly-chirped pulses to scale pulse

energies beyond the limits imposed by quantisation of classical optical solitons.

In recent years, a modern terminology has evolved to describe and extend established operating regimes and dynamics for pulsed lasers in the context of state-of-the-art mode-locked fibre systems, where the flexibility of the waveguide permits extension of such ideas to new parameter ranges [DeM04, Cho06, Ren08b]. A large body of work has focussed on mode-locked all-normal dispersion (ANDi) fibre lasers, which produce linearly-chirped pulses. In this case, the intracavity pulse dynamics require dissipative (spectral filtering, gain and loss) and conservative (dispersive and nonlinear) effects to stabilise the pulse, unlike anomalous dispersion soliton lasers which rely on a balance between dispersion and nonlinearity alone. Specifically, the pulse broadens as it propagates along normally dispersive fibre and nonlinear effects result in spectral broadening. After each round-trip the saturable absorber decreases the pulse width and a spectral filter (either explicitly added [Cho06] or an effective filter from the limited gain bandwidth of the system [Ped12]) resets the pulse characteristics. Interplay between dispersion and nonlinearity in addition to dissipative gain filtering and saturable absorber effects effectively compensate the nonlinear phase shift, stabilising the pulse. These pulses are known as *dissipative solitons* [Akh05].

Dissipative solitons are not limited by the area theorem of Eqn. 3.1.1 and can, therefore, support higher pulse energies. The flexibility of fibre waveguides enables such laser cavities to be elongated, while maintaining a small system footprint. Such length extension reduces the repetition rate, providing the opportunity to increase pulse energy based on the cavity relations:

$$E_p = \frac{P_{\text{av}}}{f_{\text{rep}}} = \frac{P_{\text{av}}\, n_{\text{eff}}\, L}{c} \tag{3.1.2}$$

where P_{av} is the average optical power, f_{rep} is the repetition rate, n_{eff} is the fibre effective index and L is cavity length.[3] This design strategy could not be applied to soliton lasers, since the additional pulse energy would cause pulse-breakup. In the normal-dispersion regime, however, the additional fibre length increases the net dispersion, so pulses broaden and acquire a chirp, in addition to increased energy.

3.1.2 State of the Art

Giant-Chirp Oscillators

Numerous all-normal dispersion lasers have been experimentally demonstrated and by elongating the fibre cavity, pulse energies up to a hundred nanojoules [Lef10] and pulse durations up to 150 ps [Ren08b] have been reported. The linear nature of the chirp has enabled extra-cavity compression to almost the transform limit using a diffraction-grating pair [Ren08b]. The term *giant-chirp oscillator* (GCO) has evolved to describe this subset

[3] Cavity elongation to increase pulse energies has, in fact, been reported with a bulk Nd:YVO_4 mode-locked laser [Kol03], although the complicated optical setup and physical space occupied by the bulk optics limit the utility of this concept in a non-fibre platform.

of all-normal dispersion lasers [Ren08b], although the value required to describe a chirp as 'giant' is not precisely defined. However, general properties of GCOs compared to typical mode-locked ANDi fibre lasers include a lower fundamental repetition rate (few megahertz), increased pulse energy, and broad chirped pulses (up to ∼150 ps), which limits the onset of detrimental nonlinear effects.

The large chirp of such pulses is of particular interest for *chirped-pulse amplification* (CPA) systems, since a chirped pulse oscillator could replace the standard oscillator, stretcher, pulse picker and pre-amplifier required in a typical fibre CPA scheme [Str85, Ren08b].

Long-Cavity Noise Burst Lasers

Fibre laser cavities have also been extended to extreme lengths of many kilometres to achieve significantly greater pulse energies. In 2008, Kobstev et al. reported a 3.8 km laser producing 3 ns pulses at 77 kHz repetition rate with 3.9 μJ pulse energy [Kob08] – orders of magnitude higher than typically achieved directly from a fibre oscillator. This was mode-locked by *nonlinear polarisation evolution* (NPE), which is an *artificial* saturable absorber technique; a detailed discussion of the various different types of saturable absorber is presented in Section 4.3.1. Further analysis of this long-cavity system suggested that the observed pulses were actually bursts of light consisting of irregular trains of sub-pulses [Kob09, Kob14]. Thus, the pulse-to-pulse energy variations and width fluctuations were high, and there was no phase coherence between pulses.

It is more appropriate to classify this operation as partially mode-locked [Bra74], producing *noise bursts* or *noise-like pulses* rather than dissipative solitons. This observation of noise-like pulses agreed with earlier reports of long (net normal and net anomalous dispersion) cavity NPE-mode-locked lasers [Hor97, Kan98]. Due to the random chirp and lack of coherence, these pulses are not compressible [Kob09], limiting their application.

Can a Long Cavity Laser Generate Coherent Pulses?

Progress with GCOs and noise burst sources raised the question: is it possible to develop a long-cavity laser for low-repetition-rate high-energy pulse generation, while maintaining the linear chirp? This could combine the advantages of both emerging designs, since compression is desirable for many applications to raise the pulse peak power.

Kelleher et al. provided the answer in 2009 by demonstrating a 1.2 km fibre cavity mode-locked with carbon nanotubes, generating 2 ns pulses at 177 kHz; critically, the pulse spectrogram was measured experimentally to confirm the linear chirp [Kel09b, Kel09a]. The pulse spectrum also exhibited steep-sided edges, which are characteristic of chirped dissipative solitons, compared to the smooth Gaussian spectra of noisy pulses. Further reports of long-cavity lasers in a cw mode-locking regime followed, using other *real* saturable absorbers such as SESAMs [Tia09b, Tia09a].

Despite these demonstrations, questions were raised regarding the compressibility of such pulses given their *giant* chirp, and concerns were stated relating to their stability

and potential as pulse sources for real-world applications [Smi11]. Such issues need to be addressed to evaluate the potential of long-cavity laser designs as useful pulse sources. It is in this context that the work in this chapter is set.

3.2 Long-Cavity Chirped-Pulse Generation

We developed an all-normal dispersion fibre laser with a long ring cavity to operate within the ytterbium gain band (below the *zero-dispersion wavelength* (ZDW) of standard step-index fibre), as illustrated in Fig. 3.2. The ytterbium-doped amplifier was formed of a 1.1 m length of double-clad ytterbium-doped fibre, pumped through a *wavelength division multiplexer* (WDM) by a 962 nm multimode laser diode and with a second WDM to couple out the undepleted pump light. We included a *polarisation controller* (PC) to adjust the state of polarisation in the cavity (enabling the mode-locked state to be optimised), an inline polarisation-independent isolator to ensure unidirectional propagation, and a fused fibre coupler to provide a 10% output port. The main novelty of our design, compared to conventional mode-locked fibre lasers, was the inclusion of an 840 m reel of fibre to reduce the repetition rate and to provide a large dispersion to linearise the pulse chirp. Apart from the active fibre, the laser was constructed entirely of IPG Flexcore fibre (equivalent to commercially-available Corning Hi1060 fibre). The total cavity length was $\sim$846 m, corresponding to $\sim$18.5 ps^2 total cavity dispersion. A bandpass filter centred at 1058 nm with 10 nm bandwidth was also spliced into the cavity; this was not essential to achieve stable mode-locking operation, although did fix the central lasing wavelength, as we discuss later.

To initiate passive mode-locking, a saturable absorber comprised of carbon nanotubes embedded in a *polyvinyl alcohol* (PVA) film ($\sim$25 μm thick) was integrated into the cavity by sandwiching a 1 mm $\times$ 1 mm piece of this film between two angled fibre connectors.[4] Angled connectors were used with index-matching gel to minimise back reflections, which could disturb the stable operation of the laser. Nanotube-based saturable absorbers are a rapidly maturing technology, following the first demonstration of a carbon nanotube mode-locked laser in 2003 [Set03]. Since then, other nanomaterials have emerged that present new opportunities for photonic devices, as we discuss in Chapter 4. Therefore, we refer the reader to Refs. [Has09, Woo14b] for a detailed report of the fabrication of the saturable absorber in this work and here, we focus on the laser design and pulse dynamics.

3.2.1 Results and Discussion

Continuous wave (CW) lasing was observed at $\sim$1 W pump power. As the pump power was increased to $\sim$1.2 W, the output showed a steady pulse train on an oscilloscope, indicating the onset of self-starting mode-locking. The interpulse spacing of 4.11 μs corresponded

[4] We thank Prof. Andrea Ferrari's group at the Cambridge Graphene Centre for fabrication of the nanotube saturable absorbers, in addition to Drs Daniel Popa and Valentin Wittwer for useful discussions.

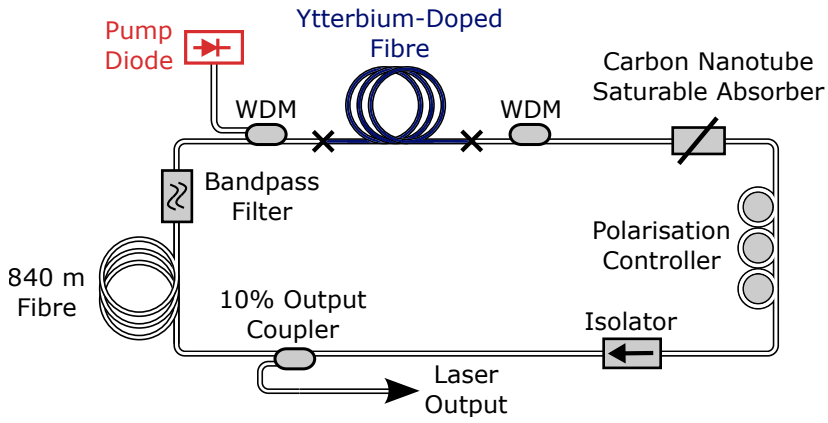


Fig. 3.2: Schematic of long-cavity fibre laser, mode-locked with a carbon nanotube saturable absorber. The total cavity length was ∼846 m.

to the fundamental cavity frequency of ∼244 kHz (Fig. 3.3a). The pulses were measured using a synchroscan streak camera (also known as an optical sampling oscilloscope), and found to be well-fitted by a sech^2 profile with a *full width at half maximum* (FWHM) duration of 1.02 ns (Fig. 3.3b). This width is much greater than pulses that are typically generated in passively mode-locked lasers with durations less than tens of picoseconds. Fig. 3.3c shows the corresponding output spectrum, centred at 1058.0 nm and with steep spectral edges and a structured 'M-shaped' peak – features that are often observed in ANDi lasers and characteristic of coherent dissipative soliton experiments [Ren08a]. Due to the structured peak, a spectral bandwidth measurement of 0.80 nm was made using the *full width at quarter maximum* (FWQM), i.e. the 6-dB width, rather than the FWHM.

To estimate the magnitude of chirp on a pulse, the *time-bandwidth product* (TBP) is commonly computed, as the product of the spectral and temporal FWHMs. Due to the structured spectral peak, we used the FWQM spectral width and FWHM pulse duration to compute a TBP of ∼220. While this was not strictly mathematically consistent, the calculated value was ∼700 times greater than the transform limit of 0.315 for a sech^2 pulse, allowing us to draw the conclusion that our laser produced pulses with a giant chirp. Previous experiments have recorded the spectrogram for similar pulse characteristics and confirmed the linear nature of the chirp [Kel09a].

Nonlinear polarisation rotation, which has previously been used to (partially) mode-lock long-cavity lasers in the noise burst regime, did not contribute to our intracavity dynamics due to the absence of polarisation-selective components (we also confirmed that mode-locked operation could not be achieved by replacing the nanotube-PVA saturable absorber with a pure PVA film – confirming the important role of carbon nanotubes for self-starting mode-locking). By varying the intracavity polarisation through adjustment of the PC, the intensity noise and jitter of the pulses could be altered to optimise the mode-locked laser operation. While the laser was able to operate stably for a full-day, due to the use of non-polarisation-maintaining fibre, physical perturbations to the cavity and changes in atmospheric temperature led to unpredictable changes in noise and jitter

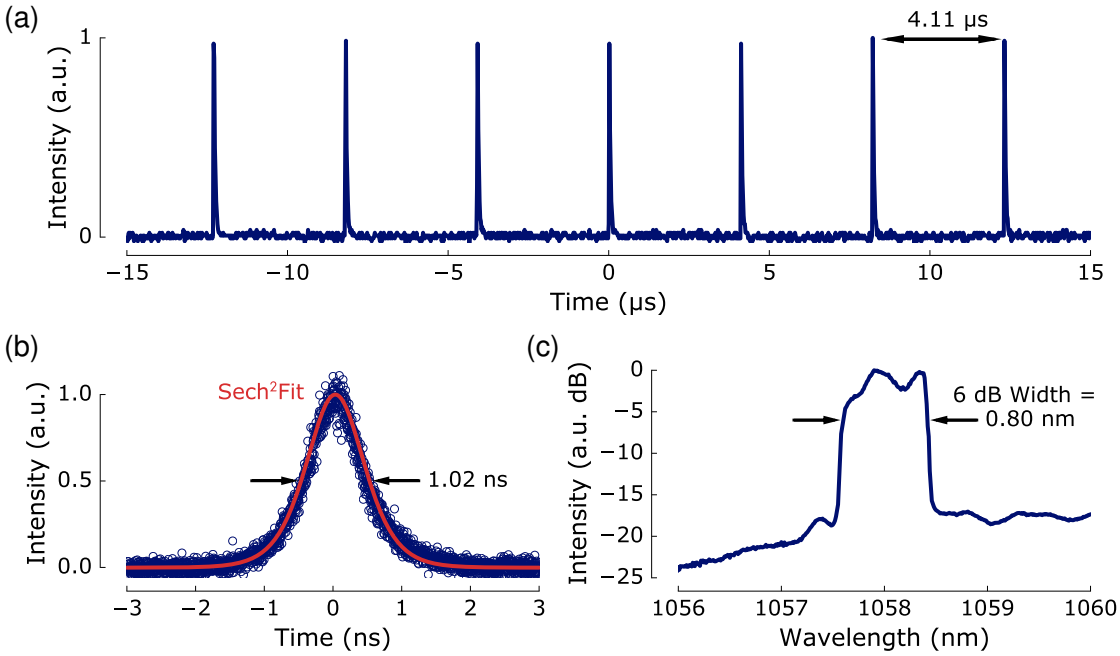


Fig. 3.3: Characteristics of long-cavity mode-locked laser output: (a) oscilloscope trace; (b) streak camera trace; (c) optical spectrum.

performance.

To confirm that the pulses were not noise bursts, we used an autocorrelator to examine the top of the pulse and found no coherence artefact, which would have indicated bursts of incoherent noise [Rho13]. However, by tuning the PC and adjusting the pump power, under certain conditions it was possible to force the long-cavity laser to operate in an unstable, incoherent noise-burst regime (defined by a broader and more rounded spectrum and a noisy pulse train [Hor97]). The pulse shape on a streak camera was similar, although believed to consist of an envelope of short pulses with no phase coherence in this case; confirmed by the observation of a coherence artefact on an autocorrelator

Stable self-starting mode-locking could also be observed without a filter in the cavity. Here, the limited gain bandwidth of the system provided a spectral filtering and stabilising effect. However, it was found that the central wavelength of the laser varied in an unpredictable way when fibres were disturbed or the PC was adjusted. This was attributed to strain-induced loss for some polarisation states which altered the cavity dynamics. Therefore, a 10 nm bandwidth spectral filter, centred at ∼1058 nm was included to provide a restoring force to fix the central wavelength.

Previous reports of long-cavity all-normal dispersion laser cavities have revealed an almost linear dependence between pulse duration and cavity length [Kel09b]. Additionally, with a fixed cavity length, we were able to vary the pulse duration between 0.85 ns and 1.1 ns by varying the pump power. As pump power was increased, the intracavity pulse energy increased, causing greater nonlinear phase accumulation. Self-phase modulation broadened the spectrum, which was coupled to temporal broadening by the large dis-

persion of the cavity, linearising the nonlinear chirp and spreading the increased spectral bandwidth throughout a longer time window. The relationship between spectral width and pulse duration was approximately linear, as shown in Fig. 3.4. A maximum output power of ∼0.25 mW was measured, corresponding to ∼1 nJ pulse energy (assuming all energy was contained in the pulses and the background level was negligible: pulse energy = average power / repetition rate) and a peak power of ∼0.89 W (peak power = shape factor × pulse energy / pulse duration, where a shape factor of 0.88 is used for sech^2 pulses). Any further increase in power resulted in a short period of unstable operation, followed by the output returning to a CW state, suggesting that the nanotube-PVA composite was thermally damaged by the intracavity average power. This indicated that the saturable absorber damage threshold was ∼8 kW cm^{-2}.

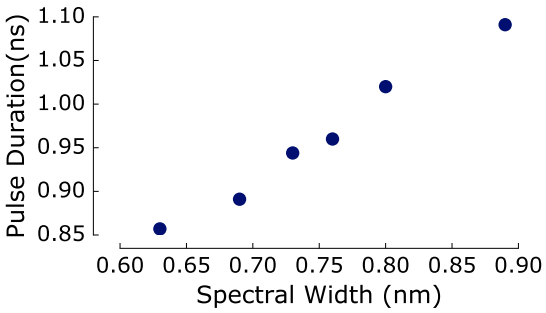


Fig. 3.4: Experimentally measured relationship between spectral width (full-width at quarter maximum) and pulse width (full-width at half maximum).

Laser Stability

We considered the laser stability by analysing the *radio frequency* (RF) spectrum, following the methods proposed by Dietrich von der Linde [vdL86]. It should be noted that the analysis assumes only small fluctuations and no correlation between intensity and phase noise, which are not always well justified. However, the technique is useful for estimating the magnitude of intensity fluctuations, enabling comparison with other mode-locked lasers since the technique is widely used in the literature.

We measured the RF spectrum using a 1 GHz bandwidth photodetector and 2.2 GHz RF spectrum analyser. The broadband spectrum across 20 MHz (Fig. 3.5a) showed a regular train of harmonics with no Q-switching instabilities. At the fundamental frequency, a high signal-to-background ratio of 50 dB (10^5 contrast) indicated good pulse-train stability (Fig. 3.5b). A low-level pedestal with a peak at ∼-50 dB was observed, from which the pulse-to-pulse energy fluctuations could be estimated [vdL86]:

$$\frac{\Delta E}{E} = \left(\frac{\Delta P \Delta f}{\Delta f_{\mathrm{rbw}}}\right)^{0.5} \tag{3.2.1}$$

where ΔP is the pedestal-peak to signal-peak power ratio, Δf is the width of the pedestal

(determined by fitting with a Gaussian profile) and Δf_{rbw} is the resolution of the spectrum analyser. With $\Delta P = 10^{-5}$, Δf = 760 Hz and Δf_{rbw} = 30 Hz, the energy fluctuation was 1.59%. The 60$^{\mathrm{th}}$ harmonic could also be seen to exhibit a high 48 dB peak-to-background ratio, further confirming the mode-locking stability (Fig. 3.5c).

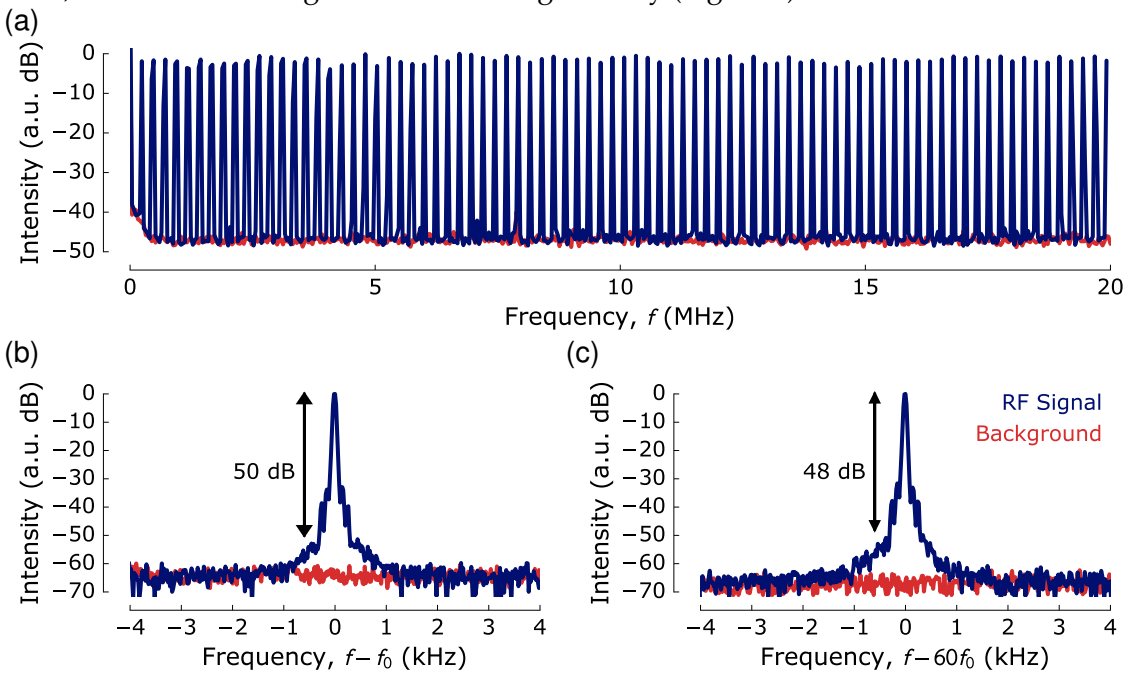


Fig. 3.5: RF spectrum of mode-locked long-cavity laser output: (a) 20 MHz span; (b) 8 kHz span about fundamental, f_0 = 244 kHz; (c) 8 kHz span about 60$^{\mathrm{th}}$ harmonic (30 Hz resolution bandwidth).

3.2.2 Numerical Simulations

To gain further insight into the dynamics of our long-cavity mode-locked laser, we performed numerical simulations (using the models outlined in Chapter 2 with the experimental parameters described in the previous section). Briefly, an initial shot noise field was repeatedly propagated through each cavity element in turn, until the field converged to a steady-state.

The temporal evolution of a coherent dissipative soliton pulse from noise over hundreds of round trips is shown in Fig. 3.6a. It can be seen that after an initially noisy regime, light localised within the simulation window forming a pulse envelope, but containing a high degree of internal structure (i.e. this was only partially mode-locked and could be described as a noise burst). Noise features within the pulse envelope formed intensity dips, which propagated away from the pulse centre (i.e. their velocity was different to the velocity of the pulse envelope). Eventually, by ∼1000 round trips, all these structures had decayed from the pulse envelope, leaving a coherent bright pulse. On further analysis, we found that the intensity dips were actually *dark solitons*, which are solitary-wave solutions to the NLSE in normal dispersion fibres. The simulation was repeated numerous times

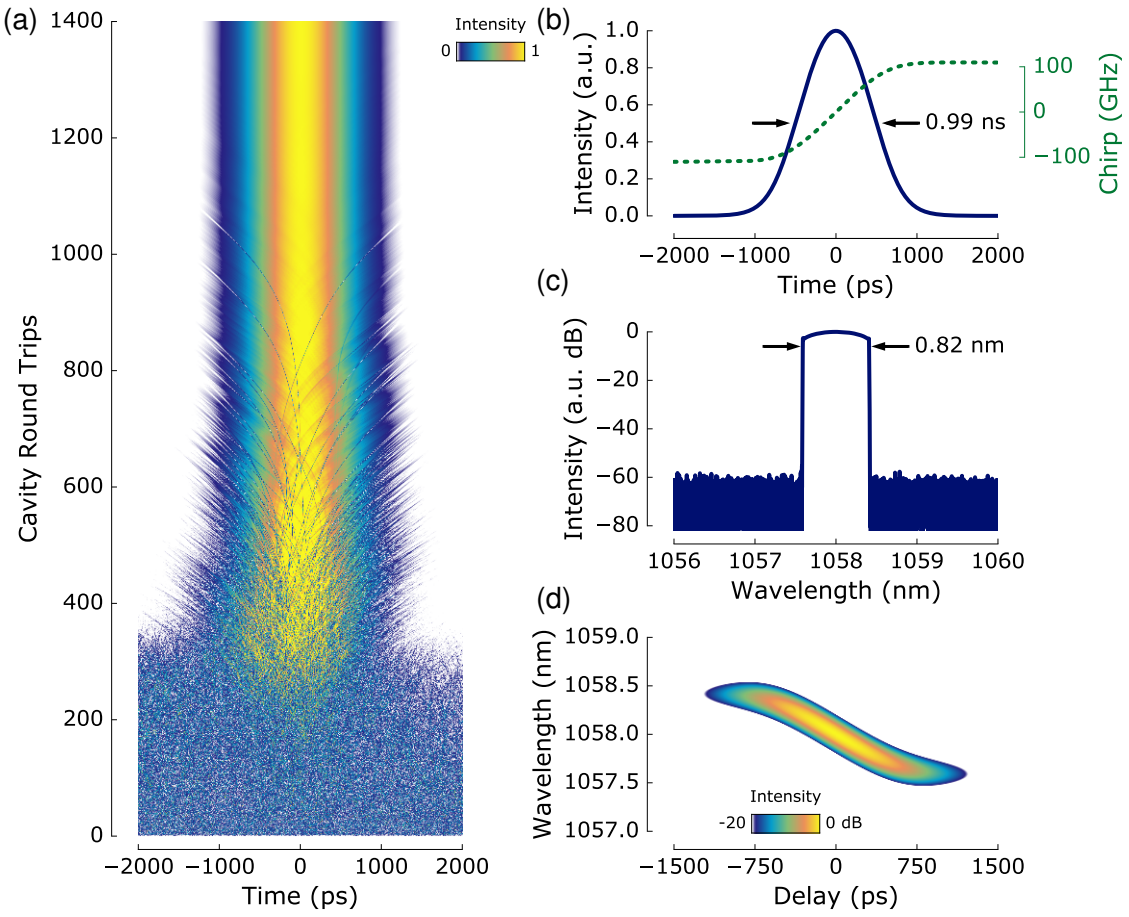


Fig. 3.6: Simulated characteristics of long-cavity mode-locked laser: (a) pulse evolution from noise; (b) output pulse profile; (c) output spectrum; (d) output spectrogram.

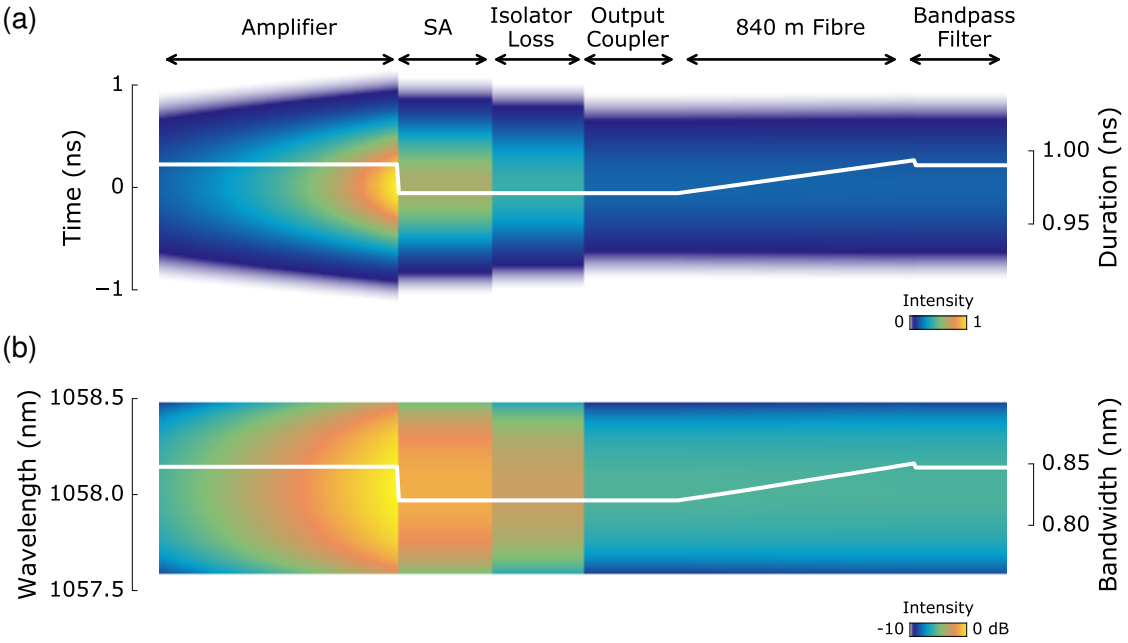


Fig. 3.7: Steady-state giant-chirped pulse dynamics within a single cavity round trip: (a) temporal evolution; (b) spectral evolution. The FWHM pulse duration and spectral bandwidth are also shown in relation to the cavity components.

from randomised noise seed fields, always converging to the same steady state, but with different dark soliton dynamics and decay rates. Such observations drove us to consider the role of dark solitons and the underlying nonlinear dynamics in more detail, which we report in Section 3.5.

Focussing on the steady-state output, we found remarkable agreement between the simulated pulses and experimentally measured values. The model resulted in 0.99 ns duration pulses and a steep-sided optical spectrum with 0.82 nm FWHM bandwidth (Fig. 3.6b & c). A monotonic frequency sweep was observed across the pulse, showing that the giant chirp was highly linear (Fig. 3.6d).

The simulation also enabled the temporal and spectral dynamics in the steady-state to be visualised on a single round-trip of the cavity, as shown in Fig. 3.7. Starting with the amplifier, the amplitude of the pulse and spectral intensity increased gradually along the Yb-doped fibre, but showed no change in width. The intensity-dependent transmission profile of the saturable absorber then attenuated the pulse wings, leading to small ∼25 ps reduction in pulse duration and since the spectral components were spread linearly throughout the pulse, this also caused a 0.02 nm reduction in spectral bandwidth. The isolator and output coupler were both modelled as lumped losses, lowering the intensity of the field but not altering the shape or width. After this, the 840 m length of passive fibre induced ∼30 ps pulse broadening and a small ∼0.025 nm increase in spectral bandwidth, driven by *self-phase modulation* (SPM).

Finally, the bandpass filter reduced the bandwidth by an almost negligible value of

$\sim$0.005 nm and correspondingly, reduced the pulse duration by $\sim$5 ps due to the chirp. We observed that the bandpass filter has less of a spectral filtering effect than the saturable absorber, explaining why we were able to achieve stable mode-locking without this component in experiments. However, it was included to prevent polarisation-induced shifts in wavelength which occurred in practice, but were omitted from our laser model. The field was then fed back into the amplifier and the evolution repeated every round trip.

We conclude that there was insignificant pulse breathing in the cavity. Dispersive broadening was compensated by the saturable absorber and the gain compensated for losses. In this simulation we ignored the short $\sim$1 m fibre patchcords between components and lumped their combined length into the long length of fibre at the end of each round trip. Fig. 3.7 shows that pulse evolution in such short lengths of passive fibre was negligible, justifying this assumption.

Finally, we note that the onset of stimulated Raman scattering has been proposed as an ultimate limit to pulse energy scaling of long mode-locked fibre laser cavities [Agu13], since Raman scattering de-linearises the chirp (due to *cross-phase modulation* (XPM) between the signal and noise-seeded Stokes fields) and inhibits pulse compression [Gom85, Wei88b]. At the power levels in our experiments, however, Raman-shifted spectral components were not observed, since we were limited by the nanotube-PVA saturable absorber damage threshold.

3.2.3 Scalar Nanosecond Chirped-Pulse Generation

For practical applications of mode-locked lasers, sensitivity to external thermal and mechanical stresses could be a problem as these disturbances alter the birefringence of cavity fibre, which can unpredictably degrade the laser performance as described in Section 1.3.3. The environmental stability of all-fibre lasers can therefore be improved by using *polarisation-maintaining* (PM) fibre.

Additionally, the majority of long-cavity mode-locked pulse sources to date have produced vector pulses, consisting of two coupled propagation modes along orthogonal polarisation axes. These modes can exchange energy as the birefringence changes (induced by external perturbations) causing the polarisation state to evolve unpredictably over time. Distinct are vector locked solitons, whose group and phase velocities along orthogonal polarisation axes are equal, such that the pulse propagates without evolution in its polarisation state [Cun99]. A scalar pulse with a fixed linear polarisation state is preferred for certain applications, for example in surface texturing where the formation of polarisation-sensitive nanostructures determines the morphology and precision of the surface features [Hna13].

In this section, we present the results of an all-PM fibre long-cavity laser generating nanosecond pulses with a fixed linear polarisation state.

Experimental Setup

The laser design employed a similar ring cavity to the previous setup, although in this case PM fibre (ThorLabs panda-style PM980) was used throughout with 0.6 m PM double-clad ytterbium-doped fibre as the gain medium, as shown in Fig. 3.8. The same carbon nanotube-based saturable absorber was used, in addition to a PM isolator and a 33% PM output coupler. In the previous section, it was found that the output spectrum in the long-cavity mode-locked regime could be broadened with increasing power. A larger spectral bandwidth is desirable for extracavity compression and supports a shorter transform-limited pulse duration. Therefore, we chose a 300 m length of highly nonlinear fibre (OFS PM Raman Fibre) to elongate the cavity and to increase the total intracavity dispersion and nonlinearity: the greater fibre nonlinearity compared to standard fibre was intended to increase spectral broadening through SPM. A fusion splicer with rotating fibre stages (Ericsson FSU 995 PM) was used to align polarisation axes when constructing the cavity. The highly nonlinear fibre was spliced to PM980 fibre using a mode-field matching algorithm with ∼0.3 dB splice loss and >30 dB calculated polarisation extinction ratio. The total cavity length was ∼312 m.

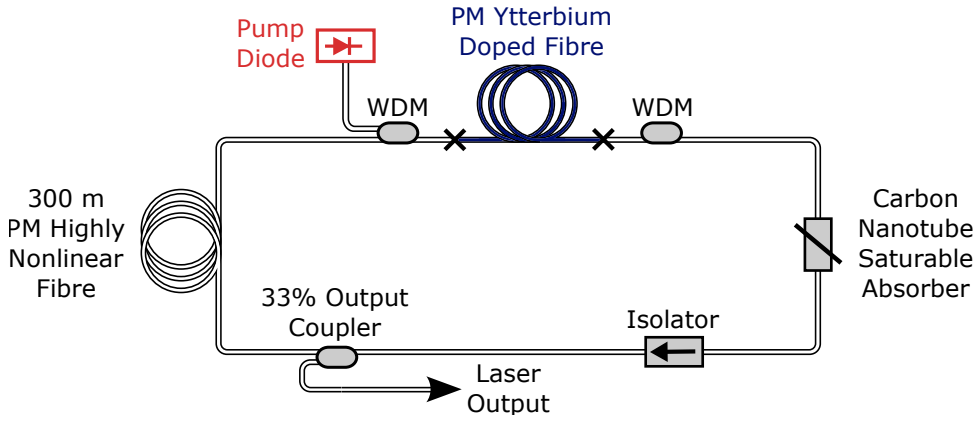


Fig. 3.8: Schematic of all-polarisation-maintaining long-cavity fibre laser, mode-locked with a carbon nanotube saturable absorber. The total cavity length was ∼312 m.

Laser Characterisation

The laser exhibited self-starting mode-locking at ∼1.4 W pump power, producing a regular train of pulses with a period of 1.56 μs, defined by the fundamental cavity frequency of 641 kHz (Fig. 3.9a). The pulse energy was ∼0.15 nJ. The output pulse had a sech^2 shape with a FWHM duration of 1.06 ns (Fig. 3.9b), which is the longest reported mode-locked pulse from an all-PM fibre laser to date. Fig. 3.9c shows the corresponding output spectrum, which was centred at 1041 nm with a 1.19 nm FWQM. As with the non-PM laser reported earlier, the pulse and steep-sided spectral shape suggested that these pulses were linearly chirped dissipative solitons with a time-bandwidth product hundreds of times greater than the transform limit.

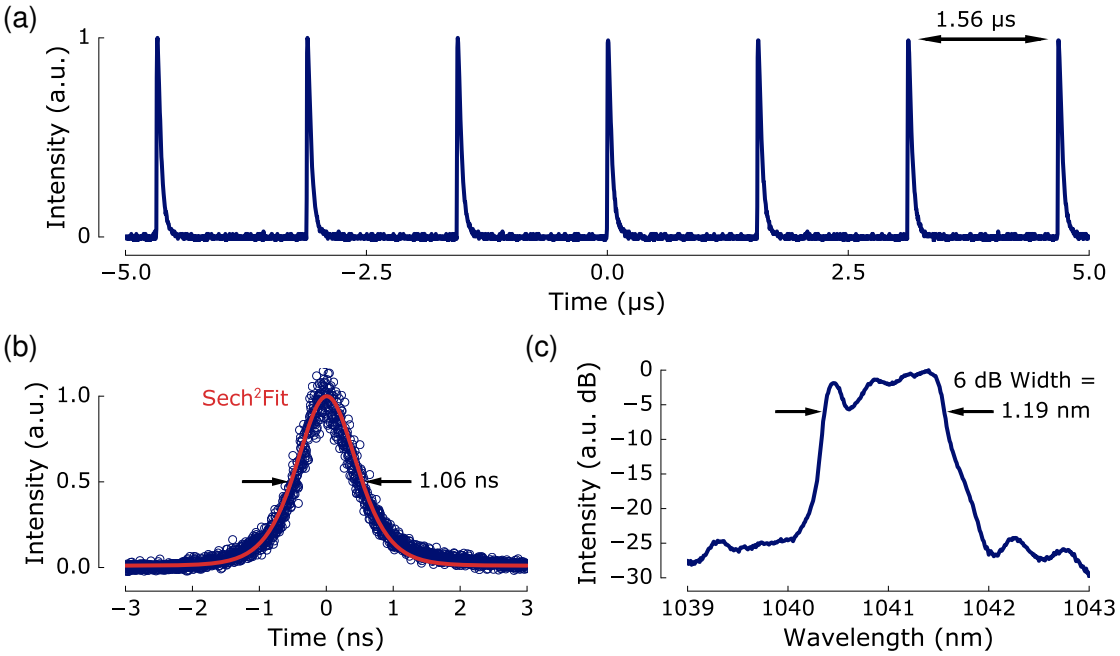


Fig. 3.9: Characteristics of all-polarisation-maintaining long-cavity mode-locked laser output: (a) oscilloscope trace; (b) streak camera trace; (c) optical spectrum.

The laser operated stably over many hours with no measurable change in output properties. Operational characteristics were also unchanged when the system was intentionally perturbed by mechanically stressing the cavity fibre, demonstrating the robust mode-locking performance and high environmental stability of the laser.

Compared to our previously demonstrated long-cavity laser, the spectral width of 1.19 nm was ∼50% broader, despite using a much shorter cavity length to achieve a similar ∼1 ns pulse duration. We attributed this to our use of highly nonlinear fibre to extend the cavity rather than standard silica fibre. This suggests that the laser architecture can be engineered to produce pulses with a wide range of durations and repetition rates by varying the length of cavity fibre and its properties.

The RF spectra for the fundamental, 60$^{\text{th}}$ harmonic and a 20 MHz span are shown in Fig. 3.10, which enabled us to quantify laser stability. The 20 MHz span plot shows a steady train of cavity harmonics without spectral modulation instabilities. We observed a high signal-to-background ratio of 61 dB ($10^{6.1}$ contrast) for the fundamental (Fig. 3.10a), which suggests good pulse-train stability. A low-level pedestal with a peak at ∼-61 dB was observed, from which the pulse-to-pulse energy fluctuations was calculated as 0.45%. This was a low pulse energy fluctuation, especially compared to the 1.6% value of the previous source and the 7% fluctuation reported for a nanosecond pulse source in Ref. [Zha13a]. Mode-locking stability was also confirmed by the high 52 dB peak-to-background ratio ($10^{5.2}$ contrast) of the 60$^{\text{th}}$ harmonic (Fig. 3.10b).

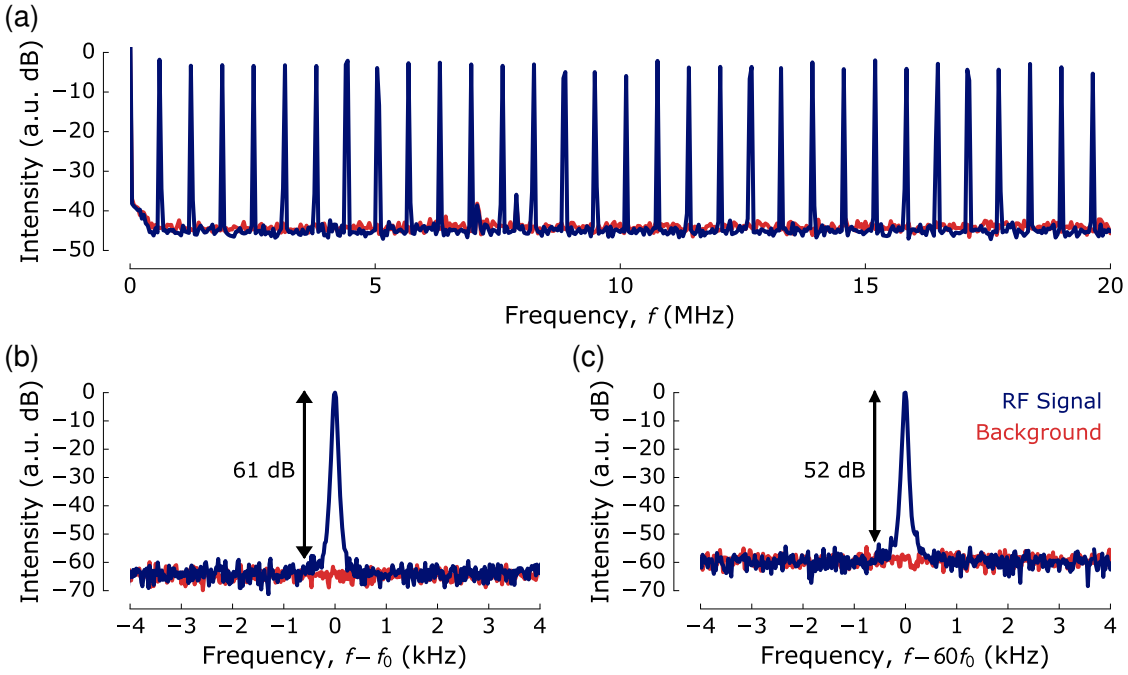


Fig. 3.10: RF spectrum of 312 m long-cavity mode-locked laser output: (a) 20 MHz span; (b) 8 kHz span about fundamental, f_0 = 641 kHz; (c) 8 kHz span about 60th harmonic (30 Hz resolution bandwidth).

Polarisation Measurements

The polarisation state of light can be fully described by a set of four values known as the Stokes parameters, which are commonly expressed as the Stokes vector: $S = (S_0, S_1, S_2, S_3)$. To measure these parameters, we collimated the output of the fibre laser and built a free-space polarimeter consisting of a rotating *quarter-wave plate* (QWP) and linear polariser followed by a power meter (Fig. 3.11a). The combination of a waveplate and polariser transform the polarisation state into an intensity value I that can be measured directly. Therefore the Stokes parameters can be deduced from only four power measurements with specific angles of the polariser θ and waveplate ϕ relative to a fixed axis [Chi95]:

$$S_0 = I(\theta = 0^\circ, \phi = 0^\circ) + I(\theta = 90^\circ, \phi = 0^\circ) \tag{3.2.2a}$$

$$S_1 = I(\theta = 0^\circ, \phi = 0^\circ) - I(\theta = 90^\circ, \phi = 0^\circ) \tag{3.2.2b}$$

$$S_2 = 2I(\theta = 45^\circ, \phi = 0^\circ) - I(\theta = 0^\circ, \phi = 0^\circ) - I(\theta = 90^\circ, \phi = 0^\circ) \tag{3.2.2c}$$

$$S_3 = 2I(\theta = 45^\circ, \phi = 90^\circ) - I(\theta = 0^\circ, \phi = 0^\circ) - I(\theta = 90^\circ, \phi = 0^\circ) \tag{3.2.2d}$$

It is common to normalise the vector to $S_0 = 1$, enabling useful polarisation parameters to be obtained from these values, including the *degree of polarisation* (DOP) and *degree of*

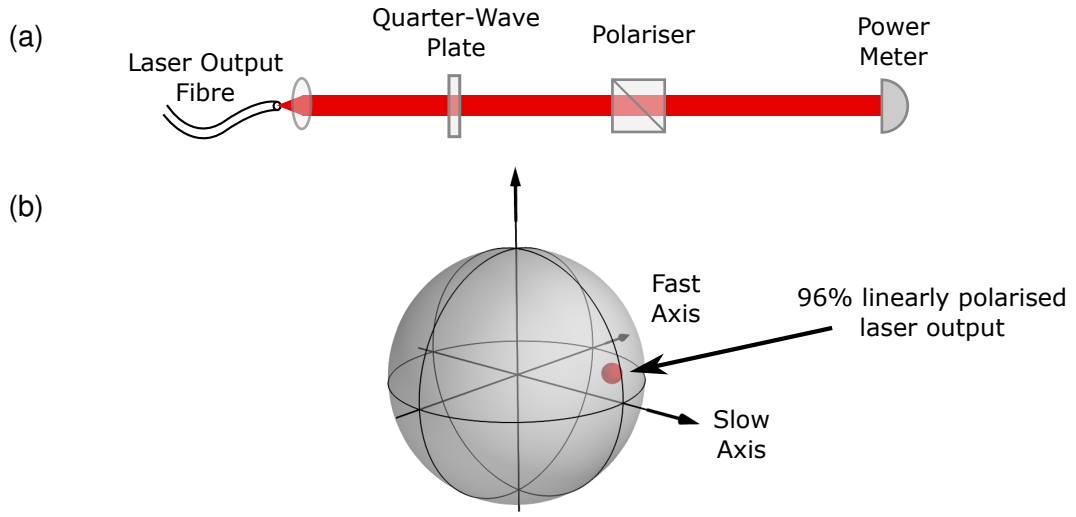


Fig. 3.11: Measurement of optical polarisation state: (a) schematic of polarimeter; (b) linearly polarised output state of 312 m long-cavity laser shown as a red dot on the Poincaré sphere.

linear polarisation (DOLP) [Chi95]:

$$DOP = \sqrt{S_1^2 + S_2^2 + S_3^2} \tag{3.2.3a}$$

$$DOLP = \sqrt{S_1^2 + S_2^2} \tag{3.2.3b}$$

Using the polarimeter and Eqn. 3.2.2 we measured the Stokes vector of the PM fibre long-cavity laser to be: $S = (1.00,\ 0.93,\ -0.27,\ 0.11)$, indicating a 97% degree of polarisation and 96% degree of linear polarisation. This confirmed that the output was strongly linearly-polarised (shown visually on a Poincaré sphere in Fig. 3.11b), highlighting that the laser produced scalar pulses. The extinction between the two polarisation axes was 14.1 dB and the polarisation state was unchanged by mechanical or thermal perturbations to the cavity. The origin of the polarisation-selectivity in the cavity was the coupler, which was optimised to give a lower cavity loss on the slow-axis; it was therefore favourable for radiation to build-up in this axis and the high-birefringence minimised coupling between the fast and slow axis to maintain a fixed linear polarisation state. In contrast, the output polarisation of the non-polarisation-maintaining 846 m-long laser was found to be partially polarised and varied randomly with disturbances to the cavity fibre, explaining the variation in performance over time.

3.3 Pulse Compression by Chirp Compensation

A pulse with a linear up-chirp can be compressed by introducing a down-chirp to compensate the frequency-sweep of the pulse. This can be achieved by using optical components with anomalous dispersion, such as a diffraction grating pair, anomalously-dispersive

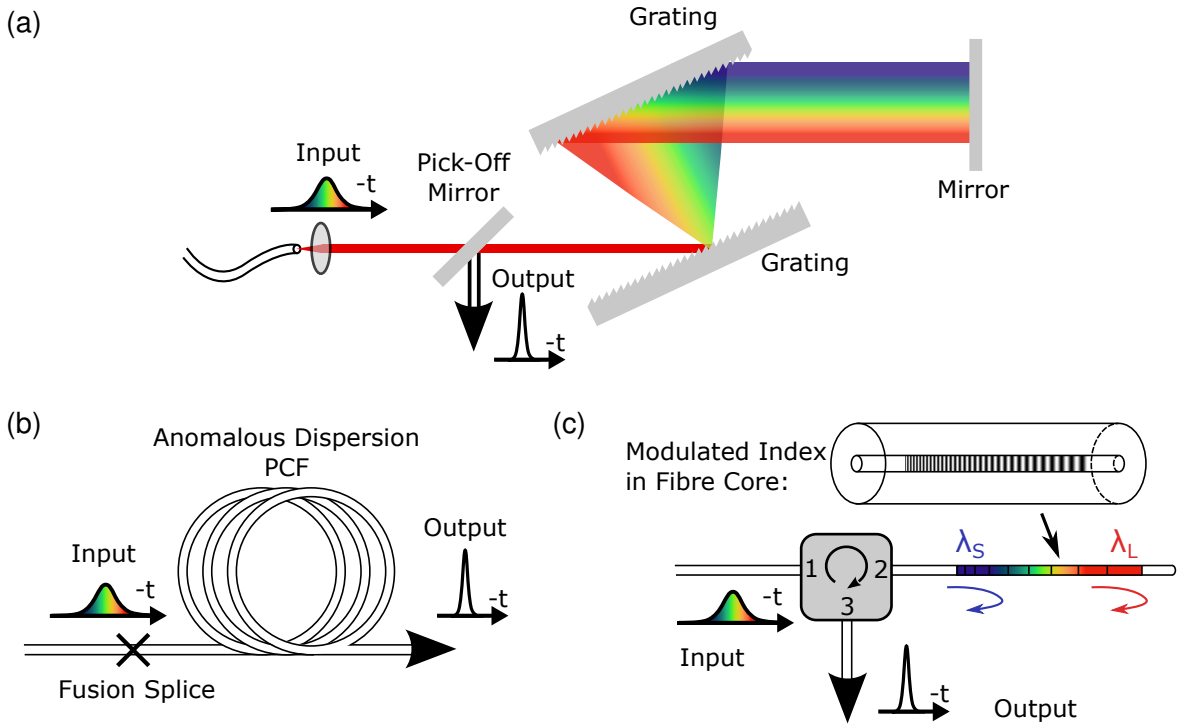


Fig. 3.12: Schematic for up-chirped pulse compression techniques: (a) double-pass bulk grating pair; (b) single-pass anomalously-dispersive PCF; (c) chirped fibre Bragg grating and circulator (with numbered ports).

fibre or a chirped fibre Bragg grating (Fig. 3.12).

Bulk Diffraction Grating Pair

Pulse compression is commonly achieved using a pair of bulk diffraction gratings, first proposed by E. B. Treacy in 1968 [Tre68]. A typical experimental setup using reflective gratings is shown in Fig. 3.12a. The beam of chirped pulses (i.e. the collimated output from the laser source) is diffracted from the first grating, angularly dispersing the pulse spectral content, with the diffraction angle given by:

$$\theta_d = \arcsin\left(\frac{m\lambda}{d} - \sin\theta_i\right) \tag{3.3.1}$$

where m is the diffracted order (typically ± 1 for highest efficiency), λ is the instantaneous wavelength, d is the grating pitch (1 / number of lines per mm) and θ_i is the incident angle. Diffraction from a second parallel grating then causes the beam to become parallel again. Since the leading part of the pulse (containing longer wavelengths) diffracts at a larger angle, the optical path length is longer. This delays the arrival time of the front of the pulse, bringing spectral components closer together in time. This compensates the chirp by realigning the spectral components in time, compressing the pulse duration. With a single-pass of the grating pair, the output beam is also spatially chirped, which

is unsuitable for focussing back into a fibre. Therefore, it is common to double-pass the compressor to undo the spatial chirp on the return pass, effectively doubling the delay that can be introduced; this is achieved with a mirror after the gratings which is very slightly angled so the reflected beam is offset from the incoming beam and thus, can be picked-off by an additional mirror.

The wavelength-dependent spectral phase delay for a single pass of the grating pair is [Tre69]:

$$\varphi(\omega) = \frac{\omega}{c} \frac{L}{\cos(\theta_i - \theta_d)} (1 + \cos\theta_m) - \frac{2\pi L}{d} \tan(\gamma - \theta_m) \tag{3.3.2}$$

where L is the parallel grating separation, θ_d is the diffracted angle and θ_m is the acute angle between incident and diffracted rays ($\theta_m = \theta_i - \theta_d$). We simulated the effect of a grating pair on our giant-chirped pulses numerically by multiplying the modelled pulse field in the frequency domain $\tilde{A}(\omega)$ by the response of a double-pass through the grating pair arrangement $\exp(-i2\varphi(\omega))$.

Gratings with 1200 lines per mm and a 45° angle of incidence were considered. By adjustment of the separation distance we found that pulse compression was possible, with an
pulse was almost zero, indicating strong chirp compensation, although small wings and a low-level pedestal could be seen that we attributed to residual nonlinear chirp. This was confirmed by observing the pulse spectrogram (Fig. 3.13b). The effect of the grating is purely linear - there is no nonlinearity, and it should be noted that practical gratings would introduce a loss of up to 25% per reflection. While this simulation confirmed that the long-cavity laser pulses were compressible, the diffraction grating separation required for this was 88.5 m. Clearly, this was not a practical solution and other methods needed to be considered.

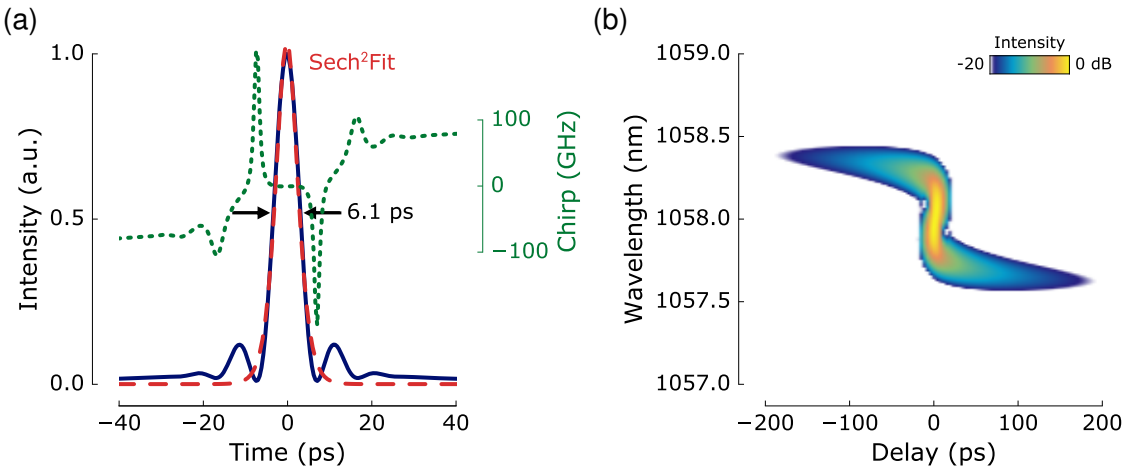


Fig. 3.13: Simulated pulse compression by a double-pass diffraction grating pair with 1200 lines per mm and 45° angle of incidence: (a) pulse shape and chirp; (b) spectrogram.

Anomalously Dispersive PCF

Since pulse broadening in the long cavity was due to normally dispersive fibre, a length of anomalously dispersive fibre could be used to undo the chirp (Fig. 3.12b). Conventional step-index fibres are always normally dispersive at our laser wavelength, due to a dominant contribution from material dispersion (silica's ZDW is$\sim$1270 nm) as discussed in Section 1.3.3. However, advances in PCF technology have enabled the fabrication of speciality fibres with large air holes, providing a high effective index contrast between the solid core and microstructured cladding which yields strong waveguide dispersion to shift the ZDW towards visible wavelengths. Consequently, anomalous dispersion is possible at 1058 nm.

We explored the possibility of employing a large-air-hole PCF for pulse compression, specifically using the commercially-available NKT NL-2.8-850 fibre. This has 2.5 μm diameter holes and a pitch of 2.6 μm . From these parameters, we constructed a numerical model of the fibre using the vector analytical effective index method described in Section 2.2.2. The ZDW was estimated as 861 nm and the dispersion at 1058 nm was $D = 61.6$ ps nm^{-1} km^{-1} nm (Fig. 3.14), in good agreement with the manufacturer datasheet.

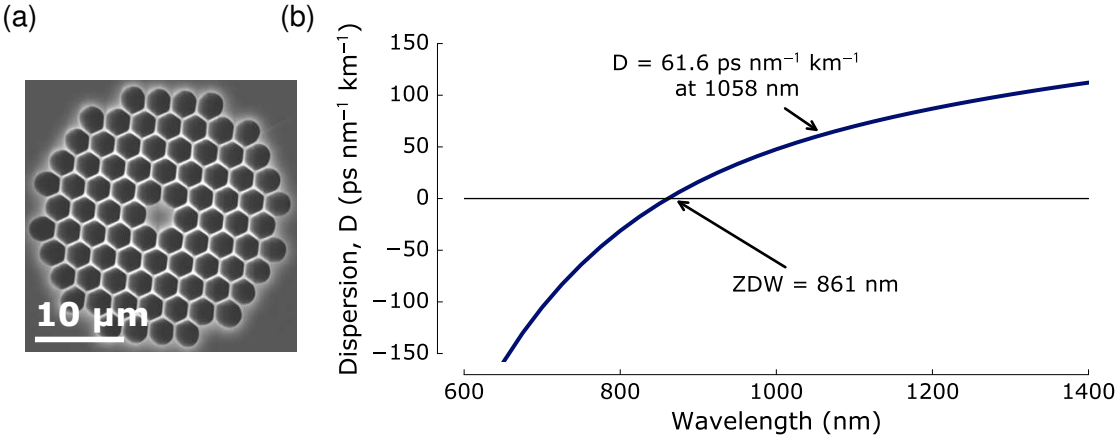


Fig. 3.14: Properties of large air hole PCF (NKT NL-2.8-850) with $d = 2.5$ μm and $\Lambda = 2.6$ μm : (a) SEM image of microstructure; (b) computed dispersion curve.

For our giant-chirped pulse with $\Delta\lambda = 0.81$ nm spectral FWHM, the transform-limited duration was $\Delta t_{\mathrm{tl}} \sim 1.5$ ps. Therefore, to compress to the transform limit, the required length of PCF was approximated by: $L \sim (\Delta t_{\mathrm{fwhm}} - \Delta t_{\mathrm{tl}})/(D\Delta\lambda_{\mathrm{fwhm}}) = 20$ km.

We simulated the pulse propagation along this fibre, with an input peak power of 1 W (Fig. 3.15). After only 0.3 km, the pulse exhibited heavy distortion. Spectral sidebands emerged and noise grew on the peak of the pulse. Such behaviour is characteristic of modulation instability: a four-wave mixing phenomena which is phase-matched by self-phase modulation and well-known to occur for broad pulses in anomalously dispersive media. Modulation instability caused the breakdown of the field into fundamental solitons,

seeded by noise fluctuations, and the linear chirp was destroyed, as confirmed by the simulation after 0.35 km.

Nonlinearity appeared detrimental for pulse compression here, although we note that modulation instability can be usefully used, as discussed in Section 3.4 in the context of supercontinuum generation. It should also be noted that nonlinear compression is an alternative route to improving compression factors, although this differs from the present situation: typically, a nonlinear stage (in a normal dispersion environment) broadens the pulse spectrum to reduce the transform-limited duration, followed by linear compression (with anomalous dispersion) to reduce the pulse width to approach this limit [Tom84]. Unfortunately, anomalously dispersive large-air-hole PCFs intrinsically possess small cores and hence, tight modal confinement yields high intensities; the nonlinear coefficient of this PCF was $\gamma = 35$ W km^{-1} at 1058 nm, an order of magnitude greater than normal fibre. Additionally, the long lengths required for sufficient dispersion lead to a large nonlinear phase accumulation, suggesting that nonlinear effects are inevitable.

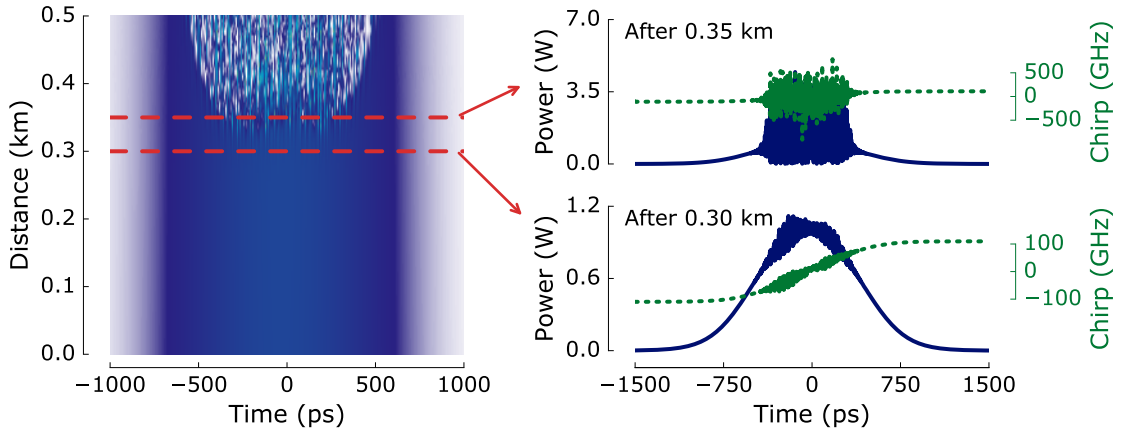


Fig. 3.15: Simulated propagation of 1 W peak power giant-chirped pulses in anomalously dispersive PCF. The strong nonlinearity of PCF resulted in modulation instability, breaking up the pulse rather than showing linear compression.

To verify if this compression strategy could work in the absence of nonlinear effects, we reduced the peak power to a very low value of 0.1 mW and repeated the simulation. In this instance, strong compression was observed while maintaining the quality of the pulse (Fig. 3.16). After 25 km, the duration was reduced to a minimum value of 5.7 ps, with a negligible change in instantaneous frequency across the pulse, indicating that the giant chirp had been compensated. Small pulse wings could be seen due to a slight nonlinear chirp on the original pulse that could not be compensated, or possibly from the effect of higher order dispersion in PCF, which could also explain why the compressed duration is not quite the transform-limited value.

From these numerical experiments, we have demonstrated that the giant linear chirp of long-cavity laser pulses can be compressed using anomalous dispersion in PCF. However, this is not a practical route experimentally as the long length of PCF would be costly and

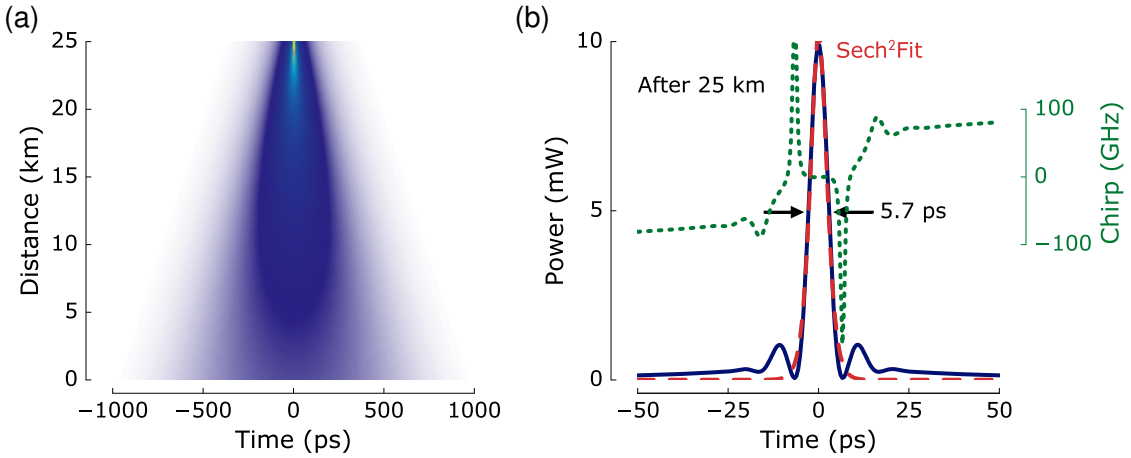


Fig. 3.16: Simulated propagation of 0.1 mW peak-power giant-chirped pulses in anomalously dispersive PCF. The low launch power avoided nonlinear effects, enabling linear compression of the pulses by compensating the chirp.

lossy (fibre loss was neglected in simulations) and the limitation of sub-milliwatt input peak powers is lower than the power required for many practical applications.

Chirped Fibre Bragg Grating

An alternative all-fibre compression technique is to engineer a chirped fibre Bragg grating to compensate the chirp. *Fibre Bragg gratings* (FBGs) are narrow-band reflectors constructed of periodic modulations of refractive index in the core of an optical fibre, first demonstrated by Kenneth Hill in 1978 [Hil78]. Wavelengths for which the Bragg condition is met are strongly reflected through constructive interference of the waves that are Fresnel reflected from each period of the grating, according to:

$$\lambda_B = 2n_{\text{eff}}\Lambda \tag{3.3.3}$$

where n_{eff} is the effective index seen by the propagating mode and Λ is the periodic structure pitch (i.e. period spacing). The reflection band of a grating corresponds to a photonic bandgap in frequency-space – a frequency range where there are no real, propagating solutions to Maxwell's equations, only evanescent waves.[5] *Chirped fibre Bragg gratings* (CFBGs) are constructed by gradually decreasing the grating pitch along the length of the device so the Bragg reflection wavelength, $\lambda_B(z)$ decreases with position, z, along the grating length, L. For an incident pulse on a CFBG, longer wavelength spectral components propagate further into the grating before being reflected (or vice versa, if the CFBG direction is reversed), introducing a wavelength-dependent delay. A chirped pulse with bandwidth $\Delta\lambda$ will experience a delay τ between the longest and shortest

[5] It can be instructive to consider the FBG in this case as an effective unstructured medium with a real refractive index at frequencies outside the bandgap and an imaginary index within the bandgap [Sip94].

wavelength components:

$$\tau = \frac{2n_{\text{eff}}\Delta\lambda}{c\,\frac{\mathrm{d}\lambda_B}{\mathrm{d}z}} \tag{3.3.4}$$

where $\frac{\mathrm{d}\lambda_B}{\mathrm{d}z}$ is the rate of change of Bragg wavelength along the CFBG. Therefore, by matching the delay to the chirped pulse width, the spectral components in the pulse will temporally realign upon reflection from the CFBG, compensating the chirp and compressing the pulse [Oue87]. The CFBG reflection bandwidth is set by the length of the grating and the strength of index modulation controls the reflectivity.

Experimentally, a CFBG can be integrated into a system using a 3-port circulator, to direct the reflected light to an output port (Fig. 3.12c). CFBG-based compression is flexible as the grating properties can be engineered to match the laser pulses and the alignment-free all-fibre format of the system is maintained. Additionally, only standard step-index fibre is required, which can be spliced with low-loss using conventional fusion splicers. Therefore, this was our chosen technique to compress the giant-chirped pulses.

3.3.1 CFBG Design and Fabrication

For optimum compression, it is important that the CFBG reflection band overlaps with the pulse spectrum and the chirp rate is equal and opposite to the frequency sweep on the pulse. Using Eqn. 3.3.4 and writing a CFBG into fibre assuming $n_{\text{eff}} \sim 1.45$, the required rate of change of Bragg wavelength to introduce a delay equivalent to the 1 ns pulse duration between the long and short wavelength components ($\Delta\lambda = 0.82$ nm) was $\frac{\mathrm{d}\lambda_B}{\mathrm{d}z} \sim 0.008$ nm mm^{-1}. Therefore, the CFBG length was to be $\sim$145 mm to yield a sufficiently broad reflection bandwidth.

Conventionally, FBGs are fabricated using a phase mask: a silica plate with etched grooves, which creates an interference pattern through diffraction of incident UV light. By positioning the interference pattern on a Ge-doped fibre, the optical intensity pattern is transferred to a refractive index grating in the fibre core, due to photosensitivity of the fibre at UV wavelengths. Specifically, photosensitivity arises from GeO defects which are typically present in the silica matrix of the core – UV light breaks these defect bonds, forming colour centres that modify the local glass absorption and hence the refractive index, according to the Kramers-Kronig relations. Prior to processing, fibres are routinely loaded with hydrogen gas, which enhances the defects and enables greater refractive index modulation depths to be achieved, creating stronger (i.e. more reflective) FBGs [Kas99].

Phase masks are produced lithographically with the required period to achieve a particular FBG period and modulation depth. CFBGs can be produced by either bending or tilting the target fibre, to cast an uneven interference pattern on the surface, or by fabricating chirped phase masks. These techniques are regularly employed for fabricating millimetre-long gratings, but are not suitable for accurately writing a varying structure over longer distances, as required for our proposed $>$100 mm CFBG.

Therefore, we established a collaboration with École Polytechnique de Montréal, Canada,

where a new direct writing system for long FBGs had recently been developed [Gag14].[6] Briefly, a phase mask mounted on a piezoelectric-driven translation stage was integrated into a Talbot interferometer to generate a moving fringe pattern on a fibre. This fibre was moved along its axis using a 1 m long high-precision translation stage while the piezo-driven phase mask was driven with a ramp signal at a frequency to match the speed of the moving fibre. To induce a chirp, the movement speed of the fibre was slightly varied linearly.

Tuning of CFBG Reflection Window

CFBGs were fabricated in Flexcore fibre from our specification, although it was difficult to precisely define the reflection window to within 0.1 nm accuracy, as required for our application. This fabrication uncertainty arises due to hydrogen evaporation from the fibre after the grating has been written, causing a shift of the reflection window to shorter wavelengths. Therefore, a variety of gratings were produced and it was necessary to tune the as-manufactured CFBG reflection band to achieve optimum compression.

Since the Bragg wavelength of a grating is proportional to the pitch, the reflection window can be red-shifted by heating or stretching the device to cause expansion. To measure this effect, a broadband ASE source was connected to the input of a 100 mm long CFBG and the transmitted light from the back of the grating was monitored on an optical spectrum analyser - the dip in transmission showed the window of reflected light.

Initially, we submerged the CFBG in a heated waterbath and observed shifts of $\sim$0.1 nm per 10°C temperature increase up to 70°C. However, the long delay between setting the temperature and the water heating up / cooling down suggested that this method was unsuitable. Therefore, we implemented a stretch-tuning setup by gluing one grating end to a fixed point and mounting the other on a linear translation stage. The CFBG elongated under increasing tension, causing a linear shift of the Bragg wavelength at a rate of $\sim$7.5 nm per mm extension and showing no distortion of spectral features (Fig. 3.17). However, at 0.5 mm extension, the fibre snapped. This corresponded to a maximum strain of 0.5% and a maximum redshift of $\sim$4 nm, which was sufficient tunability to compensate for manufacturing tolerances. We compared this to the expected theoretical shift using Eqn. 3.3.3: for an initially unstretched CFBG with reflection band centred at 1054.4 nm, we expect a grating period at the centre equal to 363.6 nm. A 0.5% strain will increase the grating period to 365.4 nm, leading to a red shift of$\sim$5 nm, in reasonable agreement with the experiment. [7]

[6] We thank Prof. Raman Kashyap and Sébastien Loranger at École Polytechnique de Montréal for CFBG fabrication and fruitful discussions regarding pulse compression.

[7] While not considered here, the temperature and strain dependence of FBGs enables them to be used as very sensitive sensors, which are widely deployed in variety of industrial environments [Kas99].

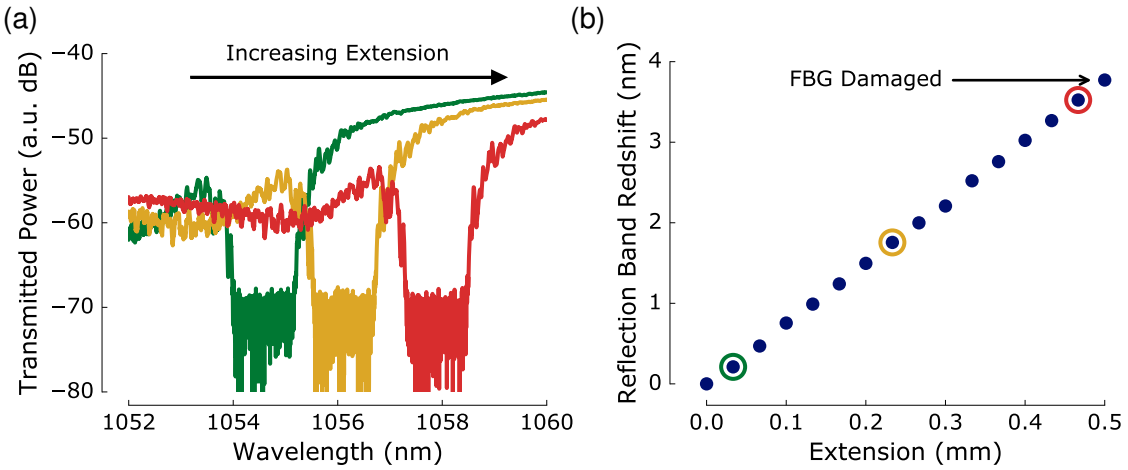


Fig. 3.17: Red-shifting of CFBG reflection window under strain: (a) Transmission profile at increasing extension values, showing a shift in wavelength with no change in shape; (b) measured wavelength shift against extension, showing a linear relationship

Preliminary Compression Results

A 100-mm long CFBG with a $\sim$0.008 nm mm^{-1} chirp rate (hereafter referred to as CFBG-1) was spliced to port 2 of a 3-port circulator, with an ASE source connected to port 1. The grating was stretch-tuned to centre the reflection band at 1058 nm, measured by monitoring the transmitted light after the CFBG (Fig. 3.18a). The ASE source was then replaced by the output of the long-cavity laser. Light reflected from the grating was monitored at port 3 using an optical spectrum analyser and streak camera.

The power of the long-cavity laser was adjusted to slightly change the spectral width, and the CFBG strain could be tweaked to fine-tune the reflection band. With poor overlap between the reflection band of CFBG-1 and the laser spectrum, a highly distorted reflected signal was recorded. Through strain tuning, as the overlap approached the optimal value, the intensity of the leading edge of the pulse increased and narrowed. In the best case, a feature with $\sim$196 ps width could be observed within a pulse envelope containing other peaks and noisy features (Fig. 3.18b). This temporal shape and spectrum were independent of the laser power, confirming the absence of nonlinear effects (as expected since the long-cavity laser average output power was < 1 mW; we discuss limitations to power-scaling later). However, despite many attempts to tune the spectral width and grating wavelength, it was not possible to produce a less distorted or narrower pulse.

In the design of CFBG-1, two effects had been overlooked. Firstly, CFBGs have a finite length: the light sees an abrupt change in the refractive index at the beginning and end of the grating structure compared to the standard fibre core index. This step function corresponds to a sinc function in the spectral domain (via the Fourier transform), which adds sidelobes to the reflection spectrum and oscillations to the group delay. From a more physical viewpoint, this can be described as Fabry-Pérot oscillations from the grating boundaries. Additionally, strong dispersion arises at the reflection band edges due to the frequency dependence of the transmission, as described by the Kramers-Kronig

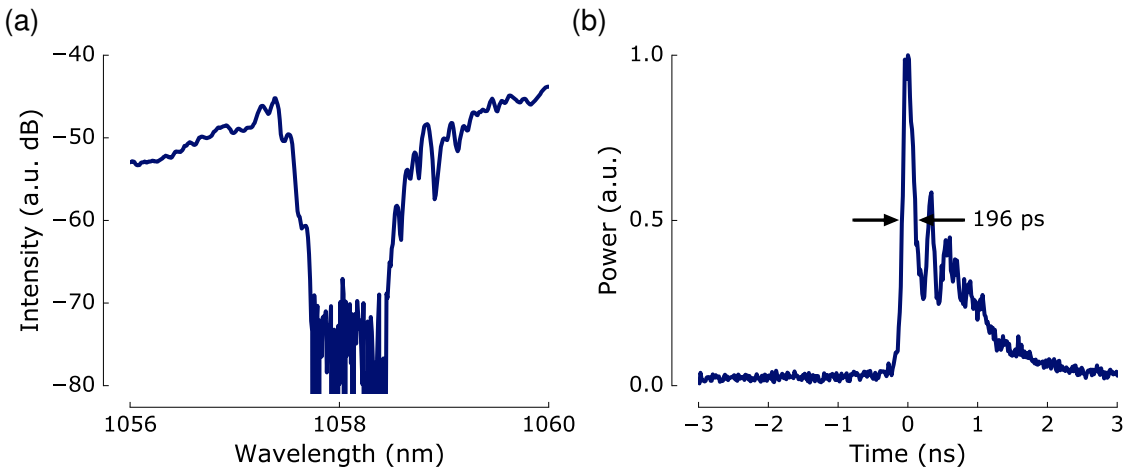


Fig. 3.18: Experimental giant-chirped pulse compression with CFBG-1: (a) grating transmission profile; (b) streak camera trace of the reflected pulse from the grating.

relations [Kra27, Kro25]. Using the Fabry-Pérot description of this situation, the enhanced dispersion can be attributed to the increased delay which is experienced by frequencies that are trapped in the Fabry-Pérot cavity for many round-trips [Sip94]. Overlap between the pulse spectrum and reflection band edges can therefore introduce additional dispersion over a narrow bandwidth, which distorts the pulse. While FBG band-edge dispersion has been usefully exploited for pulse compression [Lit97], it is much less controllable and considered as a distorting factor here.

To solve these problems, a longer grating with the same chirp rate was required, to increase the CFBG reflection bandwidth and prevent overlap between the band edges and the pulse spectrum. Additionally, to prevent reflection sidelobes, a grating can be apodised, meaning that the index modulation strength is gradually reduced towards the ends of the grating, preventing the step change. A Gaussian apodisation profile is often used (since the Fourier transform is also a Gaussian), with the form: $a(z) = \exp\left(-\frac{(z-0.5L)^2}{2w^2}\right)$ where $z = 0$ is defined as the start of the grating of length L and the Gaussian envelope FWHM is $2w\sqrt{2\ln 2}$ [Che97a].

The experiment was repeated using a second CFBG (referred to as CFBG-2) with the same chirp rate, but double the length (200 mm) and with a 80 mm FWHM Gaussian apodisation profile. The apodisation profile was created by adding a Hamming function to the piezoelectric-controlled phase mask to reduce the coupling constant during fabrication [Gag14]. In this case, the reflection band (observed by transmitting ASE through the grating) was wider than CFBG-1 and showed tapered, rather then steep, spectral edges (Fig.3.19a). As before, when the grating spectrum overlapped with the long-cavity laser spectrum, pulse compression was observed due to chirp compensation. However, the compressed pulse quality was significantly improved: a single peak was recorded, upon only a small pedestal with amplitude less than 20% of the peak height (Fig. 3.19b), suggesting the design improvements had been beneficial. The compressed duration was also slightly improved to 175 ps. For a linearly chirped pulse with 0.82 nm bandwidth,

it should be possible to approach the transform-limited duration of ∼1.4 ps, which is two orders of magnitude shorter than our measurements. This suggested that the Bragg wavelength change rate specified in Section 3.3.1 was not optimum. Therefore, in order to determine an improved CFBG specification, we simulated the problem using numerical modelling.

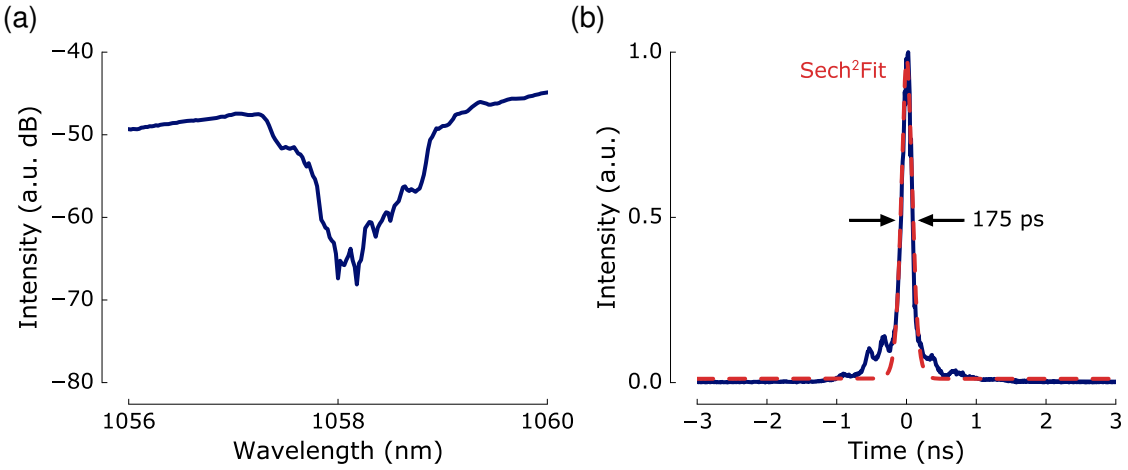


Fig. 3.19: Experimental giant-chirped pulse compression with CFBG-2: (a) grating transmission profile; (b) streak camera trace of the reflected pulse from the grating.

3.3.2 Modelling of CFBG Properties

FBGs can be considered within the established framework of electromagnetic wave propagation in periodically modulated media. A thorough mathematical treatment would solve Maxwell's equations with the periodic structure as a boundary condition, yielding a general form of the fields in terms of Bloch waves (which are the eigenmodes of periodic media) [Blo29]. However, this is highly involved and practically unnecessary for understanding FBGs, since the modulation depth is typically small ($\Delta n \ll n_{\text{eff}}$, limited by the fibre's photosensitivity) so simplifications can be made. Indeed, it is sufficient to employ coupled-mode theory to describe the problem as the interaction of two counter-propagating modes (using two coupled differential equations), representing the incident and reflected light [Mil54, Yar73]. Fortunately, an analytical solution exists for uniform FBGs with a constant period, which is commonly expressed as a transfer matrix to describe the FBG response.

For a chirped FBG with a varying periodic structure, however, there are no known closed-form solutions. Therefore, the piece-wise *transfer matrix method* method was proposed: by splitting the grating into hundreds of uniform segments with progressively varying properties, the transfer matrix for each segment can be analytically computed and the overall CFBG response found by multiplying all the transfer matrices together [Yam87], as illustrated in Fig. 3.20. This technique has been widely demonstrated to accurately simulate CFBG properties and thus, was our chosen modelling method for this problem.

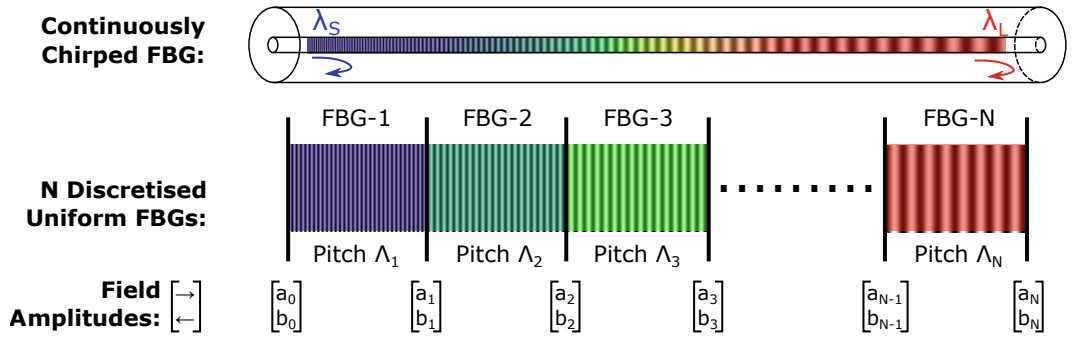


Fig. 3.20: Illustration of the numerical modelling method for simulated CFBGs. A long grating with continuously varying properties is split into many uniform FBGs for which the properties can be analytically computed. The CFBG response is found by multiplication of all the component FBG transfer matrices. Colour is used to indicate the reflected wavelength at each position: blue indicates shorter wavelengths.

Numerical Implementation

The refractive index profile of a fibre grating can be expressed as:

$$n(z) = n_0 + \Delta n_0 \, a(z) \cos\left(\frac{2\pi}{\Lambda(z)} z\right) \tag{3.3.5}$$

where z is the distance along the FBG, n_0 is the background index of the fibre, Δn_0 is the grating modulation depth, $\Lambda(z)$ is the pitch (period spacing), which varies with z and $a(z)$ is the apodisation profile.

The coupled wave equations describing the amplitudes of the transmitted field $A(z)$ and reflected field $B(z)$ are [Yar07]:

$$\frac{\mathrm{d}A(z)}{\mathrm{d}z} = -i\,\kappa(z)\,B(z)\exp(i\Delta\beta z) \tag{3.3.6a}$$

$$\frac{\mathrm{d}B(z)}{\mathrm{d}z} = i\,\kappa^*(z)\,A(z)\exp(-i\Delta\beta z) \tag{3.3.6b}$$

where we have introduced the coupling constant κ (with complex conjugate κ^*) as:

$$\kappa = \frac{\pi}{\lambda}\Delta n_0 \, a(z) \tag{3.3.7}$$

and the wavenumber mismatch $\Delta\beta$ (representing the detuning of the wavelength from the Bragg wavelength) as:

$$\Delta\beta = 2\frac{2\pi n_{\mathrm{eff}}}{\lambda} - \frac{2\pi}{\Lambda(z)} \tag{3.3.8}$$

To model a CFBG of length L, we adopted the piece-wise transfer matrix approach and divided the structure into N segments. For accurate results, many segments of length $l \approx L/N$ are required, such that $\Lambda \ll l \ll L$ and we ensured that each segment was an integer number of grating periods to give a smooth transition between them (avoiding the introduction of unphysical phase jumps). Each segment was assumed to be

an independent uniform FBG with a fixed value for the pitch and coupling constant, as set by the position of the segment along the FBG length: $\Lambda(z) = \left(\lambda_0 + \frac{\mathrm{d}\lambda_B}{\mathrm{d}z} z\right) / (2n_{\mathrm{eff}}) = \left[\left(\lambda_c - \frac{L}{2}\frac{\mathrm{d}\lambda_B}{\mathrm{d}z}\right) + \frac{\mathrm{d}\lambda_B}{\mathrm{d}z} z\right] / (2n_{\mathrm{eff}})$ where λ_0 is the Bragg wavelength at the start of the CFBG, which can be determined from the chosen reflection band central wavelength λ_c, length L and the Bragg wavelength change rate $\frac{\mathrm{d}\lambda_B}{\mathrm{d}z}$. The analytical solution relating the fields at the start and end position of the n^{th} segment is:

$$\begin{bmatrix} a_{n-1} \\ b_{n-1} \end{bmatrix} = M_n \begin{bmatrix} a_n \\ b_n \end{bmatrix} \tag{3.3.9}$$

where a_{n-1} is the input field, b_{n-1} is the reflected field (i.e. backwards field at segment entrance), a_n and b_n are the forward- and backward-propagating fields at the end of the segment, respectively, and M_n is the segment's transfer matrix [Yar07]:

$$M_n = \begin{bmatrix} \cosh(s_n\, l_n) + i\frac{\Delta\beta_n}{2s_n}\sinh(s_n\, l_n) & i\frac{\kappa_n}{s_n}\sinh(s_n\, l_n) \\ -i\frac{\kappa_n^*}{s_n}\sinh(s_n\, l_n) & \cosh(s_n\, l_n) - i\frac{\Delta\beta_n}{2s_n}\sinh(s_n\, l_n) \end{bmatrix} \tag{3.3.10}$$

where $s_n = \sqrt{|\kappa_n|^2 - (\Delta\beta_n/2)^2}$.

The overall response of the CFBG, M, is found by matrix multiplication of all the independently-computed segment matrices (illustrated in Fig. 3.20):

$$\begin{bmatrix} a_0 \\ b_0 \end{bmatrix} = M_1 M_2 M_3 \cdots M_N \begin{bmatrix} a_N \\ b_N \end{bmatrix} = M \begin{bmatrix} a_N \\ b_N \end{bmatrix} = \begin{bmatrix} M_{11} & M_{22} \\ M_{21} & M_{22} \end{bmatrix} \begin{bmatrix} a_N \\ b_N \end{bmatrix} \tag{3.3.11}$$

Principally, we are interested in determining the reflected field at the start of the CFBG, b_0 for a known input field a_0, which can be expressed by the reflection coefficient:

$$r(\omega) = \frac{b_0}{a_0} = \frac{M_{21}}{M_{11}} \tag{3.3.12}$$

To implement this model, we computed r at each wavelength in the numerical grid on which our simulated pulse field was based. The CFBG reflectivity was obtained from $|r(\omega)|^2$, and the group delay was found by differentiating the spectral phase with respect to angular frequency $\frac{\mathrm{d}\varphi}{\mathrm{d}\omega}$, where spectral phase is the angle argument of $r(\omega)$. The interaction between the pulse and grating is a time domain convolution, which we computed as a product in the frequency domain of the complex pulse field and grating reflection coefficient. Prior to applying the model to our problem, it was thoroughly tested with different numbers of segments (to ensure no dependence on the numerical gridding) and by recreating simulation results from literature, such as those summarised in Ref. [Che97a].

Simulation Results

CFBG-1 was simulated using the parameters specified in Section 3.3.1. The modulation depth Δn_0 was not precisely known, but was estimated as 5×10^{-5} by choosing a value which resulted in a similar peak reflectivity as the experimentally fabricated gratings, since the modulation depth determines the coupling constant and hence, the reflectivity. The calculated properties showed a $\sim$0.8 nm grating reflection band with steep edges and a linear group delay across the band, as intended in the CFBG design (Fig. 3.21a). The group delay was only plotted within the reflection band since at other wavelengths the reflected amplitudes are negligible so the phase is effectively undefined. With a long-cavity laser pulse as the input electric field, the reflected field from the grating is shown temporally and as a spectrogram in Figs. 3.21b & c. Compression to 161 ps FWHM was obtained, in reasonable agreement with the value of 196 ps from the experiment. Additionally, the pulse was slightly distorted and asymmetric, although less strongly than observed in the streak camera measurement. A linear chirp also remained on the pulse, indicating that further chirp compensation was possible.

Pulse distortion from CFBG-1 was caused by oscillations in the group delay (shown magnified in Fig. 3.21a inset), and from overlap between the pulse spectrum and the steep reflection band edges. Experimentally, CFBG-2 demonstrated improved compression, due to the longer length and Gaussian apodisation profile. These effects were also observed when simulating CFBG-2 (Fig. 3.22): the apodisation profile tapered the reflection band edges and removed oscillations from the group delay so the reflected pulse field was free from distortion. The remaining linear chirp on the pulse, however, suggested that the CFBG chirp rate was not optimised.

Using the numerical model, we explored the impact of grating chirp rate on the output pulse duration (using a 400 mm long CFBG length and 300 mm FWHM Gaussian apodisation to avoid the aforementioned distortion effects). A steady decrease in compressed pulse duration was observed by decreasing the chirp rate until around 0.006 nm mm^{-1}, achieving a minimum pulse duration of 6.2 ps (Fig. 3.23). Any further decrease in rate caused the compressed duration to grow again, as in this case the grating-introduced down-chirp was larger than needed to compensate the up-chirp, causing a residual down-chirp after reflection.

The characteristics of the optimum grating (CFBG-3) and the reflected pulse shape and spectrogram are shown in Fig. 3.24. The compressed pulse quality was excellent and well-fitted by a sech^2 shape. Across the pulse width there was negligible chirp, indicating almost perfect compensation of the pulse's linear chirp from the CFBG. However, a very small pedestal was observed which could be attributed to the chirp at the edges of the pulse not being perfectly linear, arising from higher-order dispersive effects in the long-cavity laser. Consequently this nonlinear up-chirp could not be compensated by the linear CFBG down-chirp. This is illustrated more clearly by comparing the giant-chirped pulse spectrogram to the CFBG response (Fig. 3.25). The grating response was highly linear

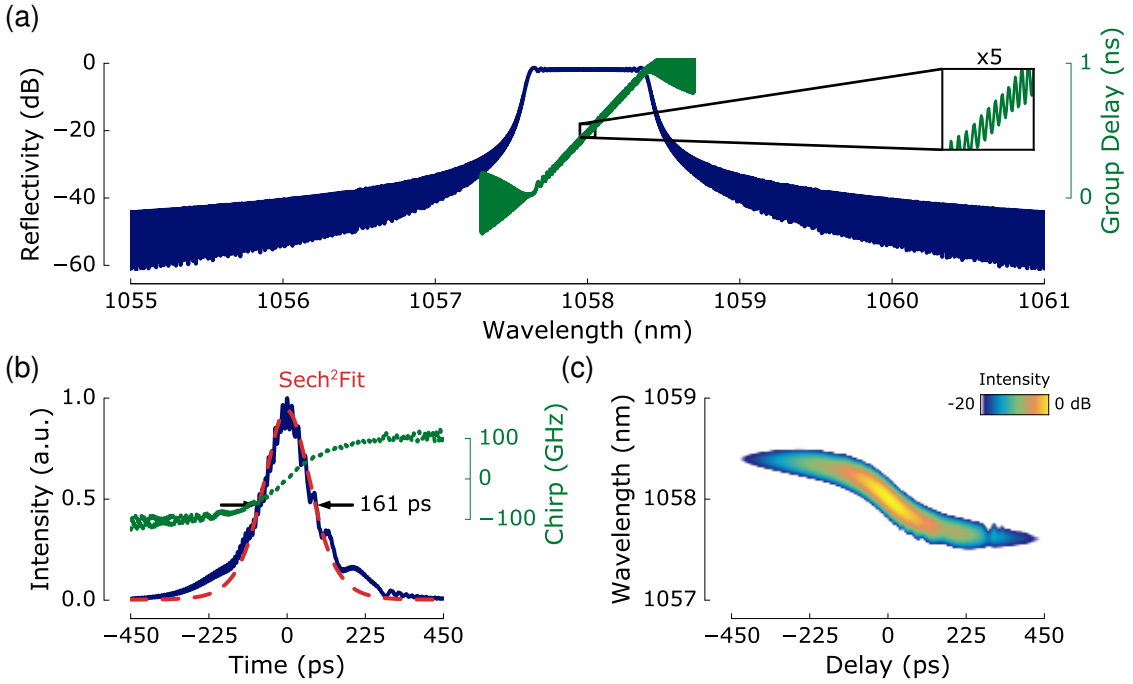


Fig. 3.21: Simulated giant-chirped pulse compression with CFBG-1: (a) grating reflectivity and group delay; (b) reflected pulse profile; (c) reflected pulse spectrogram.

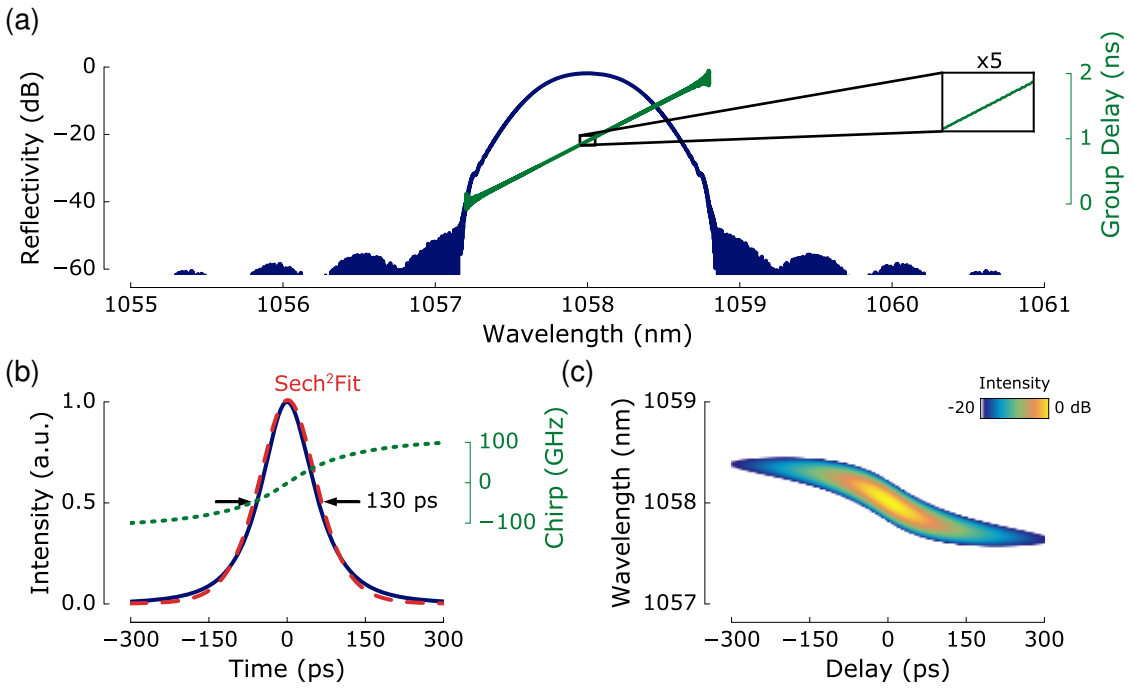


Fig. 3.22: Simulated giant-chirped pulse compression with CFBG-2: (a) grating reflectivity and group delay; (b) reflected pulse profile; (c) reflected pulse spectrogram.

across the reflection bandwidth. However, while the central region of the long-cavity laser pulses were linearly chirped, curvature of the spectrogram was noticeable towards the edges. It should also be noted that the optimum properties corresponded to an induced delay between the long and short wavelength components (0.82 nm apart) of 1.37 ns, using Eqn. 3.3.4. This value was almost equal to the FWQM duration of the original pulses. It can be understood that using the FWQM to define the required CFBG delay, rather than the FWHM delay we initially specified, gives better compression since the pulse spectrum was spread over a greater part of the pulse than contained within the middle sections of amplitude greater than half the maximum. These simulations confirmed that a grating-based compression technique should be able to achieve ultrashort pulses, and paved the way to an improved CFBG specification to realise this experimentally.

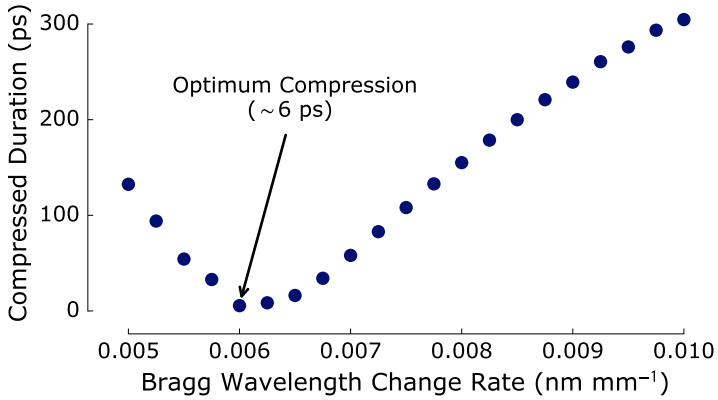


Fig. 3.23: Impact of CFBG Bragg wavelength change rate on the compressed pulse duration, determined from numerical simulations.

3.3.3 Improved Experimental Compression

A new grating was fabricated based on the optimum specification determined from numerical modelling (CFBG-3), and integrated into the compression setup at port 2 of the circulator. After stretch-tuning the length to ensure the pulse spectrum was within the grating reflection band, the reflected signal showed highly compressed pulses on a streak camera (Fig. 3.26a). The streak camera measurement was resolution-limited, necessitating the use of an intensity autocorrelator to determine the compressed width. The autocorrelation trace showed a reasonably high-quality pulse, fitted by a sech^2 profile with a width of 17 ps, which deconvolved to give a FWHM pulse duration of 11 ps (Fig. 3.26b).

The giant-chirped pulses have been compressed by a factor of $\sim$100. The reflectivity of the grating was measured to be $\sim$70%, suggesting that this compression resulted in $\sim$70 times peak power enhancement. A larger pedestal than expected from simulations was observed, due to uncompensated nonlinear chirp, although it was calculated that more than 70% of the energy was within the pulse. Additionally, the factor of two difference

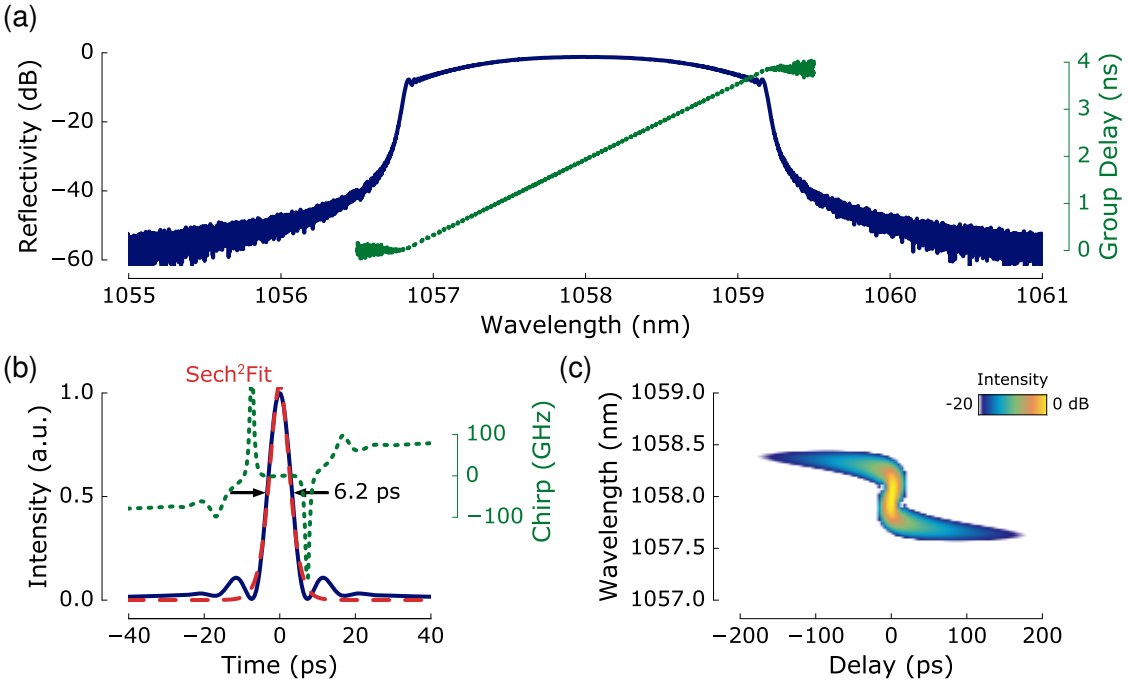


Fig. 3.24: Simulated giant-chirped pulse compression with CFBG-3 (optimised grating specification): (a) grating reflectivity and group delay; (b) reflected pulse profile; (c) reflected pulse spectrogram.

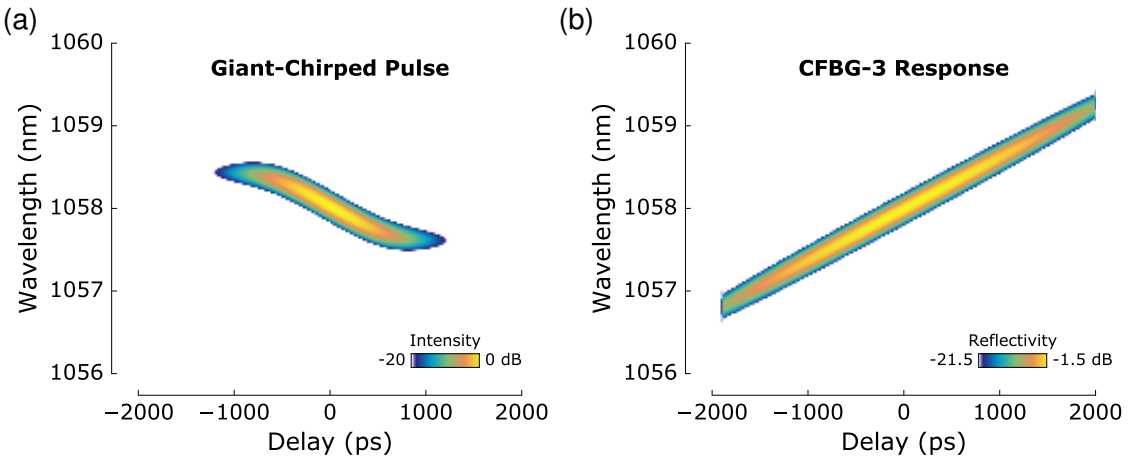


Fig. 3.25: Comparison of simulated spectrograms for (a) giant-chirped long-cavity laser output pulses and (b) CFBG-3 response.

between the measured compression factor and the numerical modelling could be due to small manufacturing imperfections during grating fabrication. The pulse spectral width was unchanged by the compression (Fig. 3.26c) confirming that this was a linear compression scheme.

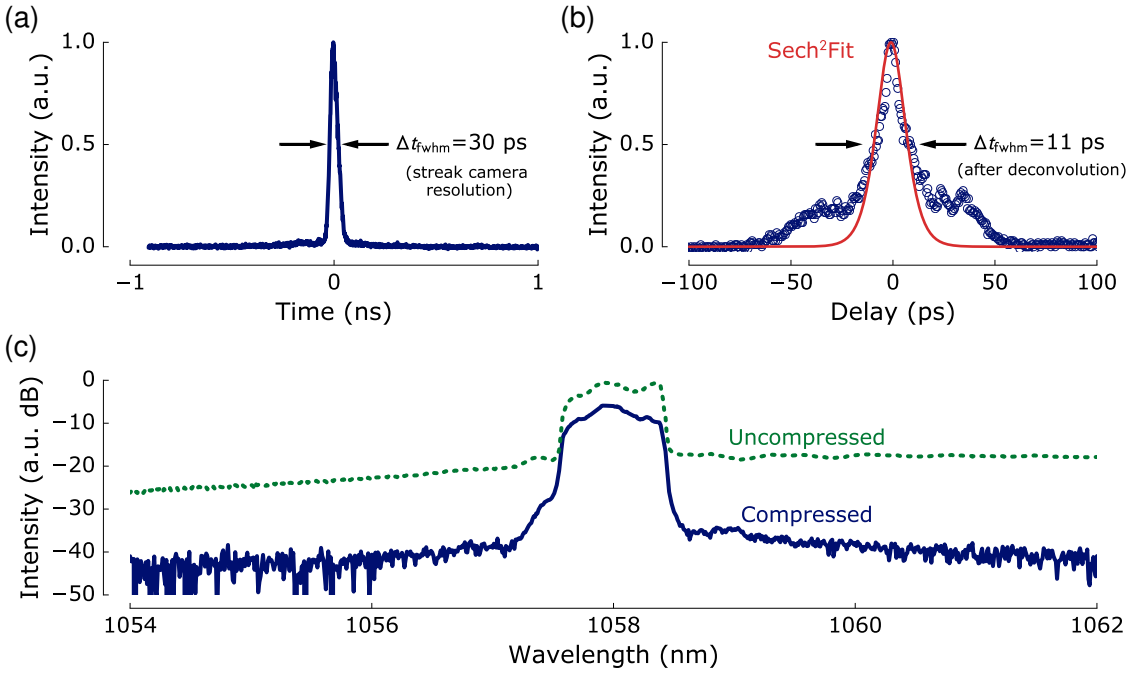


Fig. 3.26: Experimental giant-chirped pulse compression with CFBG-3: (a) resolution-limited streak camera trace and (b) autocorrelation trace of reflected pulses; (c) pulse spectrum before and after compression.

3.4 Supercontinuum Generation with Long-Cavity Lasers

We have demonstrated that long-cavity lasers can be sources of highly-chirped compressible pulses for simple and compact chirped pulse amplification systems. Additionally, compared to conventional mode-locked fibre lasers at megahertz repetition rates, the low kilohertz pulse repetition frequency enables higher peak-power-to-average-power ratios, which permit the exploitation of nonlinear effects with only moderate amplification. One such application is supercontinuum generation.

3.4.1 Introduction to Supercontinuum Generation

Supercontinuum generation is a process where the spectrum of light is significantly broadened to cover a wide spectral bandwidth with high spatial coherence, arising from a cascade of nonlinear optical effects. While numerous reports in the historical literature observed nonlinear spectral broadening, it is commonly accepted that the first supercontinuum, spanning 400 to 700 nm, was demonstrated by Alfano and Shapiro in 1970 in bulk

borosilicate glass [Alf70].[8] More recently, the development of PCFs has heralded new opportunities for supercontinuum generation in these highly nonlinear dispersion-tailorable fibres [Ran00].

Briefly, there are three main regimes for supercontinuum generation in fibre [Dud06]:

- **Anomalous dispersion with short-pulse pumping** – Short pulses that correspond to low-order solitons (typically, soliton order $N < 15$ and durations < 100 fs) undergo temporal compression and spectral broadening in the initial propagation stages. However, rather than breathing and returning to the original properties after travelling a distance corresponding to the soliton length, perturbations such as higher-order dispersion and Raman scattering alter the dynamics, leading to the break-up of the pulse into N fundamental solitons (soliton *fission*). Raman self-frequency shift of these solitons leads to further broadening of the long-wavelength edge, and the short-wavelength edge is pushed out by dispersive waves through resonant energy transfer from the Raman solitons, across the ZDW.

- **Anomalous dispersion with long-pulse / quasi-CW / CW pumping** – Long pulses (typically $N > 15$ and > 1 ps duration), very broad pulses (nanosecond and microsecond timescales, known as quasi-CW) and CW light will experience broadening dominated by modulation instability. This generates sidebands about the pump and splits the field into many fundamental solitons, which then continue to broaden the spectrum by the same Raman self-frequency shift and dispersive-wave processes described for the short-pulse case. Since modulation instability is noise-seeded, the temporal coherence of such supercontinua is very low.

- **Normal dispersion** – Soliton dynamics are absent in normal dispersion environments. Here, short high-peak power pulses generate spectral bandwidth by self-phase modulation, leading to supercontinua with high temporal coherence. Longer pulses and CW fields experience stimulated Raman scattering, pushing the spectral edge through a cascade of Stokes lines, potentially with further broadening through four-wave mixing.

In reality, these regimes are not discrete and the difference between short and long pulses is not clearly defined. The magnitude of dispersion is also a major contributing factor to the dynamics. However, this categorisation helps to broadly describe the different ways that a cascade of nonlinear processes can lead to extreme spectral broadening.

Fibre-based supercontinuum sources have rapidly transitioned from research curiosities to commercial products, with a wide range of applications including as an illumination source in fluorescence imaging and for broadband spectroscopy, in addition to frequency comb generation. We believe that the long-cavity laser architecture could be advantageous for generating low-average-power supercontinua: creating a broad spectrum of light

[8] Early publications referred to this effect as *anomalous frequency broadening* or *white light generation*; it was not until 1980 that the term *supercontinuum* was coined [Ger80].

without the cost and complexity of high-power components and amplifiers. This is made possible by the low repetition rate, leading to greater pulse energy and peak power for a given average power.

Kobtsev et al. recently demonstrated a similar concept, reporting a 500-1750 nm supercontinuum source by pumping a length of anomalously-dispersive PCF with an ultra-long 8 km mode-locked fibre laser. However, the laser was operating in a noise-burst regime, producing incompressible 10 ns pulses and consequently, amplification up to 3 W average power was required [Kob10]. Other approaches to low-threshold supercontinuum generation include Q-switched fibre pulse sources [Che97b], which operate at tens of kilohertz repetition rates and nanosecond to microsecond pulse durations. For higher peak powers, shorter pulses are required, but are limited by the length of fibre needed for a Q-switched fibre cavity. Microchip lasers, which are monolithic solid-state devices with a gain crystal sandwiched between two mirrors, can provide shorter (ps) Q-switched pulses due to the reduced cavity length, enabling low-pump-power supercontinua [Sto08]. However, microchip laser sources require their free-space output to be focussed into the PCF, losing the alignment-free, turn-key operation benefits of an all-fibre system. Therefore, compressed picosecond pulses from our mode-locked long-cavity laser could be an alternative pump format for enabling spectral extension without such significant amplification. Such sources could be cost-effective, compact tools for optical characterisation of components.

3.4.2 Experimental Setup and Results

The 11 ps duration of the compressed long-cavity laser pulses suggested that spectral broadening dynamics in the anomalous dispersion regime would be modulation instability-driven. We chose to pump at an anomalously dispersive wavelength rather than in a normally dispersive environment as this can enable broader continuum generation (otherwise, without solitonic shaping effects, pulses quickly broaden and the peak power reduces, limiting further broadening in the normal dispersion regime), although at a cost of lower temporal coherence. For optical device characterisation applications, a broad spectral width is more important than the source coherence. To maximise modulation instability-driven spectral broadening, pumping close to the ZDW is also preferable to minimise the duration of fundamental solitons which develop from the input pulse [Dud06]. For this reason, we chose to pump a PCF with a ZDW at 1040 nm.

The experimental setup for supercontinuum generation is shown in Fig. 3.27. A low-power ($<$ 100 mW) ytterbium-doped fibre amplifier was included before the circulator, to raise the energy of chirped pulses and to overcome the loss introduced by the circulator ($\sim$0.5 dB per pass) and the 70% reflectivity of the CFBG ($\sim$1.5 dB loss). Spectral and temporal pulse properties were preserved during amplification. The circulator output (port 3) was fusion-spliced to a 30 m length of solid-core PCF with 1.47 μm hole diameter, 3.20 μm pitch and $\sim$4.9 μm core diameter (Fig. 3.27 inset). To achieve a reasonably low-loss splice between Flexcore fibre and the PCF, a splice-optimisation programme was followed

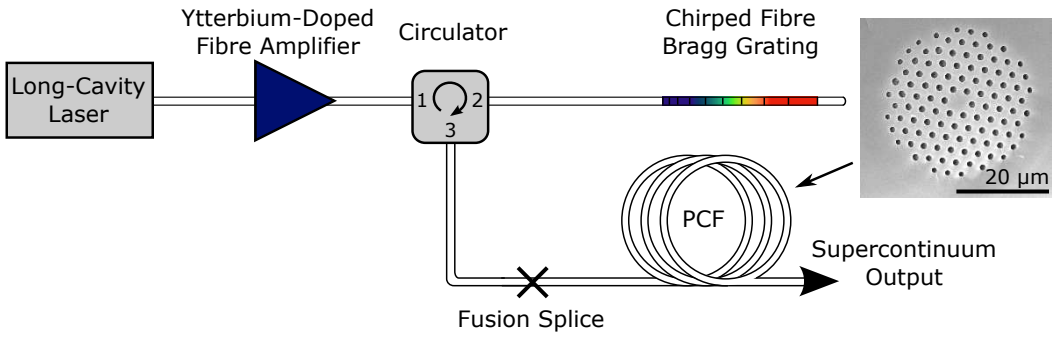


Fig. 3.27: Schematic for supercontinuum generation in PCF with compressed long-cavity laser pump pulses.

to determine the optimum fusion time and current; the lowest loss obtained was ∼0.65 dB.

As the pulse energy launched into the PCF was increased, the spectrum rapidly broadened (Fig. 3.28). For an average launch power into the PCF of only 30 mW (taking into account circulator and splice losses), a supercontinuum was observed spanning from ∼550 nm to 2050 nm; just under two octaves of spectral content. On the long wavelength side, there was less than 10 dB intensity variation between 1100 and 2000 nm. The feature at ∼1380 nm is related to water loss in the fibre, and ∼1750 nm indicates the transition between data recorded on an optical spectrum analyser (5 nm resolution) and longer wavelength data measured with a spectrometer (22 nm resolution).

Spectral sidebands on the pump were observed during the early evolution of the continuum with increasing pump power, which are a signature of modulation instability. At 30 mW average pump power, the pulse energy was ∼125 nJ, corresponding to a peak power of ∼10 kW. Therefore, from the PCF parameters (β_2 ∼-2 ps^2 km^{-1} and γ ∼11W km^{-1} at 1058 nm), we estimated the soliton order as N ∼1400. This clearly corresponded to the long-pulse pumping regime, and hence, modulation instability-initiated supercontinuum dynamics were expected. Further increase in pump power was limited by the amplifier (a small low-power device was deliberately chosen to demonstrate that the concept could work for low cost, compact components). However, as the power increased, the rate of spectral extension decreased, due to the sharply rising silica loss beyond ∼1.8 µm . Consequently, it is expected that even with higher pump powers, the supercontinuum could not extend beyond ∼2400 nm. If this was a requirement, however, alternative glasses could be considered, such as chalcogenide fibres, which can have transmission windows up to 25 µm [Pet14].

3.4.3 Simulation and Discussion

To gain further insight into the spectral broadening dynamics, we numerically simulated the propagation of our compressed pulse field through the PCF (modelling methods described in Section 2.3). The compressed field (Fig. 3.24b) was used as the input, scaled to a peak power of 10 kW as in the experiment.

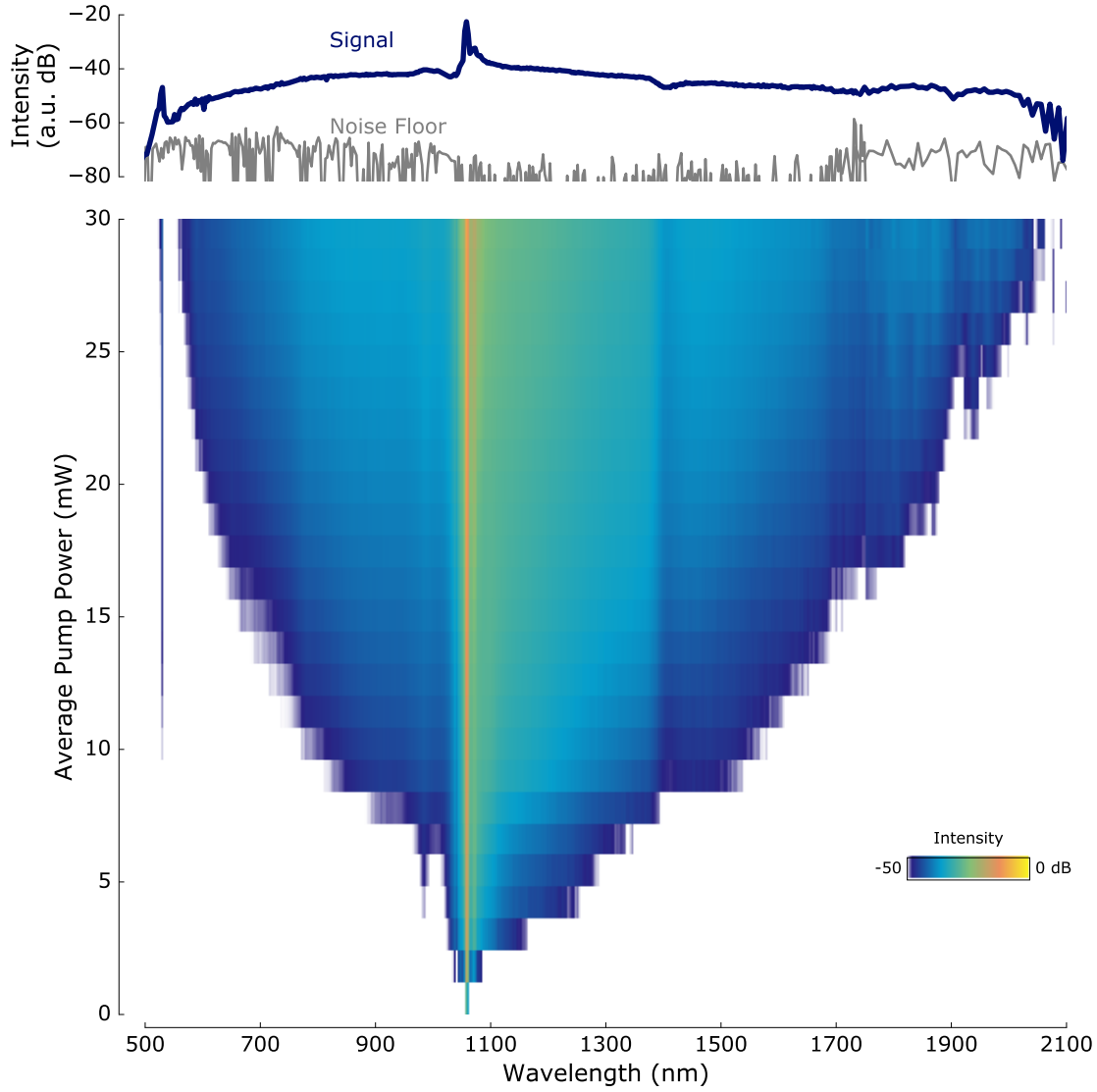


Fig. 3.28: Experimental supercontinuum generation in PCF pumped by compressed long-cavity laser pulses, showing the spectral evolution with average pump power and the spectrum at 30 mW pump power (∼10 kW peak power).

Fig. 3.29 shows the simulated spectral evolution along the length of the PCF and the output spectrum. The simulation shows many of the features of the experimental supercontinuum, with a reasonable reproduction of the spectral extent and flatness. However, it should be noted that the simulation corresponds to a single shot measurement, compared to experimental measurements on an optical spectrum analyser that are averaged over many shots within the device integration time on millisecond timescales (resolution is also a limiting factor, so the simulated field was first convolved with a 5 nm Hanning window to model this effect). Therefore, while defined peaks are visible at the long wavelength edge of Fig. 3.29 corresponding to self-frequency shifting Raman solitons (discussed in the next paragraph), the exact spectral position of these peaks is noise-dependent and will vary on a shot-to-shot basis. Consequently, these features were averaged out when viewed experimentally. Since the model appears to have reproduced the major spectral features of the measured supercontinuum, we can use it to examine the underlying nonlinear dynamics.

Rapid spectral broadening occurred in the first 1 m of the fibre. The evolution, temporally and spectrally, in this region is shown in detail in Fig. 3.30, in addition to spectrogram representations of the field at salient points during the evolution in Fig. 3.31. The 1058 nm pump pulse (Fig. 3.31 top left) experienced weak anomalous dispersion in the PCF. Consequently, a power-dependent phase-matching condition governed the position of spectral sidebands, which grew from energy transfer by a four-wave mixing process (Fig. 3.31 top right) involving the annihilation of two pump photos to create Stokes and anti-Stokes photons. The process was seeded from noise. Sideband intensities increased with propagation distance, leading to a breakdown of the temporal field into fundamental solitons (Fig. 3.31 bottom left). Such solitons were much shorter than the input pulse and possessed greater peak powers, according to the soliton area theorem (Eqn. 1.3.20). This confirmed modulation instability as the supercontinuum initiation process, leading to numerous interlinked processes that occurred simultaneously to gradually push the spectral extents of the supercontinuum along the remainder of the fibre.

Firstly, the short duration of the fundamental solitons resulted in broad bandwidths (exceeding 13.2 THz) such that the long-wavelength edge of the soliton experienced Raman gain, pumped by the short-wavelength edge. This induced a shift towards longer wavelengths, known as *soliton self-frequency shift* [Dia85, Mit86]. Due to the spectral-dependence of group velocity and effective area in the fibre, the red-shifting solitons decelerated (shown by the arcing shape in Fig. 3.31). The presence of solitons travelling at different velocities inevitably led to *collisions* too, transferring energy to the higher-energy soliton, which caused pulse narrowing and spectral broadening, followed by further Raman self-shifting to longer wavelengths [Isl89].[9]

Solitons with a bandwidth spanning to less than the ZDW can emit energy into the

[9] The growth of a small number of extremely high-energy pulses after many collisions is also occasionally interpreted in the context of rogue wave generation [Sol07], for drawing parallels between supercontinuum generation in fibre and other nonlinear systems.

normal dispersion regime in the form of *dispersive waves* (also known as *non-solitonic radiation*). Cross-phase modulation and four-wave mixing coupled the dispersive wave to the red-shifting soliton, inducing a blue-shift of the dispersive wave. This is shown clearly in Fig. 3.31 (bottom right), with an intense soliton co-propagating with a 'trapped' dispersive wave: the intense soliton modified the local refractive index, creating a potential which prevented walk-off of the dispersive wave. Four-wave mixing pumped by light in the normal dispersion regime, with sidebands at the blue and red edges also broadened the spectrum. Since the four-wave mixing could be pumped with wavelengths within a wide range, there is a broad net gain bandwidth, which leads to spectrally flat supercontinuum. The limit to spectral extension is believed to be sharply increasing loss from IR absorption on the long-wavelength side; when the simulation was repeated without loss, the long-wavelength edge extended further to $\sim$2300 nm.

Our simulation has highlighted the rich nonlinear dynamics involved in the generation of a supercontinuum from the compressed long-cavity laser pulses. The rapid initial broadening to $\sim$1900 nm was complete by $\sim$3 m, indicating that significantly shorter lengths of PCF could be used, depending on the required bandwidth of device characterisation applications. Additionally, the four-wave mixing process could be further optimised for extension to shorter wavelengths by tailoring the dispersion of the PCF or using a fibre taper with gradually varying properties [Kud06]. However, this experiment has confirmed the benefit of the low repetition rate long-cavity laser design for supercontinuum generation at a low threshold.

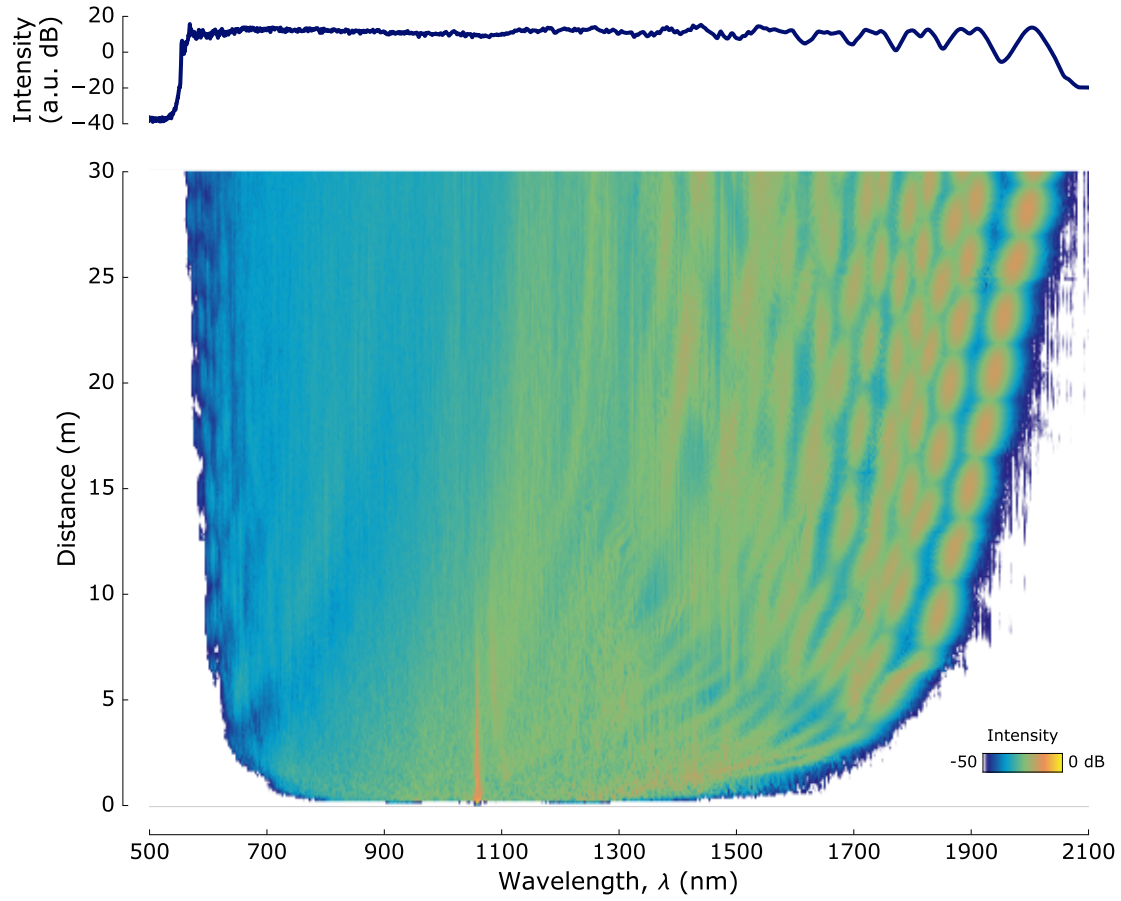


Fig. 3.29: Simulated spectral evolution and final spectrum of supercontinuum in PCF pumped by 10 kW peak power compressed long-cavity laser pulses. Note that this is a different vertical axis to Fig. 3.28, where we plotted the evolution with increasing pump power.

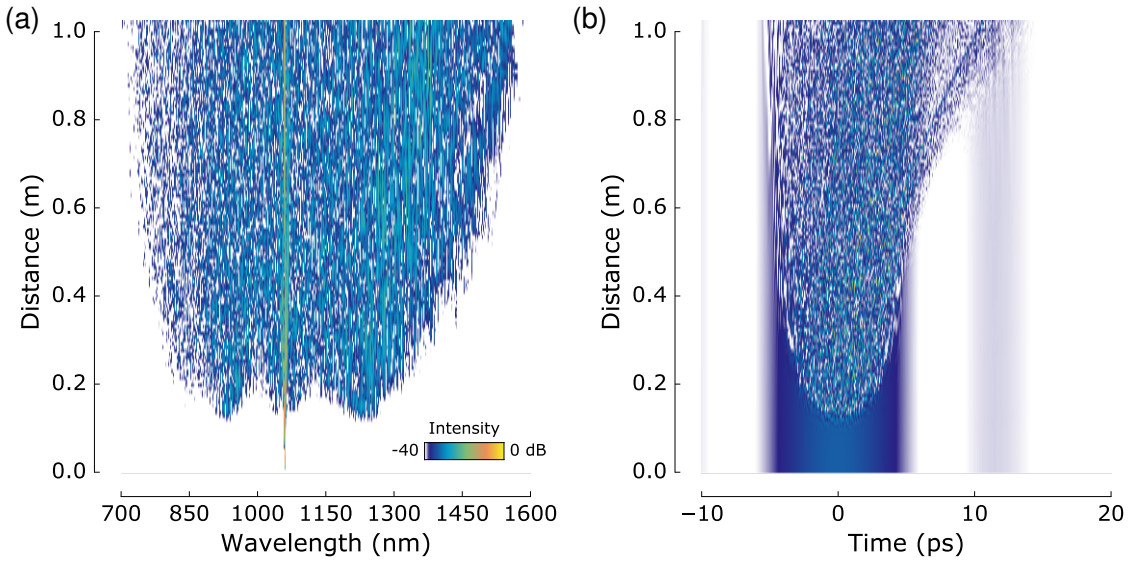


Fig. 3.30: Simulated (a) spectral and (b) temporal evolution in the first 1 m of PCF pumped by 10 kW peak power compressed long-cavity laser pulses.

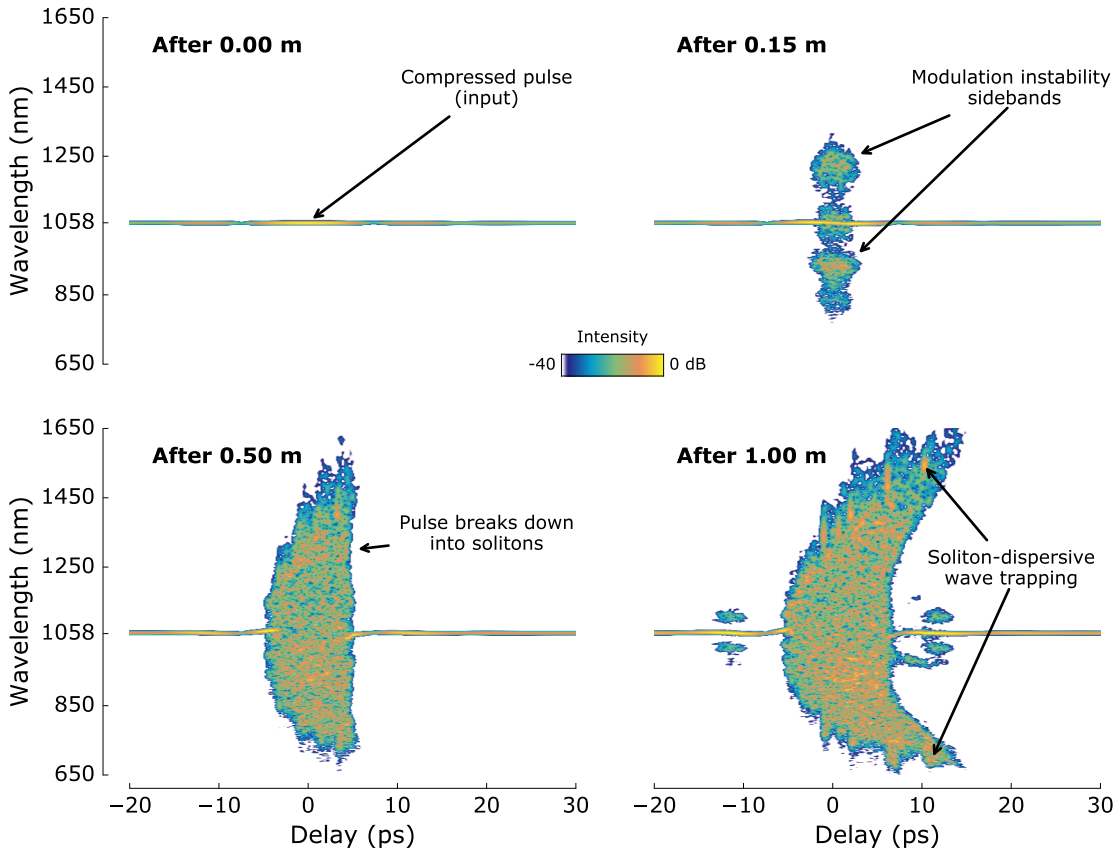


Fig. 3.31: Spectrograms showing the initial evolution of the simulated supercontinuum at salient positions along the PCF.

3.5 Radiation Build-Up Dynamics

In addition to the practical applications of long-cavity mode-locked lasers as low-repetition-rate pulse sources, these systems present an interesting platform for fundamental studies of the underlying nonlinear wave dynamics. Numerous reports have already unveiled a wealth of nonlinear physics within mode-locked fibre resonators including rogue waves [SC11], optical turbulence [Kär99, Tur09], soliton explosions [Cun02, Run15], and the manifestation of self-organisation effects to support a variety of localised bright and dark soliton structures [Str05, Chu15, Kel14]. Fibre lasers are just one example of nonlinear dispersive systems that can be described in the framework of a NLSE, however, also including hydrodynamics and Bose-Einstein condensates. Therefore, these lasers provide a convenient table-top platform for exploring such dynamics, which could offer insight into other physical systems.

While simulating our long-cavity laser (described in Section 3.2.2), we observed dark soliton-like structures as the laser turned on, which persisted for hundreds of round trips before decaying to leave a coherent pulse. In this section, we explore the radiation build-up dynamics in detail and consider the interaction of dark solitons with each other and the bright pulse background, in addition to the implications of such dynamics for laser applications and other nonlinear systems.

3.5.1 Introduction to Dark Solitons

We begin by briefly reviewing theoretical concepts and experimental observations of dark solitons in optical fibres. In Section 1.3.4, solitary wave solutions of the NLSE in anomalously dispersive fibre with nonlinearity[10] were introduced, known as *bright* solitons [Zak72, Has73a]. In the presence of normal dispersion, bright solitons are not supported and pulses will broaden temporally and spectrally as they propagate. There are, however, a class of solitary wave solutions to the NLSE in normal dispersion, which manifest as intensity dips known as *dark* solitons [Zak73, Has73b].

The fundamental (N=1) dark soliton is an anti-symmetric function which appears as an intensity-dip on a CW background, with zero intensity and an abrupt π phase jump at the centre [Tay92]. Specifically, this is a *black* soliton and dark pulses can also exist with non-zero intensity at the centre and a gradual and weaker phase shift, referred to as *gray* solitons (Fig. 3.32a). Physically, intensity dips can be explained by considering the CW background as plane waves and noting that the phase jump results in destructive interference between phase shifted plane waves on each side of the soliton [Zak98]. For total destructive interference, i.e. an intensity dip to zero (black soliton), a π phase shift is clearly required.

[10] We implicitly assume positive (focussing) nonlinearity here, which is always the case for fibres. The situation would be reversed for defocussing nonlinearity [Kiv98].

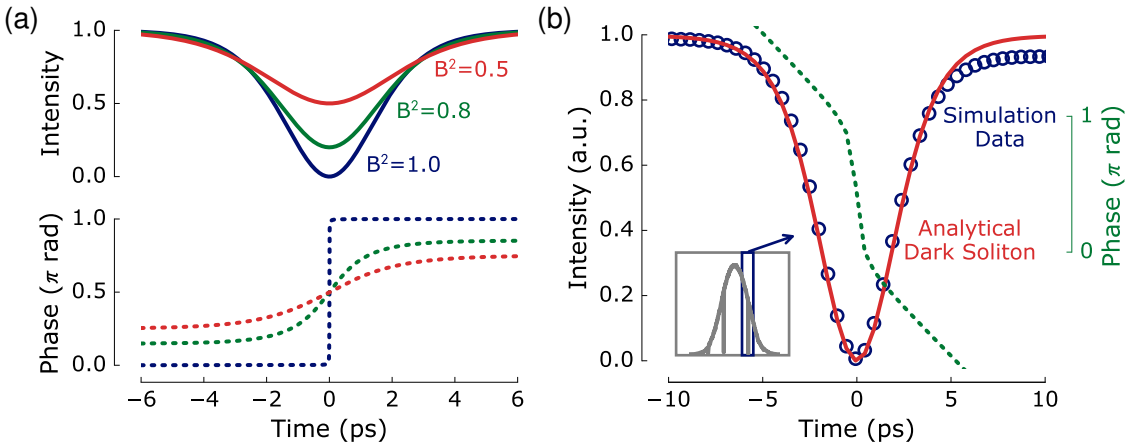


Fig. 3.32: Dark solitons: (a) analytical intensity and phase profiles for varying blackness; (b) portion of long-cavity laser simulation pulse (highlighted in inset) at round trip 940 (as originally shown in Fig. 3.6a) showing that the intensity dip is well-fitted by a black ($B = 1$) soliton profile and the dip corresponds to a $\sim\pi$ phase jump.

The profile of a dark soliton is given by [Tom89]:

$$A(t) = A_0\sqrt{B^{-2} - \text{sech}(t/t_0)^2} \times \exp[i\phi(t/t_0)] \tag{3.5.1}$$

where A_0^2 is the intensity dip and B is the blackness parameter ($0 \leq |B| \leq 1$) defining the ratio of the dip minimum to the background, such that the background power level (measured in watts) is $(A_0/B)^2$. The $1/e$ duration of the soliton is related to the fibre parameters by:

$$t_0 = \sqrt{\frac{N^2\beta_2}{A_0^2\gamma}} \tag{3.5.2}$$

and the phase is:

$$\phi(t/t_0) = \sin^{-1}\left(\frac{B\tanh(t/t_0)}{\sqrt{1 - B^2\text{sech}^2(t/t_0)}}\right) \tag{3.5.3}$$

The time-dependent phase shift results in significantly different behaviour to bright solitons, which have a constant phase. Notably, dark solitons do not form bound states nor exhibit periodic evolutions – higher-order dark solitons (and indeed, high-power dark pulses generally) will evolve into a fundamental dark soliton and dispersing gray solitons [Tay92].

Due to the complexity of generating dark soliton waveforms compared to bright pulses, it was not until 1987 that dark soliton propagation was observed experimentally [Emp87, Kro88, Wei88a]. These demonstrations created dark solitons on a background pulse – an approach which could be questioned, as to rigorously satisfy the soliton condition a CW background is required, rather than one of finite-extent. It was later shown, however, that bright background pulses only ten times wider than the dark soliton were sufficient for adiabatic dark soliton propagation to be observed, even in the presence of the bright

pulse spreading out and developing a chirp from propagation in normally dispersive fibre [Tom89, Kiv94].[11] While dark soliton evolution does not depend on the background phase, the motion of these pulses was found to affected by the local background intensity gradient [Gre90].

More recently, reports have emerged of dark pulse mode-locked lasers emitting trains of dark solitons [Zha09, Syl02], supported by numerical investigations [Abl11]. On a practical level, it has been suggested that dark solitons provide advantages over bright solitons for high-bandwidth long-distance communications, as dark solitons are less affected by noise and timing jitter [Zha89, Nak95], and they could even be leveraged to develop steerable optical waveguides [LD92, Dia95].

To explore the dark pulses we observed in our long-cavity laser simulations, we overlaid the intensity-dip structures with the analytical function describing a dark soliton in Flexcore fibre (Fig. 3.32b). The high quality of the fit and $\sim\pi$ phase step across the centre of the dark pulse affirm its designation as a dark soliton solution to the NLSE. Having confirmed our hypothesis that dark solitons exist in the radiation build dynamics, we then studied their evolution and interaction in more detail.

3.5.2 Dark Soliton Creation and Decay

The laser simulation was executed many times, starting from different randomised shot noise fields. Each time, the simulation converged to the same steady state, although the build-up dynamics and the number of round-trips required for the pulse to display negligible iteration-to-iteration changes was found to vary. Borrowing terminology from nonlinear mathematics: the laser design and cavity component parameters established the basin of attraction, creating a fixed-point attractor (the stable giant-chirped pulse) towards which all suitable initial conditions converged.

From turn-on, in the first few round-trips the shot noise field experienced strong amplification, growing in intensity at all time positions in the simulation window. The effect of the saturable absorber and gain saturation localised energy within a temporal envelope, which evolved towards a bright coherent pulse as internal envelope structure decayed. In this section, we focus on this transient regime between the initial noisy state and the coherent bright pulse, where dark solitons spontaneously formed from noise fluctuations and propagated within the bright pulse envelope over many hundreds of round trips before decaying.

Creation

Although unexpected, it is not surprising that dark solitons were observed: noise perturbations created intensity dips, which evolved into dark solitons in the presence of normal

[11] Strictly, these dark pulses on a finite background are not solitary-wave solutions to the NLSE – i.e. they are not eigenvalues of the field after an inverse scattering transform [Zak73, Gre90]. However, since the quasi-stationary dark pulses numerically and experimentally retain the properties and behaviour of dark solitons, we shall continue to refer to them as such.

dispersion since these are the stable solutions to the NLSE [Zak73]. This is analogous to arbitrary bright waveforms converging towards soliton solutions in the anomalous dispersion regime [GN89], although dark soliton generation is thresholdless and thus occurs more readily [Gre90].

It is interesting, however, that dark solitons existed for hundreds of round-trips in the radiation build-up dynamics of a bright coherent pulse and then decayed. Our simulations considered a non-conservative system, including periodic gain, loss and with Raman, shock and higher-order dispersion terms included. The temporal evolution plots (e.g. Fig. 3.6a) were constructed by stacking the field intensity arrays at the laser output for many consecutive round trips (each iteration corresponded to a propagation distance of $\sim$840 m). We therefore observed the motion and interaction of these dark features over hundreds of kilometres of fibre propagation. This is a novel situation: if we attempt to realise this in a conservative system along 100 km fibre with a dark soliton upon a bright pulse, the bright pulse would simply dispersively broaden and the gradient (and amplitude) of the pulse wings would be constantly changing. In our laser, however, the saturable absorber compensated broadening and the gain compensated losses, maintaining an almost constant bright pulse envelope around the whole cavity (as verified in Fig. 3.7).

To gain further insight, we reduced the cavity length to 120 m, which is still much longer than typical fibre lasers and permitted simpler analysis of the dynamics. We performed 600 simulations and analysed the ensemble dataset to understand the underlying behaviour.

Tracking Algorithm

To quantify dark soliton motion, it was necessary to isolate the many dark solitons in each round trip and to track their movement over the whole simulation. We developed a two-part algorithm for this purpose.

First, we searched for all dark soliton structures in the time-series data of each completed simulation. To ignore trivial noise fluctuations in the initial region, the search was commenced when the envelope width of the radiation was less than half the extent of the simulation time window. Since dark solitons possess a characteristic phase change across the pulse, we identified qualifying dark structures in each round trip by differentiating the phase of the temporal field and applying a peak detection routine. The process searched through all round trips within each full simulation dataset, identifying and storing all spatiotemporal locations of dark soliton structures to a separate array.

Secondly, the reduced dataset was re-processed to correlate structures that exhibited temporal coherence from round trip to round trip (i.e. assigning all the data points to coherent dark soliton trajectories). This was implemented by enforcing causality and searching for dark soliton structures in consecutive round trips that lay within a given time delay tolerance. When found, it was assumed that the dark solitons in adjacent round-trips were following a continuous path. If a dark structure could not be found in future round trips, it was deemed to have disappeared; if a structure was identified with

no correlation to the previous round trip, it was recorded as a new dark soliton. This process repeated until all dark solitons in the reduced dataset had been assigned to a trajectory, which enabled us to track how they moved through the bright pulse envelope.

Fig. 3.33 shows a section of a processed evolution for a 120 m cavity, where the coloured dots indicate dark soliton trajectories; visual inspection of the processed dataset and original simulation suggested that the algorithm correctly identified and tracked the dark structures.

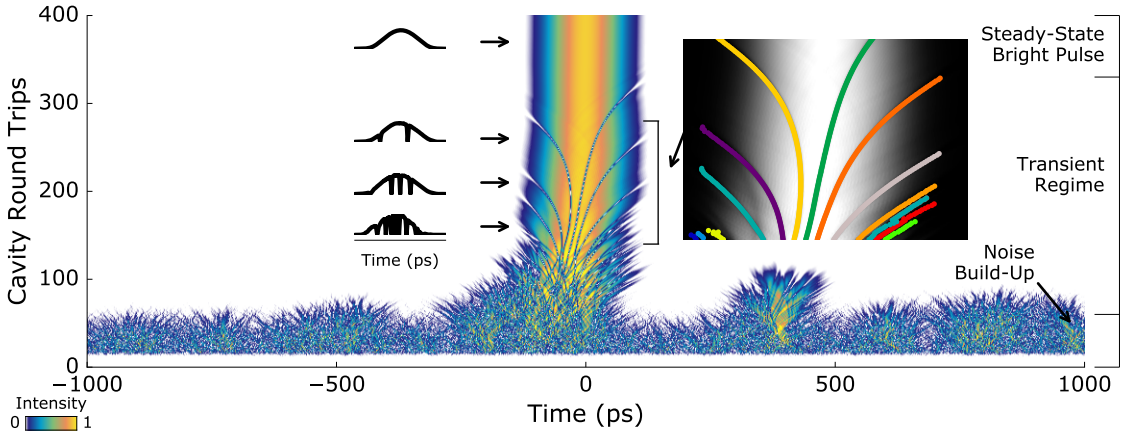


Fig. 3.33: Temporal evolution of radiation build-up in 120 m long-cavity mode-locked laser. Pulse profiles are shown as insets at various iterations and a magnified region of the evolution is shown with the tracked dark solitons overlaid as coloured trajectories.

Decay

Our basic observation of dark soliton decay refers to the intensity-dip travelling at a different group velocity to the background pulse, resulting in walk-off as it moves out of the bright envelope.

This behaviour is expected for gray ($|B| < 1$) solitons, since the slope of the phase profile (and thus, the instantaneous frequency) varies with B, changing their relative velocities [Kiv98]. Therefore, gray solitons always decay by moving out of the envelope, with 'paler' solitons travelling quicker and thus decaying faster. The phase of black solitons, however, determines that they should propagate at the same velocity as the background. In our simulations, the majority of dark structures that formed were black solitons, or at least dark grey ones (which moved very slowly relative to the envelope). Therefore, we must consider how these decay.

One explanation is due to the shape of the background. Since this was a bright pulse envelope, many dark solitons existed in the envelope wings, on a sloped background intensity. Kivshar and Yang proved that such an intensity gradient imparts a phase upon any dark solitons it contains, resulting in a gradient-dependent velocity change of the solitons relative to the background group velocity [Kiv94].

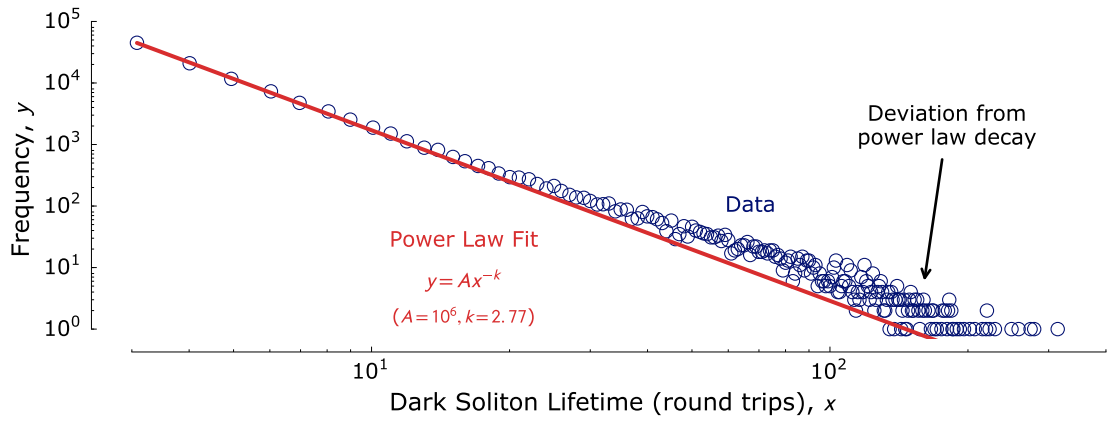


Fig. 3.34: Histogram showing that the frequency of dark soliton occurrence decreased with increasing soliton lifetime. A small number of long-lived dark solitons were observed, deviating from the expected power law decay behaviour. To create this plot, dark soliton trajectories were identified using the tracking algorithm, the lifetimes (number of round trips in each trajectory) were computed and then binned.

Therefore, dark solitons created within our bright pulse experienced a continually changing slope, and thus, changed group velocity as they moved. At the pulse peak, black solitons travelled at the same speed as the bright pulse (exhibiting quasi-stationary behaviour) and hence, should not have decayed. The peak was an unstable equilibrium point, however. Perturbations (e.g. gain, loss or small deviations from black ($B = 1$) behaviour) therefore triggered a dark solitons at the peak to begin its descent.[12] Once solitons began moving down the wings, they were accelerated, leading to the curved trajectories seen in Fig. 3.33 and ultimately, to their disappearance.

Lifetimes

After applying our tracking algorithm to the ensemble of 600 simulations, we analysed the aggregate data to study the dark soliton lifetimes, defined as the number of round trips between spontaneously forming and moving out of the background pulse. It is common to attempt to describe distributions of noise-driven transient dynamics with a power law. We computed a histogram for the soliton lifetime with a bin size of 1 round trip and fitted a power law of the form, $y = Ax^{-k}$ with scaling factor A and power k to the data (Fig. 3.34).

The data shows that short-lived dark solitons occur much more frequently than persistent solitons with a long lifetime, and a heavy-tail distribution is observed. We fit the empirical data with a power law, which is widely used to describe decay in complex systems, in addition to appearing in a broad range of noise-seeded physical phenomena [Cla09]. The frequency y is, therefore, proposed to vary with soliton lifetime x as follows: $y = Ax^{-k}$, with normalization factor $A = 1 \times 10^6$ and exponent $k = 2.77$. For

[12] This situation is analogous to marbles on a hill. A marble can be stationary at the peak, but is unstable and a small perturbation can start it rolling downhill. Initially, it moves slowly but gains speed at it continues travelling down.

lifetimes shorter than approximately 50 round trips, the power law accurately describes the distribution. Significant deviation, however, is observed for longer lifetimes. This suggests that such persistent quasi-stationary solitons can be considered as rare events: phenomena which occur with an unlikely, but non-negligible, probability. Rare events are particularly interesting in nonlinear systems tending towards an attractor, helping to reveal aspects of the underlying dynamics, which could ultimately be controlled for practical exploitation [Dud14].[13] These observations pave the way for further work to quantitatively relate the soliton decay mechanisms to their lifetime and more generally, to contribute to understanding the underlying factors responsible for rare phenomena.

To relate the lifetimes to our discussion of decay mechanisms, we plotted a 2D histogram of lifetimes relative to the position of dark solitons spontaneously forming within the bright envelope (zero refers to the centre of the pulse). The long-lived solitons are seen to be clustered towards the pulse centre. This is commensurate with our argument: dark solitons that formed here experienced a shallow background intensity gradient and travelled at a speed very similar to the background, yielding a long lifetime.

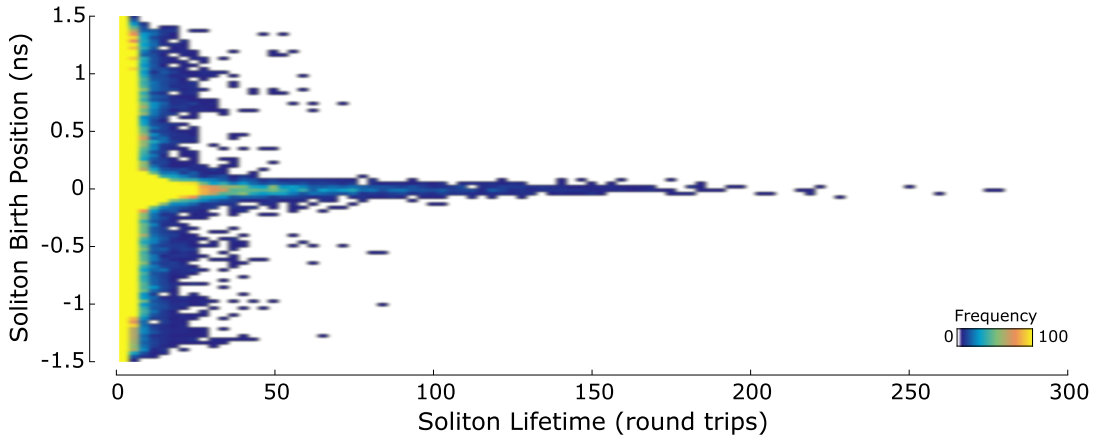


Fig. 3.35: Two-dimensional histogram showing the frequency of dark soliton lifetimes and the position at which they were spontaneously created within the bright pulse (centred at 0 ns). Long-lived dark solitons tended to be created near the centre of the background pulse.

3.5.3 Interactions and Collisions

Interactions between multiple dark solitons can also act as a destabilising factor that leads to their decay. While it has been shown (for a conservative system) that dark solitons collide elastically, they each experience a temporal shift from the interaction [Thu91].

[13] Much recent work has considered optical rogue waves, which manifest in modulation instability-driven supercontinuum as the rare occurrence of waves with significantly higher amplitude than the surrounding solitons. Studying such events has led researchers to identify signatures in the wave dynamics which precede an extreme-amplitude wave and could help predict their occurrence [Bir15]. If this understanding can be translated to ocean waves, the benefits in helping ships to avoid dangerous 'freak waves' could be significant.

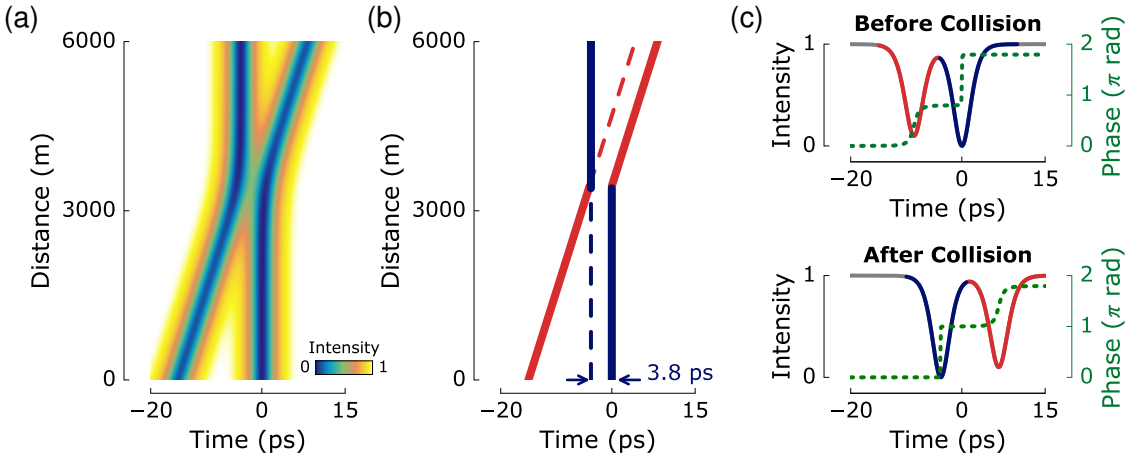


Fig. 3.36: Collision of black ($B^2 = 1$) and dark gray ($B^2 = 0.9$) solitons on a 1 W background in Flexcore fibre: (a) temporal field evolution; (b) illustration highlighting how the dark solitons pass through each other, undergoing a time shift but maintaining their direction; (c) pulse shapes and phase profiles before and after the collision (colour is used to define each soliton).

Therefore, dark solitons continue to propagate with an unchanged velocity after a collision, but their trajectory is slightly time-shifted.

We illustrate this in Fig. 3.36a by simulating a black and dark grey ($B^2 = 0.9$) soliton travelling on a CW background in Flexcore fibre. The black soliton is travelling at the velocity of the CW background and is on a constant trajectory, whereas the grey soliton is propagating more slowly. On collision, they experience a mutual time shift and then continue propagating along the same trajectory as before (highlighted by the illustration in Fig. 3.36b). The phase is also unchanged by the interaction, showing the same phase jump after the collision as before it (Fig. 3.36c).

The magnitude of the time shift is strongly dependent on the blackness of the interacting solitons. A greater B^2 value leads to a greater time shift, as shown in Fig. 3.37. We note that these dynamics have also been verified for dark solitons on backgrounds of a finite-extent [Thu91].

Interestingly, we were able to see these same patterns in the radiation build-up dynamics of our laser model. Within every simulation, the spontaneous generation of many dark solitons with different blacknesses and on different background slopes led to a wide range of soliton velocities – causing many collisions. These collision events can be seen in Fig. 3.33, and also in Fig. 3.38a that shows an additional laser turn-on evolution for the same simulation parameters.

For example, in the $\sim 220^{\text{th}}$ round trip, two almost-black solitons collided and moved through each other, experiencing time shifts (Fig. 3.38b). Other collisions between paler gray solitons were seen in the early dynamics (e.g. around 100 round trips) showing a smaller time shift. Our observations therefore suggest that the behaviour of dark soliton interactions in conservative systems can be extended to dissipative media with periodic gain and loss.

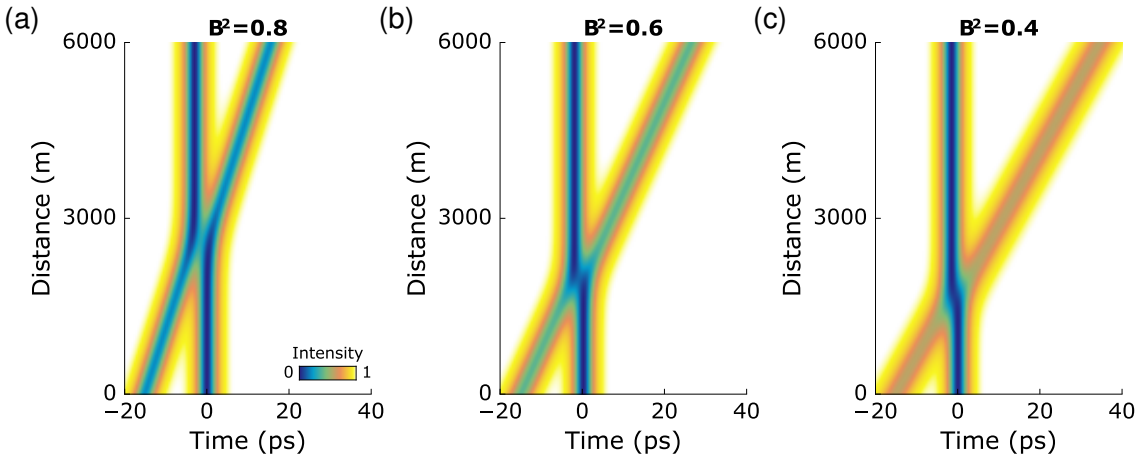


Fig. 3.37: Collision of a black ($B^2 = 1$) soliton on a 1 W background in Flexcore fibre with gray solitons possessing blackness parameters: (a) $B^2 = 0.8$; (b) $B^2 = 0.6$; (c) $B^2 = 0.4$. Darker solitons lead to larger time shifts when colliding.

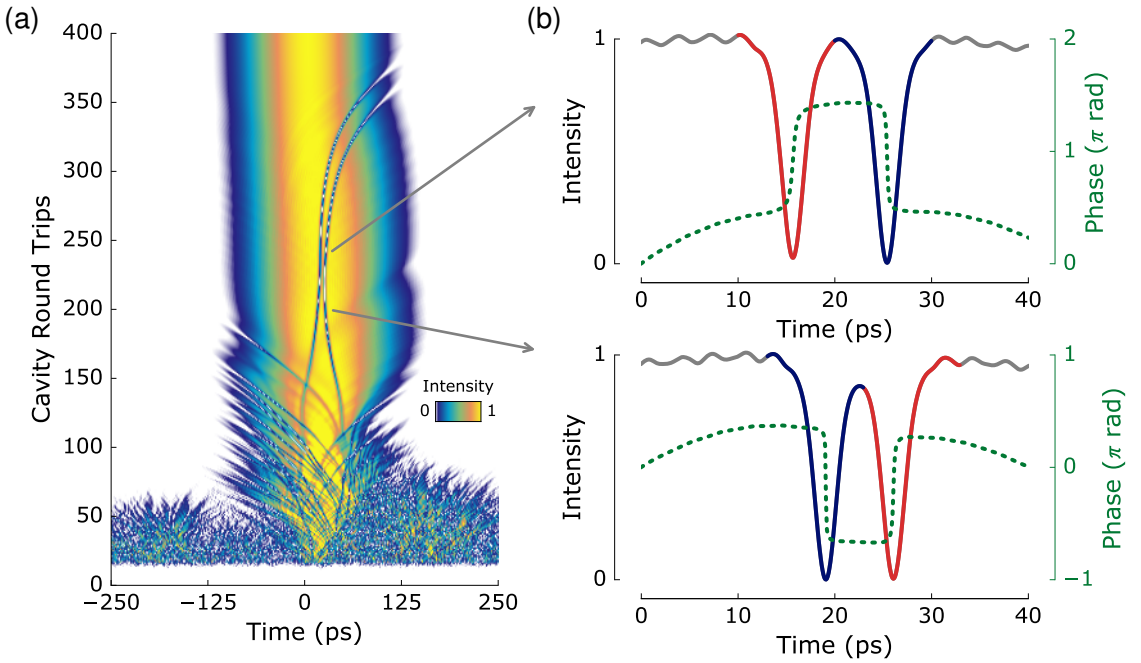


Fig. 3.38: Radiation build-up dynamics in 120 m long-cavity mode-locked laser (using the same numerical model as Fig. 3.33, but with a different initial noise field): (a) temporal evolution; (b) dark soliton profiles within the bright pulse, before and after a collision at 200 and 240 round trips, respectively (colour is used to define each soliton).

In the context of dark solitons decaying, the collision-induced time shift could have forced solitons in the quasi-stable envelope peak to shift into the sloped wings, destabilising them and accelerating their decay. Dark soliton interactions are therefore a further reason why they do not appear in the steady-state laser output.

3.5.4 Discussion

Our analysis of dark soliton dynamics within laser radiation build-up has centred on simulations of a 120 m mode-locked fibre cavity. However, we have observed dark solitons in simulations of all-normal dispersion lasers with many different length cavities (varying from tens of metres to kilometres). This is explained as dark solitons are the solitary wave solution to the NLSE in this environment. The longer cavity length merely enhances the effect as the increased cavity modal content increases the number of round trips required before all modes are phase-locked and the coherent steady state is reached. By contrast, net-anomalous dispersion lasers show no dark solitons (as shown in our soliton laser simulation in Fig. 2.9).

Experimental observation of these effects should be possible, given our simulations are based on real fibre parameters, although this will be challenging due to the transient non-periodic nature of the process, requiring single-shot picosecond-resolution measurements. Practically, our observations could be useful when considering applications of normal-dispersion mode-locked lasers, as this defines the expected start-up time required for the laser to reach a stable output.

The work in this section, however, was principally driven by curiosity and fundamental interest. It is notable that well-established dark soliton interactions in conservative systems [Thu91] are qualitatively maintained in our simulations of a novel dissipative system. The recirculation of light in fibre resonators offers a unique opportunity for exploring long-range soliton interactions by periodically sampling the optical field once per round-trip [Jan13]. In particular, mode-locked lasers – where a near constant bright pulse background is maintained by the restoring forces of the system – offer a suitable environment for studying dark soliton evolution, and their interactions.

As the NLSE underpins a variety of nonlinear dispersive systems, such studies could also offer insight into other fields. One area which is currently receiving particular academic interest is the analogy between fibre-optics and Bose-Einstein condensates (BECs) [Pro04]. A BEC is a state of matter at almost absolute-zero temperature, where the reduced thermal energy forces many atoms to occupy the lowest quantum state, enabling the observation of quantum mechanical phenomena on macroscopic length scales (e.g. superconductivity) [Bos24, Ein24]. The NLSE describes the wavefunction of the condensate, including the atomic density and phase, rather than the electromagnetic field envelope used in optics. Under conditions of a dilute atomic gas (such that the nonlinearity in a BEC resembles a Kerr-type nonlinearity) and confinement to a 1D atomic system, there are strong parallels between the two systems [Pro04].

Dark soliton matter-waves have been observed experimentally in BECs, where they can be a useful diagnostic for probing mesoscopic physics in ultracold gases [Fra10]; however, they have also been shown to be thermodynamically unstable, resulting in their eventual decay [Bec08, Fra10]. Additionally, soliton-soliton collisions have been observed to contribute to the decay mechanism [Bec08, Hua01], in analogy with the dynamics during laser radiation build-up we report here. We thus suggest that mode-locked fibre lasers could prove a useful platform for improving understanding of dark soliton interactions, with applicability to other dissipative systems.

Further work is required to evaluate the strength of the analogy, but if validated, this suggests that mode-locked lasers could be used to aid understanding of the dynamics and stabilisation of dark solitons, offering valuable insight for advancing studies of macroscopic quantum phenomena in BECs.

3.6 Summary

In this chapter we have presented a long-cavity laser architecture as a route to generating high-energy short pulses at low repetition rates. We demonstrated that near-kilometre length mode-locked cavities could produce stable nanosecond pulses at kilohertz repetition rates. The cavity length and choice of fibre nonlinearity and dispersion were found to enable variation of the output pulse duration and repetition frequency, suggesting that this is a flexible design for achieving a wide range of short-pulse laser parameters. Such pulses also possessed a giant linear chirp. While the magnitude of this chirp rendered classic compression techniques (such as using bulk diffracting pair gratings) impractical, we were able to demonstrate chirp compensation using a custom-engineered chirped fibre Bragg grating for $\sim$100 times compression to produce ultrashort pulses.

Could compressed long-cavity lasers be commercially-attractive high-energy pulse sources? The design is well-suited for chirped pulse amplification – which can be achieved by simply including an amplifier before the CFBG since the generated pulses are highly chirped – and as an all-fibre system, the laser could be conveniently packaged as a compact, robust device. Polarisation-maintaining fibre could also be used for environmental stability. However, the tightly-confined guided nature of light in fibre is also a major limitation. The compressed 125 nJ energy, 10 kW peak-power pulses in our experiment corresponded to a nonlinear length of less than 0.1 m in Flexcore fibre. This indicates that strong nonlinear effects could emerge over short distances such as the fibre pigtails of the circulator, limiting the pulse quality and spectral density of the final output as the power increased further.

Therefore, in order to access higher output powers without deleterious nonlinear effects, it will be necessary to use large mode area fibres which exhibit a significantly lower nonlinear parameter by spreading the light over a larger effective area. This approach has already been demonstrated for 0.5 μJ pulse generation with a $\sim$50 m cavity [Chi11], and we believe that further cavity elongation could yield even higher pulse energies and output powers. The precise CFBG specification and rapid deterioration of pulse quality of

compressed duration when deviating from it could also present practical problems for developing a monolithic long-cavity laser system. However, despite these limitations we were able to demonstrate that our system is a suitable pump source for low-threshold supercontinuum generation in PCF. The resulting system was a compact and relatively low-cost broadband fibre source, ideal for optical characterisation of devices.

Finally, we note that numerical modelling played an important role in this chapter, successfully simulating the output of the long-cavity laser, CFBG compression and propagation of these pulses in a PCF for supercontinuum generation. In addition to helping to guide the design process, such modelling provided additional insight into the underlying nonlinear optical physics. We observed persistent dark soliton structures as the pulses formed from noise in our simulations and considered their impact on the start-up dynamics of long-cavity mode-locked lasers. Further experimental work to verify their existence in the first few milliseconds of radiation build-up is challenging, but an interesting prospect to gain further insight into the nonlinear dynamics of mode-locked fibre lasers, with analogues to other nonlinear systems in nature.

4

FEW-LAYER TRANSITION METAL DICHALCOGENIDES

Materials science underpins the development of lasers and other photonic devices, yet simultaneously presents major limitations to their performance. Numerous optical properties must be considered in the design of such systems and the choice of materials involves a balance between their characteristics and practical aspects such as cost, scarcity and ease-of-fabrication; a compromise is usually made as every material possesses both advantages and disadvantages for a given application. Therefore, advances in materials science offer new opportunities for optical applications.

In this chapter, we consider few-layer *transition metal dichalcogenide* (TMD) nanomaterials and their prospects for nonlinear photonics. Historical developments and the optical properties of nanomaterials are briefly reviewed in Section 4.1, followed by an introduction to few-layer molybdenum disulfide (MoS_2) – the primary material we investigate in this chapter. In Section 4.2 we report a microscopy technique exploiting second- and third-harmonic generation for high-resolution imaging of few-layer MoS_2 and determination of the nonlinear optical characteristics. The exploitation of these properties to develop short-pulse fibre lasers using MoS_2 at a variety of wavelengths is described in Section 4.3, and the mechanism of wideband saturable absorption is discussed in the context of edge states. Finally, other TMD nanomaterials are considered in Section 4.4, including reports of Q-switched lasers using $MoSe_2$, and the chapter is concluded with a critical discussion of the opportunities for such nanomaterials in photonic systems in Section 4.5.

Results presented in this chapter have been published in the following journal articles and conference proceedings: [Woo14a, Woo15b, Woo15c, Woo14f, Zha15, Woo15a, Woo15d, How16].

4.1 Introduction: Optical Properties of Nanomaterials

The word 'nanomaterial' is a broad term for describing low-dimensional materials with one or more characteristic lengths of nanoscale dimensions (typically <100 nm) and size-dependent properties, as introduced in Section 1.6. As a family of materials, they exhibit many interesting characteristics due to quantum confinement effects, which are not offered by conventional 3D bulk materials. From an applications point of view, one-dimensional (1D) *nanotubes* and two-dimensional (2D) *nanosheets* have attracted the most interest.

4.1.1 Carbon Nanotubes

The explosion of interest in nanomaterials on a global scale, which continues to the present day, was arguably initiated by Sumio Iijima's fabrication of 'helical microtubules of graphitic carbon', reported in 1991 [Iij91].[1] These 1D structures were *multi-walled* carbon nanotubes, consisting of numerous sheets of sp^2-bonded carbon atoms rolled-up into cylindrical tubes of gradually increasing diameter.[2] Tubes of only 1 nm diameter (consisting of a single sheet), known as *single-walled* carbon nanotubes, were reported shortly afterwards [Iij93, Bet93].

Sheets of carbon atoms have a honeycomb structure and the angle at which the sheet is rolled to form a tube determines the electronic properties of the material. This is described by the *chiral vector* $\mathbf{c}$, which connects any two points on the single sheet lattice that become coincident when rolled [Won11]:

$$\mathbf{c} = n\mathbf{a_1} + m\mathbf{a_2} \tag{4.1.1}$$

where $\mathbf{a_1}$ and $\mathbf{a_2}$ are in-plane unit vectors and n and m are positive integers coordinates of the 1D unit cell. These two integers determine the circumference of the tube $|\mathbf{c}|$ and thus, the diameter d:

$$d = \frac{|\mathbf{c}|}{\pi} = \frac{a\sqrt{n^2 + nm + m^2}}{\pi} \tag{4.1.2}$$

where $a = 0.246$ nm is a constant related to the lattice [Won11]. The resulting structure is described as an (n, m) carbon nanotube, as illustrated in Fig. 4.1a. If $|m - n|$ is exactly divisible by three, the nanotube exhibits metallic behaviour. Otherwise, the material is a semiconductor with a direct bandgap. The 1D nature of the material gives rise to

[1] However, following this work, re-examination of earlier literature revealed reports of hollow carbon tubes with <50 nm diameter synthesised as far back as 1952 [Rad52]. We shall see in this chapter that 'rediscovery' appears to be a persistent theme within the history of nanomaterials. Perhaps this is not surprising as the pioneering reports of low-dimensional structure fabrication lacked the high-resolution characterisation tools to thoroughly study their novel properties and consequently, the materials were not exploited for practical applications. However, these reports offered significant insight and were a major contribution to the field; where possible, we include references in this section to both the original authors in addition to the more recent studies which have extended their work.

[2] It should be noted, however, that nanotubes are not fabricated physically be rolling up 2D sheets. A variety of fabrication techniques exist including electric arc discharge, laser ablation and chemical vapour deposition [Jou98].

Van Hove singularities in the electronic density of states, resulting in numerous possible optical transitions, where the lowest transitions are labelled E_{11} and E_{22} [Wil98, Avo08]. Additionally, the gap energies of transitions, which define the optical absorption, are determined by the tube diameter, which can be expressed visually in a *Kataura plot* (Fig. 4.1b) [Kat99].

Nanotubes may be grown with random distributions of chiral vectors leading to a distribution of metallic and semiconductor behaviour, and broadband absorption due to a distribution of tube diameters. However, by careful control of the growth conditions, the distribution of tube diameters can be reduced to a desired range, enabling control of the direct bandgap of the material for particular optoelectronic applications. Additionally, after photoexcitation, ultrafast carrier dynamics have been reported including relaxation within 100 fs [Ma04].

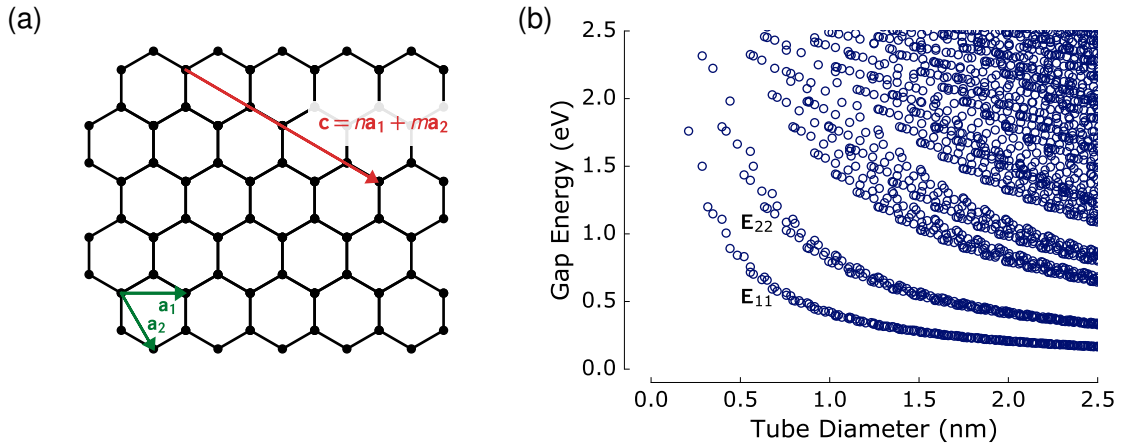


Fig. 4.1: Single-walled carbon nanotubes: (a) Schematic showing the chiral vector for a semiconducting (3,2) tube, visualised as a rolled-up planar sheet of atoms; (b) Kataura plot showing the relationship between tube diameter and bandgap for various semiconducting tube transitions. The lowest two transitions are labelled E_{11} and E_{22}. Adapted from Ref. [Kat99].

4.1.2 Graphene

The properties of the aforementioned 'unrolled' 2D sheets of carbon atoms have also been considered as a material in their own right, known as graphene. Early works theoretically studied graphene sheets in the context of understanding the properties of 3D carbon allotrope *graphite*, which consists of stacked graphene layers held together by weak van der Waals forces [Wal47].[3] Literature reports also documented observations of few-layer graphite, although the limited microscopy techniques available at the time prevented thorough characterisation of these samples [Rue48, Boe62]. The first fabrication of stable single-layer graphene sheets is attributed to Geim and Novoselov, after their

[3] It was not until 1986 that the term graphene was introduced by Boehm, Setton and Stumpp as a combination of the word graphite and the suffix -ene [Boe86].

infamous 2004 demonstration of micromechanical exfoliation of graphite using Scotch tape [Nov04]. This was closely followed by their award of the 2010 Nobel Prize for Physics for "groundbreaking experiments regarding the two-dimensional material graphene".

Graphene is a zero-bandgap semi-metal. Electrons in the material exhibit a linear relationship between energy and momentum, behaving as massless Dirac fermions (Fig. 4.2 shows the band structure at the crystal K point) [Nai08]. Ultrafast carrier dynamics have also been reported: pump-probe spectroscopy has revealed a rapid intraband carrier equilibration of $<$30 fs [Bre09].

The 2D nature and zero bandgap of graphene result in frequency-independent absorption from the visible to near-infrared spectral region with a value of 2.3%, determined by the fine-structure constant (a fundamental physical constant) [Nai08]. Consequently, for any optical excitation in this range (i.e. any incident wavelength), there is always an electron-hole pair in resonance, enabling broadband optical operation. Outside this region, a van Hove singularity in the density of states causes an absorption peak at $\sim$270 nm and beyond $\sim$2500 nm, thermal occupancy and intraband transitions impact upon the optical spectrum [Mak08]. However, while wideband optical absorption from the zero bandgap is one of graphene's greatest strengths, the lack of bandgap is also simultaneously the greatest weakness, making it challenging to turn graphene-based devices 'off' and to fully control them electronically.

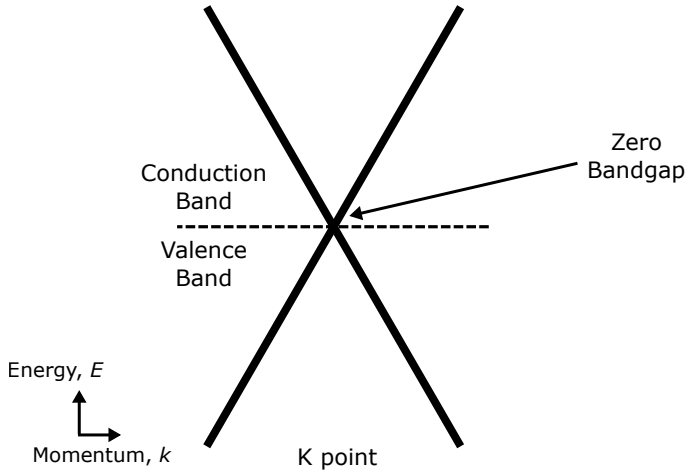


Fig. 4.2: Electronic band structure of graphene, showing the linear dispersion of electrons.

4.1.3 Few-Layer Transition Metal Dichalcogenides

While work continues to understand and exploit the properties of graphene for practical devices, there is also great interest in exploring other 2D materials. Researchers are therefore considering other layered crystal structures for the fabrication of monolayer (2D) and few-layer (quasi-2D) crystals, which could possess superior optical and electronic properties to the bulk 3D material.

Transition metal dichalcogenides (TMDs) are a family of more than 40 layered materials, with MX_2 stoichiometry. The layers consist of a single plane of hexagonally-arranged transition metal (M) atoms (e.g. molybdenum Mo, tungsten W) covalently bonded between two hexagonal planes of chalcogen (X) atoms (e.g. sulfur S, selenium Se), where the layers themselves are weakly bound together by van der Waals forces (Fig. 4.3a) [Wil69].[4] The electronic structure of TMDs is shaped by orbital hybridisation and occupation, thus depending on the position of the constituent elements in the periodic table and the electron count. Furthermore, TMDs can exhibit a variety of polymorphs (different crystal structures) such that the stacking arrangement affects the characteristics of a given material.

A diverse range of properties are offered by TMDs, including metallic (e.g. NbS_2), semiconducting (e.g. MoS_2) and insulating (e.g. HfS_2) behaviour. Additionally, monolayer and few-layer forms of TMDs have been exfoliated and found to possess distinct thickness-dependent optoelectronic properties, opening new opportunities for photonic applications and exploration of low-dimensional physics.

Recently, the TMD molybdenum disulfide (MoS_2) has received particular attention, in part due to its availability from naturally occurring molybdenite [Gan14].[5] Monolayer and few-layer MoS_2 is the primary focus of this chapter, although many of the conclusions are expected to apply to other semiconducting TMDs.

Monolayer and Few-Layer MoS_2

Bulk MoS_2 exhibits two polymorphs: *trigonal prismatic* (2H and 3R phases[6]) which results in filled orbits and indirect-gap semiconducting behaviour; and a metastable *octahedral* phase (1T) with partially-filled orbits, providing metallic characteristics. Naturally occurring MoS_2 is 2H, which is the focus of our discussion as the 1T phase is not stable and reverts to 2H under high temperature or pressure [Chh13].

Weak interlayer van der Waals forces enable facile exfoliation of MoS_2 layers. This changes the coupling between layers, the degree of quantum confinement and symmetry properties, which strongly alter the electronic structure.

Reports of few-layer MoS_2 and observations of their thickness-dependent properties first appeared in the literature many decades before the graphene-led renaissance in 2D materials. In 1963 Frindt and Yoffe studied the optical properties of thin (<10 nm thick) MoS_2 crystals, later identifying new features in the absorption spectrum of few-layer MoS_2 flakes (mechanically exfoliated with adhesive tape) [Fri63, Fri65, Fri66]. Reports of monolayer exfoliation using lithium-based intercalation techniques were also published [Joe86]. However, these early studies were limited by the instrumentation and techniques

[4] Each layer here consists of three planes of atoms. While this could be referred to as a tri-layer, it is more common to define the structure as a single layer or monolayer – a terminology we adopt herein.

[5] Bulk MoS_2 already plays a role in industry, commonly being used as a commercial lubricant and catalyst.

[6] The numbers correspond to the number of layers in the unit cell and H, R and T are the symmetry: hexagonal, rhombohedral or trigonal.

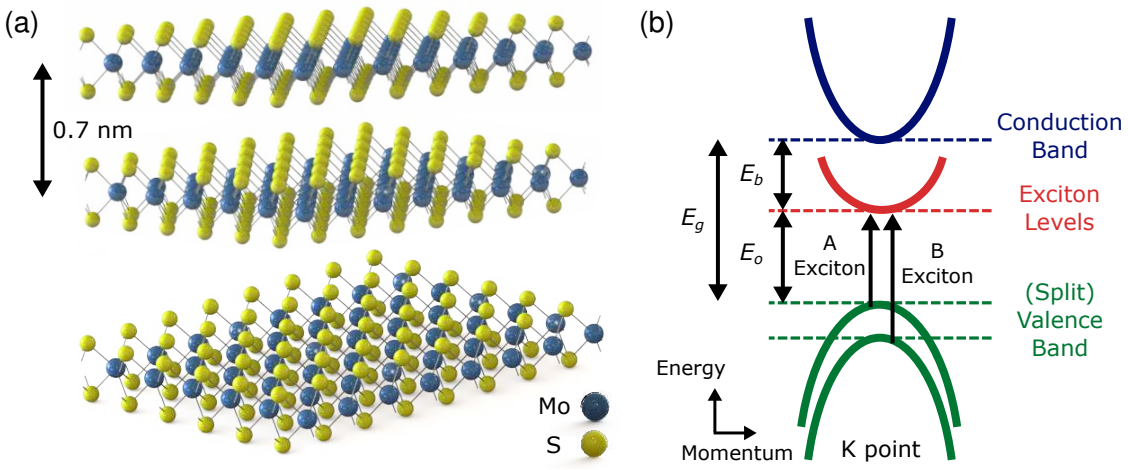


Fig. 4.3: MoS_2 structure: (a) visualisation of three-layer MoS_2; (b) simplified energy structure for monolayer MoS_2 showing the relationship between the electronic bandgap E_g, the excitonic binding energy E_b and the optical bandgap E_o.

available for characterisation and neither the nonlinear optical properties of few-layer MoS_2 nor the technological benefits were exploited.

More recently, renewed interest in low-dimensional forms of MoS_2 followed reports in 2010 of a transition from indirect to direct bandgap behaviour with a reduction in layer count and many orders of magnitude (10^4) greater photoluminescence [Mak10]. Experimental studies have confirmed that bulk MoS_2 has an indirect ~1.29 eV (961 nm) bandgap, which increases due to quantum confinement as the number of layers is reduced, eventually becoming a direct 1.80 eV (689 nm) badgap for an isolated monolayer. An additional result of the reduced dimensionality is the emergence of strong excitonic effects.

To understand the optical properties of MoS_2, it is necessary to consider the role of *excitons*, which we now discuss. In a semiconductor, photoexcitation places an electron into the conduction band, leaving a hole in the valence band. The attractive Coulombic interaction between the electron and hole can create a bound-state quasiparticle known as an *exciton*. If the electron-hole interaction is weak (e.g. due to long-distance separation or dielectric screening) or if the photoexcitation energy is great, this attraction can be overcome, resulting in free carriers (unbound electrons and holes).

Excitons can therefore be considered as the lowest energy electronic excitation in a semiconductor: the energy required to create an exciton by optical absorption is less than the threshold for creating free carriers. Hence, excitons can be represented as an energy level just beneath the conduction band on an energy level diagram (Fig. 4.3b).[7] This leads to two definitions of the bandgap: the *electronic bandgap* (or *transport bandgap*) E_g, which

[7]Strictly, this is incorrect. The typical semiconductor band structure, including a conduction band and a filled valence band as the ground state, is a *one-electron picture*. Excitons, however, are two-particle states: the ground state here contains no electron-hole pairs and hence is the origin in a *two-particle picture*, which does not include conduction or valence bands [Yu10]. However, we feel the simplified hybrid energy structure in Fig. 4.3b does help to visualise the relative energies of free carriers and excitons, and shows the different bandgap definitions.

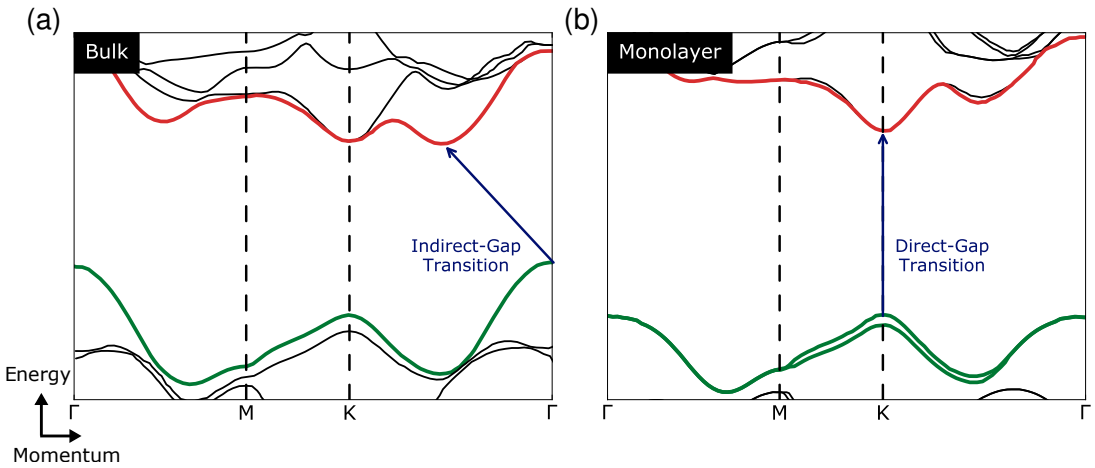


Fig. 4.4: Quasiparticle band structure of (a) bulk and (b) monolayer MoS_2, highlighting the indirect-to-direct gap transition. The labels Γ, M and K are high-symmetry points of the crystal lattice. Adapted from Ref. [Che12], where the band structure was calculated using quasiparticle self-consistent GW theory.

defines the energy needed to inject free electrons and holes into the material, and the *optical bandgap* E_o, which is the required energy for a photon to be absorbed. The energy difference is known as the *exciton binding energy*: $E_b = E_g - E_o$ [Kas06].

In classical inorganic semiconductors, electron-hole interactions are weak due to dielectric screening, yielding a small (< 10 meV) exciton binding energy and any generated excitons are rapidly ionised by collisions with optical phonons (lattice vibrations). Consequently, their effect is not observed experimentally (unless cooled to low temperatures) and the distinction between electronic and optical bandgap is neglected [Yu10].

For low-dimensional materials such as few-layer MoS_2, however, quantum confinement enhances the electron-hole Coulombic interaction and reduces the dielectric screening since the electric field induced by electron-hole pairs extends beyond the material. Consequently, large excitonic binding energies (>100 meV) have been measured and these transitions shape the absorption spectrum and carrier dynamics at room temperature. Our interest in MoS_2 is for photonic devices and in the following discussion, we thus use the term bandgap to describe the optical gap.

Many researchers have constructed numerical models for calculating the band structure. Strongly bound excitons and the need to consider many-body effects complicate these simulations and debate continues in the literature relating to interpretations of many existing theories concerning this problem. There is agreement, however, regarding the origin of the transition from indirect to direct gap behaviour, as shown by a typical computed band structure in Fig. 4.4.

Bulk MoS_2 has an indirect bandgap with a valence band maximum at the Γ point and a conduction band minimum at the midpoint of Γ-K. A direct, although higher energy, excitonic transition exists at the K point. As the layer count is reduced, the indirect gap increases while the direct gap is almost unchanged. At monolyer thickness, the direct energy gap is smaller, thus becoming the (optical) bandgap of the material.

Finally, we note that Fig. 4.4 shows a split valence band, which occurs in monolayer MoS_2 due to spin-orbit coupling. This yields two strong excitonic transitions, commonly labelled A and B, which we also show in the simplified band structure in Fig. 4.3.

4.2 Nonlinear Microscopy for Material Characterisation

Two-dimensional material fabrication techniques often produce a distribution of small flakes of the material, with different sizes and thicknesses (i.e. number of layers). Since the electronic structure and optical properties of few-layer materials are affected by their size, it is important to identify and characterise the properties of flakes before they can be successfully integrated into devices. Conventional optical microscopy enables the determination of flake positions on a substrate, where contrast is obtained from variations in the linear refractive index and linear absorption coefficient of materials that govern the transmission and reflection coefficients. The contrast can be low, however, for materials with similar indexes and no information is recorded regarding the flake's nonlinear characteristics.

To obtain such information, *nonlinear optical microscopy* can be used, where a sample is excited with high-intensity light and one or more nonlinear effects are recorded to spatially map the sample's nonlinear response [Gan78, Hel74, Bar97]. This technique offers high spatial, spectral and temporal resolution and enables nondestructive in-situ characterisation.

High intensity pump sources for nonlinear microscopy are typically achieved using a high-peak-power short-pulse pump source, focussed onto a small area; an image of a large sample can then be obtained by raster scanning the focussed spot across the sample and recording the harmonic intensity at each point (i.e. pixel). Such microscopy techniques are being enabled by progress in ultrafast laser development, offering high peak power pulses but maintaining relatively low average powers to avoid thermal damage to samples.

A variety of nonlinear effects can be used such as harmonic generation, coherent anti-Stokes Raman scattering and two-photon absorption/fluorescence, depending on the material under investigation and the characteristics to be measured. In this section, we consider harmonic generation, which can be achieved with a single pump source and relatively simple optical setup, enabling rapid assessment of a material's properties for applications including wavelength conversion and pulse characterisation. Experiments in this section were undertaken during a placement with MackGraphe, Mackenzie Presbyterian University, Brazil in May 2015.[8]

[8] I am grateful to Profs Christiano de Matos and Thoroh de Souza for supervising this placement, and Drs Rafael de Oliveira, Ciaran Phelan and Robbie Murray for fruitful discussions and support when conducting the experiments and analysing the data.

4.2.1 Introduction to Harmonic Generation

Generation of light at the nth harmonic frequency of a fundamental (pump) wave arises from the nth order nonlinear susceptibility $\chi^{(n)}$ of a material. Under intense illumination, the pump excites a nonlinear polarisation wave in the material, consisting of electric dipoles oscillating at n times the fundamental frequency. These dipoles then radiate according to Maxwell's equations, emitting an electromagnetic field at the harmonic frequency.

This process can also be understood quantum mechanically in terms of photon-induced transitions of electrons between the ground state and *virtual* states. Under incident light, a photon can excite an electron to a higher-energy virtual level. It should be stressed that these are virtual-state transitions and are not related to physical absorption processes or real energy levels in the material's electronic structure. The lifetime of virtual states is essentially equal to the pump pulse duration, resulting in a rapid energy decay to the ground state, generating a photon at the same energy as the pump. However, under intense illumination, multiple photons can excite electrons into even higher-energy virtual states. Therefore, the transition back to the ground state re-emits a single photon with a greater energy. The processes of *second-harmonic generation* (SHG) and *third-harmonic generation* (THG) are shown schematically in Fig. 4.5.

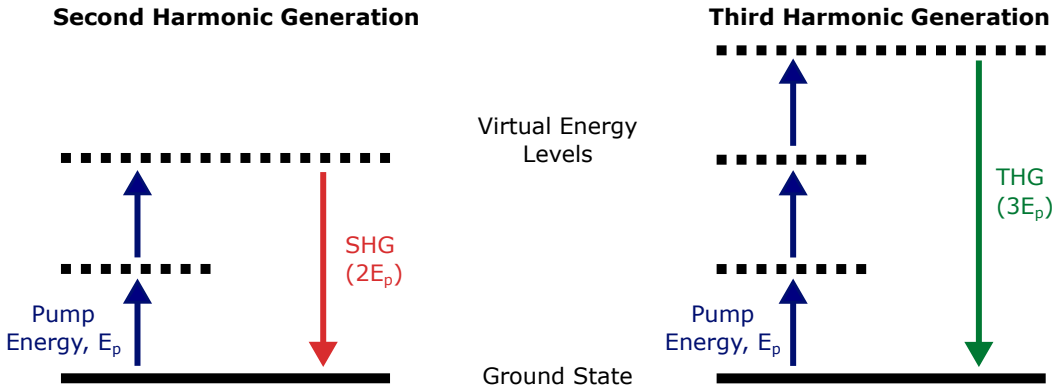


Fig. 4.5: Schematic illustration of second and third harmonic generation, involving electron transitions between the ground level and virtual states.

Harmonic generation is a phase-sensitive nonlinear process. The induced dipoles have a fixed phase relative to the well-defined phase and amplitude of the pump wave. For high conversion efficiencies, the dipoles must radiate in phase to ensure that the contributions from all dipole positions along the material (often on millimetre length scales for bulk crystals) add constructively. Therefore, *phase matching* is required. There are numerous strategies for achieving a fixed phase relationship between pump and harmonic waves (to yield zero wavenumber mismatch: $\Delta k = 0$), exploiting the use of crystal birefringence or periodic poling. However, two-dimensional nanomaterials are only a few atomic layers thick, precluding phase-matching for normal-incidence illumination as the material thickness is hundreds of times smaller than the wavelength (and thus less than the

coherence length for the process).

For the Taylor expansion of the electric susceptibility to converge, it is expected that nonlinear susceptibilities $\chi^{(n)}$ will generally decrease with increasing order n, suggesting that lower-order nonlinear effects should be more easily observed [Boy07]. However, SHG can only occur in media which lack inversion symmetry.[9] For layered nanomaterials, their centrosymmetry is determined by the parity of the layer count. Hence, for MoS_2 flakes with an even number of layers, there will be negligible SHG [Li13]. All materials exhibit a non-vanishing $\chi^{(3)}$, however, suggesting that third-harmonic microscopy is a technique that could be widely applied, providing sufficient excitation intensities and sensitive detection systems are available.

4.2.2 Harmonic Generation from Surfaces

Shortly after Peter Franken's first observation of SHG [Fra61], Bloembergen and Pershan realised the importance of boundary conditions in nonlinear media for harmonic generation, formalising the theory of nonlinear optics at interfaces [Blo62]. Specifically, it was noted that the broken symmetry at a material boundary results in a different nonlinearity for the surface and bulk. For example, at the interface between two materials (e.g. air and a solid object), structural discontinuity permits electric-dipole effects at the surface even if these were forbidden in the bulk [Blo68]. Therefore, bulk materials possessing inversion symmetry were demonstrated to radiate SHG from surfaces [Bro65]. Material surfaces can thus be treated as a thin layer with distinct nonlinear optical properties to the bulk [She89]. As understanding of surface nonlinear optics developed, it was realised that harmonic generation was an ideal tool for high-resolution surface analysis, which remains widely used to this day for characterising growth on substrates and for surface spectroscopy [She86, She00].

Following this discussion, a question arises regarding nonlinear optics in monolayer and few-layer nanomaterials: should they be treated using a bulk model or as a surface, due to their 2D dimensionality? We discuss this further in Section 4.2.6.

Finally, we note that harmonic generation has recently been reported from MoS_2 by other researchers: SHG was demonstrated from both monolayer and few-layer crystals [Li13, Kum13] and THG was observed from 10-15 atomic layers of the material [Wan14a]. We extend this work by studying THG in both monolayer and few-layer MoS_2 samples and discuss how THG can augment the capabilities offered by SHG microscopy.

4.2.3 Monolayer and Few-Layer MoS_2 Fabrication

Before presenting our nonlinear microscopy experiment and results, we briefly discuss techniques for obtaining the 2D forms of MoS_2 used in this work. Few-layer fabrication

[9] This well-known principle can be explained as follows. The nth-order polarisation term is $P_n = \varepsilon_0 \chi^{(n)} E^n$ and under inversion symmetry, the sign of P_n should change when E changes sign. However, for even n, this statement can only be true if $\chi^{(n)} = 0$. Consequently, if a crystal is centrosymmetric, even-order nonlinear effects are electric dipole forbidden.

methods can be broadly separated into two categories: top-down exfoliation and bottom-up growth. Exfoliation involves cleaving monolayer or few-layer flakes from a bulk crystal, typically achieved mechanically (e.g. using Scotch tape), chemically (e.g. lithium-based intercalation) or through dispersion in solvents (known as liquid-phase exfoliation, LPE). Alternatively, growth techniques such as chemical vapour deposition (CVD) can produce layers of the material on a substrate, from carefully controlled chemical reactions between solid precursors [Wan12a].

Mechanical exfoliation is widely used in research environments for producing high-quality single-crystal flakes, although the low yield and poor scalability render it unsuitable for practical large-scale exploitation. For real-world applications, CVD growth or LPE are more promising, where CVD typically produces large single-layer flakes (up to tens of μm across) and LPE yields smaller few-layer samples (hundreds of nm across).

For harmonic generation, we initially considered CVD-grown monolayer flakes to establish the technique and then extended our experiments to few-layer crystals obtained from mechanical exfoliation. Later in the chapter in Section 4.3, we report the study of nonlinear absorption in LPE-fabricated few-layer MoS_2 and discuss why the small flake size is advantageous for saturable absorber applications.

Chemical Vapour Deposition

Monolayer MoS_2 flakes were produced by chemical vapour deposition on a substrate consisting of silicon (Si) with a $\sim$300 nm silica (SiO_2) coating layer.[10] The substrate was carefully cleaned (by ultrasonication in acetone and washing with water) before placing it in a furnace with 14 mg MoO_3 and 120 mg sulfur at atmospheric pressure. Over a period of 75 minutes the furnace temperature was varied between 105°C and 700°C. At high temperatures, sulfur vapour reduced the MoO_3 power to form volatile $MoO_{33\text{-}x}$ compounds, which diffused towards the substrate and further reacted with the sulfur vapour to form a thin film layer of MoS_2. Samples were then characterised by *Raman microscopy* and *atomic force microscopy* (AFM) to verify the growth of high-quality MoS_2 monolayers (the use of these microscopy techniques to determine the number of layers is explained in detail in Section 4.3.2). Further details of the fabrication and characterisation of this sample are reported in Ref. [Sch14].

Mechanical Exfoliation

Few-layer MoS_2 samples were fabricated by mechanical exfoliation of large bulk crystals of the material (obtained from Graphene Supermarket).[11] Briefly, a piece of Scotch tape was pressed into the bulk crystal and peeled off, overcoming the weak interlayer van der Waals forces to remove thin layers of the material. This was followed by further

[10] We thank Dr Shisheng Li and Prof. Goki Eda from the Centre for Advanced 2D Materials (CA2DM), National University of Singapore for fabrication of the CVD-grown samples.

[11] We thank Eduardo Aiub, Dr Indayara Martins and Prof. Lucia Saito from MackGraphe, Mackenzie Presbyterian University for preparing the mechanically exfoliated samples.

applications of the adhesive tape to cleave layers from the thin crystals until single and few-layer samples remained. The exfoliated flakes were then transferred to a silicon substrate with a ∼300 nm silica coating layer and characterised using Raman microscopy and AFM to determine the layer count. Further details of this fabrication procedure are reported in Refs [Mak10, Li14].

4.2.4 Experimental Microscope Setup

A reflective imaging system was developed to enable simultaneous linear optical microscopy and nonlinear harmonic generation microscopy, as shown in Fig. 4.6.

The linear microscope section included a green (∼530 nm) LED illumination source and the detector was a *charge-coupled device* (CCD) camera with 1280×1024 pixel resolution. The emitted LED light was collected by a 20 mm focal length aspheric condenser lens and focussed onto the sample by a 20× microscope objective. The reflected light from the sample was imaged onto the CCD camera by the combination of the microscope objective and an infinity-corrected tube lens (200 mm focal length), after a 50:50 beamsplitter.

Nonlinear imaging was achieved by exciting the sample with 153 fs *full width at half maximum* (FWHM) Gaussian-shaped pulses from an ultrafast mode-locked fibre laser (Toptica FemtoFiber FFS), operating at 1560 nm with a repetition rate of 89 MHz (Fig. 4.7). An isolator was included after the laser to prevent destabilisation from back-reflections and a variable neutral density (ND) filter was included to vary the power. As light after the isolator was linearly polarised, a *half-wave plate* (HWP) and *quarter-wave plate* (QWP) were used to control the state of polarisation incident on the sample. The 1560 nm pump light was tightly focussed (after reflection from a pellicle beamsplitter) by the microscope objective to a Gaussian-shaped spot on the sample with 3.6 μm beam diameter ($1/e^2$ width, obtained by a knife-edge measurement). This spot size was limited by the available lenses, although it should be possible to obtain a diffraction-limited spot size to further improve the microscope resolution. The sample was positioned at the focus, mounted on a piezo-controlled translation stage to enable automated raster scanning of the focussed beam over a large area.

Harmonic light (at both second and third harmonic frequencies) was generated in reflection, collimated by the microscope objective and transmitted by the pellicle beamsplitter. By changing the position of a flip mirror, the harmonics could be imaged onto the CCD camera or coupled into a multimode fibre (62.5 μm core diameter) connected to a spectrometer (WITec UHTS 300, including a single 600 lines per mm grating and a CCD detector cooled to -60°C).

The camera enabled simultaneous imaging of the linear optical image showing the entire illuminated sample and the harmonic signal from a focussed illuminated spot on the sample. With careful alignment, the image from the CCD camera showed the position of the harmonic from the sample, overlaid on the full linear image, enabling regions of the sample to be identified and their nonlinear response to be probed.

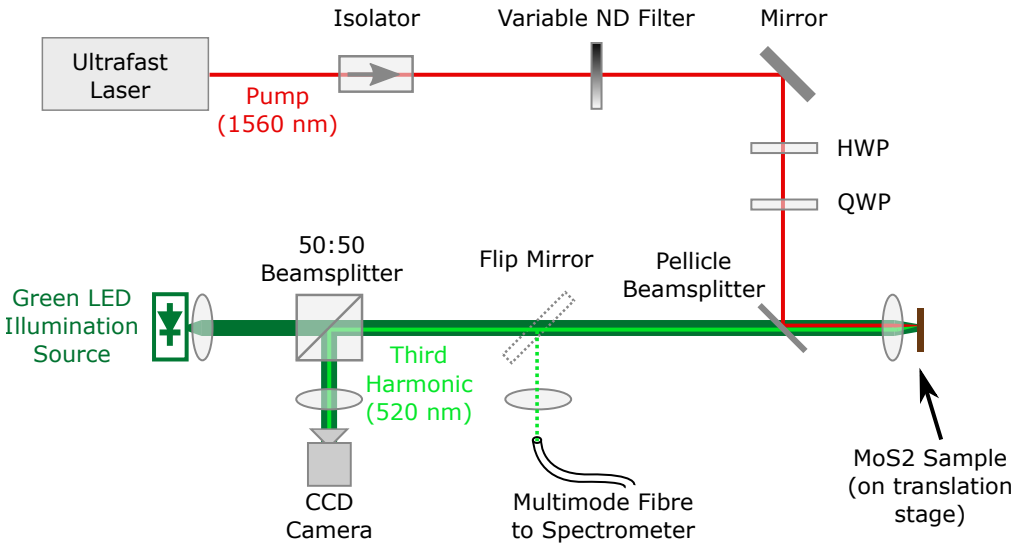


Fig. 4.6: Schematic of linear and nonlinear microscope. When the flip mirror was moved into position, the reflected harmonic was coupled into a multimode fibre (shown by the dotted line) and measured on a spectrometer. Both second and third harmonics could be generated, with collinear paths; we show only the third harmonic here for clarity.

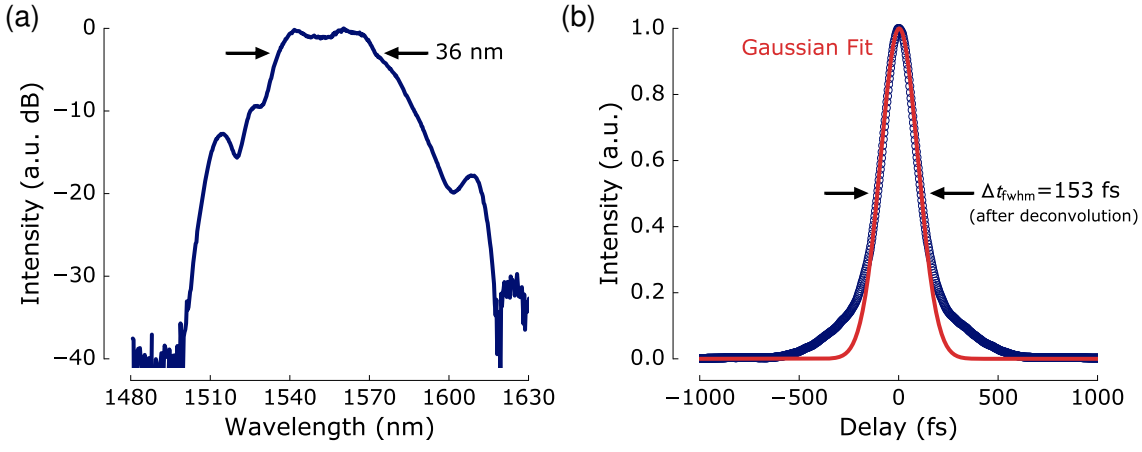


Fig. 4.7: Pump laser characterisation: (a) optical spectrum; (b) autocorrelation trace. Data courtesy of MackGraphe.

Imaging Results

Initially, we imaged the CVD-grown MoS_2 monolayer flakes. The green LED-illuminated microscope image (Fig. 4.8) showed isolated MoS_2 monolayers on a Si substrate. The contrast was poor, although it was possible to distinguish faint isolated triangles corresponding to MoS_2 monolayers, as shown in the magnified inset. This triangular shape mirrors the crystal symmetry in the trigonal prismatic structure of 1H monolayer MoS_2 [Chh13].

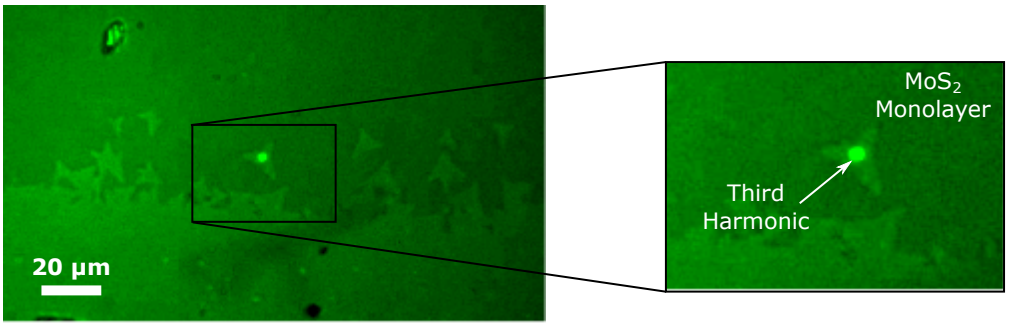


Fig. 4.8: Microscope image showing the third harmonic at the laser focal position overlaid on the linearly illuminated wide-area sample of MoS_2 monolayer islands on an Si substrate, imaged on a CCD camera (shown magnified in the inset). The contrast of linear optical imaging was poor, highlighting the benefit of alternative microscopy techniques.

With an incident power on the sample of ∼6.5 mW, the pulse peak power was ∼450 W,[12] corresponding to a peak intensity of 8.8 GW cm^{-2} when focussed to a 3.6 µm diameter spot.[13] The focal spot was moved across the sample using the piezo-controlled translation stage and a bright green spot was observed when the pump beam was incident on an MoS_2 monolayer (Fig. 4.8 inset). This was the third harmonic of the pump beam. Otherwise, with the pump beam incident on the silicon substrate, no third harmonic was observed on the CCD camera.

By adjusting the flip mirror, the reflected signal was measured on a spectrometer. A strong third harmonic was recorded, centred at ∼522 nm with a spectral FWHM of 4.8 nm (Fig. 4.9a). The greater sensitivity of the spectrometer compared to the CCD camera also enabled measurement of the THG signal from the substrate, although this was ∼150 times weaker than from the MoS_2. This confirms relatively strong third-harmonic generation in monolayer MoS_2 and we neglected the substrate contribution in our subsequent analysis. A second harmonic signal was also measured at ∼782 nm, with 10.2 nm spectral width (Fig. 4.9b). While bulk MoS_2 possesses inversion symmetry, prohibiting $\chi^{(2)}$ processes, the symmetry is broken for monolayer and odd numbers of few-layer flakes, allowing second-

[12] Computed using peak power = S × average power × (pulse duration × repetition rate)$^{-1}$, where shape factor $S = 0.94$ for Gaussian pulses.

[13] We use the definition: peak intensity = 2× peak power × (π× beam radius^2)$^{-1}$. The factor of two arises as our beam is Gaussian, with a higher intensity at the centre than in the wings. In the literature this factor is occasionally erroneously omitted or not explicitly mentioned. This can make direct comparison of computed values between published reports difficult.

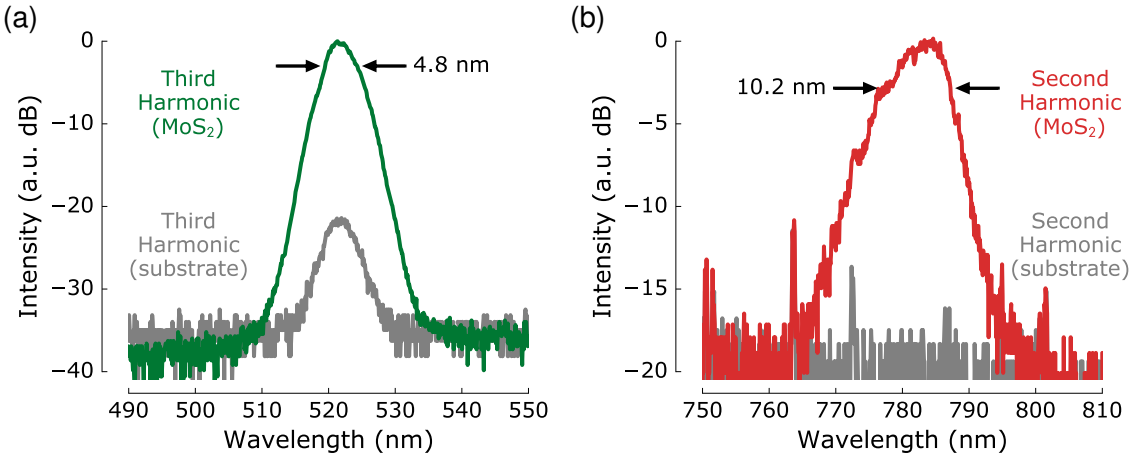


Fig. 4.9: Spectra of (a) third and (b) second harmonic light generated in a CVD-grown MoS_2 monolayer and from the Si substrate, under 1560 nm pump excitation.

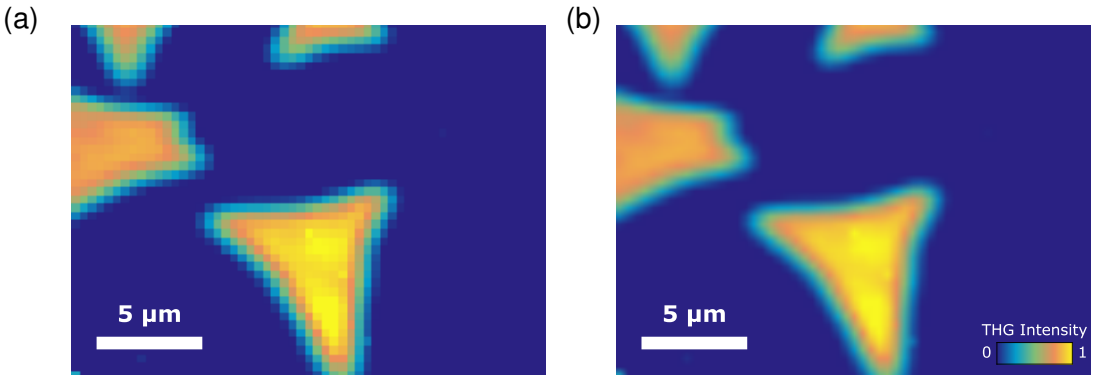


Fig. 4.10: Third-harmonic image of MoS_2 monolayers on Si substrate: (a) original image, raster scanned with 0.4 µm step; (b) bilinear interpolated image.

order nonlinear effects [Li13]. A SHG signal was not measurable from the substrate, however.

The spectrometer's CCD detector measured intensity in counts per second. To determine the power of the generated harmonic, we calibrated the system using a 650 nm laser diode with a known intensity and a broadband white light source. The polarisation-dependence of the optics was also taken into account.

To produce a high-contrast high-resolution image of the sample, generated harmonics were measured by raster scanning the focussed spot (in 0.4µm increments) across a wide area and recording the spectrum at each position. The intensity value at each position (i.e. the intensity of each pixel) was calculated by integrating over the harmonic spectrum, after processing to remove the ambient light background level. We also confirmed that the sample was not damaged and there was negligible change in the nonlinear response under this illumination over a sustained period of many hours.

The resulting THG image is shown in Fig. 4.10, in addition to the image after bilinear

interpolation to improve its appearance (we adopted this processing for all subsequently presented images). This was a significant improvement over the linear optical image, clearly highlighting the position of the MoS_2 monolayers on the substrate. We note that a similar image could be obtained here using the second-harmonic; the benefit of using the third harmonic becomes apparent later when imaging flakes with an even number of layers.

4.2.5 Polarisation-Resolved Microscopy

Oscillating dipoles induced by the incident field radiate new fields with the same direction as the material polarisation. Consequently, the relationship between the direction of incident and nonlinearly generated fields (i.e. the state of light polarisation) can provide further information about the electrical susceptibility and hence, the crystal structure of sample [Boy07]. To treat the light polarisation mathematically, we consider the nonlinear susceptibility as a tensor and briefly introduce *point groups* as a means of categorising the symmetries of common crystallographic structures.

In the most general form, third-order nonlinear processes can be expressed as:

$$\mathbf{P}^{(3)} = \varepsilon_0 \boldsymbol{\chi}^{(3)} \vdots (\mathbf{E} \otimes \mathbf{E} \otimes \mathbf{E}) \tag{4.2.1}$$

where $\mathbf{E}$ and $\mathbf{P}^{(3)}$ are the incident electric fields (which can each be different) and induced third-order material polarisation vectors, respectively, $\boldsymbol{\chi}^{(3)}$ is a fourth-rank tensor for the third-order nonlinear susceptibility, the notation $\vdots$ indicates tensor contraction (inner product) over three indices and $\otimes$ is the tensor product (outer product).

We simplify this by considering four interacting waves of the form $\omega_1 + \omega_2 + \omega_3 = \omega_4$, expressed as a summation to describe the induced polarisation wave at frequency ω_4 in a particular direction [New11]:

$$P_i(\omega_4) = \varepsilon_0 \sum_p \sum_{jkl} \chi^{(3)}_{ijkl}(\omega_4; \omega_1, \omega_2, \omega_3) E_j(\omega_1) E_k(\omega_2) E_l(\omega_3) \tag{4.2.2}$$

where i, j, k, and l can each be x, y or z directions and $\sum_p$ indicates that the right-hand side is summed over all permutations of ω_1, ω_2 and ω_3.

For third harmonic generation ($\omega + \omega + \omega = 3\omega$), this reduces to:

$$P_i(3\omega) = \varepsilon_0 \sum_{jkl} \chi^{(3)}_{ijkl}(3\omega; \omega, \omega, \omega) E_j(\omega) E_k(\omega) E_l(\omega) \tag{4.2.3}$$

The $\boldsymbol{\chi}^{(3)}$ tensor contains 81 elements, although the majority of these are zero or degenerate due to symmetry operations. All crystallographic structures can be divided into only 32 groups based on their symmetry, known as point groups, which determine the directional dependence of optical properties, in addition to whether the crystal exhibits birefringence or inversion symmetry [Boy07]. Consequently, measuring polarisation-dependent optical

effects permits analysis and identification of material samples, which could be a useful tool for studying the impact of layer count on the crystal symmetry of 2D materials.

As an example study, we consider the THG dependence upon pump polarisation in monolayer MoS_2. A single layer of 1H MoS_2 belongs to the D_{3h} point group [Chh13]. According to standardised point group tables [Boy07], there are only 21 non-zero elements of the $\boldsymbol{\chi}^{(3)}$ tensor for D_{3h} structures and since the pump light in our experiment is incident perpendicular to the plane of the MoS_2 layer, we neglect all elements in this direction (z). Therefore, for the x and y axes in the plane of the monolayer, the salient elements are: $xxxx = yyyy = xxyy + xyyx + xyxy$ where $xxyy = yyxx$, $xyyx = yxxy$ and $xyxy = yxyx$ [Boy07]. The notation $xyyy$ is shorthand for the $\chi^{(3)}_{xyyy}$ element, governing the generation of a wave polarised in the x direction arising from three waves polarised in the y direction. We assume $xxyy = xyyx = xyxy$ to simplify the mathematics since all three pump photons are degenerate, making it impossible to distinguish between these tensor elements in THG experiments. If the magnitudes are known, this procedure can be used to calculate the generated harmonic power given an input intensity value. However, in this case, our interest is in the direction of the vectors.

By evaluating Eqn. 4.2.3 for a pump wave with $E_x = X$, $E_y = Y$ and $E_z = 0$, we find:

$$\begin{aligned} P_x &= X(X^2 + Y^2) \\ P_y &= Y(X^2 + Y^2) \\ P_z &= 0 \end{aligned}$$

For a linearly polarised pump where X and Y are both real values, this indicates that the induced material polarisation, and hence the radiated THG field, will have the same optical polarisation state as the fundamental, with an intensity independent of the linear polarisation direction. We confirmed this experimentally by removing the QWP and rotating a HWP in the path of our pump light to rotate the linear polarisation; the direction of the THG polarisation state was measured using a linear polariser. We observed that the pump and THG light were always in the same polarisation state.

For a circularly polarised fundamental wave, e.g. $E_x = 1$, $E_y = \exp(i\pi/2)$ and $E_z = 0$, we find that the induced material polarisation is always zero:

$$\begin{aligned} P_x &= 1 + \exp(i\pi) = 0 \\ P_y &= \exp(i\pi/2) + \exp(3i\pi/2) = 0 \\ P_z &= 0 \end{aligned}$$

This suggests no THG from a circularly polarised pump. We explored this experimentally by rotating a QWP in the path of the linearly polarised 1560 nm beam and recording the intensity of THG from monolayer MoS_2 (Fig. 4.11). Theoretically, it can be shown that the relationship between the THG intensity[14] and QWP angle θ is $\cos^3(2\theta)$, based on the

[14]Intensity I is related to the square of the material polarisation: $I \propto E^2_{\mathrm{THG}} \propto P_x^2 + P_y^2 + P_z^2$.

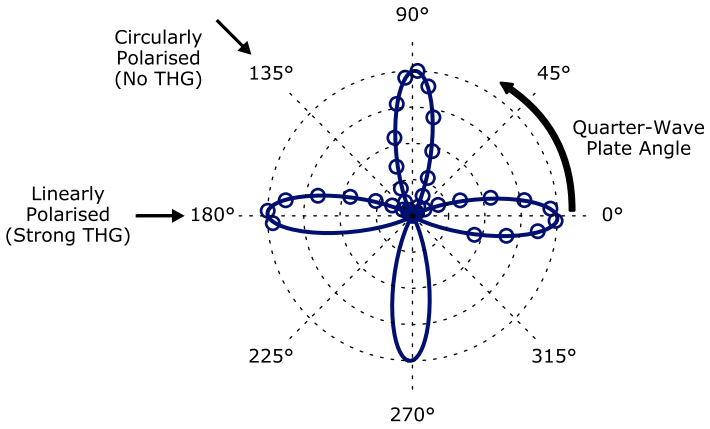


Fig. 4.11: Polar plot of third-harmonic generation intensity in monolayer MoS_2 as the pump polarisation state is rotated from linear to circular by rotating a quarter wave plate. Experimental measurements (dots) show that circular polarisation leads to zero third harmonic generation, in good agreement with the expected behaviour for a D_{3h} point group crystal (solid line).

Jones matrix of a QWP and from Eqn. 4.2.3 with the D_{3h} tensor elements. Good agreement was observed between the experiment and theoretical expectations, showing a decrease in THG intensity as the pump polarisation state changed from linear to elliptical to circular, confirming that our MoS_2 sample belonged to the expected point group.

Additional information can be provided by the polarisation dependence of SHG, determined by the $\chi^{(2)}$ tensor (with up to 27 tensor elements, which are well-known for D_{3h} materials [Boy07]). In this case, for linearly polarised pump light, the second harmonic fields in x and y directions are proportional to $\sin 3\theta$ and $\cos 3\theta$, respectively, where θ is the angle between the input polarisation and the crystallographic axis [Li13]. Consequently, by recording nonlinear images of the SHG in both x and y directions (using a polariser) from a large area sample of many MoS_2 flakes, it is possible to process these images to deduce the crystal orientation of each flake. We do not repeat such experiments here as the technique has been thoroughly studied recently [Li13, Kum13, Yin14]. With regards to circular pump polarisation states, SHG will be generated, unlike THG, and the harmonic will be circularly polarised but of opposite handedness.

4.2.6 Determination of Nonlinear Susceptibility

To evaluate the performance of few-layer nanomaterials for nonlinear optical applications, it is necessary to quantify the strength of their nonlinear response. This can be achieved by calculating the magnitude of the nonlinear susceptibility tensor through measurements of the generated harmonic powers for a known pump power.

As introduced in Section 4.2.1, Bloembergen, Pershan and Shen introduced extensive theoretical work to describe surface nonlinearities [She86, Blo62]. They proposed that interfaces could be considered as infinitesimally thin layers with a distinct dielectric

constant and nonlinear polarisation to the materials meeting at the interface. This model for thin interfaces bears strong resemblance to the emerging class of 2D nanomaterials. Consequently, we treated monolayer MoS_2 as a nonlinear sheet at the interface between air and the dielectric SiO_2 substrate, including local-field correction factors (i.e. surface transmission and reflection coefficients) to account for the boundary conditions.

A measured surface nonlinear response can include contributions from both the interfacial sheet nonlinearity and the bulk nonlinearity of the air and substrate. For our analysis, we assumed that the bulk nonlinearity of air and the SiO_2 substrate was negligible compared to the MoS_2 layer (justified as the THG was $\sim$150 times weaker and SHG was not measurable in SiO_2, as shown in Fig. 4.9). Therefore, the measured surface nonlinearity was assumed to arise solely from the MoS_2 layer(s) as a nonlinear sheet. Pump depletion was also assumed to be negligible since the conversion efficiency was low.

We derived expressions relating the pump power to the second and third harmonic powers measured in back-reflection from the MoS_2 sample. Our derivation followed the work of Shen [She89], but formulated in SI units rather than using the Gaussian unit system and extended to consider THG in addition to SHG.[15]

Radiating Sheet Polarisation

When light travelling in air (medium 1) is incident on a material (medium 2), a fraction of the field will be reflected at the surface and the remaining light will be transmitted into it (according to the Fresnel equations [Hec02]). If sufficiently intense, this field can generate a nonlinear polarisation, which behaves as a polarisation sheet embedded in a dielectric interface layer. This sheet of radiating dipoles then emits electric fields at harmonics of the pump light, some fraction of which is transmitted back into medium 1.

A thorough mathematical treatment of the problem considers the angle at which light meets the surface and the state of optical polarisation. In this case, the p and s coordinate frame is a convenient approach for describing the oscillation direction of the field, as illustrated in Fig. 4.12a. This relates electric field components to the *plane of incidence* which contains the incident and reflected wavevectors (and is perpendicular to the surface): p-polarised light has a field direction parallel to the plane of incidence, while s-polarised light is perpendicular to it.[16] The general expression for these field components from a sheet polarisation of frequency ω_s, emitted back into medium 1 is [She89]:

$$\mathbf{E_p}(\omega_s) = i\frac{k_1}{2\epsilon_1 k_{2z}}\left[k_{2z}L_{xx}P_x(\omega_s)\hat{x} + k_x L_{yy}P_z(\omega_s)\hat{z}\right]\exp(i\mathbf{k_1}\cdot\mathbf{r} - i\omega_s t) \tag{4.2.6a}$$

$$\mathbf{E_s}(\omega_s) = i\frac{1}{2\epsilon_1}\left[k_1 L_{yy}P_y(\omega_s)\hat{y}\right]\exp(i\mathbf{k_1}\cdot\mathbf{r} - i\omega_s t) \tag{4.2.6b}$$

[15] A variety of expressions exist in the literature for converting between Gaussian and SI units, and between fields and intensities due to different approaches when defining the original field. Therefore, for consistency and to ensure that the equations we derived could be related to physical properties, we note that the SI units notation from Sutherland [Sut03] was adopted throughout.

[16] The letters s and p derive from German words 'senkrecht' (meaning perpendicular) and 'parallel'.

where subscripts m and h indicate the medium ($m = 1,2$) and axis component ($h = x,y,z$), respectively, for the wavevector k_{mh}, dielectric constant ϵ_m and the nonlinear sheet polarisation P_h induced at the interface. The dielectric constant is related to the material refractive index by $\epsilon_m = \epsilon_0 n_m^2$ [Sut03]. L_{hh} is a local field correction factor accounting for the different properties of each medium across the interface; physically, these are the well-known transmission Fresnel coefficients [Hec02].

Fortunately, since our experiments were all performed at normal incidence to the sample (along z), the P_z term was negligible and E_p and E_s were degenerate ($E_p = E_s = E$), greatly simplifying the mathematics (illustrated in Fig. 4.12b). The Fresnel transmission factor for normal incidence was therefore $L = L_{xx} = L_{yy} = 2n_1/(n_1 + n_2)$. Additionally, medium 1 was air, resulting in $n_1 = 1$, and medium 2 was SiO_2, which has a relatively small dispersion that we neglected (i.e. $n_2(\omega) = n_2(2\omega) = n_2$). Therefore, Eqns. 4.2.6 were simplified, resulting in an equation for the radiated field from the polarisation sheet back into free-space:

$$E_1(\omega_s) = \frac{\omega_s}{2\epsilon_0 c}\left(\frac{2}{1+n_2}\right) P(\omega_s)\exp(ik_1 z - i\omega_s t) \tag{4.2.7}$$

where

$$P(\omega_s) = \epsilon_0|\chi_s^{(n)}|E_{\text{sheet}}^n(\omega) = \epsilon_0|\chi_s^{(n)}|\left(\frac{2}{1+n_2}\right)^n E_1^n(\omega) \tag{4.2.8}$$

depends on the nth order nonlinear effect being observed from a surface with nonlinear surface susceptibility $\chi_s^{(n)}$ and the Fresnel transmission coefficient $2/(1+n_2)$ is used to relate the incident field in the interface sheet $E_{\text{sheet}}(\omega)$ to the input field in free space $E_1(\omega)$. Since we reduced this to a scalar problem, the susceptibility tensor was replaced by its complex modulus.

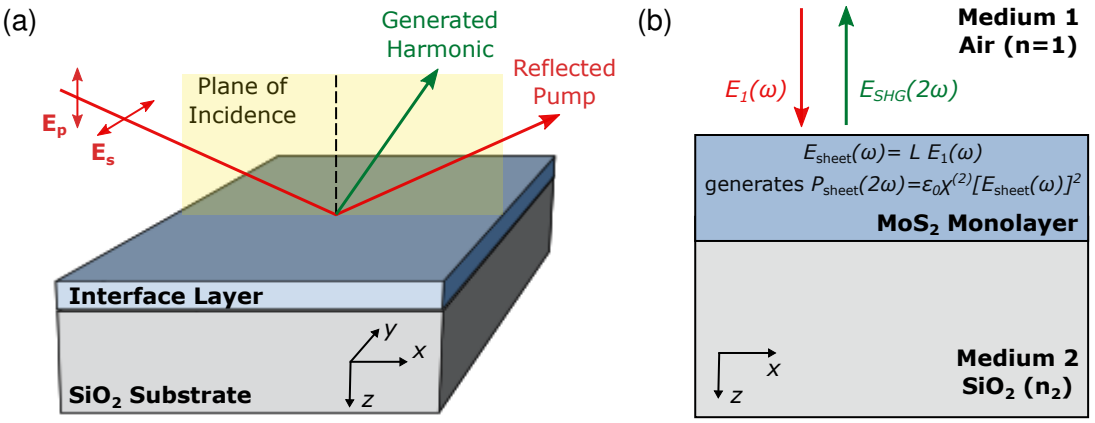


Fig. 4.12: Illustration showing the treatment of nonlinear surfaces: (a) generalised nonlinear harmonic generation from a surface, assuming a thin interface layer which acts as a radiating polarisation sheet under intense illumination; (b) our experimental setup for SHG, showing normal incidence pump light generating a nonlinear polarisation wave at frequency 2ω within the MoS_2 monolayer at the surface of the SiO_2 substrate. The surface polarisation radiated second harmonic light back into the air (we neglected reflected pump light at the interfaces and SHG transmitted into the SiO_2). Similar treatment applied for THG.

Second Harmonic Generation

For SHG, we found the backwards generated SHG amplitude in air by substituting the polarisation term $P(\omega_s = 2\omega) = \epsilon_0 |\chi_s^{(2)}| \left(\frac{2}{1+n_2}\right)^2 E_1^2(\omega)$ into Eqn. 4.2.7:

$$E_{\mathrm{SHG}}(2\omega) = \frac{(2\omega)}{2c} \left(\frac{2}{1+n_2}\right)^3 |\chi_s^{(2)}| E_1^2(\omega) \tag{4.2.9}$$

Optical intensities are related to field amplitudes by $I = 2\epsilon_0 nc|E|^2$ [Sut03]. Using this expression, we rewrote Eqn. 4.2.9 in terms of intensities:

$$I_{\mathrm{SHG}}(2\omega) = \frac{1}{\epsilon_0}\left[\frac{1}{2c}\left(\frac{2}{1+n_2}\right)^2\right]^3 (2\omega)^2 |\chi_s^{(2)}|^2 I_1^2(\omega) = \frac{32|\chi_s^{(2)}|^2\omega^2}{c^3\epsilon_0(1+n_2)^6} I_1^2(\omega) \tag{4.2.10}$$

The above intensity values are peak intensities, although in experiments we measured time-averaged powers. Temporally, the pump light was a train of Gaussian pulses, enabling us to write $P_{\mathrm{pk}} = SP_{\mathrm{av}}/(f t_{\mathrm{fwhm}})$ where the shape factor $S = 0.94$ for Gaussian pulses, f is the pulse repetition frequency and t_{fwhm} is the FWHM pulse duration. Additionally, our pump light was assumed to be a Gaussian beam in space with $I_{\mathrm{pk}} = 2P_{\mathrm{pk}}/(\pi r^2)$, leading to the expression:

$$I_{\mathrm{pk}} = \frac{2P_{\mathrm{av}}S}{\pi r^2 f t_{\mathrm{fwhm}}} \tag{4.2.11}$$

Henceforth, I is used to represent peak intensities (since this determines nonlinear effects) and P to denote the time-averaged powers, which could be measured experimentally. As second-order nonlinear polarisation is generated in proportion to the square of pump light intensity, the emitted SHG will have a beam radius and pulse duration which also have a Gaussian profile but with reduced FWHMs[17] by a factor of $\sqrt{2}$.

Finally, we substituted Eqn. 4.2.11 into Eqn. 4.2.10 for both the average input power $P_1(\omega)$ and the backwards SHG power $P_{\mathrm{SHG}}(2\omega)$, including the duration and beam width correction factor:

$$P_{\mathrm{SHG}}(2\omega) = \frac{16\sqrt{2}S|\chi_s^{(2)}|^2\omega^2}{c^3\epsilon_0 f \pi r^2 t_{\mathrm{fwhm}}(1+n_2)^6} P_1^2(\omega) \tag{4.2.12}$$

This approach was used to determine the magnitude of the surface nonlinear susceptibility $|\chi_s^{(2)}|$ at the air-SiO_2 interface. However, the interface was a layer of MoS_2 for which the material refractive index n_L and thickness δ were known. Therefore, Eqn. 4.2.12 could be rewritten in terms of an effective bulk nonlinear susceptibility for MoS_2 $|\chi_{\mathrm{eff}}^{(2)}|$:

$$P_{\mathrm{SHG}}(2\omega) = \frac{16\sqrt{2}S|\chi_{\mathrm{eff}}^{(2)}|^2\omega^2\delta^2}{c^3\epsilon_0 f \pi r^2 t_{\mathrm{fwhm}}(1+n_L)^6} P_1^2(\omega) \tag{4.2.13}$$

[17] This can be proved by squaring the expression for a Gaussian profile and comparing the width parameter to the original expression. If a different beam or pulse shape was assumed, the factor would be different.

Comparison of Eqn. 4.2.12 and Eqn. 4.2.13 suggested that the surface and effective bulk susceptibilities could be related by:

$$|\chi^{(2)}_{\text{eff}}| = \left(\frac{1+n_L}{1+n_2}\right)^3 \frac{|\chi^{(2)}_s|}{\delta} \tag{4.2.14}$$

Third Harmonic Generation

We derived an equation relating the THG field to the pump using the same method outlined for SHG, but replacing the polarisation term with $P(\omega_s = 3\omega) = \epsilon_0|\chi^{(3)}_s| \left(\frac{2}{1+n_2}\right)^3 E^3_1(\omega)$:

$$E_{\text{THG}}(3\omega) = \frac{(3\omega)}{2c}\left(\frac{2}{1+n_2}\right)^4 |\chi^{(3)}|E^3_1(\omega) \tag{4.2.15}$$

leading to THG intensity:

$$I_{\text{THG}}(3\omega) = \frac{1}{\epsilon_0^2}\left[\frac{1}{2c}\left(\frac{2}{1+n_2}\right)^2\right]^4 (3\omega)^2|\chi^{(3)}_s|^2 I^3_1(\omega) = \frac{144 I^3_1(\omega)|\chi^{(3)}_s|^2\omega^2}{c^4\epsilon_0^2(1+n_2)^8} \tag{4.2.16}$$

The cubic dependence of the THG intensity upon pump intensity led to a greater pulse and beam width reduction factor of $\sqrt{3}$, which we included when writing the intensities and powers (using Eqn. 4.2.11) to find:

$$P_{\text{THG}}(3\omega) = \frac{64\sqrt{3}S^2|\chi^{(3)}_s|^2\omega^2}{c^4\epsilon_0^2(f t_{\text{fwhm}}\pi r^2)^2(1+n_2)^8} P^3_1(\omega) \tag{4.2.17}$$

Finally, following the same procedure used for SHG, we were able to express the effective bulk third-order nonlinear susceptibility for MoS_2 as:

$$|\chi^{(3)}_{\text{eff}}| = \left(\frac{1+n_L}{1+n_2}\right)^4 \frac{|\chi^{(3)}_s|}{\delta} \tag{4.2.18}$$

In this analysis, we have modelled a three material stack of air, MoS_2 and SiO_2 by considering the MoS_2 layer as as interface between air and SiO_2. It could be argued that we must consider the MoS_2 as a material layer in its own right, forming interfaces with the air and SiO_2. However, we did not see SHG from even numbers of layer of MoS_2 (discussed later), which would be possible if the effect was interface-driven due to broken symmetry. Therefore, we believe this is a fair model of our experiment.

Experimental Results

Pump light with a linear polarisation state was focussed onto a fixed position within a MoS_2 monolayer and the intensities of the generated harmonics were recorded as a function of input power. For SHG, experimental data was well fitted by Eqn. 4.2.12, confirming the squared dependency of SHG power on fundamental pump power (Fig. 4.13).

This enabled a value of $|\chi_s^{(2)}| = 2 \times 10^{-20}$ m^2 V^{-1} to be extracted. Using n_L~4.4 [Wan15] and δ~0.7 nm [Lee10] for monolayer MoS_2 , we computed the effective bulk nonlinear susceptibility to be $|\chi_{\text{eff}}^{(2)}| = 3 \times 10^{-10}$ m V^{-1}.

For THG, experimental measurements showed a clear cubed dependence of THG power on pump power (Fig. 4.14) as expected. From this, we found $|\chi_s^{(3)}| = 6 \times 10^{-28}$ m^3 V^{-2} and an effective bulk value for MoS_2 of $|\chi_{\text{eff}}^{(3)}| = 2 \times 10^{-17}$ m^2 V^{-2} using Eqn. 4.2.18.

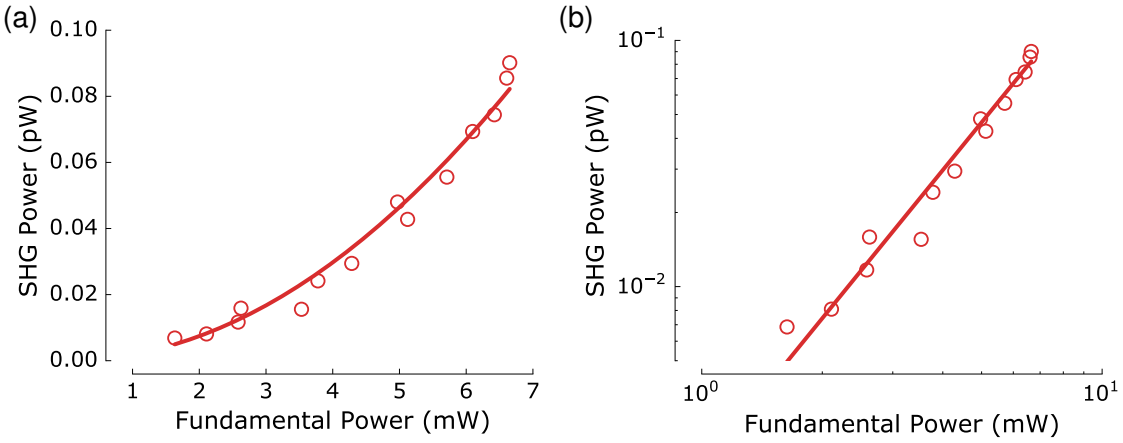


Fig. 4.13: Power of generated second harmonic from monolayer MoS_2 compared to the fundamental pump power: (a) linear axes; (b) log axes. Experimental data points have been fitted with Eqn. 4.2.12.

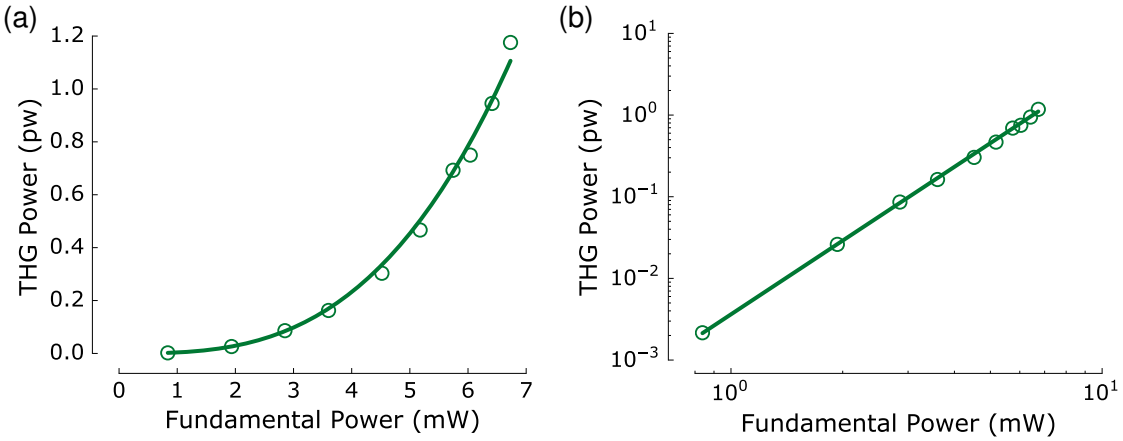


Fig. 4.14: Power of generated third harmonic from monolayer MoS_2 compared to the fundamental pump power: (a) linear axes; (b) log axes. Experimental data points have been fitted with Eqn. 4.2.17.

Comparison to Other Nonlinear Optical Materials

To assess the potential impact of monolayer MoS_2 for nonlinear optical applications, we compared our measured values to measurements on well-known materials in the literature. It is important to note that different measurement techniques can change

which contributions to the nonlinear response are included: in our case, we measured the complex modulus of MoS_2 off-resonance (1560 nm pump wavelength) at normal incidence (including only x and y components). Therefore, we compare to similar experiments using harmonic generation.

Bloembergen, Burns and Matsuoka previously considered various metals and semiconductors in THG experiments [Blo69]. For gold they found $|\chi^{(3)}| = 5.5 \times 10^{-11}$ esu, which in SI units is $|\chi^{(3)}| = 7.7 \times 10^{-19}$ m^2 V^{-2}, in agreement with many other more recent studies [Boy14]. To compare to a semiconductor material, we note that silicon was measured to possess $|\chi^{(3)}| = 2.0 \times 10^{-10}$ esu $= 2.8 \times 10^{-18}$ m^2 V^{-2} [Blo69]. Comparisons for the second-order nonlinear response are limited to non-centrosymmetric crystal structures. Measured values are often presented as second-order nonlinear coefficients d, which we converted to an estimated $|\chi^{(2)}|$ value using $|\chi^{(2)}| = 2d$ [Sut03]. Semiconductors cadmium sulfide and gallium arsenide have been measured to possess $|\chi^{(2)}| \sim 2 \times 10^{-11}$ m V^{-1}and $|\chi^{(2)}| \sim 3.4 \times 10^{-10}$ m V^{-1}, respectively [Sho02].

We conclude, therefore, that MoS_2 appears to offer up to an order of magnitude greater second and third-order nonlinearity compared to common optical materials and hence, could certainly be considered for future nonlinear photonic applications. However, an accurate assessment of the opportunities for emerging nanomaterials is heavily application-dependent and must consider the geometry of material in the setup and the laser source, since these are all factors that affect the response.

4.2.7 Imaging Few-Layer Flakes

We also applied the nonlinear microscopy technique to few-layer MoS_2 flakes fabricated by mechanical exfoliation. Fig. 4.15a shows an optical microscope image of the silicon substrate containing many few-layer MoS_2 flakes. This microscope included a 100× objective lens and was designed for visible light, whereas the beamsplitter in the linear microscope section of our linear-nonlinear setup was not anti-reflection coated and hence, back-reflection of the illumination sources degraded the image contrast (as shown in Fig. 4.15c). The image shows that many MoS_2 flakes had been deposited on the surface, each with a different contrast ratio. The large yellow and brown coloured regions are unexfoliated flakes of bulk MoS_2, whereas the dark green regions which appear partially transparent are few-layer forms of the material. Due to the mechanical exfoliation procedure, the exfoliated flakes here do not appear in triangular shapes as the CVD-grown flakes did.

We obtained SHG and THG images over a small region, shown in Fig. 4.15b. The scan range was limited by the time taken to measure the spectrum at each point, although this was a technical limitation and therefore, the technique should be scalable to much larger areas by using higher power pump signals (to reduce the integration time required in the spectrometer detector). The region of interest was known to contain a 2-layer and 7-layer flake (based on previous Raman and AFM measurements). The THG image showed these

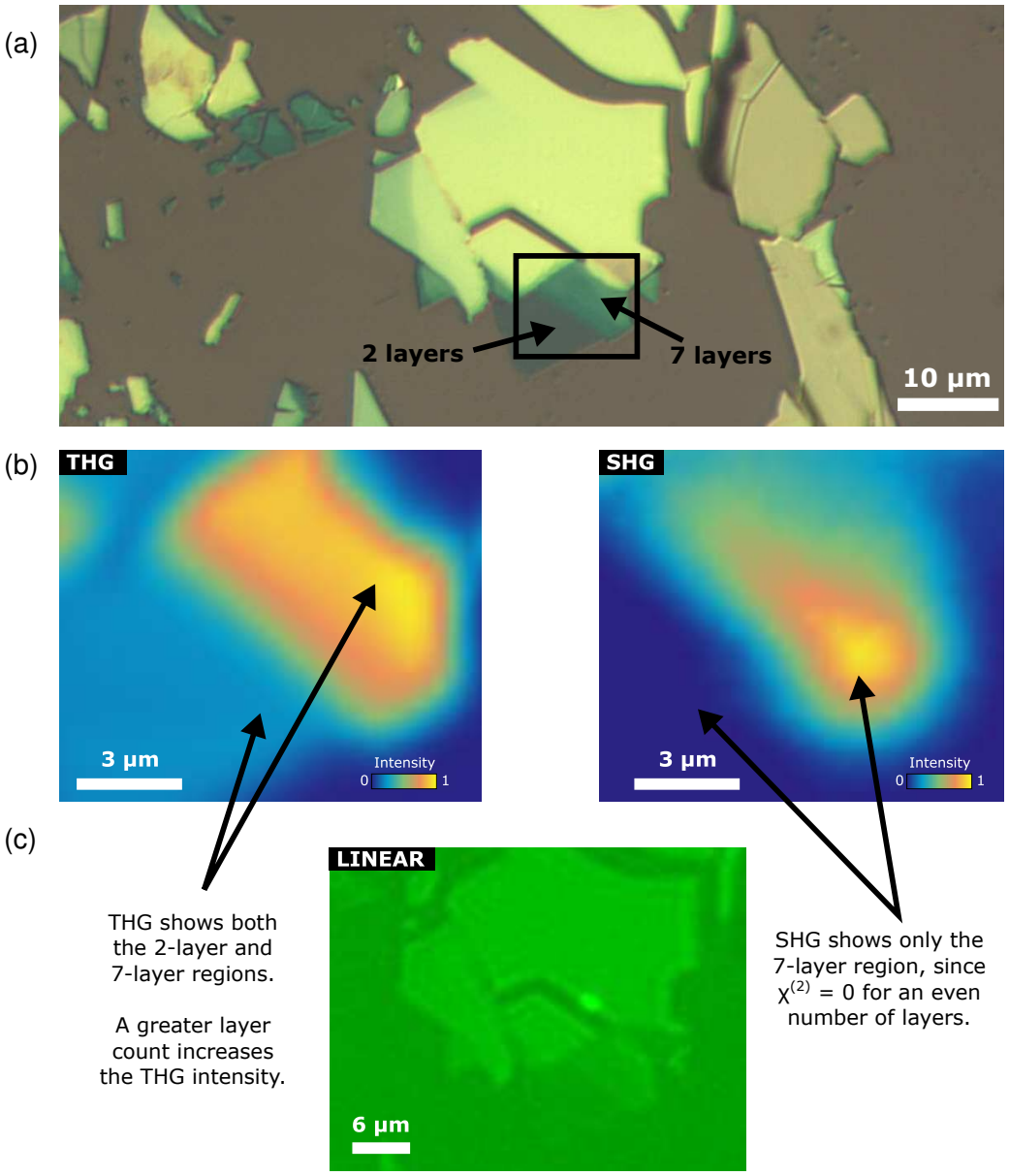


Fig. 4.15: Linear and nonlinear imaging of few-layer MoS_2 flakes: (a) standalone optical microscope image with 100× objective lens (Data courtesy of MackGraphe); (b) THG and SHG images of 2-layer and 7-layer regions; (c) optical microscope image from our integrated setup (20× objective lens).

two regions as areas of elevated pixel intensities above the negligible THG background level from the substrate, with a significantly stronger THG intensity for the greater layer count. By contrast, the 2-layer region in the SHG image was indistinguishable from the background, due to the electric dipole forbidden nature of $\chi^{(2)}$ processes for flakes with an even number of layers. We also show the linear microscope image for our system when illuminated by a green LED in Fig. 4.15c, which enabled us to determine the position of the flakes on the substrate, prior to recording the nonlinear images.

The SHG and THG intensity were recorded across numerous flakes of different thicknesses to determine the dependence of harmonic generation on the layer count (Fig. 4.16). As expected, it was found that no measurable second harmonic was generated with even numbers of layers and for the odd-layered flakes, the SHG increased slightly with an increasing number of layers. We note that the optical polarisation state of SHG from the sample depended on the orientation of the MoS_2 flake's crystallographic axis [Li13]. This orientation and hence, the polarisation state of reflected SHG was not considered in our measurements. Since the beamsplitter before the power measurements included a small ($\sim$10%) polarisation dependence, this added $\sim$10% uncertainty to the measured power values of P_{SHG} between different flakes. Further work will therefore repeat this experiment, including measurement of the SHG polarisation state and the application of correction factors for each flake independently.

A much greater dependence on the flake thickness was measured for the intensity of THG. The coherence length for backward-generated SHG and THG is [Pav13]:

$$l_{\mathrm{coh}} = \frac{\pi}{|k(h\omega) + hk(\omega)|} = \frac{\lambda}{2h(n_{h\omega} + n_{\omega})} \tag{4.2.19}$$

where h is 2 for SHG and 3 for THG, $k(\omega) = 2\pi n(\omega)/\lambda$ is the wavenumber and λ is the pump wavelength. Using MoS_2 refractive index values from Ref. [Wan15]: $n_{1560} = 3.639$, $n_{780} = 4.501$, $n_{520} = 4.341$, we found a coherence length of $\sim$35 nm for THG, and $\sim$50 nm for SHG. Since the coherence length was longer than the thickness of the flake, it was expected that harmonic intensities would be increased with a greater number of material layers [Kar15]. The relationship between harmonic intensity and layer count was expected to be quadratic from Eqn. 4.2.14 and 4.2.12. It is interesting to note that this trend was observed for our THG results, although the SHG intensity increased at a slower rate. The variation of the material properties of few-layer MoS_2 with layer count could account for this deviation. An additional factor could be absorption of generated light from one layer by adjacent layers. Finally, we note that the intensity of the third harmonic was stronger than the second harmonic, whereas the Taylor expansion of the nonlinear susceptibility function suggests that nonlinear effects should be weaker with increasing order. Work is ongoing to understand and explain these effects.

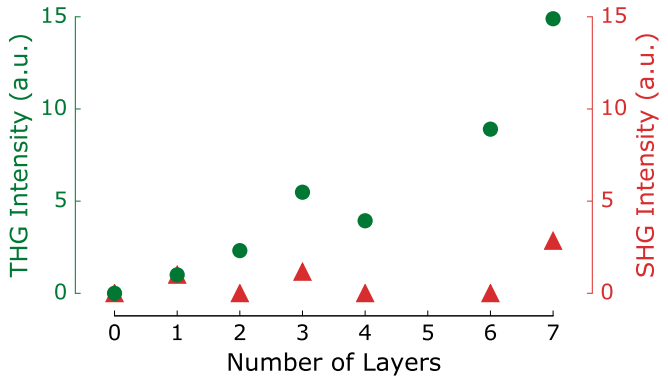


Fig. 4.16: THG and SHG intensity dependence on the number of layers in mechanically exfoliated few-layer MoS_2 flakes. SHG and THG have each been normalised to the intensity for a single layer; relatively, the THG intensity was approximately an order of magnitude stronger.

4.2.8 Discussion and Potential Applications of Nanomaterial-Based Harmonic Generation

The pump wavelength of 1560 nm (0.79 eV), second harmonic at 780 nm (1.59 ev) and third harmonic at 520 nm (2.38 eV) do not correspond to any of the excitonic peaks in monolayer MoS_2. Proximity of the virtual levels involved in harmonic generation to these resonances would enhance the conversion efficiency through greater coupling between the field and material polarisation, as recently demonstrated with SHG and THG near the A and B excitons [Cla14, Wan14a].

Another enhancement effect to SHG was recently reported from the edges of MoS_2 monolayers [Yin14]: Yin et al. observed up to 50% increased SHG intensity at the borders of flakes compared to their centres, attributed to a locally enhanced density of states. However, this resonance was wavelength dependent. We explicitly explored the edges by line raster scanning towards the corners of flakes, although observed no increase in intensity. Therefore, edge-enhanced harmonic generation does not appear to be present in our samples at 1560 nm pump wavelength.

We have demonstrated that harmonic generation can be a useful technique for materials characterisation, suitable for probing crystal symmetries, optical properties and the layer count of nanomaterial samples, but could few-layer MoS_2 benefit other nonlinear optical applications? The conversion efficiencies we achieved were poor: for over 6 mW pump power at 1560 nm, less than 2 pW light at 520 nm was generated, which could be attributed to the few nm interaction length of light with monolayer and few-layer MoS_2. However, compared to the silica substrate and other well-known semiconductors, the measured nonlinearity was up to an order of magnitude stronger. While the generation of second and third harmonics in few-layer MoS_2 cannot compete with phase-matched harmonic generation over much longer lengths in established bulk crystals for practical wavelength conversion, a potential application area is in pulse characterisation. Auto-

correlation and *frequency-resolved optical gating* (FROG) measurements measure ultrashort pulses by using nonlinearity to generate a slowly-varying 'information signal' that can be electronically measured and processed to obtain the pulse duration (and phase for the case of FROG) [Tre00]. Typically these devices employ bulk crystals and phase matching is required to generate a signal, thus limiting their wavelength range of operation and resolution. If second or third harmonics generated from pulses incident on few-layer MoS_2 could be used as the information signal, the device could technically operate over a much wider wavelength range as phase matching is not required for a measurable SHG/THG response. The device could also be very compact and would required minimal alignment, making it an interesting prospect for future work. Additionally, we suggest that few-layer MoS_2 could have a high impact as a semiconductor material for nonlinear photonics in the technologically important telecommunications spectral region, if harnessed for on-chip signal processing and optical switching.

4.3 Few-Layer MoS_2 as a Wideband Saturable Absorber

In this section we report the development of MoS_2-based *saturable absorbers* (SAs) for passive Q-switching and mode-locking of fibre lasers. The fabrication procedure and optical characterisation of nanomaterial devices are presented, followed by demonstrations of pulse generation within ytterbium and erbium gain bands. It may seem counter-intuitive that saturable absorption is exhibited at infrared wavelengths when the bandgap of the material is expected to correspond to the visible spectral region. Therefore, we propose an explanation based on nanomaterial size effects to account for this phenomena. First, however, the history of saturable absorber technologies is briefly reviewed, highlighting the motivation for this work.

4.3.1 Brief History of Saturable Absorbers

Advances in saturable absorber technologies are almost synonymous with the evolution of the laser itself. Even before the first demonstration of lasing in 1960, researchers were considering how to manipulate the temporal output properties.[18] It was no surprise, therefore, that Q-switched 'giant pulses' from a ruby laser were reported only two years after Ted Maiman's seminal demonstration [McC62].

While this first pulsed system employed *active* Q-switching using an electrically-driven Kerr cell, researchers were quick to consider nonlinear absorption of materials for *passive* pulse generation. Early note-worthy experiments included an absorbing dye [Mas63] and metallic film [Gra63] in a ruby laser cavity, which held the Q-factor low until sufficient energy built up to damage the film and to escape as a single giant pulse. This was described as 'Q-spoiling using an exploding film' and while the irreversible nature of the process perhaps restricts us from describing it as a Q-switched laser, they were certainly

[18] Gordon Gould is credited with first proposing Q-switching in his 1958 notebook [Tay07].

novel demonstration using absorbing materials to manipulate the temporal output. Stable, repeatable passive Q-switching was demonstrated shortly afterwards using dyes [Sof64a, Kaf64, Sor64] and coloured glasses [Bre64]. These materials were initially referred to as 'reversibly bleachable absorbers' and 'saturable filters', before the community converged on the term 'saturable absorber' [Sza65].

Saturable absorbers were also used to mode-lock lasers, although with limited success initially due to the more demanding cavity dynamics required for coherent phase-locking of modes. The earliest reports demonstrated very short mode-locked pulses within a Q-switched giant pulse envelope, which was achieved using intensity-dependent absorption in colour-filter glass [Moc65] and dyes [DeM66] in a ruby laser. This regime is referred to as *Q-switched mode locking*, in contrast to *cw mode locking* that produces a continuous train of equal-intensity ultrashort pulses. Indeed, it was not until 1972 that Ippen, Shank and Dienes reported a cw mode-locked laser (with a dye gain medium), producing 1.5 ps pulses, using a saturable absorber dye cell, containing diethyloxadicarbocyanine iodide in methanol [Ipp72a]. Given the broad scope of the field, we now restrict our focus to the development of saturable absorbers for fibre lasers (as illustrated in Fig. 4.17).

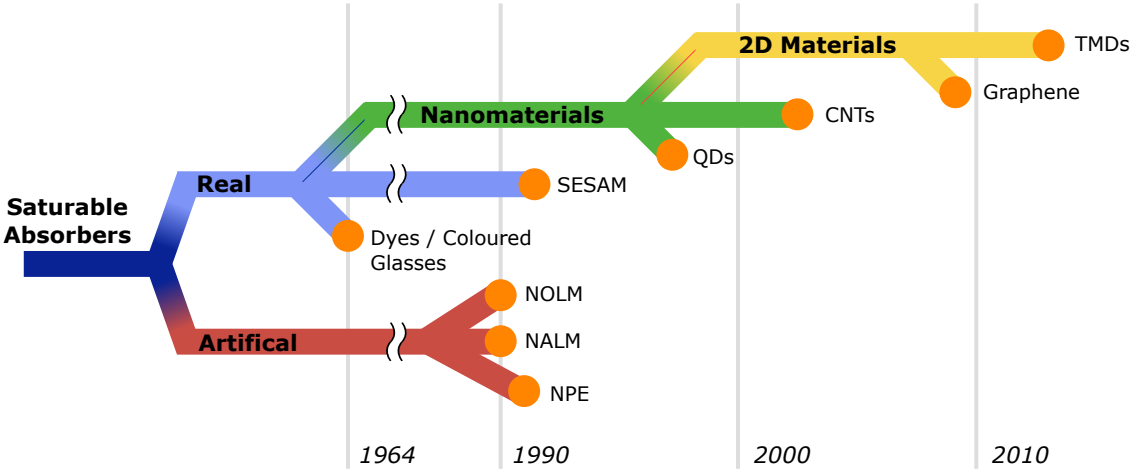


Fig. 4.17: Illustrated evolution of salient saturable absorber technologies for fibre lasers. Orange dots denote the first reported application of each technology in a pulsed laser.

Saturable Absorbers for Fibre Lasers

Shortly after demonstrating pulsation of a ruby laser using a saturable dye, Soffer and Hoskins applied the dye to Q-switch a neodymium-doped glass rod laser, paving the way to Q-switched fibre lasers [Sof64b]. Passive mode-locking with fibre gain media, however, took longer to be experimentally verified. The first reference to this feat in 1983 used a bleachable dye with neodymium-doped fibre, although the result shows partial mode locking including strong Q-switching modulations [Dzh83].

Several years passed until a flurry of successful demonstrations emerged in the early 1990s showing cw passively mode-locked fibre lasers. Notably, this included the applica-

tion of a *nonlinear-optical loop mirror* (NOLM) to form a figure-of-eight mode-locked Er:fibre laser [Bul90, Avr90, Dul94]. A NOLM is formed using a non-50% fibre coupler where the two ports on one side are connected and a length of passive fibre is included in this loop [Dor88]. The non-reciprocity of the loop results in different phase accumulation for clockwise and counter-clockwise travelling pulses, which interfere when they recombine at the output port. The asymmetric phase change also depends on the input peak power, such that the interference condition and subsequent fraction of light transmitted is power-dependent. This effect can also be achieved with a 50% coupler ratio and an amplifier in the loop, known as a *nonlinear amplifying loop mirror* (NALM) [Fer90, Dul90, Dul91b]. Other important experiments included the use of a linear external cavity to initiate fibre laser pulsation [Wig90] (which can explained as additive pulse mode locking [Blo88, Ipp89]) and exploiting nonlinear polarisation rotation in fibres followed by a polariser to create intensity-dependent loss, enabling *nonlinear polarisation evolution* (NPE) mode locking [Hof91]. These techniques were rapidly confirmed by other groups and shown to routinely produce sub-picosecond pulses [Dul91a, Hof92, Mat92, Nos92, Tam92].

These NALM-, NOLM- and NPE-based devices all exploit nonlinearity in fibre to induce an intensity-dependent loss. The response time is therefore almost instantaneous, although the quality and stability of generated pulses can be poor, due to overdriving of these effects and susceptibility to changes in the fibre properties from environmental changes (e.g. thermally-induced birefringence changes). Therefore, while the behaviour they exhibit warrants their classification as saturable absorbers, they are often described as *artificial* saturable absorbers to distinguish them from materials with intrinsic nonlinear absorption, which are *real* saturable absorbers.

The early 1990s also saw rapid progress in the development of semiconductor materials as real saturable absorbers for fibre lasers. An InGaAs/GaAs-on-GaAs superlattice fabricated using molecular beam epitaxy was found to exhibit intensity-dependent loss and enabled 1.2 ps pulse generation from an Er:fibre laser [Zir91]. Physically, saturable absorption is related to interband transitions of electrons from the valence band to the conduction band of the semiconductor when a photon is absorbed. At low optical intensities, the absorption is constant. However at high incident intensities, many electron are excited to the upper states of the material, accumulating in the conduction band. According to the Pauli Exclusion Principle, two electrons cannot occupy the same quantum state simultaneously [Pau25]; therefore, when upper energy levels are occupied, further upward transitions are blocked (*Pauli blocking*) and the optical absorption is reduced, i.e. *saturated* (illustrated in Fig. 4.18).

In 1992, the *semiconductor saturable absorber mirror* (SESAM) was developed – a semiconductor device containing a Bragg mirror and quantum well absorber [Kel92a, Kel96] – which rapidly emerged as the dominant and most successful saturable absorber technology to date. This was due, in part, to the wide variability in parameters that could be achieved by modifying the structure and materials used, enabling SESAMs to be fabricated for specific lasers and applications. Most notably, SESAMs enabled passive self-starting cw

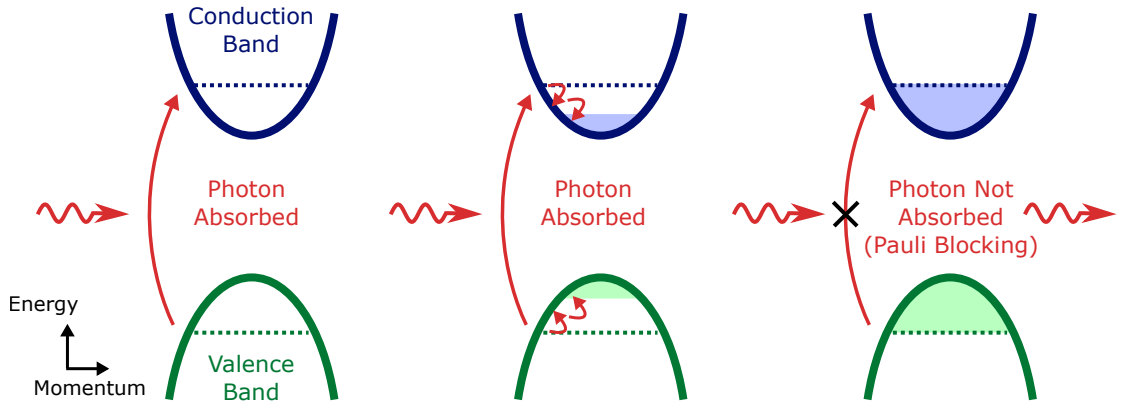


Fig. 4.18: Illustration of the saturable absorption mechanism in semiconductors based on Pauli blocking. Simplified band structures are shown at three points of material excitation: (a) initially, incident photons are absorbed, exciting electrons from the valence band to the conduction band; (b) carriers in each band then rapidly thermalise, leaving unoccupied levels for further absorption and photoexcited electrons; (c) under intense illumination (on timescales shorter than material relaxation through carrier recombination), the upper states become fully occupied, forbidding further electrons being excited into the conduction band according to the Pauli exclusion principle and thus, saturating the absorption.

mode locking of bulk lasers for the first time, but the technology also benefited fibre-based systems by allowing self-starting sub-picosecond mode-locking from inserting a monolithic device into the cavity [Loh93, DeS93]. While researchers were focussing intently on mode-locked fibre lases, it should also be noted that Q-switched lasers in fibre were under consideration for applications requiring high-energy ns-µs pulses such as laser range finding and material processing. By the end of the decade, SESAMs had been applied to Q-switch an Er:fibre system producing 0.1 mJ pulse energies [Pas99].

Performance of State-of-the-Art Saturable Absorbers

An important parameter for saturable absorbers is their recovery time: the time taken for the excited state to decay, returning the absorption to its unsaturated value. Depending on the response time relative to the pulse duration of the laser, a saturable absorber can be described as *fast* or *slow*. In general, a fast saturable absorber is preferred to produce the shortest possible pulses. However, it should be noted that slow saturable absorbers can still be used to generate bursts of light shorter than their recovery time (due to the influence of other pulse shaping mechanisms, such as soliton effects) and generally offer better self-starting performance [Kär98]. Artificial saturable absorbers operate by exploiting almost-instantaneous nonlinear responses in materials, whereas the recovery time of real saturable absorbers is highly dependent on carrier dynamics within the material. Additionally, other significant parameters include:

- Modulation depth - the maximum possible change in loss due to optical excitation.
- Saturation intensity - the optical intensity required to reduce the absorption by half

of its saturable value.

- Nonsaturable loss - the residual device loss when fully saturated.

The demands of a saturable absorber are strongly dependent on the target laser and desired pulse properties. For example, the saturation intensity and modulation depth determine the threshold for Q-switching and mode-locking. Naively, lowering either of these two values will reduce the tendency for Q-switching and Q-switched mode locking if one wanted to achieve a cw mode-locked operation. However, in a fibre laser, where significant losses can be tolerated due to the high gain, in addition to strong pulse shaping effects from dispersion and nonlinearity, a lower modulation depth can inhibit self-starting. Additionally, in a Q-switched laser, the repetition rate and pulse duration are strongly coupled to the recovery times of the gain and the absorber [Pas08]. It is generally the case, however, that fast recovery and low nonsaturable losses are preferred to improve laser efficiency.

From this brief discussion, it can be seen that we cannot specify globally optimum saturable absorber properties. We also note that in addition to these properties controlling pulse dynamics, other characteristics are important for a successful saturable absorber technology such as the damage threshold, environmental stability, range of operating wavelengths and the ease and cost of fabrication.

NPE mode locking is perhaps the mostly commonly employed technique for developing mode-locked fibre lasers in research environments, given the instantaneous response time and large variation in modulation depth and saturation intensity that can be achieved by modifying polarisation biases in the setup. However, the dependence on a change in polarisation state demands the use of low birefringence fibres, which are intrinsically sensitive to thermal and mechanical fluctuations [Agr01]. NPE-mode-locked lasers therefore lack the required stability and reliability to be industrial devices.

While SESAMs continue to enjoy commercial success for both bulk and fibre laser applications, they are not without their limitations. Firstly, their fabrication by molecular beam epitaxy is expensive and post-processing ion implantation is required to create defects states to accelerate the relaxation time to a sub-picosecond scale. Additionally, the limited operating bandwidth and requirement to operate in a reflective geometry are not suitable for all laser designs [Kel03]. Recent research has therefore considered alternative saturable absorber materials such as nanomaterials.

Nanomaterial Saturable Absorbers

It could be argued that early reports of saturable absorption using coloured glass filters exploited nanomaterials, since the glasses were doped with semiconductor nanocrystals [i.e. zero-dimensional *quantum dots* (QDs)] such as cadmium selenide [Bre64] to modify their colour. However, it was not until 1997 that QDs were explicitly engineered for the purpose of pulse generation [Gue97]. After this demonstration, the field of nanomaterial

saturable absorbers gained traction as *carbon nanotubes* (CNTs) emerged as a promising material exhibiting nonlinear absorption and ultrafast carrier dynamics [Set03]. As we discussed in Section 4.1.1, the resonant wavelength for the fundamentalE_{11} transition for semiconducting nanotubes can be varied by fabricating tubes with different diameters, enabling pulse generation demonstrations from 810 nm [Khu10] to 2100 nm [Cha12]. Higher order electronic transitions have also been used for Q-switching and mode-locking, although the saturation intensity for the E_{22} transition was found to be an order of magnitude higher than using E_{11} [Tra11]. Additionally, for broadband operation of a single saturable absorber device, a distribution of nanotubes with different diameters can be used, although the non-resonant tubes increase the non-saturable loss [Kiv09]. The response time of nanotube saturable absorbers is on sub-picosecond timescales, leading to demonstrations of nanotube-mode-locked ultrafast fibre lasers [Has09]. Visible-wavelength nonlinear optical applications of nanotubes have been restricted, however, by difficulty in fabrication nanotubes with sufficiently small diameter to yield a bandgap at visible wavelengths [Has09].

Nanotube saturable absorbers are very flexible and particularly advantageous for fibre lasers as they can be integrated into various optical components to preserve the all-fibre alignment-free format. To date, CNTs have been embedded in a polymer composite that can be sandwiched between two fibre patchcords, used to fill the holes in a *photonic crystal fibre* (PCF) and deposited on side-polished fibre and microfibres to exploit the evanescent field interaction over long distances [Mar13]. Such integrated saturable absorber devices are not possible using SESAM technology.

Following the early successes of carbon-based nanomaterial saturable absorbers, graphene was proposed as a suitable material for such applications [Has09, Bao09]. Many of the fabrication techniques for nanotubes could be applied for developing graphene-based devices, producing versatile and flexible saturable absorber devices. The major strength of graphene, however, is intrinsic wideband operation, offering saturable absorber devices that can theoretically operate resonantly from the visible through to the mid-infrared [Bon10].

The mechanism of saturable absorption in graphene is understood by considering the photoexcited electron dynamics. Optical illumination causes interband excitation of electrons across the zero bandgap, creating a non-equilibrium carrier popular in the valence and conduction bands. Rapid thermalisation occurs, with carrier relaxation due to carrier-carrier intraband collisions and phonon scattering (on $<$100 fs timescales). Electron interband relaxation also occurs on a slightly longer ($\sim$1 ps) timescale from electron-hole recombination. However, if the incident light is sufficiently intense, photoexcited carriers accumulate at the edges of the conduction and valence bands, filling the available states (according to the Pauli Exclusion Principle) and preventing further absorption. The presence of two relaxation timescales is favourable for a saturable absorber: the quickest relaxation enables the shortest possible pulses to be generated, while the slower relaxation improves the self-starting performance [Bao09, Sun10].

A wide variety of lasers have exploited graphene for passive pulse generation [Sun12, Mar13], including both fibre and bulk lasers and with operating wavelengths from 800 nm [Bae12] to 2930 nm [Zhu13]. However, while wideband operation is possible, the performance of graphene saturable absorbers is strongly wavelength dependent as the saturation intensity scales inversely with wavelength [Mar13], favouring short-pulse generation at infrared wavelengths; to date, mode-locking at visible wavelengths with a graphene SA remains a challenge to be overcome.

Therefore, great interest from the saturable absorber community followed the exfoliation of monolayer MoS_2 and the possibility of semiconducting TMDs with bandgaps at visible wavelengths, tunable by the number of layers. Studies have also computed the MoS_2 intraband relaxation time as $\sim$30 fs [Wan13] and interband transitions have been reported on picosecond timescales [Wan12b] suggesting ideal fast saturable absorber behaviour.

4.3.2 Few-Layer MoS_2-PVA Saturable Absorber Fabrication

We developed few-layer MoS_2-polymer composite films, in collaboration with the University of Cambridge, by fabricating few-layer MoS_2 flakes using *liquid-phase exfoliation* (LPE) and embedding them into a *polyvinyl alcohol* (PVA) host matrix.[19] The resulting devices were robust, easily-handled and suitable for integration into fibre systems.

Liquid Phase Exfoliation of Few-Layer MoS_2 Flakes

Procedure First, MoS_2 powder (120 mg) was mixed with 90 mg of sodium deoxycholate (SDC) bile salt (to act as a surfactant) in 10 mL of deionised water for ultrasonication, lasting $\sim$2 hr at a constant temperature of $\sim$5°C. The thick unexfoliated bulk MoS_2 flakes were then sedimented via ultracentrifugation (at 4200g), enabling the top 80% of the dispersion to be collected that is enriched in single- and few-layer flakes.

Characterisation The linear absorption spectrum of the MoS_2 dispersion, diluted to 10 vol% and measured using a spectrophotometer, is shown in Fig. 4.19a. The four observed peaks, at $\sim$665 nm, $\sim$605 nm, $\sim$440 nm and $\sim$395 nm, are termed A, B, C and D according to standard nomenclature [Wil69]. A and B are excitonic transitions, arising from spin-orbit band splitting of the valence band as discussed in Section 4.1.3. C and D represent transitions between higher density of state regions in the MoS_2 band-structure [Bea72, Bro72].

To determine the number of layers and to evaluate the crystal quality, Raman spectroscopy was used. MoS_2 has four Raman-active modes (E_{1g}, E^1_{2g}, A_{1g} and E^2_{2g}) and two IR-active modes (A_{2u} and E_{1u}) [Lee10, MS11]. The E^1_{2g} is an in-plane mode generated by the opposing vibration of the two S atoms with respect to the Mo atom, while the A_{1g} mode comes from the out-of plane modes of S atoms vibrating in opposite directions. From

[19] We thank Dr Tawfique Hasan, Richard Howe and Guohua Hu for nanomaterial fabrication and fruitful discussions throughout our collaboration.

monolayer to bulk, the E^1_{2g} mode red shifts, which has been attributed to an enhancement of the dielectric screening of the long-range Coulombic interaction between the effective charges with a growing number of layers [MS11]. The A_{1g} mode, however, blue shifts due to increased van der Waals interactions in thicker samples [Cha13]. Consequently, the frequency shift between E^1_{2g} and A_{1g} modes can be used to determine the number of layers.

The measured Raman spectra in Fig. 4.19b shows the relative position of two peaks close to 400 cm^{-1}, corresponding to the in-plane (E^1_{2g}) and out of plane (A_{1g}) vibration modes. For the dispersed MoS_2 flakes, the frequency difference was 24.62 $\pm$ 0.02 cm^{-1}, compared with 25.29 $\pm$ 0.03 cm^{-1} for bulk MoS_2, confirming the presence of few-layer MoS_2 flakes. By comparing our flake frequency difference to detailed layer-dependent studies of MoS_2 Raman spectroscopy [Cha13, MS11, Lee10], we estimated a thickness of 4-6 layers.

To verify this measurement, we used AFM to measure the distribution of flake thicknesses in the dispersion. Two traces measured across a typical flake are shown in Fig. 4.20a, and the combined distribution over hundreds of flakes (Fig. 4.20b) revealed that ~50% of the flakes had a thickness of 2-4 nm, corresponding to 3-5 layers (assuming ~1 nm measured thickness for a monolayer flake, and ~0.7 nm increase for each subsequent layer [Lee10]), in agreement with the Raman spectroscopy measurements. In terms of lateral dimensions, the average flake size was ~130 nm, with ~50% of flakes having less than 100 nm dimensions (Fig. 4.20b).

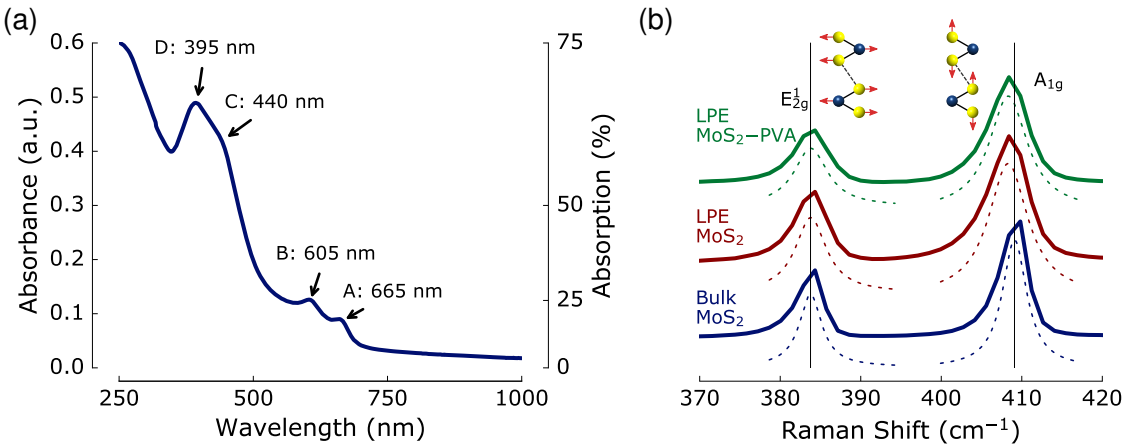


Fig. 4.19: Characterisation of dispersed MoS_2 flakes: (a) optical absorption; (b) Raman spectra comparing bulk MoS_2, dispersed few-layer MoS_2 flakes and the MoS_2-PVA composite (dotted lines show the Lorentzian peak fitting which was used to determine the Raman shift value for each peak). Data courtesy of University of Cambridge.

Integration of Few-Layer MoS_2 into a Polymer Composite

Procedure We mixed 4 mL of MoS_2 dispersion with 2 mL of 15 wt% aqueous PVA solution, followed by air drying over a 24 hour period. This produced a ~25 µm-thick

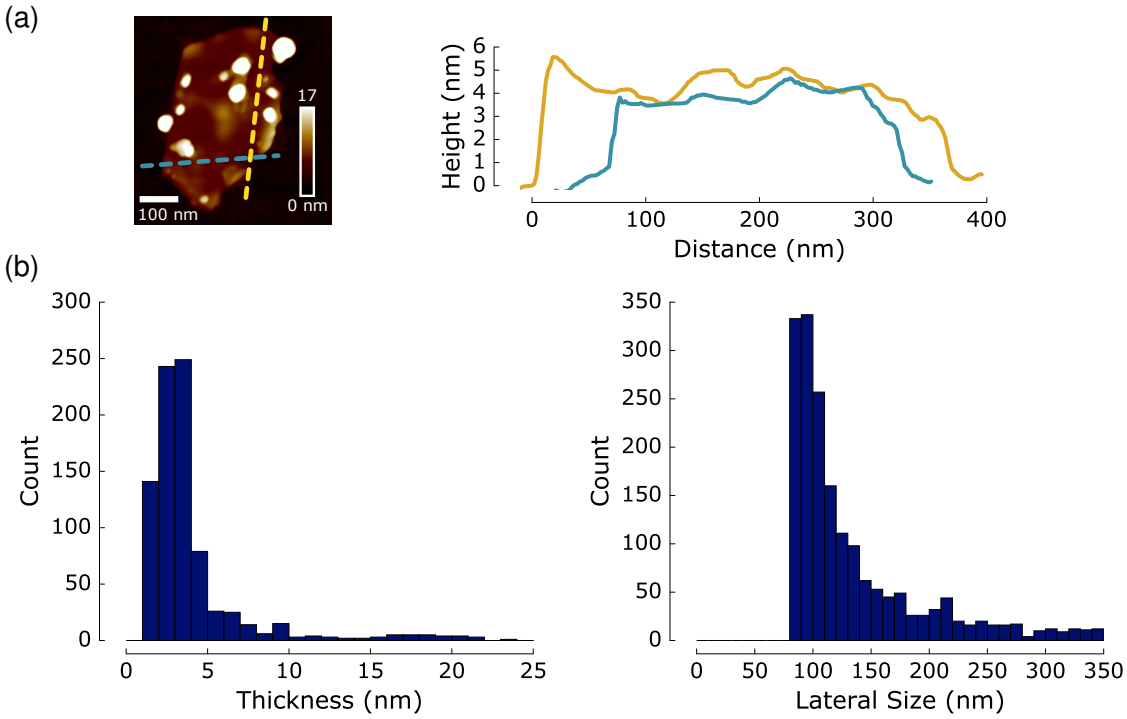


Fig. 4.20: Geometric characterisation of few-layer MoS_2 flake distributions using atomic force microscopy: (a) height profile over a whole flake, showing two traces mapped to 2D height profiles; (b) histograms showing distribution of thicknesses and lateral sizes. Data courtesy of University of Cambridge.

free-standing polymer composite film.

Characterisation An optical microscope and *scanning electron microscope* (SEM) were used to confirm a uniform distribution of flakes throughout the composite film and to verify the absence of large (>1 μm) aggregates, which could otherwise lead to scattering losses. Using Raman spectroscopy, we confirmed that the MoS_2 structure was unaffected by its inclusion in the composite, shown by a lack of significant shift in the Raman peak positions between the LPE MoS_2 and LPE MoS_2-PVA (Fig. 4.19b) The linear absorption spectrum of the composite showed the same characteristic features as the MoS_2 dispersion and a notable increase in absorption compared to a pure PVA film of the same thickness (Fig. 4.21). This suggests that MoS_2 flakes in our sample are responsible for the increased value of absorbance, confirming absorption of light (assuming negligible scattering contribution) in the near-infrared region corresponding to photon energies below the MoS_2 bandgap. We discuss this observation in detail in Section 4.3.5.

The nonlinear optical properties of our MoS_2-PVA composite were characterised using an *open-aperture Z-scan* experiment: a widely-used technique which was first proposed by Sheik-Bahae, Said and Van Stryland [SB90]. The sample was moved through the focal plane of a beam of ultrashort pulses, varying the area of illumination and consequently, the peak intensity. By recording the transmitted power, in addition to the power before the

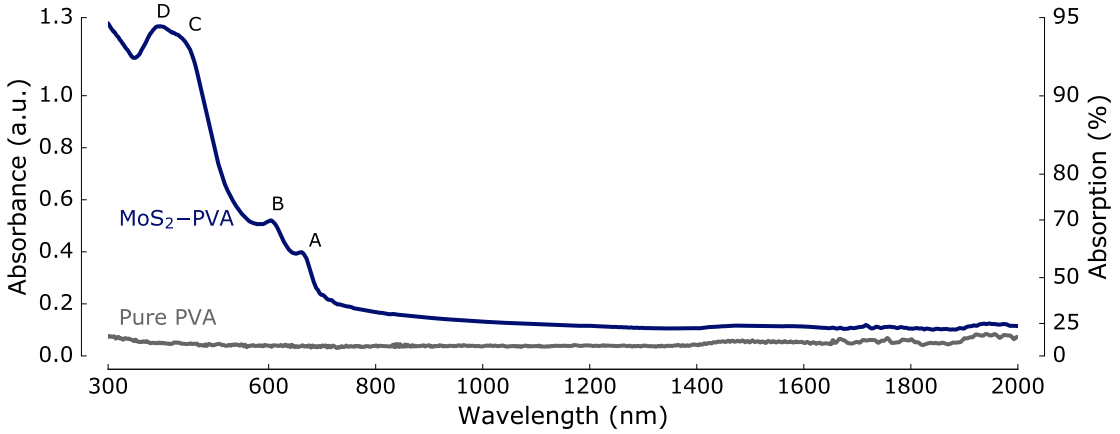


Fig. 4.21: Optical absorption spectrum of MoS_2-PVA composite film and pure PVA film, both 25 μm thick.

sample as a reference for normalisation, the material absorption was recorded with respect to the incident intensity (illustrated in Fig. 4.22a). We performed Z-scan measurements at wavelengths corresponding to ytterbium- and erbium-doped media, to assess the potential of the material as a saturable absorber for typical fibre laser spectral regions.

For the ytterbium spectral region pump source we employed an amplified, SESAM-mode-locked Yb:fibre laser, emitting 12 ps pulses at a repetition rate of 26.4 MHz with 1065 nm central wavelength (IPG YLP-10-ps). To improve the peak power, we used a double-pass diffraction grating pair compressor (with 1200 lines per mm) to reduce the pulse duration to ∼500 fs (a detailed explanation of grating-based pulse compression is presented in Section 3.3). A slight pulse pedestal was observed after compression, although it was computed that >80% of the measured power was contained within the pulses, and this was taken into consideration in calculations. For a pump source to probe the nonlinear response at 1565 nm, we developed an Er:fibre mode-locked laser, directly generating 750 fs pulses with 7.5 MHz repetition rate.

At both pump wavelengths, we observed a decreased material absorption with increasing peak intensity (Fig. 4.22b & c). This confirms that the fabricated MoS_2-PVA composite exhibited saturable absorption. To extract values for performance parameters, we fitted the intensity-dependent absorption, $\alpha(I)$, using a two-level fast saturable absorber model [Gar00]:

$$\alpha(I) = \frac{\alpha_s}{1 + I/I_{sat}} + \alpha_{ns} \tag{4.3.1}$$

where I is pump light intensity, I_{sat} is the saturation intensity, α_s and α_{ns} are the saturable loss (i.e. modulation depth) and non-saturable loss, respectively.

Experimental data at 1565 nm excitation was well fitted by the model. We found: $\alpha_s \sim 10.7\%$, $\alpha_{ns} \sim 14.7\%$, and $I_{sat} \sim 2$ MW cm^{-2}. However, the two-level model appeared less suitable for describing the absorption at 1065 nm, due to an increase in absorption towards the highest intensity values (the maximum intensity was limited by the pump

source). Similar absorption profiles have also been observed in nonlinear characterisation of SESAM devices, attributed to multiphoton absorption [Tho99]. We believe that *two-photon absorption* (TPA) was present at 1065 nm for our sample, since two pump photons had sufficient combined energy to excite a single electron across the MoS_2 bandgap. However, under 1565 nm excitation, three photons were needed to cause this transition; the occurrence of this effect was thus less probable, and not observed experimentally. TPA can be included in the fast saturable absorber model by adding a $+\beta_{\text{eff}} I$ term, where β_{eff} is the effective TPA coefficient.

With this modification, the quality of the fit to experimental data was greatly improved (Fig. 4.22a). Values for the modulation depth and saturation intensity were 6.3% and 7 MW cm^{-2} respectively, and the fit yielded a TPA coefficient value of 0.087 cm^2 MW^{-1}. We also performed a Z-scan measurement on pure PVA, but observed no change in absorption, confirming that the response in the composite arose from the MoS_2flakes. The saturable absorption response of the MoS_2-PVA composite suggested that it could be used to modulate the loss and the Q-factor of a laser cavity to generate a regular train of pulses.

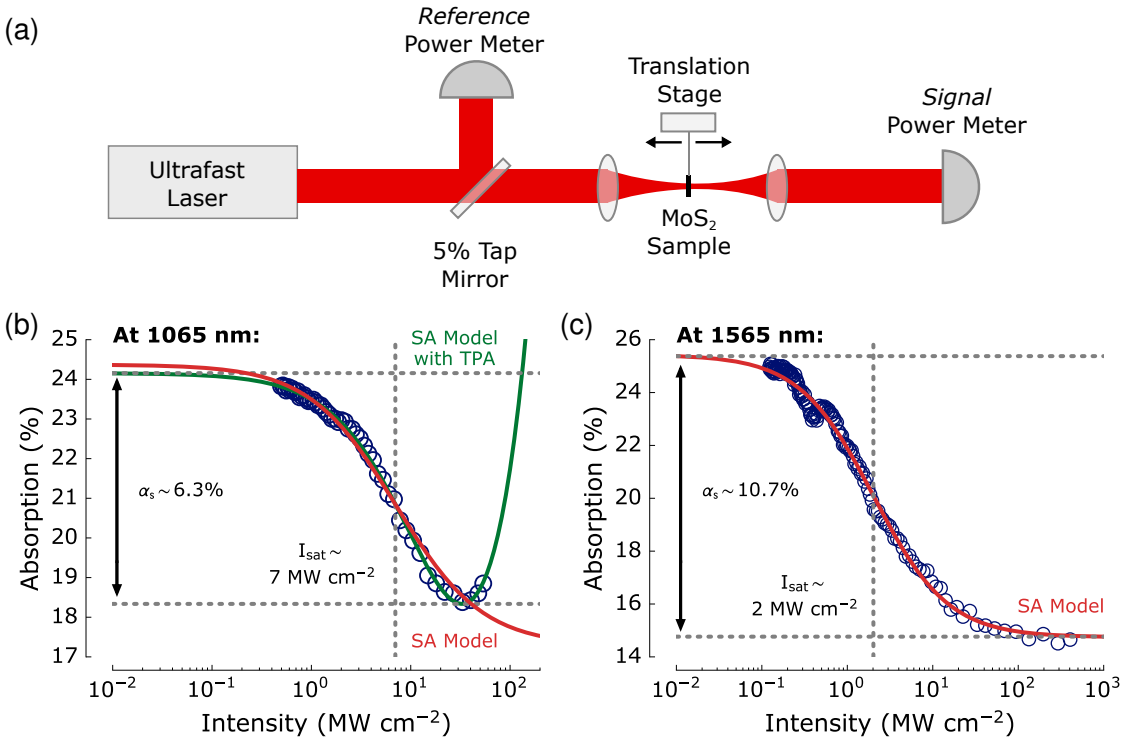


Fig. 4.22: Open-aperture Z-scan experiment for nonlinear absorption characterisation: (a) schematic; (b) measured profile at 1065 nm; (c) measured profile at 1565 nm. The solid green and red lines are fits to the two-level fast saturable absorber model with and without a two-photon absorption contribution, respectively.

4.3.3 Q-switched Yb-doped Fibre Laser

A Yb:fibre laser was developed with a ring cavity design, using a 1.5 m double-clad ytterbium-doped amplifier fibre (Fig. 4.23). The MoS_2 saturable absorber was inserted into the cavity by sandwiching a $\sim$1 mm$\times$1 mm piece of the composite between angled patch cords (Fig. 4.24). A polarisation-independent isolator, 10% output coupler and a polarisation controller were also included. To enable tuning of the lasing wavelength, we added a tunable bandpass filter, constructed from a fibre-coupled air gap with an angle-tunable 1 nm bandwidth bandpass interference filter. The total cavity length was $\sim$13 m.

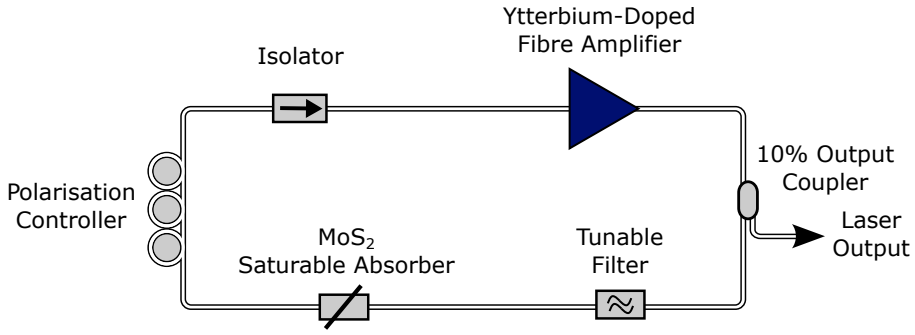


Fig. 4.23: Schematic of Q-switched Yb:fibre laser including a MoS_2-PVA saturable absorber.

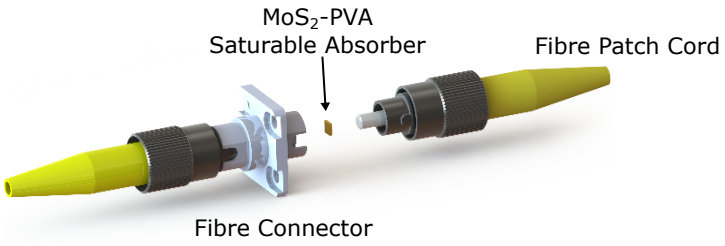


Fig. 4.24: Illustration showing the integration of MoS_2-PVA composite film into fibre-based systems by sandwiching a $\sim$1 mm $\times$ 1 mm piece of composite film between two fibre patch cords.

As the amplifier pump power was increased, the cavity initially lased in a continuous-wave regime. By further increasing the pump power, self-starting Q-switching was observed, producing a stable train of pulses. Typical output characteristics of the laser at 1055 nm wavelength and 9.36 mW average output power are shown in Fig. 4.25. Pulses were generated with 13.4 µs pulse spacing, corresponding to 74 kHz repetition rate, and a FWHM pulse duration of 2.88 µs. The pulse energy was 126 nJ and a *radio frequency* (RF) spectrum of the output showed a high peak-to-background contrast of $\sim$45 dB, indicating good pulse train stability.

The average output power in the Q-switched regime was variable from 7.0 mW to 10.5 mW, limited by the available pump power. Pulse properties in continuous-wave pumped Q-switched lasers depend on nonlinear dynamics in the gain medium and

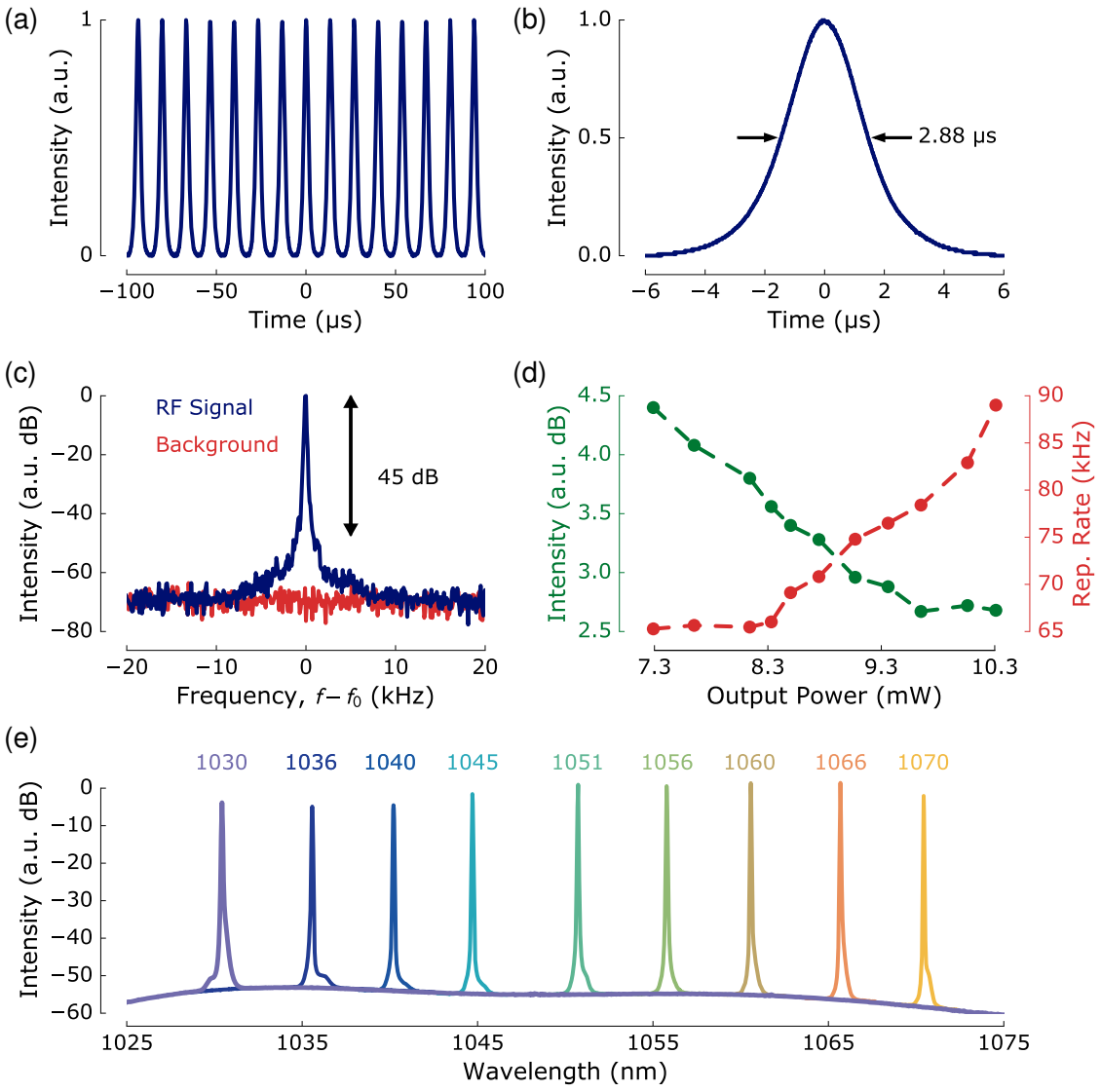


Fig. 4.25: Q-switched Yb:fibre laser characteristics: (a) pulse train; (b) single pulse profile; (c) RF spectrum of fundamental frequency, f_0=74 kHz; (d) variation of repetition frequency and pulse duration with output power; (e) output spectra for Q-switched operation at various wavelengths. The wavelength could be continuously tuned between 1030 and 1070 nm using the tunable filter.

saturable absorber, which lead to a dependence of repetition rate and pulse duration upon pump power [Deg95]. A pulse is emitted once a certain stored energy in the cavity is reached. Thus, a greater pump power enables higher repetition rates and also results in shorter pulses. This was observed experimentally as the pulse duration reduced from 4.40 μs to 2.68 μs and the repetition rate increased from 65.3 kHz to 89.0 kHz with increasing output power (Fig. 4.25d). The pulse duration could be shortened further by reducing the length of the laser cavity [Deg95].

By varying the passband of the tunable filter, stable Q-switched operation was achieved with continuous tunability from 1030 nm to 1070 nm (Fig. 4.25e). As the amplifier gain changed with wavelength, the output power of the laser varied. It was therefore necessary to adjust the pump power to maintain Q-switching (this accounts for the variations in spectral intensities in Fig. 4.25e). The tuning range was limited by the gain bandwidth of the ytterbium amplifier rather than the MoS_2 saturable absorber. Therefore, with a gain medium supporting broader band operation, we expect that tunable Q-switched laser pulses could be generated over an even wider spectral range.

4.3.4 Mode-locked Er-doped Fibre Laser

An Er:fibre laser was constructed with a similar design to the Yb:fibre cavity but including components to operate at telecommunication wavelengths and passive Corning SMF-28e fibre ($\beta_2 \sim -21.6$ ps^2 km^{-1}, $\gamma \sim 1.3$ W km^{-1} at 1550 nm). The amplifier was formed of a 1 m length of double-clad erbium-ytterbium co-doped fibre, pumped by a laser diode at 962 nm. Co-doping enables significantly greater pump absorption as ytterbium has a higher absorption cross section than erbium and after photoexcitation of ytterbium ions, energy is efficiently transferred to the erbium ions to provide gain around 1550 nm [Sni65]. A tunable filter was included in the cavity to vary the laser wavelength, with a bandwidth of 12.8 nm. The total cavity length was ∼15.4 m.

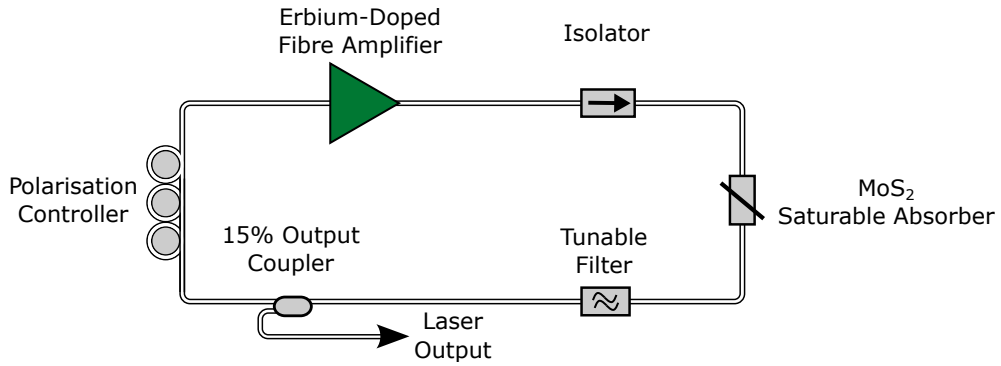


Fig. 4.26: Schematic of mode-locked Er:fibre laser including a MoS_2-PVA saturable absorber.

Self-starting mode-locking was observed at the fundamental repetition frequency of the cavity of 12.99 MHz, with 65 pJ pulse energy. The output wavelength was continuously tunable from 1535 to 1565 nm (Fig. 4.27a) by varying the angle of the interference filter

in the rotating tunable filter setup. This tuning range was limited by the maximum wavelength of the tunable filter on the long wavelength side and by the gain bandwidth of the Er-doped fibre amplifier on the short wavelength side, which caused the FWHM spectral bandwidth to reduce from ~3.0 nm to 0.4 nm as the wavelength was decreased. Ultrashort pulses were generated at every wavelength with a sech^2 shape, shown by autocorrelation traces at representative wavelengths in Fig. 4.27b. The increase in duration towards shorter wavelengths was due to the reduced spectral width, as expected from the Fourier transform.

Spectral sidebands were observed at certain wavelengths, arising from resonances between solitons and dispersive waves emitted by solitons as they adjust themselves to maintain their shape in the presence of perturbations during a round-trip (as discussed in Section 2.5.2). Sidebands are only generated when the cavity length is longer than the soliton period z_0 [Kel92b, Den94]. Pulses at 1552 nm and 1558 nm in Fig. 4.27 with ~1 ps duration corresponded to a soliton period of ~21 m, which is reasonably similar to the 15.4 m length. This explains why weak sidebands are observed at these wavelengths, whereas the longer pulses at other wavelengths have soliton lengths much longer than the cavity (e.g. at 3.9 ps, z_0 =350 m), where the pulse behaves as an unchanging average soliton in the cavity [Kel91].

The *time-bandwidth product* (TBP) for output pulses ranged from 0.37 to 0.47, slightly larger than the transform-limited value of 0.315 for sech^2 pulses, indicating a small chirp. Therefore, by careful dispersion management of the cavity, it would be possible to reduce the pulse duration further. Laser stability was inferred from the radio frequency (RF) spectra at 1552 nm (Fig. 4.28). The fundamental frequency showed a high signal to background extinction ratio of 55 dB and higher cavity harmonics, recorded on a span of 90 MHz, showed no Q-switching instabilities, indicating good mode-locking performance of the cavity. Similarly stable performance was observed throughout the tuning range of the laser.

4.3.5 Edge-State Saturable Absorption

In a perfect crystalline semiconductor, the bandgap – corresponding to the energy range with zero density of states – prohibits absorption of single photons that have an insufficient energy to excite electrons from the valence band to the conduction band [Yu10]. However, our Z-scan measurements and experimental demonstration of Q-switching and mode-locking fibre lasers using an MoS_2-PVA composite unequivocally confirmed that the material exhibited saturable absorption at wavelengths in the range 1030-1070 nm (1.20-1.16 eV) and 1535-1565 nm (0.81 -0.79 eV) despite corresponding to photon energies lower than the expected material bandgap. Additionally, numerous other research groups working concurrently with ourselves have observed sub-bandgap saturable absorption from few-layer MoS_2 [Wan13, Wan14b, Zha14a]. Despite this growing body of work, a full explanation of the governing physical mechanism has yet to be formulated. Here, we

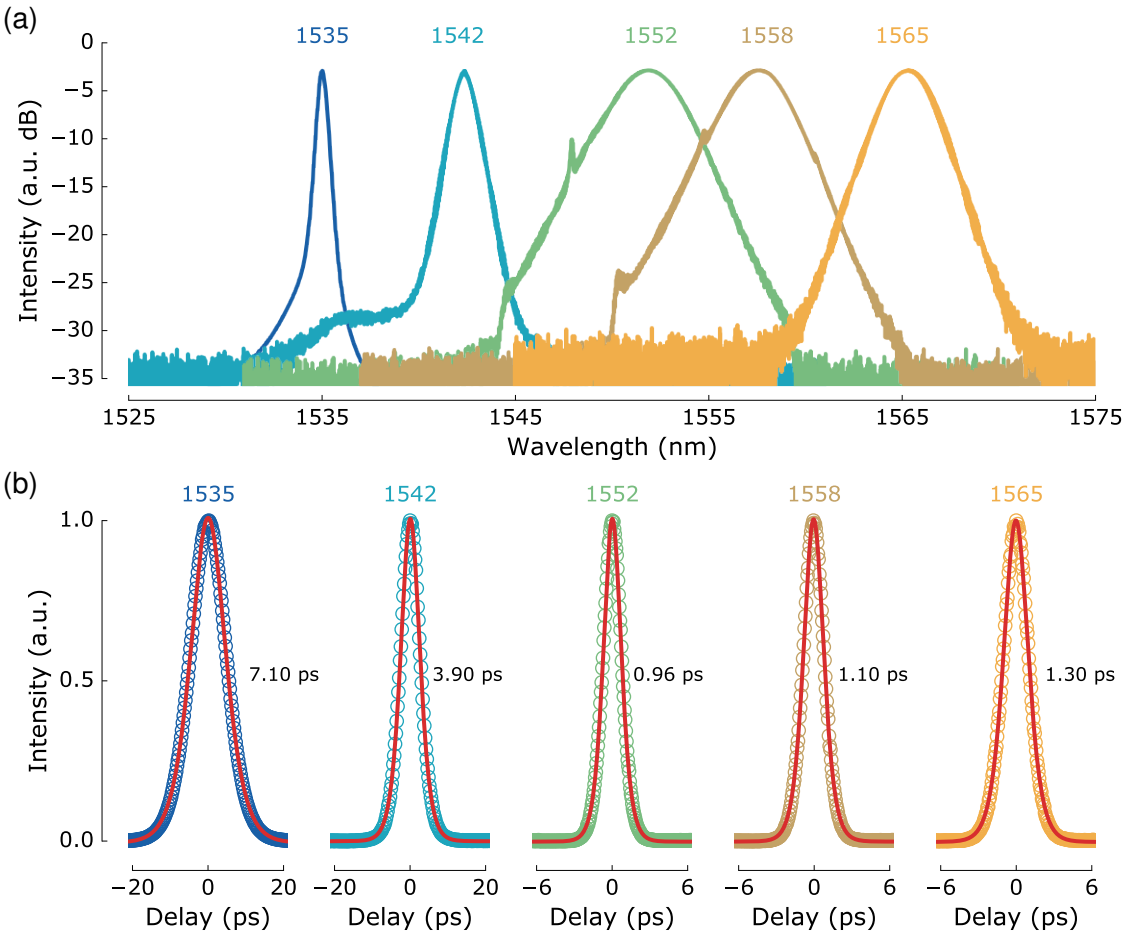


Fig. 4.27: Mode-locked Er:fibre laser characteristics: (a) optical spectra at various wavelengths within the continuous tuning range from 1535 to 1565 nm; (b) corresponding autocorrelation traces (shown with a $sech^2$ fit and the deconvolved pulse duration)

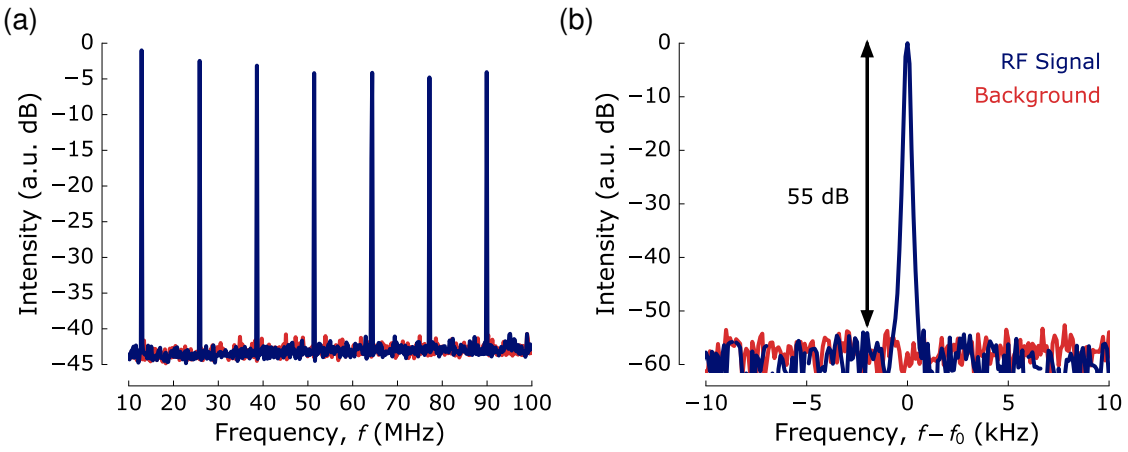


Fig. 4.28: RF spectrum of mode-locked Er:fibre laser output: (a) numerous cavity harmonics on a 90 MHz span; (b) 20 kHz span about the fundamental, f_0 = 13 MHz.

propose a possible explanation based on edge-state absorption.

The basal planes of MoS_2 crystals are known to be chemically inert due to tight bonding between the exposed S atoms with the Mo atoms underneath, and are thus expected to be optically inactive. However, small flakes of few-layer MoS_2 are not infinite, perfect crystals. At the edges of the atomic planes, crystallographic symmetry is broken and Mo and S sites are left with unsaturated bonds, which can modify the local electronic structure [Rox86b, Yu10] . We propose that the large edge to surface area ratio of few-layer nanoflakes of MoS_2 (typically $<$100 nm across and $<$4 nm in thickness, as shown in Fig. 4.20b) results in a large number of edge sites, significantly modifying the electronic structure and leading to the presence of energy states within the pristine crystal band structure.

This is supported by earlier spectroscopic studies on MoS_2. In the 1980s, Roxlo et al. performed photothermal deflection spectroscopy (PDS) measurements to characterise the absorption (PDS is unaffected by scattering) of different sizes of few-layer MoS_2 flakes at photon energies above and below the bandgap (Fig. 4.29) [Rox86b, Rox86a, Rox87]. They found very similar absorption spectra for photoexcitation at wavelengths corresponding to energies higher than the material bandgap, but at sub-bandgap photon energies, small flakes of few-layer MoS_2 ($\sim$1 μm across) showed up to two orders of magnitude greater absorption than a single crystal. Texturing of single crystals was also shown to increase sub-bandgap absorption by a factor of ten [Rox86a, Rox87].

Smaller or textured flakes possess a larger edge to surface area ratio, suggesting a greater contribution to the absorption spectra from edge states that form quasi-energy levels within the forbidden energy gap of the pristine crystal band structure [Rox86b, Rox86a, Rox87, Yu10]. Edge states, therefore, appear to promote absorption at photon energies lower than the bandgap. More recently, this has been verified by theoretical band structure studies showing that edges result in a finite local density of states within the bandgap of MoS_2 crystals [Zho13].

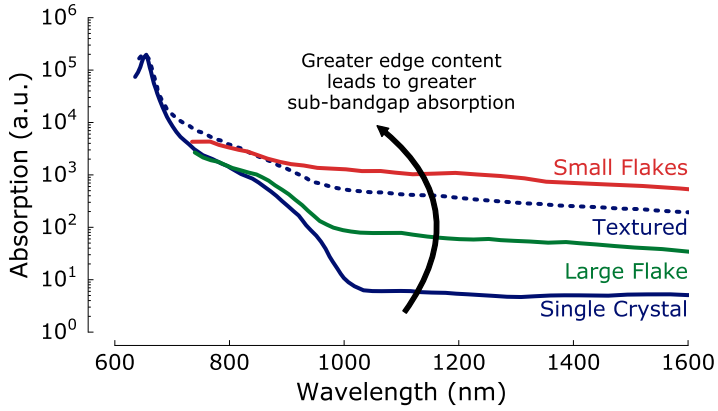


Fig. 4.29: Optical absorption of pristine and lithographically textured single MoS_2 crystals of 0.7 μm thickness, and microcrystal distributions containing large (36 μm diameter) and small (1.7 μm diameter) flakes. Adapted from [Rox87].

We suggest that these edge states could then be saturated under high intensity illumination by the principle of Pauli blocking. This mechanism for SA is supported by reports of mode-locking using defect in-bandgap states in other nonlinear crystals [Dem94, Zha92].

A distribution of edge states within the bandgap could explain the wideband saturable absorption experimentally observed here, although the density of states is not expected to be constant throughout the bandgap as shown in Ref. [Zho13], and will depend on the geometry and edge termination (whether Mo or S sites).

Wang et al. have also proposed a complementary explanation for sub-bandgap absorption based on atomic point defects, following theoretical studies of the bandgap behaviour [Wan14b]. The introduction of both Mo and S defects was found to reduce the bandgap, although an excess of Mo defects led to metallic behaviour with no SA effects, whereas S defects maintained the semiconductor behaviour and reduced the bandgap to 0.08 eV (supporting the generation of photoexcited carriers up to wavelengths as long as 15.4 μm).

Generalising the above theory, we expect edge-state sub-bandgap saturable absorption to be present in other few-layer semiconducting TMDs with a high edge to surface area ratio. Reports are also emerging of pulse generation using CVD-grown few-layer MoS_2 materials [Xia14], where the flake sizes can be hundreds of times larger, reducing the impact of edges. Crystallographic defects, dislocations and grain boundaries may contribute to sub-bandgap absorption here [Zho13] and further work is clearly required to thoroughly understand the impact of size effects on the nonlinear optical properties of few-layer TMDs. With such knowledge, it could be possible to tailor the nanomaterial properties for particular applications, which is an attractive prospect for a range of photonic devices.

4.4 Opportunities for Other Transition Metal Dichalcogenides

We have demonstrated that few-layer MoS_2 is a flexible saturable absorber material for Q-switching and mode-locking fibre lasers at a range of infrared wavelengths. Extending this work, we expect the fabrication techniques and the discussed saturable absorption mechanism to apply for other semiconducting TMDs, due to similarities in the layer-dependent band structure. Researchers have already demonstrated a bulk-to-monolayer transition from indirect to direct bandgap behaviour in tungsten disulfide (WS_2), molybdenum diselenide ($MoSe_2$) and tungsten diselenide (WSe_2), each with different bandgap ranges that are accessible by varying the number of layers [Ton12, Zha13b]. In this section, we consider an additional TMD, molybdenum diselenide ($MoSe_2$) and demonstrate its application as a wideband saturable absorber. We also consider the operation of TMD SAs at their resonant bandgap wavelengths, proposing a route to short-pulse fibre lasers at visible spectral regions.

4.4.1 Q-switched Yb-, Er-, and Tm-doped Fibre Lasers with $MoSe_2$

Molybdenum diselenide ($MoSe_2$) is a similar material to MoS_2, but with selenium atoms in place of the sulfur atoms. The heavier chalcogenide atoms result in a narrower gap bandgap, reported as 1.1 eV (1128 nm) in bulk form and reducing to a direct 1.55 eV (800 nm) gap for monolayer $MoSe_2$ [Ton12, Zha14b]. We applied the liquid-phase exfoliation processing techniques developed in Section 4.3.2 and performed similar experiments to test our hypothesis that other few-layer semiconducting TMDs could exhibit edge-state-based saturable absorption.

Few-Layer $MoSe_2$-PVA Saturable Absorber Characterisation

LPE of bulk $MoSe_2$ crystals yielded a dispersion of few-layer $MoSe_2$ flakes. An ensemble of AFM measurements revealed an average thickness of 3.8 nm, with $<$5 nm thickness for 80% of flakes, verifying that the majority of flakes consisted of only 6-7 layers, assuming 1 nm measured thickness for the first layer and 0.7 nm increase for additional layers [Ton12]. The flakes were integrated into a PVA matrix to form a free-standing $\sim$30 μm thick $MoSe_2$-polymer film.

The linear optical absorption profile of the composite (Fig. 4.30a) showed the characteristic excitonic peaks for $MoSe_2$ at $\sim$800 nm (A) and $\sim$710 nm (B). These two peaks result from spin-orbit split transitions in the valence band, similar to those observed with MoS_2 [Ton12]. The composite film absorption was 9.8%, 11.3% and 12.1% at 1060 nm, 1566 nm and 1924 nm, respectively (the three operating wavelengths of the lasers we demonstrated), highlighting a marked increase over the absorption values for the pure PVA film of 2.3%, 3.2% and 4.5%. An open-aperture Z-scan experiment showed that the $MoSe_2$-PVA composite exhibited saturable absorption, well-fitted by the standard two-level saturable absorber model and showing no evidence of two-photon absorption (Fig. 4.30b). Performance characteristics were computed as: saturation intensity $I_{\text{sat}}\sim$3.4 MW cm^{-2}; modulation depth $\alpha_s\sim$4.7% and nonsaturable loss $\alpha_{ns}\sim$6.6%, which were similar in magnitude to our MoS_2 device.

Design and Characterisation of Fibre Lasers

The demonstrated sub-bandgap saturable absorption of our few-layer $MoSe_2$-PVA composite suggested that the device could be used for short pulse generation at 1565 nm. The $MoSe_2$-PVA SA was integrated into an Er-doped fibre laser, in addition to Yb- and Tm-doped fibre lasers to explore the potential of exploiting sub-bandgap saturable absorption for short-pulse generation at different near-infrared wavelengths using a single $MoSe_2$ SA. For each laser cavity, a ring design was adopted, including a polarisation-independent isolator, output coupler and polarisation controller, in addition to the fibre amplifier (Fig. 4.31). The Yb and Er amplifiers consisted of double-clad Yb and Er fibre, which were 1.5 m and 11.6 m long, respectively. The Tm fibre amplifier was formed of a 2.9 m length of

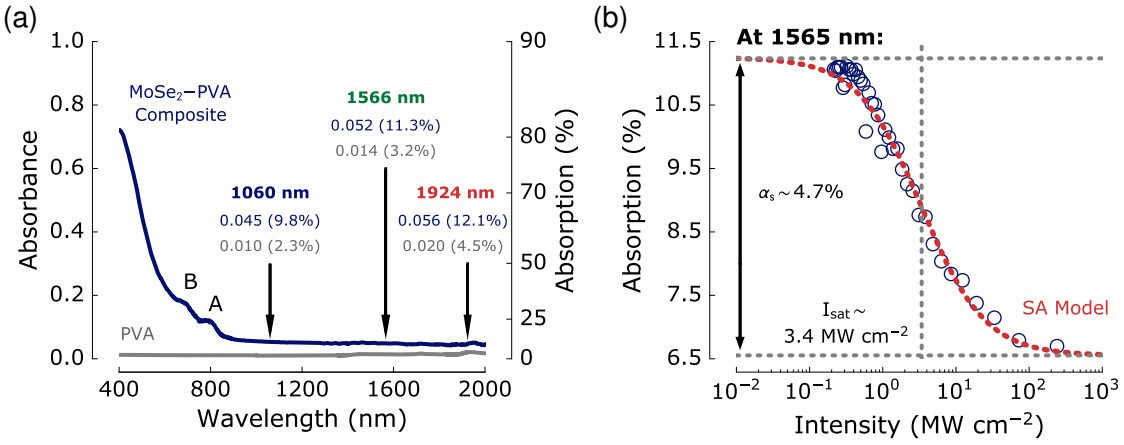


Fig. 4.30: Optical characterisation of few-layer $MoSe_2$-PVA composite: (a) linear absorption spectrum; (b) nonlinear absorption profile, recorded in an open-aperture Z-scan experiment.

single-clad Tm-doped fibre, pumped by a 1550 nm continuous wave fibre laser. The total lengths of the Yb, Er, and Tm fibre-based cavities were ∼15.9 m, ∼27.4 m and ∼13.4 m, respectively. A 1 mm × 1 mm piece of the $MoSe_2$ SA film was integrated into the cavity by placing it between two fibre patch cords.

Self-starting Q-switching was observed from the Yb:fibre laser, generating a steady train of pulses, centred at 1060 nm (Fig. 4.32). By changing the pump power, the average output power could be varied from 6.26 mW (corresponding to the threshold for Q-switched emission; below this, the laser output was a continuous wave) to 8.72 mW. With increasing power, the pulse repetition frequency was increased from 60.0 kHz to 74.9 kHz and the duration decreased from 4.6 µs to 2.8 µs (Fig. 4.33a).

The Er:fibre laser with the few-layer $MoSe_2$-PVA composite also exhibited self-starting Q-switching at an average output power of 18.9 mW, operating at 1566 nm (Fig. 4.31b). By varying the pump power, the repetition rate could be changed from 26.5 kHz to 35.4 kHz and the duration from 7.9 µs to 4.8 µs as the average output power increased from 18.9 mW to 29.2 mW (Fig. 4.33b).

Continuous-wave lasing at 1924 nm was initially observed as the pump power of the Tm:fibre laser was increased, until the Q-switching threshold was reached, corresponding to 0.13 mW average output power (Fig. 4.32c). Beyond threshold, a steady train of Q-switched pulses was generated. The average output power increased with pump power and the Q-switched pulse duration reduced from 16.0 µs to 5.5 µs while the repetition rate increased from 14.0 kHz to 21.8 kHz (Fig. 4.33c).

We have demonstrated that the few-layer $MoSe_2$-PVA composite exhibited wideband saturable absorption, enabling Q-switching at three wavelengths in the near-infrared region from a single device. Such wavelengths corresponded to sub-bandgap absorption, which we attributed to edge states in the material following the same argument developed in Section 4.3.5 to explain the operation of MoS_2 devices. It was interesting to note that

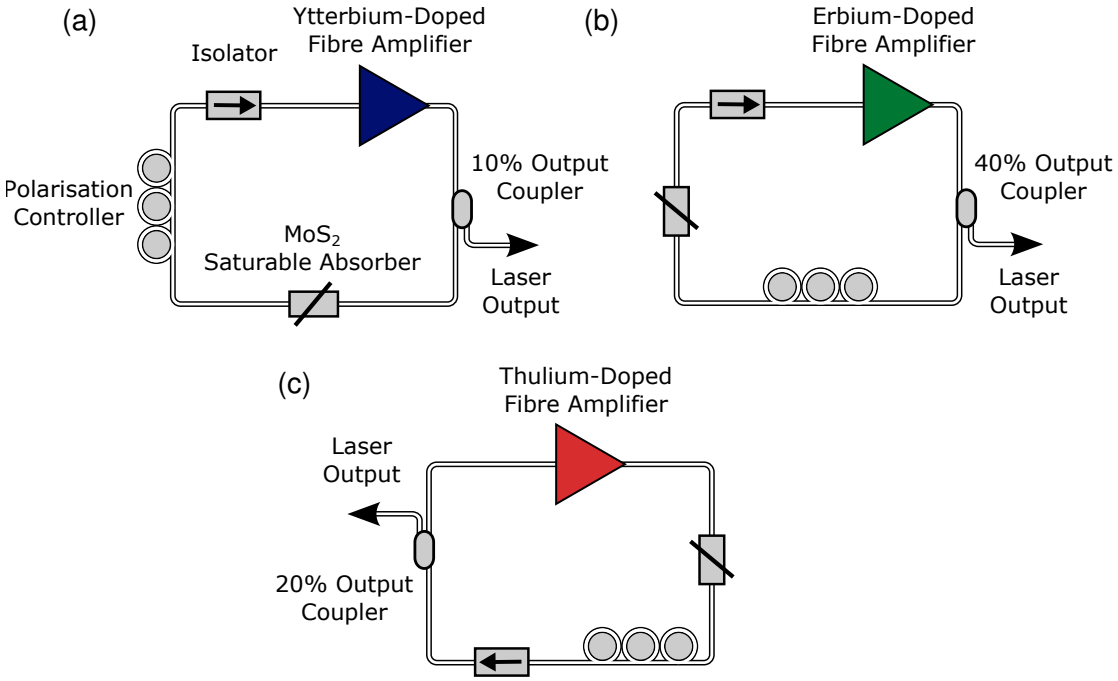


Fig. 4.31: Schematics of Q-switched (a) Yb-, (b) Er-, (c), Tm-doped fibre lasers including a $MoSe_2$-PVA saturable absorber.

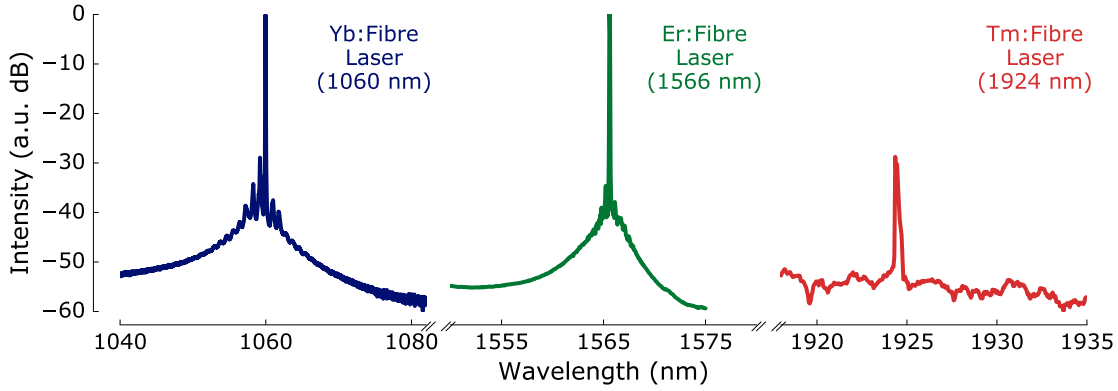


Fig. 4.32: Optical spectra for few-layer $MoSe_2$ Q-switched Yb-, Er- and Tm-doped fibre lasers. The Yb and Er spectrum were measured using an optical spectrum analyser (0.02 nm resolution), while the Tm spectrum was measured on a spectrometer (0.1 nm resolution).

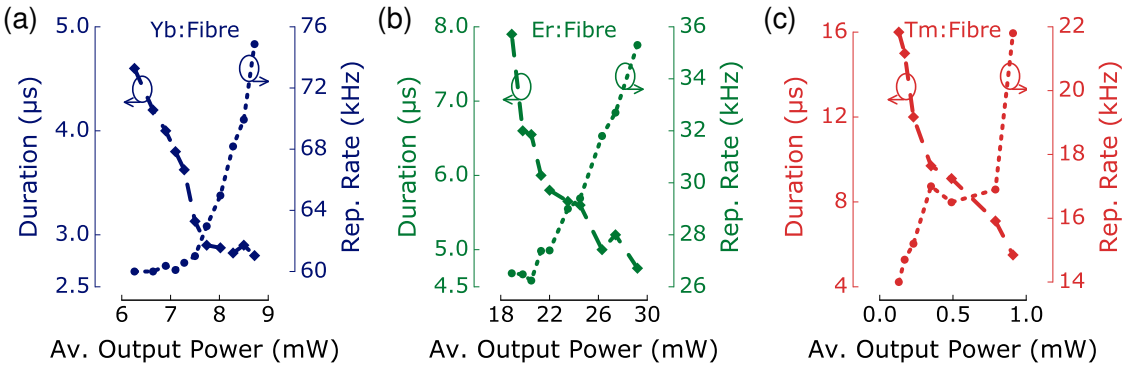


Fig. 4.33: Variation of pulse duration and repetition rate with average output power for (a) Yb-, (b) Er-, and (c) Tm-doped fibre lasers, Q-switched with a few-layer MoSe2 SA. The dotted lines are intended to guide the eye – they are not a result of curve fitting.

mode-locking was not achieved in any of the cavities, whereas this was possible using MoS_2 at 1550 nm. Investigations are ongoing to optimise 2D material-based saturable absorbers for mode-locked fibre laser systems.

4.4.2 Visible Short-Pulse Fibre Lasers

A greater nonlinear response could be expected for resonant operation – i.e. using the device at a wavelength corresponding to the bandgap energy or excitonic peaks. A variety of different transition metal dichalcogenides are emerging with different bandgaps throughout the visible spectral region and the exact resonant wavelength can be tuned by varying the flake thickness (to engineer the flake size, one can relatively easily change the fabrication conditions, for instance, by varying the ultracentrifugation rate in an LPE process [Zho15]). We believe that few-layer transition metal dichalcogenides could offer particular advantages as saturable absorbers at visible wavelengths – a region where other nanomaterial-based saturable absorber technologies have struggled.

The success of fibre lasers at infrared wavelengths has not translated to the visible spectrum, despite great demand for flexible, reliable laser sources in this region (especially for biomedical applications). While great progress has been made by frequency doubling the output of fibre lasers and exploiting other nonlinear processes to generate visible light, active fibres with visible emission hold untapped potential. A suitable rare-earth dopant, trivalent Praseodymium Pr^{3+}, is available and offers many transitions throughout the visible region (Fig. 4.34) [Sma91]. Unfortunately however, the phonon energy of silica is relatively high ($\sim$1100 cm^{-1} [Dig01]), which causes depopulation of excited energy levels through nonradiative phonon interactions and results in weak emission cross sections for many transitions, inhibiting lasing.

To circumvent this problem, fluoride glass can be used, such as ZBLAN (a multi-composite glass including numerous heavy metal fluorides: ZrF_4-BaF_2-LaF_3-AlF_3-NaF) which has a lower phonon energy of $\sim$500 cm^{-1} [Dig01]. While ZBLAN fibres are hygro-

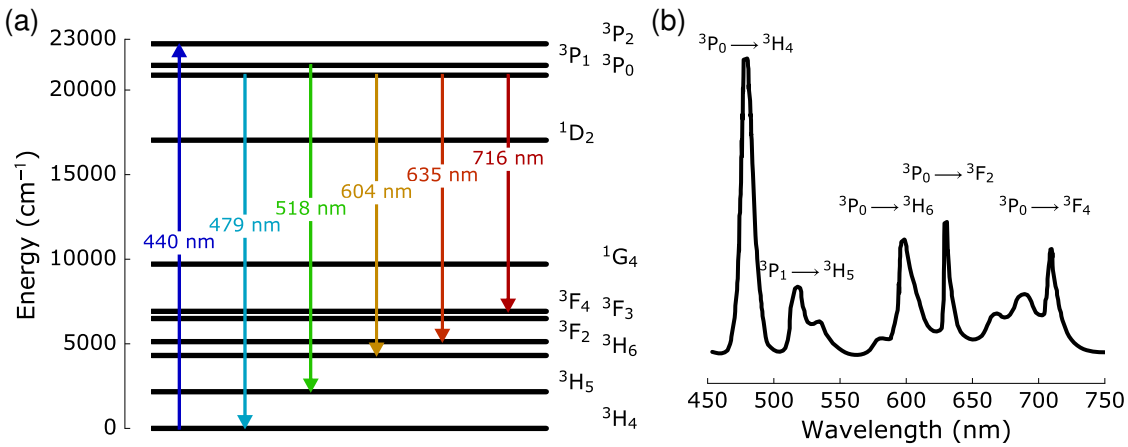


Fig. 4.34: Pr^{3+}in ZBLAN glass: (a) energy level diagram showing a selection of laser transitions; (b) emission spectrum. Adapted from Ref. [Sma91].

scopic and more challenging to handle, advances in fluoride fibre manufacture are enabling more robust and lower loss fibres. Recent developments have also shown low-loss splicing to silica fibre [Oka11], low-cost gallium nitride (GaN) blue diode pumping [Fuj13] and actively Q-switched operation [Koj13]. Therefore, we believe that Pr:ZBLAN fibres combined with transition metal dichalcogenide saturable absorbers could be an ideal route towards next-generation short-pulse laser sources throughout the visible region.

4.5 Summary

In this chapter we have studied the nonlinear optical properties of emergent 2D nanomaterials: few-layer transition metal dichalcogenides, with a particular focus on molybdenum disulfide. We developed an in-situ characterisation technique based on second- and third-harmonic generation microscopy, which was capable of high-resolution imaging and non-destructive testing of samples. The setup enabled us to determine the number of layers in a flake and to probe the crystal structure through symmetries in the nonlinear susceptibility tensor by resolving the polarisation of incident and nonlinearly generated light. We also obtained an estimate of the magnitude of the second- and third-order susceptibility by modelling the 2D material as a nonlinear polarisation sheet and applying established theory from surface nonlinear optics. We confirmed that the nonlinear response was much stronger from monolayer and few-layer MoS_2 than the silica substrate, although comparison of 2D materials and conventional bulk material requires further theoretical work and derivations of figure of merits.

Future work will consider the nonlinear response of additional 2D materials and will explore other $\chi^{(3)}$ effects such as four-wave mixing. The few nanometre thickness of these materials results in low interaction lengths, suggesting that high conversion efficiencies are not possible. While the materials may not be suitable for practical wavelength conversion devices, we could exploit their nonlinearity to develop compact and broadband pulse

characterisation systems.

With a focus on applications, the second part of this chapter considered the fabrication of few-layer TMD-PVA composite films for integration into fibre lasers as saturable absorbers. High modulation depths of a few percent and low saturation intensities were measured (alongside unfavourably high nonsaturable losses), enabling short pulse generation at a range of near infrared wavelengths. Q-switching was obtained in all systems we developed, although only the Er:fibre laser with MoS_2 was able to exhibit mode-locking. Work continues to understand how to achieve mode-locking at other wavelengths by optimising these materials.

The observation of wideband saturable absorption is a compelling merit for further work into few-layer MoS_2, potentially enabling single saturable absorber devices to operate over a wide wavelength range. An explanation for this mechanism was proposed based on saturable edge-state absorption. The visible bandgap, however, may be the real strength of few-layer TMDs, offering resonant operation which is tunable with the number of layers. Short pulse generation in the visible is a challenging area for fibre lasers, presenting problems for current nanomaterial saturable absorbers using nanotubes and graphene, but with great demand for pulsed sources in biomedical applications. Future work is therefore planned using Pr:ZBLAN fibre to realise this ambition.

5

STIMULATED BRILLOUIN SCATTERING IN PHOTONIC CRYSTAL FIBRE

Photonic crystal fibres (PCFs) can be fabricated with a small core to provide tight modal confinement and consequently, the ability to guide high optical intensities. This enables effective nonlinear parameters that are orders of magnitude greater than those offered by conventional step-index fibre, suggesting that such PCFs could permit the generation of significant nonlinear effects at reduced pump powers.

In this chapter, we explore *stimulated Brillouin scattering* (SBS) in small-core PCFs and develop a self-mode-locked Brillouin PCF laser.[1] Section 5.1 introduces the basic concepts of Brillouin scattering, mediated by optoacoustic interactions, and discusses recent reports in the literature of unexpected observations concerning Brillouin interactions in PCF. We experimentally characterise SBS at 532 nm and 1550 nm in two different PCF structures in Section 5.2 and discuss the impact of the pump wavelength relative to fibre length-scales on the underlying acoustic dynamics. Section 5.3 reports the development of a Brillouin PCF laser and studies the temporal dynamics of the output, showing pulsed behaviour under certain conditions. Finally, we end the chapter with an outlook for harnessing nonlinear optoacoustic phenomena in PCFs for practical applications.

The results in this chapter have been reported in the following journal articles and conference proceedings: [Woo14d, Woo14c, Woo15h].

[1] Our initial aim for this work was to develop a Raman laser at visible wavelengths using PCF, although strong Brillouin gain was found to dominate all other nonlinear effects. While we were not able to achieve stimulated Raman scattering, the differences we observed between our SBS measurements and recently published literature results motivated further study of the effect, as presented in this chapter.

5.1 Introduction: Brillouin Scattering in Fibre

5.1.1 Fundamental Principles

The inelastic scattering of light from acoustic vibrations was theoretically predicted by Léon Brillouin in 1922 [Bri22], and independently by Leonid Mandelstam in 1926 [Man26].[2] Experimental observation of this Brillouin scattering effect shortly followed [Gro30]. Specifically, it was shown that the interaction of pump light at frequency ω_p with acoustic waves in the medium could shift the optical frequency to create a Stokes wave at frequency ω_s and scattering angle θ. According to energy and momentum conservation, the Brillouin frequency shift is $\omega_b = \omega_p - \omega_s$ and the pump and Stokes wavevectors ($\mathbf{k_p}$ and $\mathbf{k_s}$, respectively) are related to the acoustic wavevector $\mathbf{k_a}$ by $\mathbf{k_a} = \mathbf{k_p} - \mathbf{k_s}$ (Fig. 5.1a) [Agr13, Dam03].

These conditions can be combined using the dispersion relation to express the Brillouin shift in terms of the acoustic velocity in the medium v_a:

$$\omega_b = v_a|\mathbf{k_a}| = 2v_a|\mathbf{k_p}|\sin(\theta/2) \tag{5.1.1}$$

where $|\mathbf{k_p}| = |\mathbf{k_s}|$ has been assumed since the Brillouin shift is much smaller than the optical frequency.

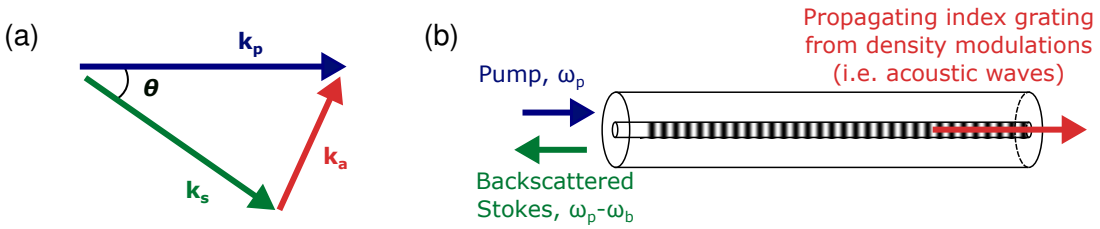


Fig. 5.1: Illustration of Brillouin scattering: (a) wavevector orientations in the general case; (b) orientation of wavevectors in fibre showing the stimulated Brillouin backscattering of pump light to create a Stokes wave which is downshifted by the Brillouin frequencyω_b.

Early measurements of Brillouin scattering considered relatively low-intensity pump light, where the scattering is *spontaneous* and arises from thermally excited acoustic waves (i.e. density variations) in the medium. Decades later, the invention of the laser enabled significantly higher pump intensities, leading to the observation of *stimulated* Brillouin scattering [Chi64]. In this case, beating between the pump and Stokes light modulates the density of the medium, driving acoustic waves through electrostriction[3], which results in stronger nonlinear scattering.

[2] It is claimed that Mandelstam first performed this study in 1918, many years before the work (and that of Brillouin) was published [Fei02]. Therefore, the effect is occasionally referred to as Brillouin-Mandelstam scattering.

[3] Electrostriction is a property of all dielectrics, where applied electric fields induce strain in the material [New11]. If the medium absorbs strongly at the pump wavelength, a temperature wave can also be induced to drive an acoustic wave [Dam03], although this is neglected herein as we always work within the transparency window of silica.

Optical fibres present an ideal platform for generating SBS with long interaction lengths, as first observed by Ippen and Stolen in 1972 [Ipp72b]. In single-mode fibres, the only possible scattering directions are forwards ($\theta = 0$) and backwards ($\theta = 180^\circ$), suggesting that the Brillouin effect always occurs as backscattering according to Eqn. 5.1.1 (illustrated in Fig. 5.1b). The Brillouin frequency shift can then be written in terms of the pump wavelength using $|\mathbf{k}_p| = 2\pi n_{\text{eff}}/\lambda_p$ where n_{eff} is the effective index of guided pump light [Agr13]:

$$f_b = \frac{\omega_b}{2\pi} = \frac{2n_{\text{eff}}v_a}{\lambda_p} \tag{5.1.2}$$

The Brillouin scattering process can be explained physically as acoustic waves inducing a periodic index modulation, which acts as a Bragg grating and scatters the pump light through diffraction. As the grating is travelling along the fibre at the acoustic velocity v_a, the backscattered light is Doppler downshifted in frequency. The process can also be visualised quantum mechanically as annihilation of a pump photon to create a Stokes photon and an acoustic phonon.

The waveguide structure affects both optical and acoustic modes, which relaxes the momentum conservation equations. Therefore, weak forwards-travelling Stokes light can be generated in fibres, known as *guided acoustic wave Brillouin scattering* [She85]. The waveguide structure and the inclusion of core dopants also affect the backwards Brillouin gain spectrum. Compared to bulk silica which exhibits a Brillouin gain profile with a single Lorentz peak (typically tens of megahertz wide), Brillouin gain measurements in step-index fibres have shown multiple-peaked shapes, attributed to dopants and the presence of numerous different acoustic modes. However, as the pump power increases and the process becomes stimulated, spectral narrowing occurs and a single peak from the gain spectrum dominates, imprinting this single peak on the backscattered light. While Brillouin scattering is the strongest nonlinear effect in optical fibres [Agr13], the gain bandwidth is very narrow (<100 MHz) and the spectral power density of broadband pump sources is often insufficient to stimulate this phenomena.

SBS in fibre can be used for various applications including the development of Brillouin lasers (e.g. for laser gyroscopes), slow-light generation and optical sensing [Zar91, Son05]. A critical parameter is the *threshold* pump power for the onset of SBS, at which point the dependence of backscattered light upon incident intensity becomes exponential, compared to the linear relationship for spontaneous Brillouin scattering. Typically, this is measured as the pump power for which the scattered signal is 1% of the input power.

The SBS threshold is given by [Smi72]:[4]

$$P_{\text{th}} = \frac{21KA_{\text{eff}}}{g_{\text{B}}L_{\text{eff}}} \tag{5.1.3}$$

[4]We note that the factor of 21 is approximate and other authors have proposed alternative threshold equations. However, Eqn. 5.1.3 remains widely used and gives reasonable accuracy with experiments [Agr13]. We therefore adopt this equations to enable comparison of our results with recent published work.

where L_{eff} is the effective fibre length, $L_{\text{eff}} = (1 - e^{-\alpha L})/\alpha$, to account for loss, α, in a physical fibre length L, A_{eff} is the optical mode effective area and g_{B} is the peak Brillouin gain. K is a polarisation-dependent factor: $K = 1$ when the pump is coupled into a principal axis of strongly birefringent fibre and $K = 2$ when launched at 45° to an axis [Dev94]. This equation also assumes that the pump light spectrum is narrower than the gain bandwidth.

5.1.2 Peculiar Observations in Small-Core PCF

Small-core PCFs offer opportunities for generating nonlinear effects at only modest pump powers: as highlighted by Eqn. 5.1.3, higher intensities result from reduced effective areas, lowering the threshold power. Additionally, PCFs can be endlessly single-moded, offering high brightness and excellent beam quality at visible wavelengths, where conventional fibres often support multiple modes. Therefore, small-core PCFs should be an ideal platform for achieving SBS. Recently published results, however, suggest that this is not the case.

Thresholds up to a factor of five times higher than predicted by established theory have been reported [Lee02, Dai06, Beu07, McE08b] (Fig. 5.2a), which have been attributed to differences in optoacoustic interactions in PCF compared to step-index fibres (for which Eqn. 5.1.3 was originally developed).

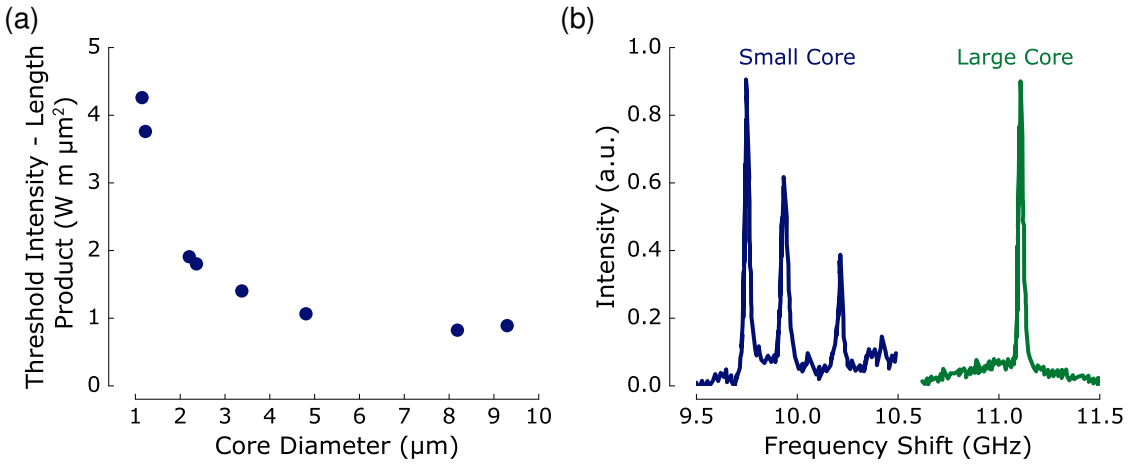


Fig. 5.2: Impact of PCF core diameter on Brillouin scattering at 1550 nm: (a) threshold intensity-effective length product against core diameter, showing an increase in the intensity required for SBS with decreasing core diameter (contrary to expected behaviour from Eqn. 5.1.3); (b) backscattered spectra for a small core (1.2 μm diameter) and large core (9.3 μm) PCF. Adapted from Ref. [Dai06].

The magnitude and shape of the Brillouin gain spectrum depends on the overlap between acoustic and optical modes, which is strongly influenced by fibre geometry [Agr13]. Acoustic modes can contain both *longitudinal-wave* and *shear-wave* components, although it is the longitudinal component that dominates the Brillouin response [Dai06]. In conventional step-index fibre the small acoustic impedance mismatch between core and cladding materials results in weak reflections at their interface and minimal coupling between

longitudinal and shear waves. Consequently, the acoustic waves which are generated in the core through electrostriction by intense pump light are principally longitudinal, resulting in strong Bragg backscattering of light and a single Brillouin peak [Bon02, Dai06].

PCFs with a small silica core exhibit a more complex Brillouin response due to richer acoustic dynamics. The air-glass boundaries result in strong reflections and coupling between longitudinal and shear acoustic waves [Dai06]. The resulting hybrid modes exhibit different acoustic velocities and can each yield different Stokes shifts [Dai06]. Therefore, multiple peaks have been observed in both spontaneous [Lee02, Dai06, Beu07] and stimulated [McE08b, McE08a] Brillouin spectra (Fig. 5.2b). Dainese et al. also reported the evolution of the backscattered signal spectrum, with more peaks forming as the pump power increased, attributed to parametric mixing [Dai06]. The increased shear and reduced longitudinal wave content in acoustic modes has a minimal contribution to SBS, raising the threshold [Dai06].

This higher threshold could suggest that PCFs offer no benefit over conventional step-index fibre for Brillouin scattering applications. However, to date, studies of SBS in PCF have been restricted to infrared wavelengths and further study of this effect is required to critically assess this statement.

5.2 Experimental Characterisation of Stimulated Brillouin Scattering

To explore the impact of pump wavelength on SBS in small-core PCFs, we developed experiments to characterise Brillouin scattering at 532 nm and 1550 nm. In this section, we discuss these results and the impact of the pump wavelength on the SBS threshold, in the context of optoacoustic interactions governed by the PCF structure.

5.2.1 Experimental Setup

Our experimental setup for characterising SBS in PCFs is shown in Fig. 5.3. Pump light at 532 nm with a linear polarisation state was provided by a single-frequency (15 MHz linewidth) *continuous wave* (CW) frequency-doubled Yb:fibre laser. The power was controlled with a variable optical attenuator formed from a *half-wave plate* (HWP) and polariser. Light was focussed into the PCF (with 55% coupling efficiency) after a second HWP, which was rotated to vary the incident polarisation direction. The rear end of the fibre was angle cleaved (at 8°) to prevent feedback from Fresnel reflections.

We used a 10 m long small-core PCF, hereafter referred to as PCF-1, which was endlessly single-moded with air-hole pitch $\Lambda = 1.90$ μm and hole diameter $d = 0.70$ μm, corresponding to core diameter $d_c = 3.10$ μm defined as $d_c = 2\Lambda - d$ (Fig. 5.4). A 50% beam-splitter enabled simultaneous monitoring of the pump light (for normalising out any pump laser power fluctuations) and backscattered signal. The transmitted power through the PCF was also monitored. Additionally, we measured the polarisation of the backscattered

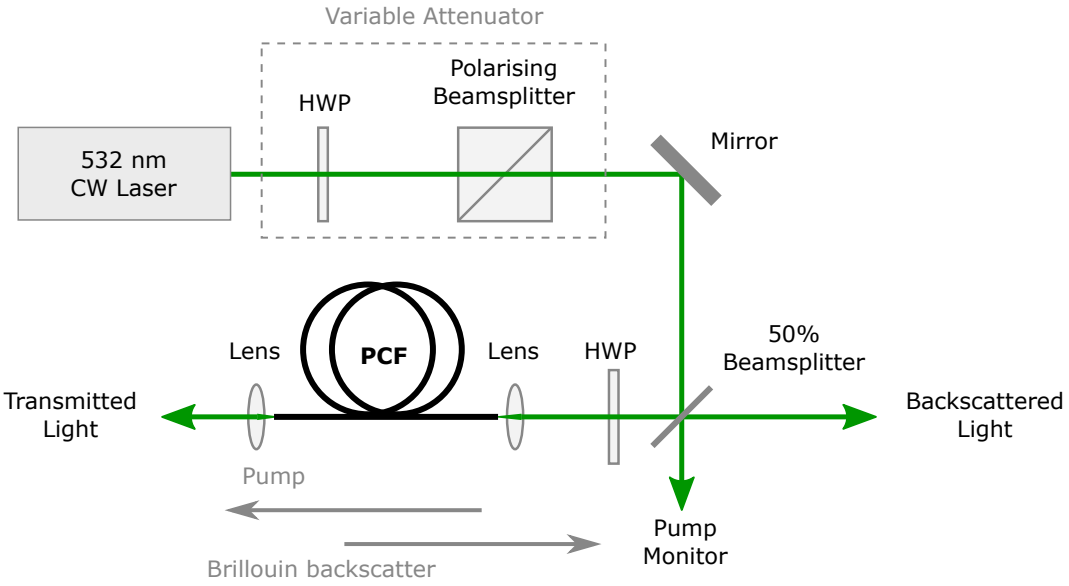


Fig. 5.3: Schematic of experimental setup for characterisation of stimulated Brillouin scattering in PCF.

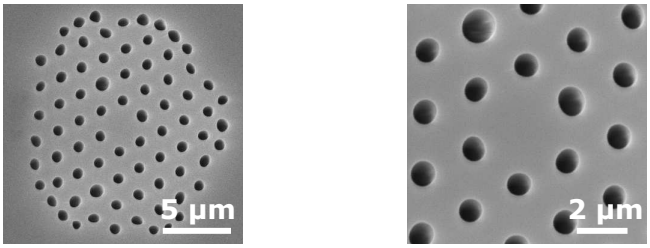


Fig. 5.4: SEM images of PCF-1 microstructure at different magnifications. The PCF parameters – hole diameter $d = 0.70$ µm, pitch $\Lambda = 1.90$ µm, effective core diameter $d_c = 3.10$ µm – are average values, as manufacturing imperfections led to slight variations between hole sizes.

signal so corrections could be applied to account for the small polarisation-dependence of the beamsplitter.

5.2.2 Initial Characterisation

The linear pump polarisation was aligned with a principal axis of the PCF and as the pump power increased, characteristic SBS behaviour was observed. The transmitted power increased linearly with increasing pump power until a threshold was reached, after which the transmitted power saturated and the backscattered signal increased sharply (Fig. 5.5a). The threshold power was calculated as $P_{\text{th}} = 220$ mW, as described in Section 5.1.1. Above threshold, additional pump power was reflected; the nonlinear process effectively created a *Brillouin mirror*.

Similar results were obtained when the input polarisation was rotated through 90° to align with the other principal axis of the fibre, although when aligning the polarisation between two fibre axes (∼45° rotation), the threshold and saturated transmitted power

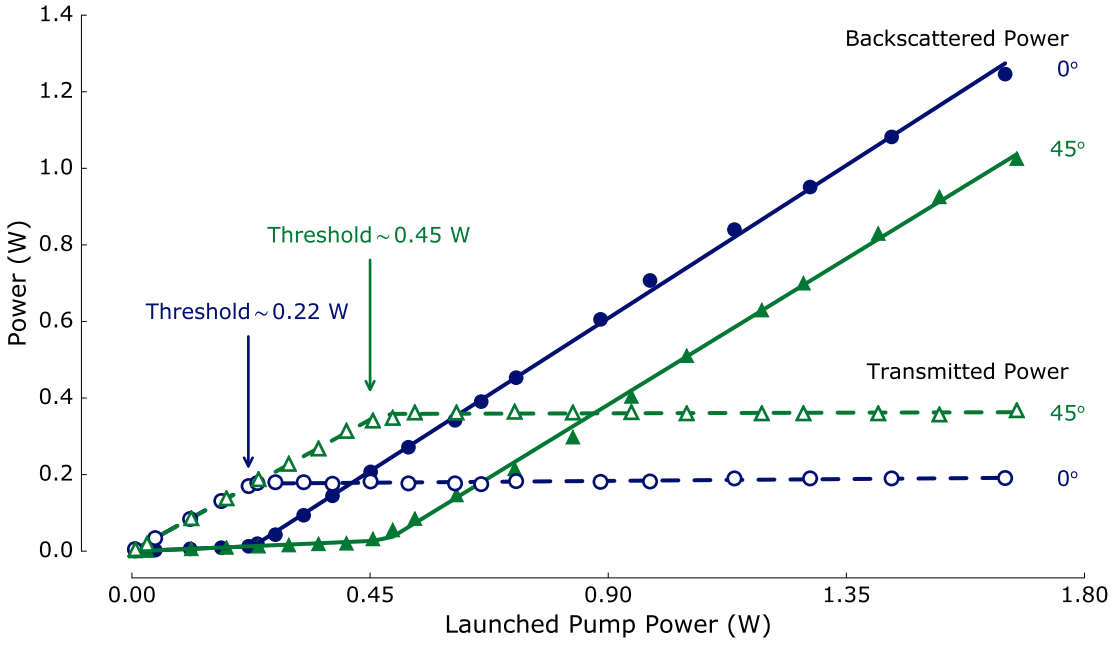


Fig. 5.5: Variation of Brillouin backscattered and transmitted powers in PCF-1 with pump power, for linearly polarised light launched along a fibre principal axis (0°) and between axes (45°). SBS thresholds are shown, highlighting a factor of two threshold reduction when light is polarised along a fibre axis.

were approximately doubled (Fig. 5.5a). This behaviour is typical of a strongly birefringent fibre [Dev94]. However, an ideal sixfold symmetric PCF microstructure should not exhibit birefringence [Ste01].

The apparent strong birefringence in PCF-1 is therefore attributed to structural asymmetry from imperfections in the PCF microstructure [McE08a], which can be seen in the SEM cross-sectional image (Fig. 5.3b). We further examined the Brillouin gain dependence on the input polarisation angle (with 0° defined as polarisation along a fibre principal axis) by rotating the HWP (Fig. 5.5b). A sinusoidal variation in backscattered and transmitted powers was seen above threshold, due to the polarisation dependence of Brillouin gain [Dev94]. Below threshold the transmission was independent of the HWP angle, confirming the absence of polarisation-dependent loss in the fibre.

For PCF-1, we measured a loss value of 61 dB km^{-1} at 532 nm from cut-back measurements and a value of $A_{\text{eff}} = 4.73$ μm^2 was extracted from numerical modelling based on the PCF structure (discussed in Section 5.2.4). Using these properties and our recorded threshold values, the peak Brillouin gain was calculated as 4.8×10^{-11} m W^{-1}. This value is in good agreement with typical gain values recorded for silica fibres: $3 - 5 \times 10^{-11}$ m W^{-1} [Agr13].

Brillouin backscattered light is Stokes shifted from the pump wavelength according to Eqn. 5.1.2. This shift was measured experimentally using a scanning Fabry-Pérot interferometer, monitoring the backreflected light containing both Brillouin backscattered light and a small component of pump light from Fresnel reflections off the fibre front facet.

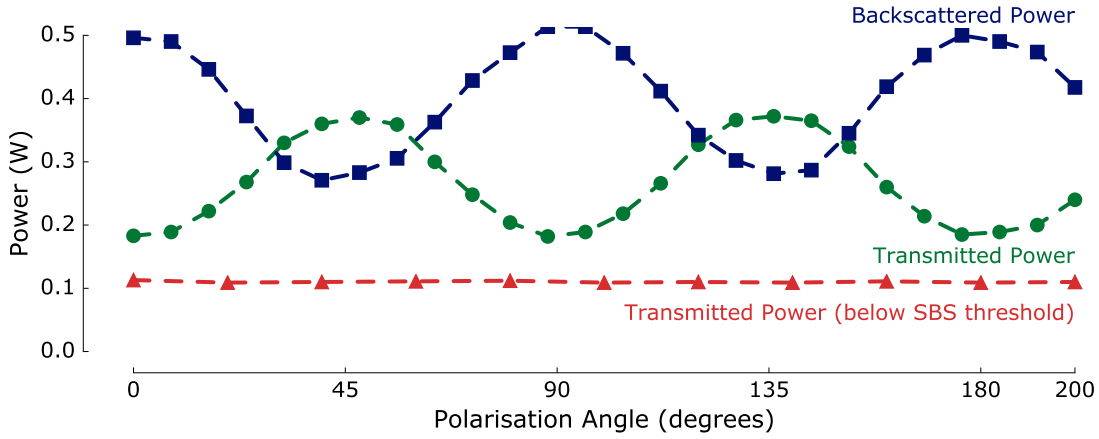


Fig. 5.6: Variation of Brillouin backscattered and transmitted power with pump polarisation (angle measured relative to a fibre principal axis). Above the SBS threshold, strong variation is observed due to the polarisation-dependent Brillouin gain, although the power is constant below threshold, showing no polarisation-dependent fibre loss.

A Fabry-Pérot interferometer (or *etalon*) is a linear optical cavity with two parallel highly reflective mirrors (that are back-polished to couple a fraction of light in/out to be measured, and back-angled to prevent spurious interference), resulting in sharp transmission resonances where the frequency separation between them is called the *free spectral range* (FSR):

$$\mathrm{FSR} = \frac{c}{2n_{\mathrm{air}}d} \tag{5.2.1}$$

where $n_{\mathrm{air}} \sim 1$ and d is the mirror spacing. By periodically varying d with a piezo actuator and recording the transmitted intensity on a photodiode, the temporal response can be mapped to the optical spectrum of the light. The scanning interferometer can enable significantly higher spectral resolution than an optical spectrum analyser [Hec02]. The resolution is limited by the cavity *finesse*:

$$\mathrm{Finesse} = \frac{\pi(R_1R_2)^{0.25}}{1-(R_1R_2)^{0.5}} \tag{5.2.2}$$

where R_1 and R_2 are the reflectivities of the cavity mirrors.

With an interferometer FSR of 42.2 GHz, we recorded a Brillouin shift of 33.5 GHz (Fig. 5.7b). Using $n_{\mathrm{eff}} = 1.456$ (obtained from modelling), the measured shift relates to an acoustic velocity of ∼6100 m s^{-1}, corresponding reasonably well and within 2% of the known longitudinal acoustic velocity in silica of ∼5960 m s^{-1} [Agr13]. The shape of the Stokes signal (Fig. 5.7a) was measured by reducing the interferometer FSR to 2.9 GHz, with 50 MHz resolution (limited by interferometer finesse). While the measured Stokes peak width of 50 MHz was resolution-limited, we observed no asymmetry or multiple-peaked structure. The backscattered signal was also observed using a CCD camera: the Gaussian-shaped beam confirmed that it propagated as a fundamental core mode (Fig. 5.7c).

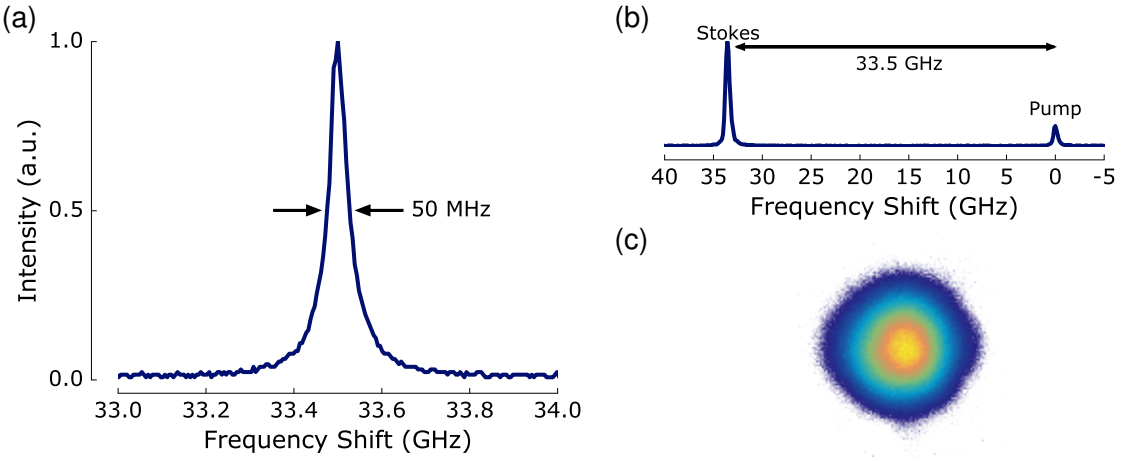


Fig. 5.7: Stimulated Brillouin backscattered spectrum in PCF-1, measured using a scanning interferometer with: (a) 2.9 GHz free spectral range to show a single peaked Brillouin spectrum; (b) 42.2 GHz free spectral range to indicate the Brillouin frequency downshift from the pump. Measurements were made with 0.5 W pump power aligned to a PCF principal axis and the backscattered beam profile observed on a CCD camera (c) showed a single fundamental mode profile.

The observation of an isolated single Stokes peak and the agreement between measured and theoretical threshold power at 532 nm are distinct from recent reports of Brillouin scattering measurements in small-core PCF at ∼1550 nm [Dai06, McE08b, McE08a, Beu07, Lee02]. Therefore, to make comparative measurements we developed a narrow linewidth (1 MHz) pump source at 1550 nm based on a external-cavity diode laser amplified in an erbium-doped fibre amplifier (the remainder of the setup was the same as Fig. 5.3, but replacing the optics with components for 1550 nm operation). Unfortunately, SBS could not be observed in PCF-1 at infrared wavelengths due to high confinement loss in the fibre at longer wavelengths.[5]

5.2.3 Comparison between 532 and 1550 nm Pump Light

To compare stimulated Brillouin scattering in small-core PCF pumped at visible and infrared wavelengths, we performed characterisation measurements on a second 40 m long PCF with a similar microstructure (PCF-2: $d = 0.55$ μm and $\Lambda = 1.48$ μm , corresponding to $d_c = 2.41$ μm , as shown in Fig. 5.8). This fibre had a greater number of air holes layers than PCF-1 to reduce the confinement loss. Additionally, PCF-2 was fabricated many years after PCF-1, once fabrication technology had become more established. Therefore, the microstructure showed better uniformity and lower loss than PCF-1 (compare Figs. 5.4 and Fig. 5.8).

The measurements outlined in Section 5.2.2 were repeated with this PCF and both

[5]Since the core of a PCF has the same refractive index as the region beyond the finite periodic air-hole cladding, guided modes are actually *leaky modes* and experience confinement loss from the core. The magnitude of confinement loss depends on the number of air hole layers and modal area (which is related to the wavelength) [Fin03].

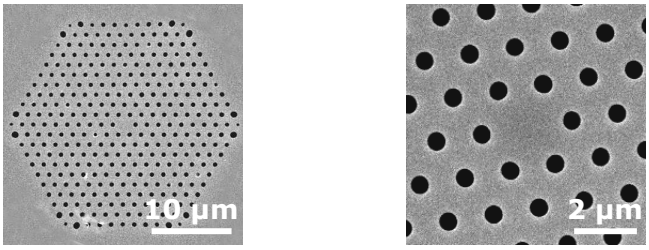


Fig. 5.8: SEM images of PCF-2 microstructure at different magnifications. The PCF parameters are hole diameter $d = 0.55$ µm, pitch $\Lambda = 1.48$ µm and effective core diameter $d_c = 2.41$ µm.

Pump Wavelength λ	Λ/λ	A_{eff}	n_{eff}	Loss α	Threshold Power	
(nm)		(μm^2)		(dB km^{-1})	Theory (mW)	Experiment (mW)
532	2.79	3.53	1.45	44	70	69
1550	0.96	7.87	1.41	153	240	1160

Table 5.1: PCF-2 properties at 532 nm and 1550 nm. Theoretical and experimental threshold values are in good agreement at 532 nm, but not at 1550 nm.

the 532 nm and 1550 nm pump laser. PCF-2's microstructure was more uniform and symmetric than PCF-1 and the pump polarisation angle was found to have a minimal effect on the Brillouin gain. This behaviour is typical of a low birefringence fibre, for which a factor of $K = 1.5$ should be used in threshold calculations [Dev94]. The measured loss at each wavelength and the effective area and index values obtained from modelling are shown in Table 5.1. Using Eqn. 5.1.3, the predicted threshold values were 70 mW at 532 nm and 240 mW at 1550 nm (while the peak Brillouin gain is approximately independent of wavelength [Agr13], the effective area and loss for PCF-2 are greater at 1550 nm leading to a higher SBS threshold).

Experimentally we measured threshold values of 69 mW at 532 nm, in excellent agreement with theoretical calculations. The threshold at 1550 nm, however, was recorded as 1160 mW, $\sim$5 times higher than predicted.

The spectral shape and frequency shift of the SBS Stokes component at 532 nm and 1550 nm (recorded with the interferometer) are shown in Fig. 5.10a. The 11.0 GHz Stokes shift measured at 1550 nm corresponded to an acoustic velocity of $\sim$6050 m s^{-1} and the 33.4 GHz shift at 532 nm indicated a velocity of $\sim$6110 m s^{-1}, both in reasonable agreement with the known velocity in silica [Agr13]. The Brillouin signal at 532 nm was a symmetric single peak showing no substructure, similar to the shape observed with PCF-1. In contrast, the Stokes peak at 1550 nm showed strong asymmetry. While the limited resolution and sensitivity of our scanning interferometer prohibited a detailed analysis of the structure and acoustic mode content, the asymmetry at 1550 nm suggested an interaction between the optical field and the numerous acoustic modes that each gave slightly different frequency shifts. These observations support reports in literature

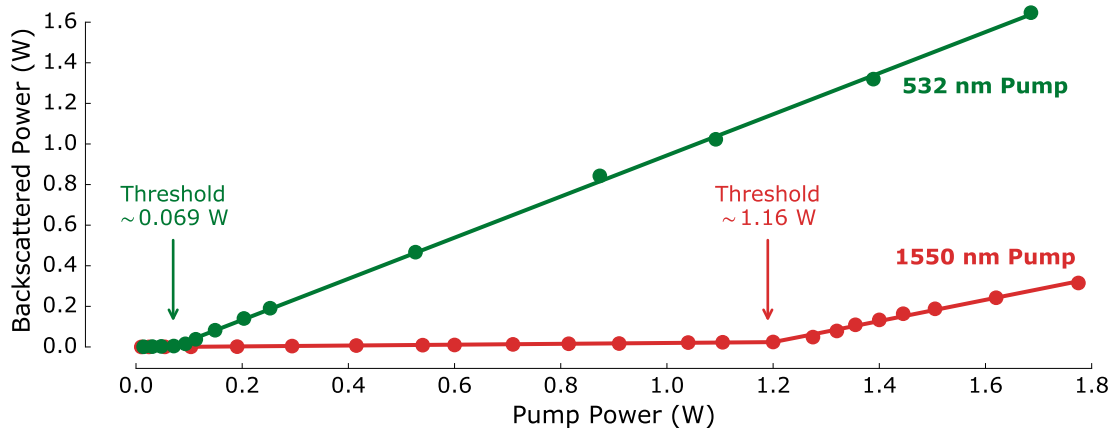


Fig. 5.9: Variation of Brillouin backscattered power with pump power launched into the fibre at 532 nm and 1550 nm pump wavelengths.

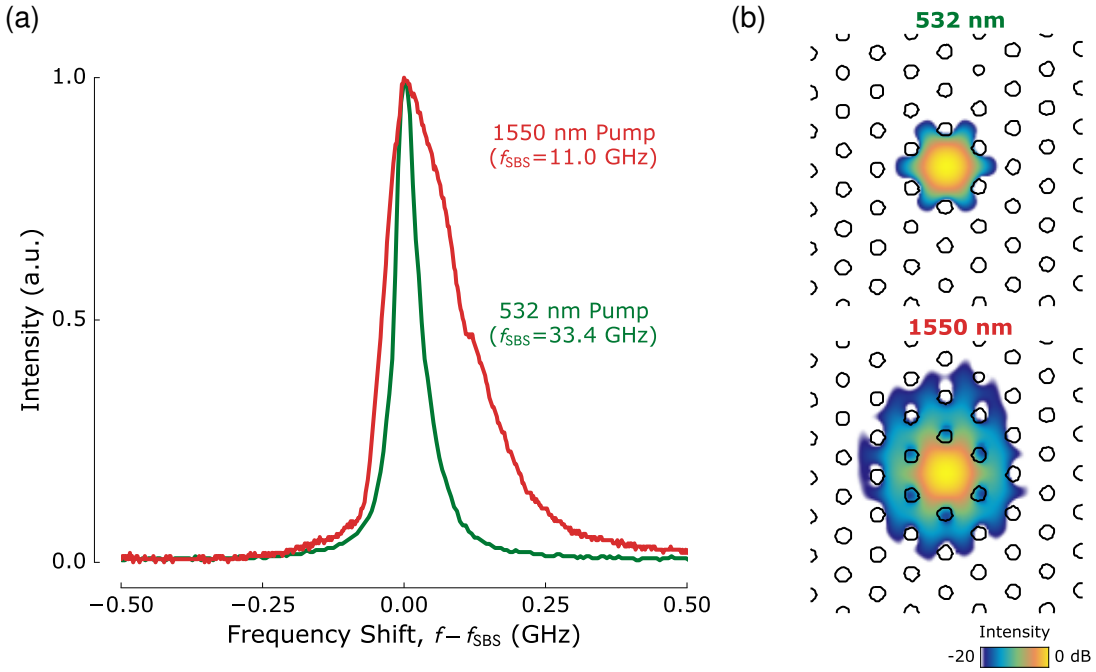


Fig. 5.10: Contrasting SBS characteristics in PCF-2 for 532 nm and 1550 nm pump wavelengths: (a) stimulated Brillouin backscattered spectra showing strong asymmetry for infrared light; (b) modal intensity profiles showing greater overlap with the cladding air holes at longer wavelengths.

of multiple-peaked and high-threshold SBS behaviour in small-core PCFs at 1550 nm, whereas at a pump wavelength of 532 nm, we saw no such irregularity.

We discuss these observations in the context of optoacoustic interactions in the PCF in Section 5.2.5, after a brief review of modelling methods for understanding the optical mode distributions.

5.2.4 Modelling Mode Shapes

The optical properties of PCFs can be accurately determined using the vector analytical effective index model introduced in Section 2.2.2, which reduces the complex PCF microstructure to an equivalent step-index fibre geometry. This approach is limited, however, if we wish to visualise the modal profile and the interaction with air holes, since the method assumes a continuous cladding with a constant refractive index (resulting in the intensity profile in Fig. 5.11a for PCF-2 at 532 nm).

For an improved model, we used the open-source software package MIT Photonic Bands. Briefly, the software uses a *block conjugate gradient* method to find the eigenmodes of Maxwell's equations for a dielectric structure given periodic boundary conditions [Joh01]. A PCF microstructure is not perfectly periodic, however, since the core is a defect in the photonic crystal structure where the field will localise. Therefore, a *supercell approximation* is used: a large computational cell is constructed including numerous unit cells surrounding the defect, so its boundaries become irrelevant [Joa08]. This increases the computational cost, although the use of this approach has become a widely used technique for accurately modelling PCFs.

To improve the accuracy of simulations using MIT Photonic Bands, the dielectric structure was created from an SEM image of the PCF microstructure, thus taking into account imperfections in the manufacturing process compared to a perfect lattice. Fig. 5.11b shows a computed mode profile for PCF-2 at 532 nm using this method, indicating that light is concentrated in the high-index silica bridges in the cladding and absent from the air holes. This is in much better agreement with the expected behaviour of light in such a structure [Joa08], hence this modal modelling approach was adopted throughout this chapter.

5.2.5 Optoacoustic Interactions

To explain our observations, we consider the interaction of optical and acoustic waves in PCFs. While weak backscattering will occur spontaneously at all transverse positions in the fibre geometry (i.e. in both silica core and microstructured cladding regions) due to thermally-created elastic waves, we focus here on stimulated Brillouin backscattering and optically-driven acoustic waves by electrostriction. The magnitude of optoacoustic interaction is governed by the overlap of optical and acoustic modes, where wave dynamics are related to the local environment with different behaviour in the core and cladding regions.

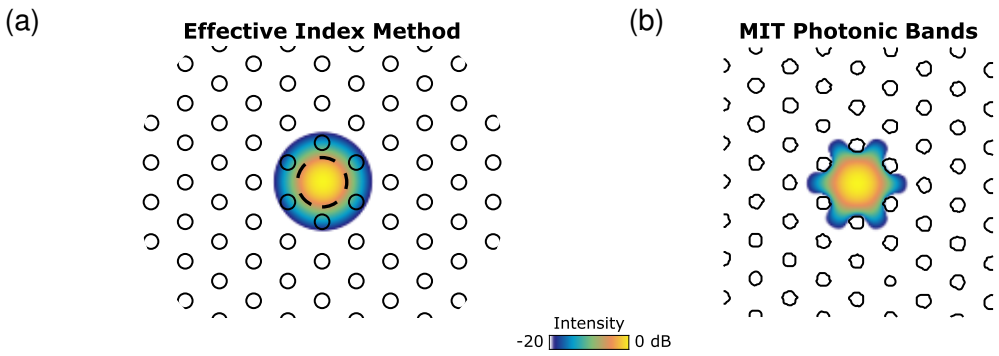


Fig. 5.11: Modal intensity profiles at 532 nm for PCF-2 computed by: (a) vector analytic effective index method; (b) MIT Photonic Bands. The effective index method simplifies the structure as a step-index fibre (equivalent core region shown by black dashed line) and cannot correctly predict the field distribution.

To elucidate the influence of wavelength on the SBS response, we introduce dimensionless length scales: Λ/λ and $A_{\text{eff}}/A_{\text{core}}$, where the effective optical mode area is defined in Eqn. 1.3.19 and the physical core area is $A_{\text{core}} = \pi d_c^2/4$ ($= 4.56$ μm^2 in PCF-2). Additionally, we note that acoustic waves spread out inside the fibre by diffraction, with a characteristic acoustic diffraction length $l_d = A_{\text{core}}/\lambda_s$ where λ_s is the wavelength of sound in the fibre, related to the free-space pump wavelength λ by $\lambda_s = \lambda/(2n_{\text{eff}})$ [Zel86]. The impact of diffraction is related to the lifetime of acoustic phonons T_a through the sound attenuation length $l_a = v_a T_a$; the diffraction efficiency can then be expressed as [Zel86]:

$$\frac{l_a}{l_d} = \frac{\lambda v_a T_a}{2n_{\text{eff}} A_{\text{core}}} \tag{5.2.3}$$

At 532 nm, $A_{\text{eff}} < A_{\text{core}}$ (Table 5.1) suggesting tight core confinement of the optical mode, as verified by the computed mode profiles (Fig. 5.10b). Beating between spontaneously backscattered light and pump light drives acoustic waves of longitudinal strain along the fibre axis, Bragg scattering additional pump light backwards. Further beating amplifies the acoustic wave yielding strong stimulated Brillouin scattering. Localisation of the optical mode to the core suggests weak interaction with cladding acoustic waves and consequently, negligible SBS effects here. Therefore, the backscattered spectrum shows a single peak corresponding to Doppler shifted light from longitudinal waves travelling at the speed of sound in silica [Dai06].

At 1550 nm, however, the optical field penetrates the cladding significantly since $A_{\text{eff}} > A_{\text{core}}$ (Table 5.1), suggesting stronger interaction in the holey region. Light cannot be completely concentrated in the silica if $\lambda > \Lambda$, thus the pump field overlaps air holes (Fig. 5.10b), which reduces the net Brillouin gain since air does not contribute to SBS here. Additionally, the high acoustic impedance contrast between silica bridging sections and air holes yield strong reflections that couple longitudinal and shear waves. This results in numerous *hybrid* acoustic modes which can have significant shear components and each give slightly different frequency shifts. Consequently, a multiple-peaked backscattered

spectra is formed and the Brillouin gain is reduced as the shear components do not significantly modify the local refractive index to form a Bragg grating [Dai06, Lau05].

In addition, even acoustic waves formed in the core will be affected more strongly by the cladding at longer wavelengths. From Eqn. 5.2.3, we see that the diffraction efficiency depends on λ and T_a (which increases with λ) so the spreading of acoustic strains outwards from the core at 1550 nm will be more than 3 times greater than at 532 nm, reducing the overlap with the optical mode. Furthermore, core-generated acoustic waves which spread out will experience longitudinal-shear component coupling at the glass-air interfaces, forming hybrid modes which each have a different acoustic spectrum. This yields multiple spectral peaks and a net reduction in Brillouin gain. It has also been suggested that the air-hole cladding layer can act as a resonant cavity to directly modulate backscattered light, imposing additional peaks on the backscattered spectrum [McE08b, Bon02].

We suggest that the multiple peaks which are expected in the Stokes spectrum at 1550 nm contribute to the asymmetric shape in our scanning interferometer trace (Fig. 5.10a), since we are limited by measurement resolution. A reduced Brillouin gain was also observed at infrared wavelengths as a significantly higher SBS threshold than predicted theoretically. We briefly note that another explanation has been proposed for increased SBS thresholds in PCF by Ref. [Lee02]: structural variations along the fibre due to manufacturing imperfections. This effect, however, would be expected to increase the threshold at both 532 nm and 1550 nm, which is not supported by our measurements. Our conclusions are similar to works considering the impact of varying the PCF core diameter at a fixed infrared wavelength [Dai06, McE08b] since both situations depend on Λ/λ and $A_{\text{eff}}/A_{\text{core}}$ ratios.

5.2.6 Is PCF Advantageous for Stimulated Brillouin Scattering?

While many reports to date have suggested that the enhanced effective nonlinearity in small-core PCFs is negated by complex acoustic dynamics, raising the SBS threshold, we believe that PCF does offer advantages over conventional fibre for exploiting SBS if shorter wavelength pump light is used.

We adopt the *threshold power-effective length product* $P_{\text{th}}L_{\text{eff}}$ as a figure of merit and compare PCF-2 to a conventional step-index fibre (with $A_{\text{eff}} = 30\ \mu\text{m}^2$ and $\alpha = 0.2$ dB km^{-1}). Table 5.2 shows that for an arbitrary length of fibre, the SBS threshold in small-core PCF pumped at 1550 m will exceed the threshold in a step-index fibre, suggesting no advantage to using PCF. However, by using a 532 nm pump source with the same PCF, the threshold

Step-Index Fibre ($\sim\lambda$ independent)	PCF-2 ($\lambda = 1550$ nm)	PCF-2 ($\lambda = 532$ nm)
19.7	25.1	2.3

Table 5.2: Figures of merit – threshold power-effective length product (W m) – for SBS generation in conventional and small-core photonic crystal fibre. A lower value is better, indicating a reduced SBS threshold.

can be reduced compared to step-index fibre by nearly an order of magnitude, which is attractive for SBS applications such as slow-light generation and the development of Brillouin lasers.

5.3 Brillouin PCF Laser

To exploit the benefits of small-core PCF for low-threshold SBS, we constructed a Brillouin laser. Hill, Kawasaki and Johnson were the first to demonstrate a Brillouin fibre laser in 1976 [Hil76a] and interest continues to this day in Brillouin scattering as a laser gain medium, principally for sensing applications [Agr13]. In this section, we report a simple linear-cavity Brillouin laser and study the temporal output properties.

5.3.1 Laser Design

We adapted our SBS characterisation setup to form a Fabry-Pérot laser cavity by planar cleaving the ends of the PCF (here, we returned to using PCF-1) to provide feedback (Fig. 5.12a). Using $n_{\text{air}} = 1$ and $n_{\text{eff}} = 1.456$ at 532 nm, the Fresnel reflectivity of each fibre facet was calculated as 3.4%. The pump polarisation was aligned to a fibre axis to maximise the Brillouin gain and we note that the fibre length was $\sim$9 m, slightly shorter than in Section 5.2.2 after a cut-back loss measurement.

The Brillouin laser threshold was recorded to be 130 mW (Fig. 5.12b). This was lower than the threshold for SBS generation without feedback (measured as 220 mW in Section 5.2.2 and predicted to increase to $\sim$245 mW due to the length reduction here according to Eqn. 5.1.3). It is expected that the Brillouin laser spectrum will differ from the single-pass SBS spectrum due to gain narrowing [Agr13], although this could not be resolved due to our limited interferometer resolution of 50 MHz and the measured laser spectrum was identical to Fig. 5.7a. We did, however, confirm that only one Stokes order was generated: the total cavity feedback ($3.4\% \times 3.4\% = 0.1\%$) was insufficient to cause cascaded Brillouin scattering to higher orders.

While a number of works have considered Brillouin PCF lasers, in both ring and linear cavities [Lee02, Dav02, dM04], their temporal output properties remain less well explored.

5.3.2 Temporal Dyamics

Brillouin fibre lasers can exhibit a rich variety of temporal dynamics [Lec96].[6] First, however, we consider the dynamic response of single-pass SBS. In the absence of feedback, Stokes light can exhibit temporal structure (despite CW-pumping) arising from amplification of spontaneous scattering [Gae91] and relaxation oscillations [Joh71]. Relaxation oscillations can be physically understood by periodic pump depletion and the finite nonlinear medium length: towards the fibre input, the pump depletes as the back-propagating

[6] We thank Prof. Carlos Montes and Dr Eric Picholle at the University of Nice, France for useful discussions regarding the temporal dynamics of Brillouin lasers.

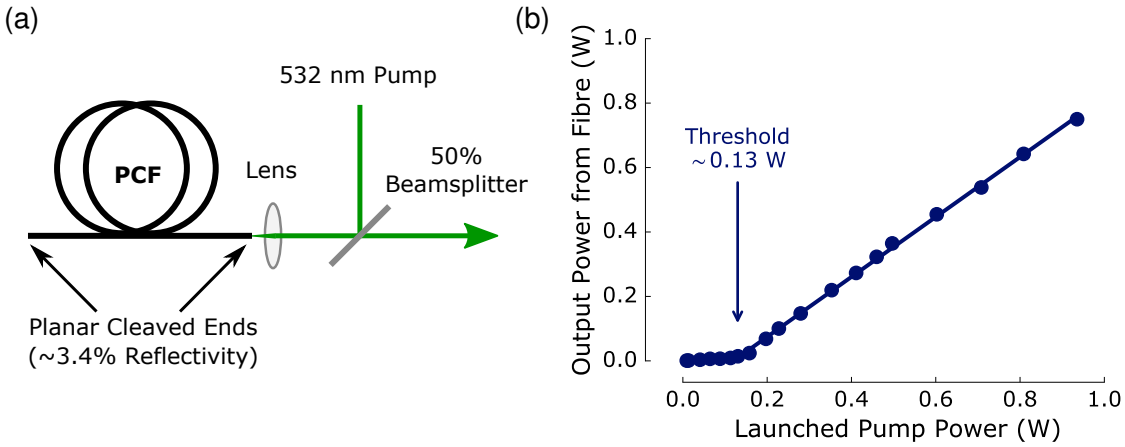


Fig. 5.12: Linear-cavity Brillouin laser using 9 m PCF-1: (a) schematic; (b) pump power launched into the PCF versus laser output power from the fibre. To extract the laser output from the system, light was taken after the beamsplitter, corresponding to a power reduction of 50%.

Stokes signal grows, reducing the gain; subsequent sections along the fibre experience lower gain from the forward-propagating depleted pump wave so additional backscattered Stokes power is weaker; the depleted pump region eventually passes out the end of the fibre as after initial depletion, in the absence of a strong Stokes signal, newly-injected pump light remains stronger; the process then repeats, creating low-modulation-depth oscillations related to the fibre length. This temporal behaviour is stochastic and appears as noisy fluctuations [Gae91]. We verified this in our experiment by observing the SBS signal in Section 5.2.2 on a photodector and oscilloscope.

The situation is very different in a Brillouin laser, where feedback is introduced to the SBS process, which can stabilise the oscillations leading to pulsed operation [Kaw78, BJ85, Dam93]. Specifically, the numerous longitudinal modes of a cavity within the Brillouin gain bandwidth (N∼13 in our experiment, using $N \sim 2L/(5\lambda^2 \times 10^{12})$ [Mon99]) are coupled by power transfer between pump and Stokes light, mediated by acoustic waves throughout the cavity. This introduces a phase relationship between them, partially locking them and generating periodic pulsations related to the cavity round-trip time. This phenomena has been referred to as *self* or *partial* mode-locking [Kaw78].[7]

Experimentally, we observed periodic pulse trains from our Brillouin PCF laser (Fig. 5.13a) where the pulse duration and repetition rate varied with pump power (Fig. 5.13b), between 9–27 ns and 11.2–12.2 MHz, respectively. The fundamental frequency for the ∼9 m Fabry-Pérot cavity was ∼11.5 MHz. Observation of greater repetition frequencies may seem concerning therefore, suggesting that a pulse is traversing the cavity faster than the speed of light in the medium. Fortunately, this was not a violation of special relativity and can be explained within the framework of slow- and fast-light effects: Brillouin gains acts

[7] An additional, distinct mode-locking technique for Brillouin lasers is to generate multiple Stokes orders through cascaded Brillouin scattering, then phase-lock these to provide a wider bandwidth and the possibility of generating ultrashort pulses [Lug72, Dam91].

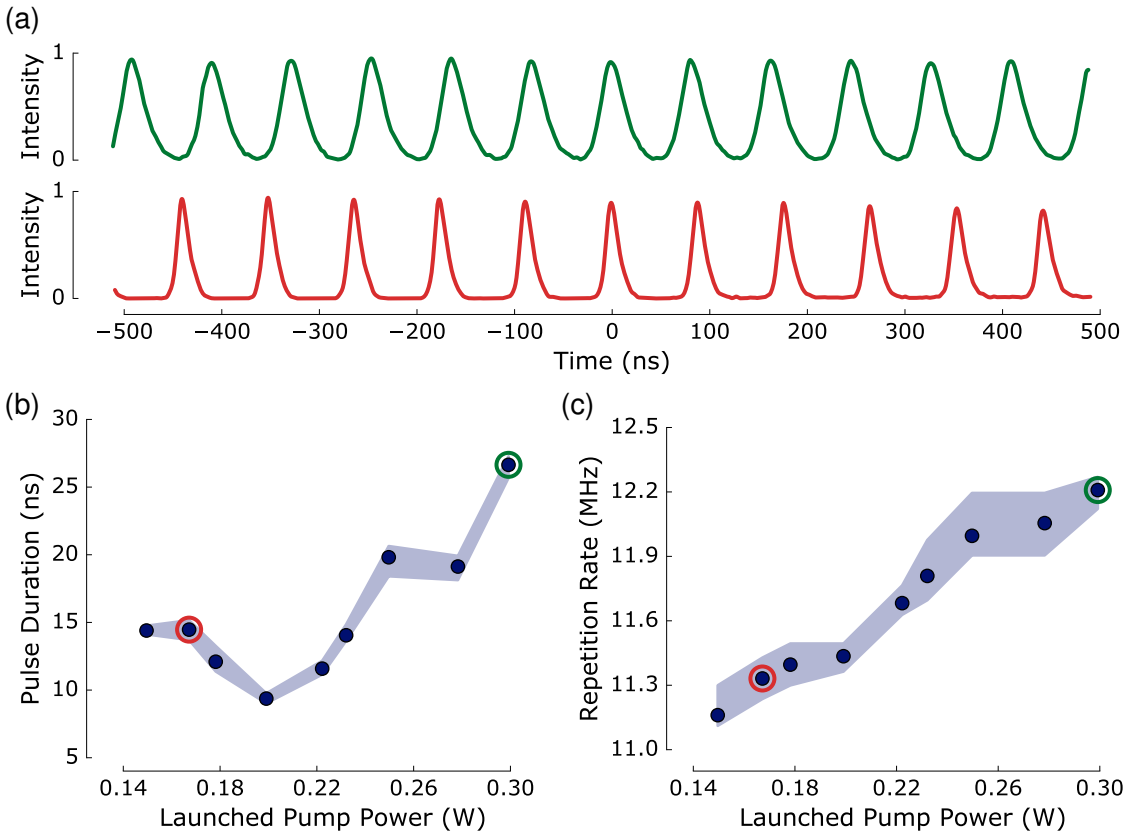


Fig. 5.13: Self-mode-locked temporal dynamics in our Brillouin PCF laser: (a) measured pulse trains, where the (b) pulse duration and (c) repetition rate vary with pump power. The trains in (a) correspond to the red and green ringed points in (b). Pulse-to-pulse properties showed flucations; the plotted points (blue dots) are the averaged values and the range is indicated by the shaded region.

as a narrowband spectral resonance, which can induce a large change in the group index, changing the delay of a pulse envelope travelling through the fibre [Son05]. Additionally, amplification of the leading edge of the Stokes pulse from the counter-propagating pump wave (and correspondingly, attenuation of the trailing edge due to pump depletion) results in an additional time shift [Pic91]. These pulses have thus been referred to as *superluminous dissipative Brillouin solitons*, confirmed by numerical simulations using a coherent three-wave model that included pump and Stokes light, in addition to acoustic waves with finite phonon lifetime [Mon99]. Unequal leading-edge amplification and trailing-edge attenuation explain the variations in pulse duration.

While stable pulse trains could be measured, they exhibited fluctuations in pulse properties over time (shown by the shaded regions in Fig. 5.13 after recording numerous pulse trains at separate times). Additionally, the pulses dispersed every few seconds, before quickly forming a stable train again. This long-term instability relates to the weak mode coupling of the process (hence the term partial, rather than full mode-locking) which is regularly perturbed by fluctuations, such as thermally-induced changes in cavity length [Dam93]. Long-term-stable mode-locked Brillouin pulses have been demonstrated,

however, by including an acousto-optic modulator in the cavity to stabilise the modulation [Kaw78].

These periodic pulsations were observed for pump powers over the laser threshold, up to ∼300 mW, where this value corresponded to entering the region of significant single-pass SBS (as shown in Section 5.2.2). Above this pump power, the temporal output became constant. In this case, the pump light was always depleted by the end of the fibre, saturating the Brillouin gain and forming a time-independent Brillouin mirror [Mon99].

5.4 Summary

In this chapter, we characterised SBS in small-core PCF and observed a reduction in SBS threshold at 532 nm compared to conventional step-index fibre. The benefits of PCF over step-index fibre for Brillouin applications are wavelength-dependent however, due to the spectrally dependent optical mode area increasingly overlapping with air holes at longer wavelengths. Increased interaction between the optical mode and acoustic waves in the cladding reduces the Brillouin gain, and 'hard' air-silica boundaries at the holes couple longitudinal and shear acoustic waves to form a family of hybrid acoustic modes, in contrast to a dominant longitudinal elastic wave for larger core fibres.

We demonstrated this benefit by developing a proof-of-principle Brillouin PCF laser and analysing the temporal dynamics that arise naturally for this phenomena. For certain pump powers, stable pulse trains with tunable nanosecond pulse durations and megahertz repetition rates could be obtained. Conceptually, this is a simple approach to pulse generation, requiring only a narrow linewidth pump source and short (< 10 m) lengths of PCF. However, the long-term stability was poor, prohibiting practical applications of such a source without additional stabilisation (e.g. intracavity acousto-optic modulation), which add complexity and cost.

Further work will consider the temporal dynamics in regimes with hybrid acoustic modes, which affects the power transfer between pump and Stokes light and thus, could alter the coupling between modes. Additionally, we note that acoustic phenomena in fibre can have a significant effect on pulse dynamics. For instance, acoustic waves have been observed to affect pulse spacing in a mode-locked fibre laser [Dia91, Pil95], which can lead to self-organisation of multiple pulses in a single cavity round trip for high repetition rate harmonic mode-locking up to ∼1 GHz in single-mode fibres [Gru93, Guy94]. The development of small-core PCF enables even greater acoustic-driven modulation frequencies, which has recently been applied to induce harmonic mode-locking at >2 GHz repetition rates [Pan15].

These results highlight that in addition to enabling new regimes of optical parameters, PCFs offer novel acoustic properties, which can be detrimental or usefully exploited, depending on the desired optical response. This adds acoustic-driven optical interactions to the toolbox of nonlinear fibre optic effects which are available when designing photonic systems, although further work is required to quantify and exploit such phenomena.

6

Conclusion and Outlook

We began this thesis by noting that rapid progress has been achieved in fibre-optic and laser technology since its origins in the mid-twentieth century. Today, short-pulse fibre lasers and optical fibres are mature technologies, which have had a revolutionary impact on science, medicine and industry, yielding palpable benefits to society (the Internet is perhaps the most obvious example). The significance of this, alongside many other important optical developments is spotlighted this year by the United Nations designation of 2015 as the 'International Year of Light and Light-based Technologies' to celebrate such achievements [Dud15].

Despite great progress, however, end-users requirements for laser systems continue to grow as the breadth of fibre laser applications increases, driving further research. This thesis has explored the nonlinear optical properties of emerging nanomaterials and fibres and their opportunities for advancing short-pulse laser technology. In this concluding chapter we briefly summarise the main results we have achieved and place our contributions in a broader context. We also offer a personal outlook for future directions in this field.

Long-Cavity Lasers

In Chapter 3 we introduced a long-cavity (near-kilometre length) fibre laser architecture, extending established concepts of dispersion and nonlinearity management and frequency-swept pulses to increase the parameter space that can be offered by mode-locked fibre lasers. Our design produced stable pulse trains with hundreds of kilohertz repetition rates and nanosecond-duration pulses with a giant chirp. This concept enables pulse properties to be varied over many orders of magnitude by simply varying the cavity length.

The low repetition rate and high chirp of such pulses are ideal for chirped pulse amplification schemes (eliminating the need for pulse stretchers and pulse pickers), although concerns had been raised about the compressibility of such a *giant* chirp. While we agreed that conventional bulk diffraction grating-based chirp compensation was impractical, we

were able to demonstrate compression (and correspondingly, peak-power enhancement) by a factor of ∼100 using a custom-engineered *chirped fibre Bragg grating* (CFBG).

Is this laser design a serious competitor to existing *chirped-pulse amplification* (CPA) technologies? Unfortunately, the greatest asset of the design is also its main drawback: full fibre integration. While the all-fibre design achieves a compact, robust and alignment-free system, compression in a long CFBG and high peak power pulse propagation in subsequent fibre pigtails can lead to significant nonlinear effects (e.g. self-phase modulation and stimulated Raman scattering). These phenomena can distort the pulse, limiting the maximum peak power that can be usefully achieved to ∼10 kW. A possible solution, however, is to consider large-mode area fibres, where the increased modal area decreases the intensity and thus, the nonlinear phase accumulation.

Long-cavity lasers with a low repetition rate and high pulse-energy-to-average-power ratio are useful, however, for simple, compact low-threshold supercontinuum generation systems. We showed that compressed pulses at a low average power of ∼30 mW were sufficient for generating broadband light spanning over an octave in a *photonic crystal fibre* (PCF), with applications in spectroscopy and optical device characterisation. Similar low-power white light sources are already available commercially, and our architecture could be of interest here, perhaps competing with Q-switched microchip lasers.

Numerical simulations were used pervasively during the design of this laser architecture, following the development of computationally efficient models for calculating fibre properties and modelling pulse propagation in Chapter 2. These techniques are invaluable in research and industry for laser design and continued development will extend the validity of numerical models and enable new parameter spaces to be efficiently explored.

Modelling also provides additional insight into the underlying physics and enabled us to observe persistent dark soliton-like structures in the radiation build-up dynamics for our long-cavity laser. We note that long-cavity lasers can be considered as an interesting nonlinear system where the dephasing and extreme number of cavity modes lead to novel nonlinear interactions, which can be controlled by dispersion. Due to similarities in the mathematical treatment (based on the nonlinear Schrödinger equation) of fibre optics with wave interactions in a range of nonlinear dispersive physical systems (e.g. hydrodynamics and Bose-Einstein condensates) fibre lasers provide a convenient, table-top platform for exploring nonlinear physics to provide cross-discipline insight. Rogue waves are a particularly successful example: a poorly understood and potentially dangerous phenomena in oceans with fundamental similarities to statistical fluctuations of modulation instability-driven supercontinua [Sol07].

While the applications of such studies may not be obviously apparent, we argue that such curiosity-driven research is important to advance our understanding of nonlinear physics. Additionally, the history of science is filled with invaluable technological concepts arising tangentially to seemingly interesting-but-purposeless observations (arguably, the laser itself is ultimately a by-product of Charles Townes's initial interest in microwave spectroscopy [Tow99]). Therefore, further studies of nonlinear wave dynamics in lasers

offer the exciting possibility of uncovering new operating regimes with tangible benefits for pulsed lasers.

Nanomaterials

Two-dimensional (2D) nanomaterials were the focus of Chapter 4, specifically focussing on few-layer *transition metal dichalcogenides* (TMDs). Despite the first fabrication of these materials being reported in the 1960s, their potential for optoelectronic applications remained unexplored until the graphene-led renaissance in 2D materials started in 2004. Today, intense global research activity is focussed on this topic, searching for new physics and technological breakthroughs, with significant backing from governments, funding agencies and even the mass media. Our interest centred on the photonic applications of these nanomaterials and characterisation of their nonlinear optical properties.

We developed a microscopy technique enabling linear imaging of monolayer and few-layer MoS_2 flakes and harmonic generation imaging simultaneously, offering significantly improved contrast. Second- and third-harmonic generation were found to be ideal tools for characterising nanomaterial samples, enabling the crystal symmetry, layer count and magnitude of nonlinear response to be probed non-destructively. We plan to extend this technique to other transition metal dichalcogenides ($MoSe_2$, WS_2 etc.) and critically compare their nonlinear response, in addition to advancing the technique to enable tuning of the pump wavelength, permitting spectroscopy to explore the impact of strong excitonic resonances that are a particularly novel feature of such materials.

Few-layer MoS_2 and $MoSe_2$ were then demonstrated to behave as ultrafast wideband saturable absorbers for mode-locking and Q-switching fibre lasers across the near infrared region from $\sim$1 to 2 μm . This may seem surprising given the materials's bandgaps correspond to visible wavelengths. We therefore proposed a mechanism of edge-state saturable absorption to explain this, which is compatible with early fundamental absorption spectroscopy studies. We hope to further investigate this mechanism and consider how to engineer the edge states through different fabrication procedures. We also plan to develop visible lasers using Pr:ZBLAN fibre to operate at the resonant bandgap wavelength of such 2D material saturable absorbers, providing much-needed compact pulse sources for biological imaging applications.

Despite phenomenal research interest in nanomaterials, their commercial applications have been limited to date. Only a small number of mode-locked lasers are available on the market that include nanomaterial saturable absorbers, all of which are from university spin-out companies. That said, following our work, we have enjoyed discussions with industrial laser manufacturers on this topic; their response has always indicated great scientific interest and commercial possibility of such wideband and flexible intensity-dependent materials, coupled with resistance to implementing them until the technology becomes more established and their reliability is proven to the same degree as incumbent SESAM technology. The non-saturable losses of current 2D material absorbers, typically

above ten percent for the devices in this thesis, are also too high, limiting the laser efficiency which could be achieved. These issues are both pressing research problems to be addressed.

Beyond saturable absorbers, will 2D nanomaterials have a revolutionary technological impact in photonics to match the current research investment in this field? The global fascination with such low dimensional systems is understandable: they offer a playground for physicists to explore new effects (e.g. the quantum hall effect [Nov04]) and optical properties unlike conventional bulk materials. Additionally, manufacturing techniques are now available (based on liquid phase exfoliation) to scale fabrication to industrial quantities [Pat14] and the resulting materials are very flexible and well-suited for integration with a variety of optical components.

While graphene is the most celebrated 2D material, the absence of a bandgap raises serious problems for optoelectronic applications requiring electronic control. Monolayer TMDs are therefore promising alternatives, with direct bandgaps at visible wavelengths. Proof-of-principle experiments have already highlighted their possible applications in transistors and photodetectors [LS13], and as an active laser material [Wu15]. The difficulty will be in translating these controlled laboratory demonstrations to robust, mass-manufacturable devices. We also note a need for further critical study to compare and characterise emerging materials: within the literature, reported values for the magnitude of $\chi^{(3)}$ in graphene vary over six orders of magnitude [Che14]! This is related, in part, to attempts to apply experiments and models for bulk materials directly to their 2D counterparts, sometimes with questionable validity. Further theoretical work is therefore essential to complement continued experiments for improving our understanding of these structures.

To achieve true technological success, it is also important to demonstrate both technical and economic superiority over incumbent electrical and optical materials. The level of sunk investment in silicon and III-Vs may make this challenging, although the ferocious extent of the global research effort and the significant promise of 2D TMDs suggest that they certainly cannot be ignored from future technology predictions.

We foresee much continued research interest here too. Van der Waals heterostructures appear to be the next frontier: combining layers from a variety of different 2D materials to create new crystal structures [Gei13]. This could combine the advantages of each constituent material and offers a platform for engineering new materials to suit particular applications. This is an exciting prospect, with new physics to be discovered, but time will tell whether the technological impact is as transformative as many claim.

Acoustic Interactions in Photonic Crystal Fibre

Our investigation of *stimulated Brillouin scattering* (SBS) in PCF in Chapter 5 revealed the importance of the acoustic properties of a fibre in determining the full nonlinear optical response. We showed that the ratio of excitation wavelength to core size and hole pitch

determined the excited acoustic mode content, with very different acoustic behaviour in the solid core and microstructured cladding and coupling at the air-glass interfaces. This resulted in five times greater SBS threshold for 1550 nm pump light than expected from widely-accepted theory, suggesting that the existing theoretical models need augmenting to be universally applicable to new microstructured fibre designs.

With careful choice of pump wavelength for a small-core PCF, the increased core confinement enhanced nonlinear interactions and reduced the SBS threshold compared to a standard step-index fibre. We then exploited this to develop a Brillouin PCF laser and analysed the temporal dynamics, showing that under certain conditions a train of nanosecond pulses could be generated at megahertz repetition rates in a very simple setup. Further work will consider the role of acoustic interactions on such temporal dynamics.

In general, the novel acoustic properties of PCF are often overlooked in favour of focussing on the flexibility they offer for dispersive and nonlinear effects. We suggest that nonlinear optoacoustic interactions could be an additional asset to the toolkit of nonlinear phenomena which are used for improving short-pulse lasers. Recent progress has highlighted the use of acoustic resonances in PCFs to harmonically mode-lock a fibre laser at gigahertz repetition rates [Pan15] and we believe there is further progress to be made here for controlling cavity dynamics without expensive electrical modulators.

Final Remarks

The fact that short-pulse fibre laser research remains such an active and vibrant field, despite the maturity and existing market share of current fibre technology, is a testament to the importance of such devices and the wealth of opportunities that lie ahead. We hope that the work detailed in this thesis represents a small contribution to showing what can be achieved by exploiting nonlinearity. Looking forwards, there is a great deal of exciting work to be done.

List of Publications

The following peer-reviewed publications form the basis of the thesis:

Journal Papers

1. **Scalar nanosecond pulse generation in a nanotube mode-locked environmentally stable fiber laser**, IEEE Photon. Technol. Lett. **26**, 1672 (2014).
   R. I. Woodward, E. .J. R. Kelleher, D. Popa, T. Hasan, F. Bonaccorso, A. C. Ferrari, S. V. Popov, and J. R. Taylor.

2. **Stimulated Brillouin scattering of visible light in small-core photonic crystal fibers**, Opt. Lett. **39**, 2330 (2014).
   R. I. Woodward, E. J. R. Kelleher, S. V. Popov, and J. R. Taylor.

3. **Tunable Q-switched fiber laser based on saturable edge-state absorption in few-layer molybdenum disulfide (MoS_2)**, Opt. Express **22**, 31113 (2014).
   R. I. Woodward, E. J. R. Kelleher, R. C. T. Howe, G. Hu, F. Torrisi, T. Hasan, S. V. Popov, and J. R. Taylor.

4. **Solution processed MoS_2-PVA composite for sub-bandgap mode-locking of a wideband tunable ultrafast Er:fiber laser**, Nano Res. **8**, 1522 (2015).
   M. Zhang, R. C. T. Howe, R. I. Woodward, E. J. R. Kelleher, F. Torrisi, G. Hu, S. V. Popov, J. R. Taylor, and T. Hasan.

5. **Fiber grating compression of giant-chirped nanosecond pulses from an ultra-long nanotube mode-locked fiber laser**, Opt. Lett. **40**, 38 (2015).
   R. I. Woodward, E. .J. R. Kelleher, T. H. Runcorn, S. Loranger, D. Popa, V. J. Wittwer, A. C. Ferrari, S. V. Popov, R. Kashyap, and J. R. Taylor.

6. **Few-layer MoS_2 saturable absorbers for short-pulse laser technology: current status and future perspectives [Invited]**, Photon. Res. **3**, A30 (2015).
   R. I. Woodward, R. C. T. Howe, G. Hu, F. Torrisi, M. Zhang, T. Hasan, and E. J. R. Kelleher.

7. **Wideband saturable absorption in few-layer molybdenum diselenide ($MoSe_2$) for Q-switching Yb-, Er- and Tm-doped fiber lasers**, Opt. Express **23**, 20051 (2015).
   R. I. Woodward, R. C. T. Howe, T. H. Runcorn, G. Hu, F. Torrisi, E. J. R. Kelleher, and T. Hasan.

8. **2D Saturable Absorbers for Fiber Lasers [Invited]**, Appl. Sci. **5**, 1440 (2015).
   R. I. Woodward and E. J. R. Kelleher.

9. **Surfactant-aided exfoliation of molydenum disulphide for ultrafast pulse generation through edge-state saturable absorption**, Phys. Status Solidi B, In Press (2016).
   R. C. T. Howe, R. I. Woodward, G. Hu, Z. Yang, E. J. R. Kelleher, and T. Hasan.

10. **Dark solitons in laser radiation build-up dynamics**, Phys. Rev. E, In Press (2016).
    R. I. Woodward and E. J. R. Kelleher.

Conference Proceedings

1. **Q-switched fiber laser with MoS2 Saturable Absorber**, CLEO:2014, OSA Technical Digest (Optical Society of America), paper SM3H.6 (2014).
   R. I. Woodward, E. J. R. Kelleher, T. H. Runcorn, S. V. Popov, F Torrisi, R. C. T. Howe, and T. Hasan.

2. **Visible light stimulated Brillouin scattering in small-core photonic crystal fibers**, CLEO:2014, OSA Technical Digest (Optical Society of America), paper SM4N.1 (2014).
   R. I. Woodward, E. J. R. Kelleher, S. V. Popov, and J. R. Taylor.

3. **Nanotube mode-locked, low repetition rate pulse source for fiber-based supercontinuum generation at low average pump power**, CLEO:2014, OSA Technical Digest (Optical Society of America), paper STh3N.8 (2014).
   R. I. Woodward, E. J. R. Kelleher, T. H. Runcorn, D. Popa, T. Hasan, A. C. Ferrari, S. V. Popov, and J. R. Taylor.

4. **Nanosecond to picosecond fiber Bragg grating compression of giant-chirped pulses from an ultra-long mode-locked fiber laser**, CLEO Europe:2015, OSA Technical Digest (Optical Society of America), paper CJ-9.6 (2015).
   R. I. Woodward, E. .J. R. Kelleher, T. H. Runcorn, S. Loranger, D. Popa, V. J. Wittwer, A. C. Ferrari, S. V. Popov, R. Kashyap, and J. R. Taylor.

5. **Dark soliton statistics during radiation build-up of bright dissipative solitons in long-cavity mode-locked fiber lasers**, CLEO Europe:2015, OSA Technical Digest (Optical Society of America), paper EF-5.4 (2015).
   R. I. Woodward and E. J. R. Kelleher.

6. **Optical nonlinearity of few-layer MoS2 devices and applications in short-pulse laser technology [Invited]**, OECC:2015, paper JSuB.08 (2015).
   R. I. Woodward, T. Hasan, and E. J. R. Kelleher.

7. **Solitons Brillouin en présence de dispersion acoustique dans un oscillateur à fibre optique micro-structurée**, JNOG'35, Optique Bretagne (2015).
   R. I. Woodward, E. Picholle, and C. Montes.

8. **Characterization of the nonlinear susceptibility of monolayer MoS_2 using second- and third-harmonic generation microscopy**, Submitted (2016).
   R. I. Woodward, R. T. Murray, C. F. Phelan, R. E. P. de Oliveira, S. Li, G. Eda, and C. J. S. de Matos.

Additional Publications

In addition, the following work was published during the period October 2012 – October 2015, but is beyond the scope of this thesis:

1. **Graphene-based passively mode-locked bidirectional fiber ring laser**, Opt. Express **22**, 4539 (2014).
   V. Mamidala, R. I. Woodward, Y. Yang, H. H. Liu, and K. K. Chow.

2. **Fiber-integrated 780 nm source for visible parametric generation**, Opt. Express **22**, 29726 (2014).
   D. J. J. Hu, R. T. Murray, T. Legg, T. H. Runcorn, M. Zhang, R. I. Woodward, J. L. Lim, Y. Wang, F. Luan, B. Gu, P. P. Shum, E. J. R. Kelleher, S. V. Popov, and J. R. Taylor.

REFERENCES

[Abl11] M. J. Ablowitz, T. P. Horikis, S. D. Nixon, and D. J. Frantzeskakis, *Dark solitons in mode-locked lasers*, Opt. Lett. **36**, 793 (2011).

[Agr01] G. P. Agrawal, *Applications of Nonlinear Fibre Optics*, Academic Press (2001).

[Agr13] G. P. Agrawal, *Nonlinear Fiber Optics*, Academic Press (2013).

[Agu13] C. Aguergaray, A. Runge, M. Erkintalo, and N. G. R. Broderick, *Raman-driven destabilization of mode-locked long cavity fiber lasers: fundamental limitations to energy scalability*, Opt. Lett. **38**, 2644 (2013).

[Akh05] N. Akhmediev and A. Ankiewicz, *Dissipative Solitons*, Springer (2005).

[Alf70] R. R. Alfano and S. L. Shapiro, *Emission in the region 4000 to 7000 Å via four-photon coupling in glass*, Phys. Rev. Lett. **24**, 584 (1970).

[All91] J. Allain, M. Monerie, and H. Poignant, *Tunable CW lasing around 610, 635, 695, 715, 885 and 910 nm in praseodymium-doped fluorozirconate fibre*, Electron. Lett. **27**, 189 (1991).

[Avo08] P. Avouris, M. Freitag, and V. Perebeinos, *Carbon-nanotube photonics and optoelectronics*, Nature Photon. **2**, 341 (2008).

[Avr90] H. Avramopoulos, H. Houh, N. A. Whitaker, M. C. Gabriel, and T. Morse, *A passively mode-locked erbium fibre laser*, in *Opt. Amplifiers Their Appl. Vol. 13 1990 OSA Tech. Dig. Ser.*, p. PDP8, Optical Society of America (1990).

[Bae12] I. H. Baek, H. W. Lee, S. Bae, B. H. Hong, Y. H. Ahn, D. I. Yeom, and F. Rotermund, *Efficient mode-locking of sub-70-fs Ti:Sapphire laser by graphene saturable absorber*, Appl. Phys. Express **5**, 2 (2012).

[Bai14] J. Bai and E. Towe, *Unified model for analysis of light amplification in rare-earth doped fibers*, J. Opt. Soc. Am. B **31**, 2809 (2014).

[Bal13] S. Balac and F. Mahé, *Embedded Runge-Kutta scheme for step-size control in the interaction picture method*, Comput. Phys. Commun. **184**, 1211 (2013).

[Bao09] Q. Bao, H. Zhang, Y. Wang, Z. Ni, Y. Yan, Z. X. Shen, K. P. Loh, and D. Y. Tang, *Atomic-layer graphene as a saturable absorber for ultrafast pulsed lasers*, Adv. Funct. Mater. **19**, 3077 (2009).

[Bar91] W. L. Barnes, R. I. Laming, E. J. Tarbox, and P. R. Morkel, *Absorption and emission cross section of Er3+ doped silica fibers*, IEEE J. Quantum Electron. **27**, 1004 (1991).

[Bar94] C. Barnard, P. Myslinski, J. Chrostowski, and M. Kavehrad,*Analytical model for rare-earth-doped fiber amplifiers and lasers*, IEEE J. Quantum Electron. **30**, 1817 (1994).

[Bar97] Y. Barad, H. Eisenberg, M. Horowitz, and Y. Silberberg, *Nonlinear scanning laser microscopy by third harmonic generation*, Appl. Phys. Lett. **70**, 922 (1997).

[Bea72] A. R. Beal, J. C. Knights, and W. Y. Liang, *Transmission spectra of some transition metal dichalcogenides : II. Group VIA: trigonal prismatic coordination*, J. Phys. C Solid State Phys. **5**, 3540 (1972).

[Bec08] C. Becker, S. Stellmer, P. Soltan-Panahi, S. Dörscher, M. Baumert, E. M. Richter, J. Kronjäger, K. Bongs, and K. Sengstock, *Oscillations and interactions of dark and dark-bright solitons in Bose-Einstein condensates*, Nat. Phys. **4**, 496 (2008).

[Bet93] D. S. Bethune, C. H. Klang, M. S. de Vries, G. Gorman, R. Savoy, J. Vazquez, and R. Beyers, *Cobalt-catalysed growth of carbon nanotubes with single-atomic-layer walls*, Nature **363**, 605 (1993).

[Beu07] J. C. Beugnot, T. Sylvestre, D. Alasia, H. Maillotte, V. Laude, A. Monteville, L. Provino, N. Traynor, S. F. Mafang, and L. Thévenaz, *Complete experimental characterization of stimulated Brillouin scattering in photonic crystal fiber*, Opt. Express **15**, 15517 (2007).

[Bir97] T. A. Birks, J. C. Knight, and P. S. J. Russell, *Endlessly single-mode photonic crystal fiber.*, Opt. Lett. **22**, 961 (1997).

[Bir99] T. A. Birks, D. Mogilevtsev, J. C. Knight, P. S. J. Russell, J. Broeng, P. J. Roberts, J. A. West, D. C. Allan, and J. C. Fajardo, *The analogy between photonics crystal fibres and step index fibres*, in *Opt. Fiber Commun. Conf. 1999*, pp. 114/FG4–1 (1999).

[Bir15] S. Birkholz, C. Brée, A. Demircan, and G. Steinmeyer, *Predictability of rogue events*, Phys. Rev. Lett. **114**, 213901 (2015).

[BJ85] I. Bar-Joseph, A. A. Friesem, E. Lichtman, and R. G. Waarts, *Steady and relaxation oscillations of stimulated Brillouin scattering in single-mode optical fibers*, J. Opt. Soc. Am. B **2**, 1606 (1985).

[Blo29] F. Bloch, *Über die quantenmechanik der elektronen in kristallgittern [About the quantum mechanics of electrons in crystal lattices]*, Zeitschrift für Phys. **52**, 555 (1929).

[Blo62] N. Bloembergen and P. S. Pershan, *Light waves at the boundary of nonlinear media*, Phys. Rev. **128**, 606 (1962).

[Blo68] N. Bloembergen, R. K. Chang, S. S. Jha, and C. H. Lee, *Optical second-harmonic generation in reflection from media with inversion symmetry*, Phys. Rev. **174**, 813 (1968).

[Blo69] N. Bloembergen, W. K. Burns, and M. Matsuoka, *Reflected third harmonic generated by picosecond laser pulses*, Opt. Commun. **1**, 195 (1969).

[Blo88] K. J. Blow and D. Wood, *Mode-locked lasers with nonlinear external cavities*, J. Opt. Soc. Am. B **5**, 629 (1988).

[Blo89] K. J. Blow and D. Wood, *Theoretical description of transient stimulated Raman scattering in optical fibers*, IEEE J. Quantum Electron. **25**, 2665 (1989).

[Boe62] H. P. Boehm, A. Clauss, G. Fischer, and U. Hofmann, *Surface properties of extremely thin graphite lamellae*, Proc. Fifth Conf. Carbon p. 73 (1962).

[Boe86] H. Boehm, R. Setton, and E. Stumpp, *Nomenclature and terminology of graphite intercalation compounds*, Carbon N. Y. **24**, 241 (1986).

[Bon02] I. Bongrand, E. Picholle, and C. Montes, *Coupled longitudinal and transverse stimulated Brillouin scattering in single-mode optical fibers*, Eur. Phys. J. D **20**, 121 (2002).

[Bon10] F. Bonaccorso, Z. Sun, T. Hasan, and A. C. Ferrari, *Graphene photonics and optoelectronics*, Nature Photon. **4**, 611 (2010).

[Bos24] S. N. Bose, *Plancks gesetz und lichtquantenhypothese [Planck's law and light quantum hypothesis]*, Zeitschrift für Phys. **26**, 178 (1924).

[Bou71] J. Boussinesq, *Théorie de l'intumescence liquide, appelée onde solitaire ou de translation, se propageant dans un canal rectangulaire [Theory of swelling liquid called solitary wave, or propagation in a rectangular canal]*, Comptes rendus Hebd. des séances l'Académie des Sci. **72**, 755 (1871).

[Boy07] R. W. Boyd, *Nonlinear Optics*, Academic Press (2007).

[Boy14] R. W. Boyd, Z. Shi, and I. De Leon, *The third-order nonlinear optical susceptibility of gold*, Opt. Commun. **326**, 74 (2014).

[Bra74] D. J. Bradley and G. H. C. New, *Ultrashort pulse measurements*, Proc. IEEE **62**, 313 (1974).

[Bra97] T. Brabec and F. Krausz, *Nonlinear optical pulse propagation in the single-cycle regime*, Phys. Rev. Lett. **78**, 3282 (1997).

[Bre64] G. Bret and F. Gires, *Giant-pulse laser and light amplifier using variable transmission coefficient glasses as light switches*, Appl. Phys. Lett. **4**, 175 (1964).

[Bre09] M. Breusing, C. Ropers, and T. Elsaesser, *Ultrafast carrier dynamics in graphite*, Phys. Rev. Lett. **102**, 086809 (2009).

[Bri22] L. Brillouin, *Diffusion de la lumière et des rayonnes X par un corps transparent homogéne; influence del'agitation thermique [Diffusion of light and X-rays by a transparent homogeneous medium: influence of thermal agitation]*, Ann. des Phys. **17**, 88 (1922).

[Bro65] F. Brown, R. E. Parks, and A. M. Sleeper, *Nonlinear optical reflection from a metallic boundary*, Phys. Rev. Lett. **14**, 1029 (1965).

[Bro72] R. A. Bromley, R. B. Murray, and A. D. Yoffe, *The band structures of some transition metal dichalcogenides: III. Group VIA : trigonal prism materials*, J. Phys. C Solid State Phys. **5**, 759 (1972).

[Buc95] J. A. Buck, *Fundamentals of Optics Fibers*, Wiley (1995).

[Bul90] A. G. Bulushev, E. M. Dianov, and O. G. Okhotnikov, *Passive mode locking of a laser with a nonlinear fiber reflector*, Opt. Lett. **15**, 968 (1990).

[CD00] B. M. Caradoc-Davies, *Vortex dynamics in Bose-Einstein condensates*, Ph.D. thesis, University of Otago (2000).

[Cha12] A. Y. Chamorovskiy, A. V. Marakulin, A. S. Kurkov, and O. G. Okhotnikov, *Tunable Ho-doped soliton fiber laser mode-locked by carbon nanotube saturable absorber*, Laser Phys. Lett. **9** (2012).

[Cha13] B. Chakraborty, H. S. S. R. Matte, A. K. Sood, and C. N. R. Rao, *Layer-dependent resonant Raman scattering of a few layer MoS2*, J. Raman Spectrosc. **44**, 92 (2013).

[Che97a] L. R. Chen, S. D. Benjamin, P. W. E. Smith, and J. E. Sipe, *Ultrashort pulse reflection from fiber gratings: a numerical investigation*, J. Light. Technol. **15**, 1503 (1997).

[Che97b] S. V. Chernikov, Y. Zhu, J. R. Taylor, and V. P. Gapontsev, *Supercontinuum self-Q-switched ytterbium fiber laser*, Opt. Lett. **22**, 298 (1997).

[Che12] T. Cheiwchanchamnangij and W. R. L. Lambrecht, *Quasiparticle band structure calculation of monolayer, bilayer, and bulk MoS2*, Phys. Rev. B **85**, 205302 (2012).

[Che14] J. L. Cheng, N. Vermeulen, and J. E. Sipe, *Third order optical nonlinearity of graphene*, New J. Phys. **16**, 053014 (2014).

[Chh13] M. Chhowalla, H. S. Shin, G. Eda, L.-J. Li, K. P. Loh, and H. Zhang, *The chemistry of two-dimensional layered transition metal dichalcogenide nanosheets*, Nat. Chem. **5**, 263 (2013).

[Chi64] R. Chiao, C. Townes, and B. Stoicheff, *Stimulated Brillouin scattering and coherent generation of intense hypersonic waves*, Phys. Rev. Lett. **12**, 592 (1964).

[Chi95] R. A. Chipman, *Polarimetry*, in *Handb. Opt. II* (edited by M. Bass), chapter 22, McGraw-Hill (1995).

[Chi11] N. B. Chichkov, C. Hapke, K. Hausmann, T. Theeg, D. Wandt, U. Morgner, J. Neumann, and D. Kracht, *0.5 µJ pulses from a giant-chirp ytterbium fiber oscillator*, Opt. Express **19**, 3647 (2011).

[Cho06] A. Chong, J. Buckley, W. Renninger, and F. Wise, *All-normal-dispersion femtosecond fiber laser*, Opt. Express **14**, 10095 (2006).

[Chu15] D. V. Churkin, S. Sugavanam, N. Tarasov, S. Khorev, S. V. Smirnov, S. M. Kobtsev, and S. K. Turitsyn, *Stochasticity, periodicity and localized light structures in partially mode-locked fibre lasers*, Nat. Commun. **6**, 7004 (2015).

[Cla09] A. Clauset, C. R. Shalizi, and M. E. J. Newman, *Power-law distributions in empirical data*, SIAM Rev. **51**, 661 (2009).

[Cla14] D. J. Clark, V. Senthilkumar, C. T. Le, D. L. Weerawarne, B. Shim, J. I. Jang, J. H. Shim, J. Cho, Y. Sim, M.-J. Seong, S. H. Rhim, A. J. Freeman, K.-H. Chung, and Y. S. Kim, *Strong optical nonlinearity of CVD-grown MoS2 monolayer as probed by wavelength-dependent second-harmonic generation*, Phys. Rev. B **90**, 1 (2014).

[Coh79] L. G. Cohen, C. Lin, and W. G. French, *Tailoring zero chromatic dispersion into the 1.5 - 1.6 µm low-loss spectral region of single-mode fibres*, Electron. Lett. **15**, 334 (1979).

[Col42] D. Colladon, *Sur les réflexions d'un rayon de lumière à l'intérieur d'une veine liquide parabolique (on the reflections of a ray of light inside a parabolic liquid stream)*, Comptes Rendus **15**, 800 (1842).

[Col09] P. Colomban, *The use of metal nanoparticles to produce yellow, red and iridescent colour, from Bronze Age to present times in lustre pottery and glass: solid state chemistry, spectroscopy and nanostructure*, J. Nano Res. **8**, 109 (2009).

[Con13] M. Conforti, A. Marini, T. X. Tran, D. Faccio, and F. Biancalana, *Interaction between optical fields and their conjugates in nonlinear media*, Opt. Express **21**, 31239 (2013).

[Cou11] A. Couairon, E. Brambilla, T. Corti, D. Majus, O. Ramírez-Góngora, and M. Kolesik, *Practitioner's guide to laser pulse propagation models and simulation*, Eur. Phys. J. Spec. Top. **199**, 5 (2011).

[Cre99] R. F. Cregan, B. J. Mangan, J. C. Knights, T. A. Birks, P. S. J. Russell, P. J. Roberts, and D. C. Allan, *Single-mode photonic band gap guidance of light in air*, Science **285**, 1537 (1999).

[Cun99] S. T. Cundiff, B. C. Collings, N. N. Akhmediev, J. M. Soto-Crespo, K. Bergman, and W. H. Knox, *Observation of polarization-locked vector solitons in an optical fiber*, Phys. Rev. Lett. **82**, 3988 (1999).

[Cun02] S. T. Cundiff, J. M. Soto-Crespo, and N. Akhmediev, *Experimental evidence for soliton explosions*, Phys. Rev. Lett. **88**, 073903 (2002).

[Dai06] P. Dainese, P. S. J. Russell, N. Joly, J. C. Knight, G. S. Wiederhecker, H. L. Fragnito, V. Laude, and A. Khelif, *Stimulated Brillouin scattering from multi-GHz-guided acoustic phonons in nanostructured photonic crystal fibre*, Nat. Phys. **2**, 388 (2006).

[Dam91] M. Damzen, R. Lamb, and G. Wong, *Ultrashort pulse generation by phase locking of multiple stimulated Brillouin scattering*, Opt. Commun. **82**, 337 (1991).

[Dam93] M. Dammig, G. Zinner, F. Mitschke, and H. Welling, *Stimulated Brillouin scattering in fibers with and without external feedback*, Phys. Rev. **48**, 3301 (1993).

[Dam03] M. J. Damzen, V. I. Vlad, V. Babin, and A. Mocofanescu, *Stimulated Brillouin Scattering: Fundamentals and Applications*, IOP Publishing (2003).

[Dav02] E. J. H. Davies, S. Y. Texier, R. K. Patlnaik, L. Farr, B. J. Mangan, J. C. Knight, J. Toulouse, and P. S. J. Russell, *Stimulated Brillouin scattering and lasing in low loss photonic crystal fibers*, in *Nonlinear Guid. Waves Their Appl.*, volume 80 of *OSA Trends in Optics and Photonics*, p. PD7, Optical Society of America (2002).

[Deg95] J. Degnan, *Optimization of passively Q-switched lasers*, IEEE J. Quantum Electron. **31**, 1890 (1995).

[DeM66] A. J. DeMaria, D. A. Stetser, and H. Heynau, *Self mode-locking of lasers with saturable absorbers*, Appl. Phys. Lett. **8**, 174 (1966).

[Dem94] M. I. Demchuk, N. V. Kuleshov, and V. P. Mikhailov, *Saturable absorbers based on impurity and defect centers in crvstals*, IEEE J. Quantum Electron. **30**, 2120 (1994).

[DeM04] C. J. S. DeMatos, S. V. Popov, A. B. Rulkov, J. R. Taylor, J. Broeng, T. P. Hansen, and V. P. Gapontsev, *All-fiber format compression of frequency chirped pulses in air-guiding photonic crystal fibers*, Phys. Rev. Lett. **93**, 103901 (2004).

[Den94] M. L. Dennis and I. N. Duling, *Experimental study of sideband generation in femtosecond fiber lasers*, IEEE J. Quantum Electron. **30**, 1469 (1994).

[DeS93] E. A. DeSouza, C. E. Soccolich, W. Pleibel, R. H. Stolen, J. R. Simpson, and D. J. DiGiovanni, *Saturable absorber modelocked polarisation maintaining erbium-doped fibre laser*, Electron. Lett. **29**, 447 (1993).

[Dev94] M. O. V. Deventer and A. J. Boot, *Polarization properties of stimulated Brillouin scattering in single-mode fibers*, J. Light. Technol. **12**, 585 (1994).

[Dia85] E. M. Dianov, A. Y. Karasik, P. V. Mamyshev, A. M. Prokhorov, V. N. Serkin, M. F. Stel'makh, and A. A. Fomichev, *Stimulated-Raman conversion of multisoliton pulses in quartz optical fibers*, JETP Lett. **41**, 242 (1985).

[Dia91] E. M. Dianov, A. V. Luchnikov, A. N. Pilipetskii, and A. N. Starodumov, *Long-range interaction of soliton pulse trains in a single-mode fibre*, Sov. Light. Commun. **1**, 37 (1991).

[Dia95] G. Diankov and I. Uzunov, *Soliton interaction of dark pulses on a background of finite width in optical fiber*, Opt. Commun. **117**, 424 (1995).

[Dia12] E. M. Dianov, *Bismuth-doped optical fibers: a challenging active medium for near-IR lasers and optical amplifiers*, Light Sci. Appl. **1**, e12 (2012).

[Die06] J.-C. Diels and W. Rudolph, *Ultrashort Laser Pulse Phenomena*, Academic Press (2006).

[Dig01] M. J. F. Digonnet, *Rare-Earth-Doped Fiber Lasers and Amplifiers*, CRC Press (2001).

[dM04] C. de Matos, J. Taylor, and K. Hansen, *All-fibre Brillouin laser based on holey fibre yielding comb-like spectra*, Opt. Commun. **238**, 185 (2004).

[Dor88] N. J. Doran and D. Wood, *Nonlinear-optical loop mirror*, Opt. Lett. **13**, 56 (1988).

[Dru01] P. D. Drummond and J. F. Corney, *Quantum noise in optical fibers. I. Stochastic equations*, J. Opt. Soc. Am. B **18**, 139 (2001).

[Dud06] J. M. Dudley, G. Genty, and S. Coen, *Supercontinuum generation in photonic crystal fiber*, Rev. Mod. Phys. **78**, 1135 (2006).

[Dud10] J. M. Dudley and J. R. Taylor (editors), *Supercontinuum Generation in Optical Fibers*, Cambridge University Press (2010).

[Dud14] J. M. Dudley, F. Dias, M. Erkintalo, and G. Genty, *Instabilities, breathers and rogue waves in optics*, Nature Photon. **8**, 755 (2014).

[Dud15] J. M. Dudley, *Editorial: lighting up research*, Phys. Rev. Lett. **114**, 120001 (2015).

[Dul90] I. N. Duling, *All-fiber modelocked figure eight laser*, in *OSA 1990 Tech. Dig. Ser. (Optical Soc. Am.*, volume 5, pp. 306–10 (1990).

[Dul91a] I. Duling, *Subpicosecond all-fibre erbium laser*, Electron. Lett. **27**, 544 (1991).

[Dul91b] I. Duling, *All-fiber ring soliton laser mode locked with a nonlinear mirror*, Opt. Lett. **16**, 539 (1991).

[Dul94] I. N. Duling, C. J. Chen, P. K. A. Wai, and C. R. Menyuk, *Operation of a nonlinear loop mirror in a laser cavity*, IEEE J. Quantum Electron. **30**, 194 (1994).

[Dzh83] M. I. Dzhibladze, Z. G. Esiashvili, E. S. Teplitskit, S. K. Isaev, and V. R. Sagaradze, *Mode locking in a fiber laser*, Sov. J. Quantum Electron. **13**, 245 (1983).

[Ein17] A. Einstein, *Zur Quantentheorie der Strahlung [On the quantum theory of radiation]*, Phys. Zeitschrift **18**, 121 (1917).

[Ein24] A. Einstein, *Quantentheorie des einatomigen idealen Gases [Quantum theory of the monatomic ideal gas]*, Sitzungsberichte der Preuss. Akad. der Wissenschaften p. 261 (1924).

[Emp87] P. Emplit, J. P. Hamaide, F. Reynaud, C. Froehly, and A. Barthelemy,*Picosecond steps and dark pulses through nonlinear single mode fibers*, Opt. Commun. **62**, 374 (1987).

[Far57] M. Faraday, *The bakerian lecture: experimental relations of gold (and other metals) to light*, Philos. Trans. R. Soc. London **147**, 145 (1857).

[Fei02] E. L. Feinberg, *The forefather (about Leonid Isaakovich Mandelstam)*, Physics-Uspekhi **45**, 81 (2002).

[Fer90] M. E. Fermann, F. Haberl, M. Hofer, and H. Hochreiter, *Nonlinear amplifying loop mirror*, Opt. Lett. **15**, 752 (1990).

[Fin03] V. Finazzi, T. M. Monro, and D. J. Richardson, *The role of confinement loss in highly nonlinear silica holey fibers*, IEEE Photonics Technol. Lett. **15**, 1246 (2003).

[Fra61] P. A. Franken, A. E. Hill, C. W. Peters, and G. Weinreich, *Generation of optical harmonics*, Phys. Rev. Lett. **7**, 118 (1961).

[Fra91] P. L. Francois, *Nonlinear propagation of ultrashort pulses in optical fibers: total field formulation in the frequency domain*, J. Opt. Soc. Am. B **8**, 276 (1991).

[Fra10] D. J. Frantzeskakis, *Dark solitons in atomic Bose-Einstein condensates: from theory to experiments*, J. Phys. A **43**, 213001 (2010).

[Fri63] R. F. Frindt and A. D. Yoffe, *Physical properties of layer structures: optical properties and photoconductivity of thin crystals of molybdenum disulphide*, Proc. R. Soc. London A **273**, 69 (1963).

[Fri65] R. F. Frindt, *Optical absorption of a few unit-cell layers of MoS2*, Phys. Rev. **140**, A536 (1965).

[Fri66] R. F. Frindt, *Single crystals of MoS2 several molecular layers thick*, J. Appl. Phys. **37**, 1928 (1966).

[Fuj13] Y. Fujimoto, J. Nakanishi, T. Yamada, O. Ishii, and M. Yamazaki, *Visible fiber lasers excited by GaN laser diodes*, Prog. Quantum Electron. **37**, 185 (2013).

[Gab46] D. Gabor, *Theory of communication. Part 1: The analysis of information*, J. Inst. Electr. Eng. - Part III Radio Commun. Eng. **93**, 429 (1946).

[Gae91] A. L. Gaeta and R. W. Boyd, *Stochastic dynamics of stimulated Brillouin scattering in an optical fiber*, Phys. Rev. A **44**, 3205 (1991).

[Gag14] M. Gagné, S. Loranger, J. Lapointe, and R. Kashyap, *Fabrication of high quality, ultra-long fiber Bragg gratings: up to 2 million periods in phase.*, Opt. Express **22**, 387 (2014).

[Gan78] J. N. Gannaway and C. J. R. Sheppard, *Second-harmonic imaging in the scanning optical microscope*, Opt. Quantum Electron. **10**, 435 (1978).

[Gan14] R. Ganatra and Q. Zhang, *Few-layer MoS2: a promising layered semiconductor*, ACS Nano **8**, 4074 (2014).

[Gar00] E. Garmire, *Resonant optical nonlinearities in semiconductors*, IEEE J. Sel. Top. Quantum Electron. **6**, 1094 (2000).

[Gei13] A. K. Geim and I. V. Grigorieva, *Van der Waals heterostructures*, Nature **499**, 419 (2013).

[Gen07] G. Genty, P. Kinsler, B. Kibler, and J. M. Dudley, *Nonlinear envelope equation modeling of sub-cycle dynamics and harmonic generation in nonlinear waveguides*, Opt. Express **15**, 5382 (2007).

[Ger80] J. I. Gersten, R. R. Alfano, and M. Belic, *Combined stimulated Raman scattering and continuum self-phase modulations*, Phys. Rev. A **21**, 1222 (1980).

[Glo71] D. Gloge, *Weakly guiding fibres*, Appl. Opt. **10**, 2252 (1971).

[GN89] A. S. Gouveia-Neto and J. R. Taylor, *Soliton evolution from noise bursts*, Electron. Lett. **25**, 736 (1989).

[Gom85] A. S. L. Gomes, U. Osterberg, and W. Sibbett, *An experimental study of the primary parameters that determines the temporal compression of CW Nd:YAG laser pulses*, Opt. Commun. **54**, 377 (1985).

[Gor55] J. P. Gordon, H. J. Zeiger, and C. H. Townes, *The maser - new type of microwave amplifier, frequency standard, and spectrometer*, Phys. Rev. **99**, 1264 (1955).

[Gra63] D. G. Grant, *A technique for obtaining single, high peak power pulses from a ruby lasers*, Proc. IEEE **51**, 604 (1963).

[Gre90] A. Gredeskul, Y. S. Kivshar, and M. V. Yanovskaya, *Dark-pulse solitons in nonlinear-optical fibers*, Phys. Rev. A **41**, 3994 (1990).

[Gro30] E. Gross, *Change of wave-length of light due to elastic heat waves at scattering in liquids*, Nature **126**, 201 (1930).

[Gru92a] S. G. Grubb, K. W. Bennett, R. S. Cannon, and W. F. Humer, *CW room-temperature blue upconversion fibre laser*, Electron. Lett. **28**, 1243 (1992).

[Gru92b] A. B. Grudinin, D. J. Richardson, and D. N. Payne, *Energy quantisation in figure eight fibre laser*, Electron. Lett. **28**, 67 (1992).

[Gru93] A. Grudinin, D. Richardson, and D. Payne, *Passive harmonic modelocking of a fibre soliton ring laser*, Electron. Lett. **29**, 1860 (1993).

[Gue63] K. Guers and R. Mueller, *Breitband-modulation durch steuerung der emission eines optischen masers (auskoppelmodulation) [Broadband modulation by controlling the emission of an optical maser]*, Phys. Lett. **5**, 179 (1963).

[Gue97] P. T. Guerreiro, S. Ten, N. F. Borrelli, J. Butty, G. E. Jabbour, and N. Peyghambarian, *PbS quantum-dot doped glasses as saturable absorbers for mode locking of a Cr: forsterite laser*, Appl. Phys. Lett. **71**, 1595 (1997).

[Guy94] M. J. Guy, D. U. Noske, A. Boskovic, and J. R. Taylor, *Femtosecond soliton generation in a praseodymium fluoride fiber laser*, Opt. Lett. **19**, 828 (1994).

[Hal62] R. N. Hall, G. E. Fenner, J. D. Kingsley, T. J. Soltys, and R. O. Carlson, *Coherent light emission from GaAs junctions*, Phys. Rev. Lett. **9**, 366 (1962).

[Han27] C. W. Hansell, *Picture Transmission*, US Pat. 1751584 (1927).

[Har64] L. E. Hargrove, R. L. Fork, and M. A. Pollack, *Locking of HeNe laser modes induced by synchronous intracavity modulation*, Appl. Phys. Lett. **5**, 4 (1964).

[Har73] R. H. Hardin and F. D. Tappert, *Application of the split step Fourier method to the numerical solution of nonlinear and variable coefficient wave equations*, SIAM Rev. Chron. **15**, 423 (1973).

[Has73a] A. Hasegawa and F. Tappert, *Transmission of stationary nonlinear optical pulses in dispersive dielectric fibers. I. Anomalous dispersion*, Appl. Phys. Lett. **23**, 142 (1973).

[Has73b] A. Hasegawa and F. Tappert, *Transmission of stationary nonlinear optical pulses in dispersive dielectric fibers. II. Normal dispersion*, Appl. Phys. Lett. **23**, 171 (1973).

[Has90] A. Hasegawa and Y. Kodama, *Guiding-center soliton in optical fibers*, Opt. Lett. **15**, 1443 (1990).

[Has09] T. Hasan, Z. Sun, F. Wang, F. Bonaccorso, P. H. Tan, A. G. Rozhin, and A. C. Ferrari, *Nanotube-polymer composites for ultrafast photonics*, Adv. Mater. **21**, 3874 (2009).

[Hec02] E. Hecht, *Optics*, Pearson Education (2002).

[Hec04] J. Hecht, *City of Light: The Story of Fiber Optics*, Oxford University Press (2004).

[Hec10] J. Hecht, *Beam: The Race to Make the Laser*, Oxford University Press (2010).

[Hel74] R. Hellwarth and P. Christensen, *Nonlinear optical microscopic examination of structure in polycrystalline ZnSe*, Opt. Commun. **12**, 318 (1974).

[Hil76a] K. O. Hill, B. S. Kawasaki, and D. C. Johnson, *cw Brillouin laser*, Appl. Phys. Lett. **28**, 608 (1976).

[Hil76b] K. O. Hill, B. S. Kawasaki, and D. C. Johnson, *Low-threshold cw Raman laser*, Appl. Phys. Lett. **29**, 181 (1976).

[Hil78] K. O. Hill, Y. Fujii, D. C. Johnson, and B. S. Kawasaki, *Photosensitivity in optical fiber waveguides: application to reflection filter fabrication*, Appl. Phys. Lett. **32**, 647 (1978).

[Hna13] C. Hnatovsky, V. G. Shvedov, and W. Krolikowski, *The role of light-induced nanostructures in femtosecond laser micromachining with vector and scalar pulses*, Opt. Express **21**, 12651 (2013).

[Hof91] M. Hofer, M. E. Fermann, F. Haberl, M. H. Ober, and A. J. Schmidt, *Mode locking with cross-phase and self-phase modulation*, Opt. Lett. **16**, 502 (1991).

[Hof92] M. Hofer, M. H. Ober, F. Haberl, and M. E. Fermann, *Characterization of ultrashort pulse formation in passively mode-locked fiber lasers*, IEEE J. Quantum Electron. **28**, 720 (1992).

[Hol02] D. Hollenbeck and C. D. Cantrell, *Multiple-vibrational-mode model for fiber-optic Raman gain spectrum and response function*, J. Opt. Soc. Am. B **19**, 2886 (2002).

[Hor97] M. Horowitz, Y. Barad, and Y. Silberberg, *Noiselike pulses with a broadband spectrum generated from an erbium-doped fiber laser*, Opt. Lett. **22**, 799 (1997).

[How16] R. C. T. Howe, R. I. Woodward, G. Hu, Z. Yang, E. J. R. Kelleher, and T. Hasan, *Surfactant-aided exfoliation of molydenum disulphide for ultrafast pulse generation through edge-state saturable absorption*, Phys. Status Solidi B **253**, 1 (2016).

[Hua01] G. Huang, M. G. Velarde, and V. A. Makarov, *Dark solitons and their head-on collisions in Bose-Einstein condensates*, Phys. Rev. A **64**, 013617 (2001).

[Hul07] J. Hult, *A fourth-order Runge-Kutta in the interaction picture method for simulating supercontinuum generation in optical fibers*, J. Light. Technol. **25**, 3770 (2007).

[Iij91] S. Iijima, *Helical microtubules of graphitic carbon*, Nature **354**, 56 (1991).

[Iij93] S. Iijima and T. Ichihashi, *Single-shell carbon nanotubes of 1-nm diameter*, Nature **363**, 603 (1993).

[Ipp72a] E. P. Ippen, C. V. Shank, and A. Dienes, *Passive mode locking of the cw dye laser*, Appl. Phys. Lett. **21**, 348 (1972).

[Ipp72b] E. P. Ippen and R. H. Stolen, *Stimulated Brillouin scattering in optical fibers*, Appl. Phys. Lett. **21**, 539 (1972).

[Ipp89] E. P. Ippen, H. A. Haus, and L. Y. Liu, *Additive pulse mode locking*, J. Opt. Soc. Am. B **6**, 1736 (1989).

[Isl87] M. N. Islam, L. F. Mollenauer, R. H. Stolen, J. R. Simpson, and H. T. Shang, *Cross-phase modulation in optical fibers*, Opt. Lett. **12**, 625 (1987).

[Isl89] M. N. Islam, G. Sucha, I. Bar-Joseph, M. Wegener, J. P. Gordon, and D. S. Chemla, *Broad bandwidths from frequency-shifting solitons in fibers.*, Opt. Lett. **14**, 370 (1989).

[Jac99] S. Jackson and T. King, *Theoretical modeling of Tm-doped silica fiber lasers*, J. Light. Technol. **17**, 948 (1999).

[Jan13] J. K. Jang, M. Erkintalo, S. G. Murdoch, and S. Coen, *Ultraweak long-range interactions of solitons observed over astronomical distances*, Nature Photon. **7**, 657 (2013).

[Jav61] A. Javan, W. R. Bennett, and D. R. Herriott, *Population inversion and continuous optical maser oscillation in a gas discharge containing a He-Ne mixture*, Phys. Rev. Lett. **6**, 106 (1961).

[Joa08] J. D. Joannopoulos, S. G. Johnson, J. N. Winn, and R. D. Meade, *Photonic Crystals: Molding the Flow of Light*, Princeton University Press (2008).

[Joe86] P. Joensen, R. F. Frindt, and S. R. Morrison, *Single-layer MoS2*, Mater. Res. Bull. **21**, 457 (1986).

[Joh71] R. Johnson and J. Marburger, *Relaxation oscillations in stimulated Raman and Brillouin scattering*, Phys. Rev. A **4**, 1175 (1971).

[Joh01] S. G. Johnson and J. D. Joannopoulos, *Block-iterative frequency-domain methods for Maxwell's equations in a planewave basis*, Opt. Express **8**, 173 (2001).

[Jou98] C. Journet and P. Bernier, *Production of carbon nanotubes*, Appl. Phys. A **67**, 1 (1998).

[Kaf64] P. Kafalas, J. I. Masters, and E. M. E. Murray, *Photosensitive liquid used as a nondestructive passive Q-switch in a ruby laser*, J. Appl. Phys. **35**, 2349 (1964).

[Kan98] J. U. Kang and R. Posey, *Demonstration of supercontinuum generation in a long-cavity fiber ring laser*, Opt. Lett. **23**, 1375 (1998).

[Kao66] K. C. Kao and G. A. Hockham, *Dielectric-fibre surface waveguides for optical frequencies*, Proc. Inst. Electr. Eng. **113**, 1151 (1966).

[Kap70] F. P. Kapron, D. B. Keck, and R. D. Maurer, *Radiation losses in glass optical waveguides*, Appl. Phys. Lett. **17**, 423 (1970).

[Kär98] F. X. Kärtner, J. A. der Au, and U. Keller, *Mode-locking with slow and fast saturable absorbers - What's the difference?*, IEEE J. Sel. Top. Quantum Electron. **4**, 159 (1998).

[Kär99] F. X. Kärtner, D. M. Zumbühl, and N. Matuschek, *Turbulence in mode-locked lasers*, Phys. Rev. Lett. **82**, 4428 (1999).

[Kar15] L. Karvonen, A. Säynätjoki, S. Mehravar, R. D. Rodriguez, S. Hartmann, D. R. T. Zahn, S. Honkanen, R. a. Norwood, N. Peyghambarian, K. Kieu, H. Lipsanen, and J. Riikonen, *Investigation of second- and third-harmonic generation in few-layer gallium selenide by multiphoton microscopy*, Sci. Rep. **5**, 10334 (2015).

[Kas90] R. Kashyap, J. R. Armitage, R. Wyatt, S. T. Davey, and D. L. Williams, *All-fibre narrowband reflection gratings at 1500 nm*, Electron. Lett. **26**, 730 (1990).

[Kas99] R. Kashyap, *Fiber Bragg Gratings*, Academic Press (1999).

[Kas06] S. Kasap and P. Capper, *Springer Handbook of Electronic and Photonic Materials*, Springer (2006).

[Kat99] H. Kataura, Y. Kumazawa, Y. Maniwa, I. Umezu, S. Suzuki, Y. Ohtsuka, and Y. Achiba, *Optical properties of single-wall carbon nanotubes*, Synth. Met. **103**, 2555 (1999).

[Kaw78] B. S. Kawasaki, D. C. Johnson, Y. Fujii, and K. O. Hill, *Bandwidth-limited operation of a mode-locked Brillouin parametric oscillator*, Appl. Phys. Lett. **32**, 429 (1978).

[Kaw81] B. S. Kawasaki, K. O. Hill, and R. G. Lamont, *Biconical-taper single-mode fiber coupler*, Opt. Lett. **6**, 327 (1981).

[Kaw01] K. Kawano and T. Kitoh, *Introduction to Optical Waveguide Analysis*, Wiley (2001).

[Kel91] S. M. Kelly, K. Smith, K. J. Blow, and N. J. Doran, *Average soliton dynamics of a high-gain erbium fiber laser*, Opt. Lett. **16**, 1337 (1991).

[Kel92a] U. Keller, D. A. B. Miller, G. D. Boyd, T. H. Chiu, J. F. Ferguson, and M. T. Asom, *Solid-state low-loss intracavity saturable absorber for Nd:YLF lasers: an antiresonant semiconductor Fabry-Perot saturable absorber*, Opt. Lett. **17**, 505 (1992).

[Kel92b] S. M. J. Kelly, *Characteristic sideband instability of periodically amplified average soliton*, Electron. Lett. **28**, 806 (1992).

[Kel96] U. Keller, K. J. Weingarten, F. X. Kartner, D. Kopf, B. Braun, I. D. Jung, R. Fluck, C. Honninger, N. Matuschek, and J. Aus der Au, *Semiconductor saturable absorber mirrors (SESAM's) for femtosecond to nanosecond pulse generation in solid-state lasers*, IEEE J. Quantum Electron. **2**, 435 (1996).

[Kel03] U. Keller, *Recent developments in compact ultrafast lasers*, Nature **424**, 831 (2003).

[Kel09a] E. J. R. Kelleher, J. C. Travers, E. P. Ippen, Z. Sun, A. C. Ferrari, S. V. Popov, and J. R. Taylor, *Generation and direct measurement of giant chirp in a passively mode-locked laser*, Opt. Lett. **34**, 3526 (2009).

[Kel09b] E. J. R. Kelleher, J. C. Travers, Z. Sun, A. G. Rozhin, A. C. Ferrari, S. V. Popov, and J. R. Taylor, *Nanosecond-pulse fiber lasers mode-locked with nanotubes*, Appl. Phys. Lett. **95**, 111108 (2009).

[Kel14] E. J. R. Kelleher and J. C. Travers, *Chirped pulse formation dynamics in ultra-long mode-locked fiber lasers*, Opt. Lett. **39**, 1398 (2014).

[Ker75] J. Kerr, *A new relation between electricity and light: dielectrified media birefringent*, Philos. Mag. **50**, 337 (1875).

[Khu10] D. V. Khudyakov, A. S. Lobach, and V. a. Nadtochenko, *Passive mode locking in a Ti:sapphire laser using a single-walled carbon nanotube saturable absorber at a wavelength of 810 nm*, Opt. Lett. **35**, 2675 (2010).

[Kiv94] Y. S. Kivshar and X. Yang, *Dark solitons on backgrounds of finite extent*, Opt. Commun. **107**, 93 (1994).

[Kiv98] Y. Kivshar and B. Luther-Davies, *Dark optical solitons: physics and applications*, Phys. Rep. **298**, 81 (1998).

[Kiv09] S. Kivistö, T. Hakulinen, A. Kaskela, B. Aitchison, D. P. Brown, A. G. Nasibulin, E. I. Kauppinen, A. Härkönen, and O. G. Okhotnikov, *Carbon nanotube films for ultrafast broadband technology.*, Opt. Express **17**, 2358 (2009).

[Kni96] J. C. Knight, T. A. Birks, P. S. J. Russell, and D. M. Atkin, *All-silica single-mode optical fiber with photonic crystal cladding*, Opt. Lett. **21**, 1547 (1996).

[Kni98] J. C. Knight, T. A. Birks, P. S. J. Russell, and J. P. de Sandro, *Properties of photonic crystal fiber and the effective index model*, J. Opt. Soc. Am. A **15**, 748 (1998).

[Kni00] J. C. Knight, J. Arriaga, T. A. Birks, A. Ortigosa-Blanch, W. J. Wadsworth, and P. S. J. Russell, *Anomalous dispersion in photonic crystal fiber*, IEEE Photonics Technol. Lett. **12**, 807 (2000).

[Kob08] S. Kobtsev, S. Kukarin, and Y. Fedotov, *Ultra-low repetition rate mode-locked fiber laser with high-energy pulses*, Opt. Express **16**, 21936 (2008).

[Kob09] S. Kobtsev, S. Kukarin, S. Smirnov, S. Turitsyn, and A. Latkin, *Generation of double-scale femto/pico-second optical lumps in mode-locked fiber lasers*, Opt. Express **17**, 20707 (2009).

[Kob10] S. M. Kobtsev, S. V. Kukarin, and S. V. Smirnov, *All-fiber high-energy supercontinuum pulse generator*, Laser Phys. **20**, 375 (2010).

[Kob14] S. Kobtsev, S. Smirnov, S. Kukarin, and S. Turitsyn, *Mode-locked fiber lasers with significant variability of generation regimes*, Opt. Fiber Technol. **20**, 615 (2014).

[Kod87] Y. Kodama and a. Hasegawa, *Nonlinear pulse propagation in a monomode dielectric guide*, IEEE J. Quantum Electron. **23**, 510 (1987).

[Koe64] C. J. Koester and E. Snitzer, *Amplification in a fiber laser*, Appl. Opt. **3**, 1182 (1964).

[Koj13] J. Kojou, Y. Watanabe, P. Agrawal, T. Kamimura, and F. Kannari, *Wavelength tunable Q-switch laser in visible region with Pr 3+-doped fluoride-glass fiber pumped by GaN diode laser*, Opt. Commun. **290**, 136 (2013).

[Kol03] V. Z. Kolev, M. J. Lederer, B. Luther-Davies, and A. V. Rode, *Passive mode locking of a Nd:YVO4 laser with an extra-long optical resonator*, Opt. Lett. **28**, 1275 (2003).

[Kol14] M. Kolesik and J. V. Moloney, *Modeling and simulation techniques in extreme nonlinear optics of gaseous and condensed media*, Reports Prog. Phys. **77**, 016401 (2014).

[Kor95] D. J. Korteweg and G. DeVries, *On the change of form of long waves advancing in a rectangular canal, and on a new type of long stationary waves*, Philos. Mag. **39**, 422 (1895).

[Kos04] M. Koshiba and K. Saitoh, *Applicability of classical optical fiber theories to holey fibers*, Opt. Lett. **29**, 1739 (2004).

[Kra27] H. A. Kramers, *La diffusion de la lumiere par les atomes [The diffusion of light by atoms]*, Atti Cong. Intern. Fis. (Transactions Volta Centen. Congr. **2**, 545 (1927).

[Kro25] R. d. L. Kronig, *On the theory of dispersion of X-rays*, J. Opt. Soc. Am. **12**, 547 (1925).

[Kro85] H. W. Kroto, J. R. Heath, S. C. O'Brien, R. F. Curl, and R. E. Smalley, *C60: Buckminsterfullerene*, Nature **318**, 162 (1985).

[Kro88] D. Krokel, N. J. Halas, G. Giuliani, and D. Grischkowsky, *Dark-pulse propagation in optical fibers*, Phys. Rev. Lett. **60**, 29 (1988).

[Kud06] A. Kudlinski, A. K. George, J. C. Knight, J. C. Travers, A. B. Rulkov, S. V. Popov, and J. R. Taylor, *Zero-dispersion wavelength decreasing photonic crystal fibers for ultraviolet-extended supercontinuum generation.*, Opt. Express **14**, 5715 (2006).

[Kum13] N. Kumar, S. Najmaei, Q. Cui, F. Ceballos, P. Ajayan, J. Lou, and H. Zhao, *Second harmonic microscopy of monolayer MoS2*, Phys. Rev. B **87**, 161403 (2013).

[Lam30] H. Lamm, *Biegsame optische geräte [Flexible optical instruments]*, Zeitschrift für Instrumentenkd. **50**, 579 (1930).

[Lam64] W. E. Lamb, *Theory of an optical maser*, Phys. Rev. **134**, A1429 (1964).

[Lau05] V. Laude, A. Khelif, S. Benchabane, M. Wilm, T. Sylvestre, B. Kibler, A. Mussot, J. M. Dudley, and H. Maillotte, *Phononic band-gap guidance of acoustic modes in photonic crystal fibers*, Phys. Rev. B **71**, 045107 (2005).

[Lav15] A. Lavrinenko, N. Gregersen, J. Lægsgaard, and T. Søndergaard, *Numerical Methods in Photonics*, CRC Press (2015).

[LD92] B. Luther-Davies and X. Yang, *Steerable optical waveguides formed in self-defocusing media by using dark spatial solitons*, Opt. Lett. **17**, 1755 (1992).

[Lec96] V. Lecoeuche, S. Randoux, B. Segard, and J. Zemmouri, *Dynamics of stimulated Brillouin scattering with feedback*, Quantum Semiclass. Opt. **8**, 1109 (1996).

[Lee02] J. H. Lee, Z. Yusoff, W. Belardi, M. Ibsen, T. M. Monro, and D. J. Richardson, *Investigation of Brillouin effects in small-core holey optical fiber: lasing and scattering*, Opt. Lett. **27**, 927 (2002).

[Lee10] C. Lee, H. Yan, L. E. Brus, T. F. Heinz, J. Hone, and S. Ryu, *Anomalous lattice vibrations of single- and few-layer MoS2*, ACS Nano **4**, 2695 (2010).

[Lef10] S. Lefrançois, K. Kieu, Y. Deng, J. D. Kafka, and F. W. Wise, *Scaling of dissipative soliton fiber lasers to megawatt peak powers by use of large-area photonic crystal fiber*, Opt. Lett. **35**, 1569 (2010).

[Lew26] G. N. Lewis, *The conservation of photons*, Nature **118**, 874 (1926).

[Lew41] G. N. Lewis, D. Lipkin, and T. T. Magel, *Reversible photochemical processes in rigid media. A study of the phosphorescent state*, J. Am. Chem. Soc. **63**, 3005 (1941).

[Li04] Y.-F. Li, C.-Y. Wang, and M.-L. Hu, *A fully vectorial effective index method for photonic crystal fibers: application to dispersion calculation*, Opt. Commun. **238**, 29 (2004).

[Li06] Y. Li, C. Wang, Y. Chen, M. Hu, B. Liu, and L. Chai, *Solution of the fundamental space-filling mode of photonic crystal fibers: numerical method versus analytical approaches*, Appl. Phys. B **85**, 597 (2006).

[Li08] Y. Li, Y. Yao, M. Hu, L. Chai, and C. Wang,*Improved fully vectorial effective index method for photonic crystal fibers: evaluation and enhancement*, Appl. Opt. **47**, 399 (2008).

[Li13] Y. Li, Y. Rao, K. F. Mak, Y. You, S. Wang, C. R. Dean, and T. F. Heinz, *Probing symmetry properties of few-layer MoS2 and h-BN by optical second-harmonic generation*, Nano Lett. **13**, 3329 (2013).

[Li14] H. Li, J. Wu, Z. Yin, and H. Zhang, *Preparation and applications of mechanically exfoliated single-layer and multilayer MoS2 and WSe2 nanosheets*, Acc. Chem. Res. **47**, 1067 (2014).

[Lim00] J. Limpert, H. Zellmer, P. Riedel, G. Maze, and A. Tünnermann, *Laser oscillation in yellow and blue spectral range in Dy3+:ZBLAN*, Electron. Lett. **36**, 1386 (2000).

[Lit97] N. Litchinitser and D. Patterson, *Analysis of fiber Bragg gratings for dispersion compensation in reflective and transmissive geometries*, J. Light. Technol. **15**, 1323 (1997).

[Loh93] W. H. Loh, D. Atkinson, P. R. Morkel, M. Hopkinson, A. Rivers, A. J. Seeds, and D. N. Payne, *All-solid-state subpicosecond passively mode locked erbium-doped fiber laser*, Appl. Phys. Lett. **63**, 4 (1993).

[LS13] O. Lopez-Sanchez, D. Lembke, M. Kayci, A. Radenovic, and A. Kis, *Ultrasensitive photodetectors based on monolayer MoS2*, Nat. Nanotechnol. **8**, 497 (2013).

[Lug72] V. N. Lugovoi and V. N. Strel'tsoc, *Stimulated Mandel'shtam-Brillouin emission in an optical resonator*, Sov. Phys. JETP **15**, 692 (1972).

[Ma04] Y.-Z. Ma, J. Stenger, J. Zimmermann, S. M. Bachilo, R. E. Smalley, R. B. Weisman, and G. R. Fleming, *Ultrafast carrier dynamics in single-walled carbon nanotubes probed by femtosecond spectroscopy*, J. Chem. Phys. **120**, 3368 (2004).

[Mai60] T. H. Maiman, *Stimulated optical radiation in ruby*, Nature **187**, 494 (1960).

[Mak08] K. F. Mak, M. Y. Sfeir, Y. Wu, C. H. Lui, J. A. Misewich, and T. F. Heinz, *Measurement of the optical conductivity of graphene*, Phys. Rev. Lett. **101**, 196405 (2008).

[Mak10] K. F. Mak, C. Lee, J. Hone, J. Shan, and T. F. Heinz, *Atomically thin MoS2: a new direct-gap semiconductor*, Phys. Rev. Lett. **105**, 136805 (2010).

[Mal65] I. H. Malitson, *Interspecimen comparison of the refractive index of fused silica*, J. Opt. Soc. Am. **55**, 1205 (1965).

[Mam90] P. V. Mamyshev and S. V. Chernikov, *Ultrashort-pulse propagation in optical fibers.*, Opt. Lett. **15**, 1076 (1990).

[Man26] L. I. Mandelstam, *On light scattering by inhomogeneous media [in Russian]*, Zh. Rus. Fiz. Khim. Obs. **58**, 381 (1926).

[Mar79] D. Marcuse, *Interdependence of waveguide and material dispersion*, Appl. Opt. **18**, 2930 (1979).

[Mar13] A. Martinez and Z. Sun, *Nanotube and graphene saturable absorbers for fibre lasers*, Nature Photon. **7**, 842 (2013).

[Mas63] J. I. Masters, J. Ward, and E. Hartouni, *Laser Q-spoiling using an exploding film*, Rev. Sci. Instrum. **34**, 365 (1963).

[Mat92] V. J. Matsas, T. P. Newson, D. J. Richardson, and D. N. Payne, *Selfstarting passively mode-locked fibre ring soliton laser exploiting nonlinear polarisation rotation*, Electron. Lett. **28**, 1391 (1992).

[Max65] J. C. Maxwell, *A dynamical theory of the electromagnetic field*, Philos. Trans. R. Soc. London **155**, 459 (1865).

[McC62] F. J. McClung and R. W. Hellwarth, *Giant optical pulsations from ruby*, J. Appl. Phys. **33**, 828 (1962).

[McE08a] J. E. McElhenny, R. Pattnaik, and J. Toulouse, *Polarization dependence of stimulated Brillouin scattering in small-core photonic crystal fibers*, J. Opt. Soc. Am. B **25**, 2107 (2008).

[McE08b] J. E. McElhenny, R. K. Pattnaik, J. Toulouse, K. Saitoh, and M. Koshiba, *Unique characteristic features of stimulated Brillouin scattering in small-core photonic crystal fibers*, J. Opt. Soc. Am. B **25**, 582 (2008).

[Mea85] R. J. Mears, L. Reekie, S. B. Poole, and D. N. Payne, *Neodymium-doped silica single-mode fibre lasers*, Electron. Lett. **21**, 738 (1985).

[Mea87] R. Mears, L. Reekie, I. Jauncey, and D. Payne, *Low-noise erbium-doped fibre amplifier operating at 1.54 m*, Electron. Lett. **23**, 1026 (1987).

[Mid00] M. Midrio, M. Singh, and C. Someda, *The space filling mode of holey fibers: an analytical vectorial solution*, J. Light. Technol. **18**, 1031 (2000).

[Mil54] S. E. Miller, *Coupled wave theory and waveguide applications*, Bell Syst. Tech. J. **33**, 661 (1954).

[Mil98] D. Milam, *Review and assessment of measured values of the nonlinear refractive-index coefficient of fused silica*, Appl. Opt. **37**, 546 (1998).

[Mit86] F. M. Mitschke and L. F. Mollenauer, *Discovery of the soliton self-frequency shift*, Opt. Lett. **11**, 659 (1986).

[Moc65] H. W. Mocker and R. J. Collins, *Mode competition and self-locking effects in a Q-switched ruby laser*, Appl. Phys. Lett. **7**, 270 (1965).

[Mol80] L. Mollenauer, R. Stolen, and J. Gordon, *Experimental observation of picosecond pulse narrowing and solitons in optical fibers*, Phys. Rev. Lett. **45**, 1095 (1980).

[Mol84] L. F. Mollenauer and R. H. Stolen, *The soliton laser*, Opt. Lett. **9**, 13 (1984).

[Mol86] L. F. Mollenauer, J. P. Gordon, and M. N. Islam, *Soliton propagation in long fibers with periodically compensated loss*, IEEE J. Quantum Electron. **QE-22**, 157 (1986).

[Mon99] C. Montes, D. Bahloul, I. Bongrand, J. Botineau, A. Mamhoud, E. Picholle, and A. Picozzi, *Self-pulsing and dynamic bistability in cw-pumped Brillouin fiber ring lasers*, J. Opt. Soc. Am. B **16**, 932 (1999).

[MS11] A. Molina-Sánchez and L. Wirtz, *Phonons in single-layer and few-layer MoS2 and WS2*, Phys. Rev. B **84**, 155413 (2011).

[Nai08] R. R. Nair, P. Blake, A. N. Grigorenko, K. S. Novoselov, T. J. Booth, T. Stauber, N. M. R. Peres, and A. K. Geim, *Fine structure constant defines visual transperency of graphene*, Science **320**, 2008 (2008).

[Nak95] M. Nakazawa and K. Suzuki, *10 Gbit/s pseudorandom dark soliton data transmission over 1200km*, Electron. Lett. **31**, 1076 (1995).

[New11] G. New, *Nonlinear Optics*, Cambridge University Press (2011).

[Nos92] D. U. Noske, N. Pandit, and J. R. Taylor, *Subpicosecond soliton pulse formation from self-mode-locked erbium fibre laser using intensity dependent polarisation rotation*, Electron. Lett. **28**, 2185 (1992).

[Nov04] K. Novoselov, A. Geim, S. Morozov, D. Jiang, Y. Zhang, S. V. Dubonos, I. V. Grigorieva, and A. A. Firsov, *Electric field effect in atomically thin carbon films*, Science **306**, 666 (2004).

[OB00] A. Ortigosa-Blanch, J. C. Knight, W. J. Wadsworth, J. Arriaga, B. J. Mangan, T. A. Birks, and P. S. J. Russell, *Highly birefringent photonic crystal fibers*, Opt. Lett. **25**, 1325 (2000).

[Oka11] H. Okamoto, K. Kasuga, and Y. Kubota, *Efficient 521 nm all-fiber laser: splicing Pr3+-doped ZBLAN fiber to end-coated silica fiber*, Opt. Lett. **36**, 1470 (2011).

[Ost59] H. Osterberg, E. Snitzer, M. Polanyi, and R. Hilberg, *Optical wave-guide modes in small glass fibers. II. Experimental*, Progr. 1959 Annu. Meet. Opt. Soc. Am. **49**, 1128 (1959).

[Oue87] F. Ouellette, *Dispersion cancellation using linearly chirped Bragg grating filters in optical waveguides.*, Opt. Lett. **12**, 847 (1987).

[Ove14] G. Overton, A. Nogee, and C. Holton, *Laser Marketplace 2014: Lasers forge 21st century innovations*, Laser Focus World (2014).

[Pan15] M. Pang, X. Jiang, W. He, G. K. L. Wong, G. Onishchukov, N. Y. Joly, G. Ahmed, C. R. Menyuk, and P. S. J. Russell, *Stable subpicosecond soliton fiber laser passively mode-locked by gigahertz acoustic resonance in photonic crystal fiber core*, Optica **2**, 29 (2015).

[Pas95] H. M. Pask, R. J. Carman, D. C. Hanna, A. C. Tropper, C. J. Mackechnie, P. R. Barber, and J. M. Dawes, *Ytterbium-doped silica fiber lasers: versatile sources for the 1-1.2 µm region*, IEEE J. Sel. Top. Quantum Electron. **1**, 2 (1995).

[Pas97] R. Paschotta, J. Nilsson, A. C. Tropper, and D. C. Hanna, *Ytterbium-doped fiber amplifiers*, IEEE J. Quantum Electron. **33**, 1049 (1997).

[Pas99] R. Paschotta, R. Häring, E. Gini, H. Melchior, U. Keller, H. L. Offerhaus, and D. J. Richardson, *Passively Q-switched 0.1-mJ fiber laser system at 1.53 um*, Opt. Lett. **24**, 388 (1999).

[Pas04] R. Paschotta, *Noise of mode-locked lasers (Part I): numerical model*, Appl. Phys. B **79**, 153 (2004).

[Pas08] R. Paschotta, *Encyclopedia of Laser Physics and Technology*, Wiley-VCH (2008).

[Pat14] K. R. Paton, E. Varrla, C. Backes, R. J. Smith, U. Khan, A. O'Neill, C. Boland, M. Lotya, O. M. Istrate, P. King, T. Higgins, S. Barwich, P. May, P. Puczkarski, I. Ahmed, M. Moebius, H. Pettersson, E. Long, J. Coelho, S. E. O'Brien, E. K. McGuire, B. M. Sanchez, G. S. Duesberg, N. McEvoy, T. J. Pennycook, C. Downing, A. Crossley, V. Nicolosi, and J. N. Coleman, *Scalable production of large quantities of defect-free few-layer graphene by shear exfoliation in liquids*, Nat. Mater. **13**, 624 (2014).

[Pau25] W. Pauli, *Uber den Zusammenhang des Abschlusses der elektronengruppen im atom mit der komplexstruktur der spektren [On the connection between the completion of electron groups in an atom with the complex structure of spectra]*, Zeitschrift für Phys. **31**, 765 (1925).

[Pav13] F. S. Pavone and P. J. Campagnola (editors), *Second Harmonic Generation Imaging*, CRC Press (2013).

[Ped12] M. E. V. Pedersen, E. J. R. Kelleher, J. C. Travers, Z. Sun, T. Hasan, A. C. Ferrari, S. V. Popov, and J. R. Taylor, *Stable gain-guided soliton propagation in a polarized Yb-doped mode-locked fiber laser*, IEEE Photonics J. **4**, 1058 (2012).

[Pet14] C. R. Petersen, U. Møller, I. Kubat, B. Zhou, S. Dupont, J. Ramsay, T. Benson, S. Sujecki, N. Abdel-Moneim, Z. Tang, D. Furniss, A. Seddon, and O. Bang, *Mid-infrared supercontinuum covering the 1.413.3 µm molecular fingerprint region using ultra-high NA chalcogenide step-index fibre*, Nature Photon. **8**, 830 (2014).

[Pic91] E. Picholle, C. Montes, C. Leycuras, O. Legrand, and J. Botineau,*Observation of dissipative superluminous solitons in a Brillouin fiber ring laser*, Phys. Rev. Lett. **66**, 1454 (1991).

[Pil95] A. N. Pilipetskii, E. A. Golovchenko, and C. R. Menyuk, *Acoustic effect in passively mode-locked fiber ring lasers*, Opt. Lett. **20**, 907 (1995).

[Poc94] F. Pockels, *Ueber den einfluss des elektrostatischen feldes auf das optische verhalten piezoelektrischer krystalle [On the influence of the electrostatic field on the optical behavior of piezoelectric crystals]*, Abhandlungen der Gesellschaft der Wissenschaften Göttingen, Math. Klasse **39**, 1 (1894).

[Pol01] M. Pollnan and S. Jackson, *Erbium 3 µm fiber lasers*, IEEE J. Sel. Top. Quantum Electron. **7**, 30 (2001).

[Poo85] S. Poole, D. Payne, and M. Fermann, *Fabrication of low-loss optical fibres containing rare-earth ions*, Electron. Lett. **21**, 737 (1985).

[Pro04] N. P. Proukakis, N. G. Parker, D. J. Frantzeskakis, and C. S. Adams, *Analogies between dark solitons in atomic Bose-Einstein condensates and optical systems*, J. Opt. B **6**, S380 (2004).

[Rad52] L. Radushkevich and V. M. Lukyanovich, *The structure of carbon forming in thermal decomposition of carbon monoxide on an iron catalyst [in Russian]* (1952).

[Ram28] C. V. Raman and K. S. Krishnan, *A new type of secondary radiation*, Nature **121**, 501 (1928).

[Ran00] J. K. Ranka, R. S. Windeler, and A. J. Stentz, *Visible continuum generation in air-silica microstructure optical fibers with anomalous dispersion at 800 nm*, Opt. Lett. **25**, 25 (2000).

[Ray76] L. Rayleigh, *On waves*, Philos. Mag. **1**, 257 (1876).

[Ren08a] W. H. Renninger, A. Chong, and F. W. Wise, *Dissipative solitons in normal-dispersion fiber lasers*, Phys. Rev. A **77**, 023814 (2008).

[Ren08b] W. H. Renninger, A. Chong, and F. W. Wise, *Giant-chirp oscillators for short-pulse fiber amplifiers*, Opt. Lett. **33**, 3025 (2008).

[Ren12] W. H. Renninger, A. Chong, and F. W. Wise, *Pulse shaping and evolution in normal-dispersion mode-locked fiber lasers*, IEEE J. Sel. Top. Quantum Electron. **18**, 389 (2012).

[Rho13] M. Rhodes, G. Steinmeyer, J. Ratner, and R. Trebino, *Pulse-shape instabilities and their measurement*, Laser Photon. Rev. **7**, 557 (2013).

[Rox86a] C. B. Roxlo, M. Daage, D. P. Leta, K. S. Liang, S. Rice, A. F. Ruppert, and R. R. Chianelli, *Catalytic defects at molybdenum disulfide "edge" planes*, Solid State Ionics **22**, 97 (1986).

[Rox86b] C. B. Roxlo, M. Daage, A. F. Rupper, and R. R. Chianelli, *Optical absorption and catalytic activity of molybdenum sulfide edge surfaces*, J. Catal. **100**, 176 (1986).

[Rox87] C. B. Roxlo, R. R. Chianelli, H. W. Deckman, A. F. Ruppert, and P. P. Wong, *Bulk and surface optical absorption in molybdenum disulfide*, J. Vac. Sci. Technol. A **5**, 555 (1987).

[Rue48] G. Ruess and F. Vogt, *Höchstlamellarer kohlenstoff aus graphitoxyhydroxyd*, Monatshefte für Chemie und verwandte Teile anderer Wissenschaften **78**, 222 (1948).

[Run01] C. Runge, *Über empirische funktionen und die interpolation zwischen äquidistanten ordinaten [About empirical functions and the interpolation between equidistant ordinates]*, Zeitschrift für Math. und Phys. **46**, 224 (1901).

[Run14] A. F. J. Runge, C. Aguergaray, R. Provo, M. Erkintalo, and N. G. R. Broderick, *All-normal dispersion fiber lasers mode-locked with a nonlinear amplifying loop mirror*, Opt. Fiber Technol. **20**, 657 (2014).

[Run15] A. F. J. Runge, N. G. R. Broderick, and M. Erkintalo, *Observation of soliton explosions in a passively mode-locked fiber laser*, Optica **2**, 36 (2015).

[Rup95] P. A. Ruprecht, M. J. Holland, K. Burnett, and M. Edwards, *Time-dependent solution of the nonlinear Schrödinger equation for Bose-condensed trapped neutral atoms*, Phys. Rev. A **51**, 4704 (1995).

[Rus44] J. S. Russell, *Report on waves*, in *Rep. 14th Meet. Br. Assoc. Adv. Sci.*, p. 331 (1844).

[Rus06] P. S. Russell, *Photonic-Crystal Fibers*, J. Light. Technol. **24**, 4729 (2006).

[Sai05] K. Saitoh and M. Koshiba, *Empirical relations for simple design of photonic crystal fibers*, Opt. Express **13**, 267 (2005).

[SB90] M. Sheik-Bahae, A. A. Said, T.-H. Wei, D. Hagan, and E. Van Stryland, *Sensitive measurement of optical nonlinearities using a single beam*, IEEE J. Quantum Electron. **26**, 760 (1990).

[SC11] J. M. Soto-Crespo, P. Grelu, and N. Akhmediev,*Dissipative rogue waves: extreme pulses generated by passively mode-locked lasers*, Phys. Rev. E **84**, 016604 (2011).

[Sch58] A. L. Schawlow and C. H. Townes, *Infrared and optical masers*, Phys. Rev. **112**, 1940 (1958).

[Sch14] H. Schmidt, S. Wang, L. Chu, M. Toh, R. Kumar, W. Zhao, A. H. Castro Neto, J. Martin, S. Adam, B. Özyilmaz, and G. Eda, *Transport properties of monolayer MoS2 grown by chemical vapor deposition*, Nano Lett. **14**, 1909 (2014).

[Sel71] W. Sellmeier, *Zur erklärung der abnormen farbenfolge im spectrum einiger substanzen [To explain the abnormal sequence of colors in the spectrum of some substances]*, Ann. der Phys. und Chemie **219**, 272 (1871).

[Set03] S. Y. S. Set, H. Yaguchi, Y. Tanaka, M. Jablonski, Y. Sakakibara, A. Rozhin, M. Tokumoto, H. Kataura, Y. Achiba, and K. Kikuchi, *Mode-locked fiber lasers based on a saturable absorber incorporating carbon nanotubes*, in *Opt. Fiber Commun. Conf. 2003*, p. PD44 (2003).

[She85] R. M. Shelby, M. D. Levenson, and P. W. Bayer, *Guided acoustic-wave Brillouin scattering*, Phys. Rev. B **31**, 5244 (1985).

[She86] Y. R. Shen, *Surface second harmonic generation: a new technique for surface studies*, Annu. Rev. Mater. Sci. **16**, 69 (1986).

[She89] Y. Shen, *Optical second harmonic generation at interfaces*, Annu. Rev. Phys. Chem. **40**, 327 (1989).

[She00] Y. R. Shen, *Surface nonlinear optics: A historical perspective*, IEEE J. Sel. Top. Quantum Electron. **6**, 1375 (2000).

[Sho02] I. Shoji, T. Kondo, and R. Ito, *Second-order nonlinear susceptibilities of various dielectric and semiconductor materials*, Opt. Quantum Electron. **34**, 797 (2002).

[Sin03] O. V. Sinkin, R. Holzlöhner, S. Member, J. Zweck, and C. R. Menyuk, *Optimization of the split-step Fourier method in modeling optical-fiber communications systems*, J. Light. Technol. **21**, 61 (2003).

[Sip94] J. E. Sipe, L. Poladian, and C. M. D. Sterke, *Propagation through nonuniform grating structures*, J. Opt. Soc. Am. A **11**, 1307 (1994).

[Sma91] R. G. Smart, J. N. Carter, A. C. Tropper, D. C. Hanna, S. T. Davey, S. F. Carter, and D. Szebesta, *CW room temperature operation of praseodymium-doped fluorozirconate glass fibre lasers in the blue-green, green and red spectral regions*, Opt. Commun. **86**, 337 (1991).

[Smi72] R. G. Smith, *Optical power handling capacity of low loss optical fibers as determined by stimulated Raman and Brillouin scattering*, Appl. Opt. **11**, 2489 (1972).

[Smi11] S. V. Smirnov, S. M. Kobtsev, S. V. Kukarin, and S. K. Turitsyn,*Mode-locked fibre lasers with high-energy pulses*, in *Laser Syst. Appl.* (edited by K. Jakubczak), chapter 3, InTech (2011).

[Sni59] E. Snitzer and J. W. Hicks, *Optical wave-guide modes in small glass fibers. I. Theoretical*, Progr. 1959 Annu. Meet. Opt. Soc. Am. **49**, 1128 (1959).

[Sni61a] E. Snitzer, *Proposed fiber cavities for optical masers*, J. Appl. Phys. **32**, 36 (1961).

[Sni61b] E. Snitzer, *Optical maser action of Nd+3 in a barium crown glass*, Phys. Rev. Lett. **7**, 444 (1961).

[Sni65] E. Snitzer and R. Woodcock, *Yb3+-Er3+ glass laser*, Appl. Phys. Lett. **6**, 45 (1965).

[Sni88] E. Snitzer, H. Po, F. Hakimi, R. Tumminelli, and B. C. McCollum, *Double clad, offset core Nd fiber laser*, in *Proc. Conf. Opt. Fiber Sensors*, p. PD5 (1988).

[Sny83] A. W. Snyder and J. Love, *Optical Waveguide Theory*, Chapman and Hall Ltd (1983).

[Sof64a] B. H. Soffer, *Giant pulse laser operation by a passive, reversibly bleachable absorber*, J. Appl. Phys. **35**, 2551 (1964).

[Sof64b] B. H. Soffer and R. H. Hoskins, *Generation of giant pulses from a neodymium laser by a reversibly bleachable absorber*, Nature **204**, 276 (1964).

[Sol07] D. R. Solli, C. Ropers, P. Koonath, and B. Jalali,*Optical rogue waves*, Nature **450**, 1054 (2007).

[Son05] K. Y. Song, M. G. Herráez, and L. Thévenaz, *Observation of pulse delaying and advancement in optical fibers using stimulated Brillouin scattering*, Opt. Express **13**, 82 (2005).

[Sor64] P. P. Sorokin, J. J. Luzzi, J. R. Lankard, and G. D. Pettit, *Ruby laser Q-switching elements using phthalocyanine molecules in solution*, IBM J. Res. Dev. **8**, 182 (1964).

[Sor66] P. P. Sorokin and J. R. Lankard, *Stimulated emission observed from an organic dye chloro-aluminum phthalocyanine*, IBM J. Res. Dev. **10**, 162 (1966).

[Ste01] M. J. Steel, T. P. White, C. Martijn de Sterke, R. C. McPhedran, and L. C. Botten, *Symmetry and degeneracy in microstructured optical fibers*, Opt. Lett. **26**, 488 (2001).

[Ste10] W. M. Steen and J. Mazumder, *Laser Material Processing*, Springer (2010).

[Sto72] R. H. Stolen, E. P. Ippen, and A. R. Tynes, *Raman oscillation in glass optical waveguide*, Appl. Phys. Lett. **20**, 62 (1972).

[Sto75a] R. Stolen, *Phase-matched-stimulated four-photon mixing in silica-fiber waveguides*, IEEE J. Quantum Electron. **QE-11**, 100 (1975).

[Sto75b] J. Stone, *cw Raman fiber amplifier*, Appl. Phys. Lett. **26**, 163 (1975).

[Sto78] R. H. Stolen and C. Lin, *Self-phase-modulation in silica optical fibers*, Phys. Rev. A **17**, 1448 (1978).

[Sto82a] R. Stolen and J. Bjorkholm, *Parametric amplification and frequency conversion in optical fibers*, IEEE J. Quantum Electron. **QE-18**, 1062 (1982).

[Sto82b] J. Stone and G. E. Walrafen, *Overtone vibrations of OH groups in fused silica optical fibers*, J. Chem. Phys. **76**, 1712 (1982).

[Sto89] R. H. Stolen, J. P. Gordon, W. J. Tomlinson, and H. A. Haus, *Raman response function of silica-core fibers*, J. Opt. Soc. Am. B **6**, 1159 (1989).

[Sto08] J. M. Stone and J. C. Knight, *Visibly "white" light generation in uniform photonic crystal fiber using a microchip laser*, Opt. Express **16**, 2670 (2008).

[Str85] D. Strickland and G. Mourou, *Compression of amplified chirped optical pulses*, Opt. Commun. **56**, 219 (1985).

[Str05] M. Stratmann, T. Pagel, and F. Mitschke, *Experimental observation of temporal soliton molecules*, Phys. Rev. Lett. **95**, 1 (2005).

[Sud86] S. Sudo, T. Hosaka, H. Itoh, and K. Okamoto, *High-Δn, small-core single-mode fibres for efficient nonlinear optical effects* (1986).

[Sun10] Z. Sun, T. Hasan, F. Torrisi, D. Popa, G. Privitera, F. Wang, F. Bonaccorso, D. M. Basko, and A. C. Ferrari, *Graphene mode-locked ultrafast laser*, ACS Nano **4**, 803 (2010).

[Sun12] Z. Sun, T. Hasan, and A. C. Ferrari, *Ultrafast lasers mode-locked by nanotubes and graphene*, Phys. E **44**, 1082 (2012).

[Sut03] R. L. Sutherland, *Handbook of Nonlinear Optics*, Marcel Dekker (2003).

[Sve10] O. Svelto, *Principles of Lasers*, Springer (2010).

[Syl02] T. Sylvestre, S. Coen, P. Emplit, and M. Haelterman, *Self-induced modulational instability laser revisited: normal dispersion and dark-pulse train generation.*, Opt. Lett. **27**, 482 (2002).

[Sza65] A. Szabo and R. A. Stein, *Theory of laser giant pulsing by a saturable absorber*, J. Appl. Phys. **36**, 1562 (1965).

[Tam92] K. Tamura, H. A. Haus, and E. P. Ippen, *Self-starting additive pulse mode-locked erbium fibre ring laser*, Electron. Lett. **28**, 2226 (1992).

[Tam93] K. Tamura, E. Ippen, H. Haus, and L. Nelson, *77-fs pulse generation from a stretched-pulse mode-locked all-fiber ring laser*, Opt. Lett. **18**, 1080 (1993).

[Tan14] F. Tani, J. C. Travers, and P. St.J. Russell, *Multimode ultrafast nonlinear optics in optical waveguides: numerical modeling and experiments in kagomé photonic-crystal fiber*, J. Opt. Soc. Am. B **31**, 311 (2014).

[Tay92] J. R. Taylor, *Optical Solitons: Theory and Experiment*, Cambridge University Press (1992).

[Tay07] N. Taylor, *Laser: The Inventor, the Nobel Laureate, and the Thirty-Year Patent War*, Simon and Schuster (2007).

[Ter62] R. W. Terhune, P. D. Maker, and C. M. Savage, *Optical harmonic generation in calcite*, Phys. Rev. Lett. **8**, 404 (1962).

[Tho99] E. R. Thoen, E. M. Koontz, M. Joschko, P. Langlois, T. R. Schibli, F. X. Kaertner, E. P. Ippen, and L. A. Kolodziejski, *Two-photon absorption in semiconductor saturable absorber mirrors*, Appl. Phys. Lett. **74**, 3927 (1999).

[Thu91] R. N. Thurston and A. M. Weiner, *Collisions of dark solitons in optical fibers*, J. Opt. Soc. Am. B **8**, 471 (1991).

[Tia09a] X. Tian, M. Tang, X. Cheng, P. P. Shum, Y. Gong, and C. Lin, *High-energy wave-breaking-free pulse from all-fiber mode-locked laser system*, Opt. Express **17**, 7222 (2009).

[Tia09b] X. Tian, M. Tang, P. P. Shum, Y. Gong, C. Lin, S. Fu, and T. Zhang, *High-energy laser pulse with a submegahertz repetition rate from a passively mode-locked fiber laser*, Opt. Lett. **34**, 1432 (2009).

[Tom84] W. J. Tomlinson, R. H. Stolen, and C. V. Shank, *Compression of optical pulses chirped by self-phase modulation in fibers*, J. Opt. Soc. Am. B **1**, 139 (1984).

[Tom85] W. J. Tomlinson, R. H. Stolen, and A. M. Johnson, *Optical wave breaking of pulses in nonlinear optical fibers*, Opt. Lett. **10**, 457 (1985).

[Tom89] W. J. Tomlinson, R. J. Hawkins, A. M. Weiner, J. P. Heritage, and R. N. Thurston, *Dark optical solitons with finite-width background pulses*, J. Opt. Soc. Am. B **6**, 329 (1989).

[Ton12] S. Tongay, J. Zhou, C. Ataca, K. Lo, T. S. Matthews, J. Li, J. C. Grossman, and J. Wu, *Thermally driven crossover from indirect toward direct bandgap in 2D semiconductors: MoSe2 versus MoS2*, Nano Lett. **12**, 5576 (2012).

[Tow99] C. H. Townes, *How the Laser Happened: Adventures of a Scientist*, Oxford University Press (1999).

[Tra11] J. C. Travers, J. Morgenweg, E. D. Obraztsova, A. I. Chernov, E. J. R. Kelleher, and S. V. Popov, *Using the E22 transition of carbon nanotubes for fiber laser mode-locking*, Laser Phys. Lett. **8**, 144 (2011).

[Tre68] E. B. Treacy, *Compression of picosecond light pulses*, Phys. Lett. **28A**, 34 (1968).

[Tre69] E. B. Treacy, *Optical pulse compression with diffraction gratings*, IEEE J. Quantum Electron. **5**, 454 (1969).

[Tre00] R. Trebino, *Frequency-Resolved Optical Gating: The Measurement of Ultrashort Laser Pulses*, Springer (2000).

[Tur09] E. G. Turitsyna, G. Falkovich, V. K. Mezentsev, and S. K. Turitsyn, *Optical turbulence and spectral condensate in long-fiber lasers*, Phys. Rev. A **80**, 031804 (2009).

[vdL86] D. von der Linde, *Characterization of the noise in continuously operating mode-locked lasers*, Appl. Phys. B **39**, 201 (1986).

[vH54] A. C. S. van Heel, *A new method of transporting optical images without aberrations* (1954).

[Wal47] P. R. Wallace, *The band theory of graphite*, Phys. Rev. **71**, 622 (1947).

[Wal86] S. S. Walker, *Rapid modeling and estimation of total spectral loss in optical fibers*, J. Light. Technol. **4**, 1125 (1986).

[Wan12a] Q. H. Wang, K. Kalantar-Zadeh, A. Kis, J. N. Coleman, and M. S. Strano, *Electronics and optoelectronics of two-dimensional transition metal dichalcogenides*, Nat. Nanotechnol. **7**, 699 (2012).

[Wan12b] R. Wang, B. A. Ruzicka, N. Kumar, M. Z. Bellus, H.-Y. Chiu, and H. Zhao, *Ultrafast and spatially resolved studies of charge carriers in atomically thin molybdenum disulfide*, Phys. Rev. B **86**, 045406 (2012).

[Wan13] K. Wang, J. Wang, J. Fan, M. Lotya, A. O'Neill, D. Fox, Y. Feng, X. Zhang, B. Jiang, Q. Zhao, H. Zhang, J. N. Coleman, L. Zhang, and W. J. Blau, *Ultrafast saturable absorption of two-dimensional MoS2 nanosheets*, ACS Nano **7**, 9260 (2013).

[Wan14a] R. Wang, H.-C. Chien, J. Kumar, N. Kumar, H.-Y. Chiu, and H. Zhao, *Third-harmonic generation in ultrathin films of MoS2*, ACS Appl. Mater. Interfaces **6**, 314 (2014).

[Wan14b] S. Wang, H. Yu, H. Zhang, A. Wang, M. Zhao, Y. Chen, L. Mei, and J. Wang, *Broadband few-layer MoS2 saturable absorbers*, Adv. Mater. **26**, 3538 (2014).

[Wan15] W. Wang, X. Cui, E. Yang, Q. Fan, and B. Xiang, *Negative refraction in molybdenum disulfide*, Opt. Express **23**, 22024 (2015).

[Wei88a] A. M. Weiner, J. P. Heritage, R. J. Hawkins, R. N. Thurston, E. M. Kirschner, D. E. Leaird, and W. J. Tomlinson, *Experimental observation of the fundamental dark soliton in optical fibers*, Phys. Rev. Lett. **61**, 2445 (1988).

[Wei88b] A. M. Weiner, R. H. Stolen, and J. P. Heritage, *Self-phase modulation and optical pulse compression influenced by stimulated Raman scattering in fibers*, J. Opt. Soc. Am. B **5**, 364 (1988).

[Whi91] T. J. Whitley, C. A. Millar, R. Wyatt, M. C. Brierley, and D. Szebesta, *Upconversion pumped green lasing in erbium doped fluorozirconate fibre*, Electron. Lett. **20**, 1785 (1991).

[Wig90] P. G. J. Wigley, P. M. W. French, and J. R. Taylor, *Mode locking of a continuous wave neodymium doped fibre laser with a linear external cavity*, Electron. Lett. **26**, 1238 (1990).

[Wil69] J. A. Wilson and A. Yoffe, *The transition metal dichalcogenides: discussion and interpretation of the observed optical, electrical and structural properties*, Adv. Phys. **18**, 193 (1969).

[Wil98] J. W. G. Wilder, L. C. Venema, A. G. Rinzler, R. E. Smalley, and C. Dekker, *Electronic structure of atomically resolved carbon nanotubes*, Nature **391**, 59 (1998).

[Won11] H.-S. P. Wong and D. Akinwande, *Carbon nanotube and graphene device physics*, Cambridge University Press (2011).

[Woo62] E. J. Woodbury and W. K. Ng, *Ruby laser operation in the near IR*, Proc. IRE. **50**, 2367 (1962).

[Woo14a] R. I. Woodward, E. J. R. Kelleher, R. C. T. Howe, G. Hu, F. Torrisi, T. Hasan, S. V. Popov, and J. R. Taylor, *Tunable Q-switched fiber laser based on saturable edge-state absorption in few-layer molybdenum disulfide (MoS2)*, Opt. Express **22**, 31113 (2014).

[Woo14b] R. I. Woodward, E. J. R. Kelleher, D. Popa, T. Hasan, F. Bonaccorso, A. C. Ferrari, S. V. Popov, and J. R. Taylor, *Scalar nanosecond pulse generation in a nanotube mode-locked environmentally stable fiber laser*, IEEE Photonics Technol. Lett. **26**, 1672 (2014).

[Woo14c] R. I. Woodward, E. J. R. Kelleher, S. V. Popov, and J. R. Taylor, *Visible light stimulated Brillouin scattering in small-core photonic crystal fibers*, in *CLEO2014, OSA Tech. Dig.*, p. SM4N.1, Optical Society of America (2014).

[Woo14d] R. I. Woodward, E. J. R. Kelleher, S. V. Popov, and J. R. Taylor, *Stimulated Brillouin scattering of visible light in small-core photonic crystal fibers*, Opt. Lett. **39**, 2330 (2014).

[Woo14e] R. I. Woodward, E. J. R. Kelleher, T. H. Runcorn, D. Popa, T. Hasan, A. C. Ferrari, S. V. Popov, and J. R. Taylor, *Nanotube mode-locked, low repetition rate pulse source for fiber-based supercontinuum generation at low average pump power*, in *CLEO2014, OSA Tech. Dig.*, p. STh3N.8, Optical Society of America (2014).

[Woo14f] R. I. Woodward, E. J. R. Kelleher, T. H. Runcorn, S. V. Popov, F. Torrisi, R. C. T. Howe, and T. Hasan, *Q-switched fiber laser with MoS2 saturable absorber*, in *CLEO2014, OSA Tech. Dig.*, p. SM3H.6, Optical Society of America (2014).

[Woo15a] R. I. Woodward, T. Hasan, and E. J. R. Kelleher, *Optical nonlinearity of few-layer MoS2 devices and applications in short-pulse laser technology [Invited]*, in *Opto-Electronics Commun. Conf. 2015*, p. JSuB.08 (2015).

[Woo15b] R. I. Woodward, R. C. T. Howe, G. Hu, F. Torrisi, M. Zhang, T. Hasan, and E. J. R. Kelleher, *Few-layer MoS2 saturable absorbers for short-pulse laser technology: current status and future perspectives [Invited]*, Photonics Res. **3**, A30 (2015).

[Woo15c] R. I. Woodward, R. C. T. Howe, T. H. Runcorn, G. Hu, F. Torrisi, E. J. R. Kelleher, and T. Hasan, *Wideband saturable absorption in few-layer molybdenum diselenide (MoSe2) for Q-switching Yb-, Er- and Tm-doped fiber lasers*, Opt. Express **23**, 20051 (2015).

[Woo15d] R. I. Woodward and E. J. R. Kelleher, *2D saturable absorbers for fibre lasers*, Appl. Sci. **5**, 1440 (2015).

[Woo15e] R. I. Woodward and E. J. R. Kelleher, *Dark soliton statistics during radiation build-up of bright dissipative solitons in long-cavity mode-locked fiber lasers*, in *Eur. Quantum Electron. Conf. 2015*, pp. EF–5.4 (2015).

[Woo15f] R. I. Woodward, E. J. R. Kelleher, T. H. Runcorn, S. Loranger, D. Popa, V. J. Wittwer, A. C. Ferrari, S. V. Popov, R. Kashyap, and J. R. Taylor, *Fiber grating compression of giant-chirped nanosecond pulses from an ultra-long nanotube mode-locked fiber laser*, Opt. Lett. **40**, 387 (2015).

[Woo15g] R. I. Woodward, E. J. R. Kelleher, T. H. Runcorn, S. Loranger, D. Popa, V. J. Wittwer, A. C. Ferrari, S. V. Popov, R. Kashyap, and J. R. Taylor, *Nanosecond to picosecond fiber Bragg grating compression of giant-chirped pulses from an ultra-long mode-locked fiber laser*, in *Eur. Conf. Lasers Electro-Optics 2015*, pp. CJ–9.6, Optical Society of America (2015).

[Woo15h] R. I. Woodward, E. Picholle, and C. Montes, *Solitons Brillouin en présence de dispersion acoustique dans un oscillateur à fibre optique micro-structurée*, in *Les Journées Natl. d'Optique Guid.* (2015).

[Woo16] R. I. Woodward and E. J. R. Kelleher, *Dark solitons in laser radiation build-up dynamics*, Phys. Rev. E **93**, 1 (2016).

[Wu15] S. Wu, S. Buckley, J. R. Schaibley, L. Feng, J. Yan, D. G. Mandrus, F. Hatami, W. Yao, J. Vučković, A. Majumdar, and X. Xu, *Monolayer semiconductor nanocavity lasers with ultralow thresholds*, Nature **520**, 69 (2015).

[Xia14] H. Xia, H. Li, C. Lan, C. Li, X. Zhang, S. Zhang, and Y. Liu, *Ultrafast erbium-doped fiber laser mode-locked by a CVD-grown molybdenum disulfide (MoS2) saturable absorber*, Opt. Express **22**, 17341 (2014).

[Yab87] E. Yablonovitch, *Inhibited spontaneous emission in solid-state physics and electronics*, Phys. Rev. Lett. **58**, 2059 (1987).

[Yam87] M. Yamada and K. Sakuda, *Analysis of almost-periodic distributed feedback slab waveguides via a fundamental matrix approach*, Appl. Opt. **26**, 3474 (1987).

[Yar73] A. Yariv, *Coupled-mode theory for guided-wave optics*, IEEE J. Quantum Electron. **QE-9**, 919 (1973).

[Yar07] A. Yariv and P. Yeh, *Photonics: Optical Electronics in Modern Communications*, Oxford University Press (2007).

[Yin14] X. Yin, Z. Ye, D. A. Chenet, Y. Ye, K. O'Brien, J. C. Hone, and X. Zhang, *Edge nonlinear optics on a MoS2 atomic monolayer*, Science **344**, 488 (2014).

[Yu10] P. Y. Yu and M. Cardona, *Fundamentals of Semiconductors: Physics and Materials Properties*, Springer (2010).

[Zab65] N. J. Zabusky and M. D. Kruskal, *Interaction of "solitons" in a collisionless plasma and the recurrence of initial states*, Phys. Rev. Lett. **15**, 240 (1965).

[Zak68] V. E. Zakharov, *Stability of periodic waves of finite amplitude on the surface of a deep fluid*, J. Appl. Mech. Tech. Phys. **9**, 190 (1968).

[Zak72] V. E. Zakharov and A. B. Shabat, *Exact theory of two-dimensional self-focusing and one-dimensional self-modulation of waves in nonlinear media*, Sov. Phys. JETP **34**, 62 (1972).

[Zak73] V. E. Zakharov and A. B. Shabat, *Interaction between solitons in a stable medium*, Sov. Phys. JETP **37**, 823 (1973).

[Zak98] V. E. Zakharov and S. Wabnitz (editors), *Optical Solitons: Theoretical Challenges and Industrial Perspectives*, Springer (1998).

[Zar91] F. Zarinetchi, S. P. Smith, and S. Ezekiel, *Stimulated Brillouin fiber-optic laser gyroscope*, Opt. Lett. **16**, 229 (1991).

[Zel86] B. Y. Zel'dovich and A. N. Pilipetski, *Influence of sound diffraction on stimulated Brillouin scattering in a single-mode waveguide*, Sov. J. Quantum Electron. **546**, 546 (1986).

[Zha89] W. Zhao and E. Bourkoff, *Periodic amplification of dark solitons using stimulated Raman scattering*, Opt. Lett. **14**, 808 (1989).

[Zha92] Z. Zhang, L. Qian, D. Fan, and X. Deng, *Gallium arsenide: A new material to accomplish passively mode-locked Nd:YAG laser*, Appl. Phys. Lett. **60**, 419 (1992).

[Zha09] H. Zhang, D. Y. Tang, L. M. Zhao, and X. Wu, *Dark pulse emission of a fiber laser*, Phys. Rev. A **80**, 045803 (2009).

[Zha13a] L. Zhang, A. R. El-Damak, Y. Feng, and X. Gu, *Experimental and numerical studies of mode-locked fiber laser with large normal and anomalous dispersion*, Opt. Express **21**, 12014 (2013).

[Zha13b] W. Zhao, R. M. Ribeiro, M. Toh, A. Carvalho, C. Kloc, A. H. C. Neto, and G. Eda, *Origin of indirect optical transitions in few-layer MoS2 , WS2 , and WSe2*, Nano Lett. **13**, 5627 (2013).

[Zha14a] H. Zhang, S. B. Lu, J. Zheng, J. Du, S. C. Wen, D. Y. Tang, and K. P. Loh, *Molybdenum disulfide (MoS2) as a broadband saturable absorber for ultra-fast photonics*, Opt. Express **22**, 7249 (2014).

[Zha14b] Y. Zhang, T.-R. Chang, B. Zhou, Y.-T. Cui, H. Yan, Z. Liu, F. Schmitt, J. Lee, R. Moore, Y. Chen, H. Lin, H.-T. Jeng, S.-K. Mo, Z. Hussain, A. Bansil, and Z.-X. Shen, *Direct observation of the transition from indirect to direct bandgap in atomically thin epitaxial MoSe2*, Nat. Nanotechnol. **9**, 111 (2014).

[Zha15] M. Zhang, R. C. T. Howe, R. I. Woodward, E. J. R. Kelleher, F. Torrisi, G. Hu, S. V. Popov, J. R. Taylor, and T. Hasan, *Solution processed MoS2-PVA composite for sub-bandgap mode-locking of a wideband tunable ultrafast Er:fiber laser*, Nano Res. **8**, 1522 (2015).

[Zho13] W. Zhou, X. Zou, S. Najmaei, Z. Liu, Y. Shi, J. Kong, J. Lou, P. M. Ajayan, B. I. Yakobson, and J.-C. Idrobo, *Intrinsic structural defects in monolayer molybdenum disulfide*, Nano Lett. **13**, 2615 (2013).

[Zho15] K.-G. Zhou, M. Zhao, M.-J. Chang, Q. Wang, X.-Z. Wu, Y. Song, and H.-L. Zhang, *Size-dependent nonlinear optical properties of atomically thin transition metal dichalcogenide nanosheets*, Small **11**, 694 (2015).

[Zhu13] G. Zhu, X. Zhu, K. Balakrishnan, R. a. Norwood, and N. Peyghambarian, *Fe2+:ZnSe and graphene Q-switched singly Ho3+-doped ZBLAN fiber lasers at 3 µm*, Opt. Mater. Express **3**, 1365 (2013).

[Zir91] M. Zirngibl, L. W. Stulz, J. Stone, J. Hugi, D. J. DiGiovanni, and P. B. Hansen, *1.2 ps pulses from passively mode-locked laser diode pumped Er-doped fibre ring laser*, Electron. Lett. **27**, 1734 (1991).

[Zol05] F. Zolla, G. Renversez, and A. Nicolet, *Foundations of Photonic Crystal Fibres*, Imperial College Press (2005).

ACRONYMS

AFM atomic force microscopy

ASE amplified spontaneous emission

CCD charge-coupled device

CFBG chirped fibre Bragg grating

CNT carbon nanotube

CPA chirped-pulse amplification

CW continuous wave

DOLP degree of linear polarisation

DOP degree of polarisation

FBG fibre Bragg grating

FFT Fast Fourier Transform

FROG frequency-resolved optical gating

FSR free spectral range

FWHM full width at half maximum

FWM four-wave mixing

FWQM full width at quarter maximum

GCO giant-chirp oscillator

GNLSE generalised NLSE

GVD group velocity dispersion

HWP half-wave plate

IR infrared

LPE liquid-phase exfoliation

NALM nonlinear amplifying loop mirror

NLSE nonlinear Schrödinger equation

NOLM nonlinear-optical loop mirror

NPE nonlinear polarisation evolution

PC polarisation controller

PCF photonic crystal fibre

PM polarisation-maintaining

PVA polyvinyl alcohol

QD quantum dot

QWP quarter-wave plate

RF radio frequency

SA saturable absorber

SBS stimulated Brillouin scattering

SEM scanning electron microscope

SESAM semiconductor saturable absorber mirror

SHG second-harmonic generation

SPM self-phase modulation

TBP time-bandwidth product

THG third-harmonic generation

TMD transition metal dichalcogenide

TPA two-photon absorption

UV ultraviolet

WDM wavelength division multiplexer

XPM cross-phase modulation

ZDW zero-dispersion wavelength